STRUCTURAL HEALTH MONITORING OF INLAND NAVIGATION INFRASTRUCTURE

BY

BRIAN A. EICK

DISSERTATION

Submitted in partial fulfillment of the requirements
for the degree of Doctor of Philosophy in Civil Engineering
in the Graduate College of the
University of Illinois at Urbana-Champaign, 2020

Urbana, Illinois

Doctoral Committee:

Professor Billie F. Spencer, Jr., Chair and Director of Research
Professor Larry A. Fahnestock
Professor John S. Popovics
Dr. Matthew D. Smith, U.S. Army Corps of Engineers

ABSTRACT

The inland navigation system in the U.S. is a civil infrastructure network that relies on the performance of a vast array of infrastructure assets scattered across the nation to function successfully. The system is critical to the U.S. economy, allowing the transportation of billions of dollars in goods annually. The primary infrastructure assets of the inland navigation system are locks and dams, which are structures that allow vessels to traverse inland waterways. Of all the components of locks and dams, the gates are the weak links and are the primary cause of closures and downtime on the inland navigation system. The closure of a lock and dam can have significant impacts to the economy, because traffic will be unable to move on the river and goods will remain stalled on the waterways.

Inspection of lock and dam gates is expensive, generally requiring the complete closure of the site, and occurs relatively infrequently. Thus, lock gates are generally maintained in a reactive, manner, meaning they are operated until something breaks, at which time a portion of the inland navigation system is shut down for emergency repairs. The research presented herein addresses the difficulty in inspection of lock gates by developing a structural health monitoring (SHM) system that can be used by the stakeholders of inland navigation infrastructure to obtain the necessary information to assess the integrity and condition of their structures continuously. While SHM is being increasingly implemented on civil infrastructure, such as framed buildings and bridges, research into the application of SHM on navigation infrastructure is lacking.

To accomplish the goal of developing an SHM system for navigation infrastructure, this research focuses on development of methods for the detection and assessment of several critical problems common to lock and dam gates, with emphasis given to the most common gates used in the U.S.; miter gates and Tainter gates. The layout of this dissertation is as follows: first, a general overview of inland navigation is given that explores the importance of locks and dams to the global economy. Then, design and behavior of miter and Tainter gates are discussed in detail. As an initial step to the development of a structural health monitoring system, numerical models are created of lock gates to obtain detailed information on the behavior of the structures both with and without the presence of damage. A discussion of best practices for numerical models of lock gates is provided with the models of two specific lock gates used as examples. Next, the methods

developed for this dissertation to detect and assess the identified critical issues of lock gates are discussed.

The first method discussed is the use of Principal Component Analysis combined with a novel strain gage data processing technique to detect boundary condition degradation of miter gates. The developed method addresses environmental variation frequently present in strain gage data and is validated by utilizing data from an in-service miter gate combined with results of a numerical model. Next, a discussion is given on the development of a non-contact, vision-based method to monitor the tension in a component of miter gates known as diagonals. The method utilizes optical-flow to track the displacement of a vibrating diagonal, from which the frequency is obtained and the tension found using Euler-Bernoulli beam theory. Partial submersion of the diagonals and the non-prismatic nature of the components are challenges that are addressed, and the method is validated with experimental and field data. Finally, the methods utilized to detect uneven hoisting of a Tainter gate are discussed. This method relies on a multi-faceted approach to show definitively that uneven hoisting is occurring on an operating Tainter gate. This approach is performed first by comparing strain gage data to numerical model results. Then data collected from inclinometers on the gate are inspected for the presence of uneven hoisting. Finally, indirect measurements of the tension in hoisting cables using vibration measurements taken during gate operation is used to show that an operating Tainter gate is hoisting unevenly. All three approaches are shown to be sensitive to the presence of uneven hoisting.

The research presented herein addresses critical issues with inland navigation infrastructure. The method developed in this dissertation will be leveraged to provide the owners and operators of lock gate with the necessary information to extend the useful life of this critical infrastructure. More importantly, a structural health monitoring system of inland navigation infrastructure will aid in ensuring the continued operability of the inland navigation system, allowing river-borne traffic to continue to get goods to market.

For my son, Sage.

May you read this far off in the future and be proud.

Acknowledgments

I would initially like to express my sincerest gratitude to my advisor, Professor Bill Spencer. As I started the Ph.D. program, the quality of students in his research group, coupled with his intelligence and expertise, made the prospect of pursuing a Ph.D. daunting at best, and terrifying at worst. His guidance and always-humble demeanor helped me navigate the intricacies of scholastic life and helped me build the confidence and abilities to get to where I am today. Where I saw in myself a brash and slovenly hooligan, infinitely out of place in the world of academia, he saw in me the ability to succeed and he never let me waiver in my path towards obtaining my degree. For that, I am infinitely grateful.

I would like to acknowledge the valuable input from my committee, all of whom were, in some way, teachers of mine. Their world-renowned expertise and dedication to scholastic pursuit have set the highest of standards for myself to follow in all aspects of my academic and professional life. Special recognition must be given to Dr. Matthew D. Smith of the U.S. Army Corps of Engineers. He has been a constant champion of the work I do and has been a mentor in the truest sense of the word. He has (and I say this with no malice) unapologetically thrashed many of my ideas into oblivion, demanding that I have a sound and reasonable footing for any of the work I propose, which has forced me to be a more rigorous and confident researcher. I very much owe a great deal of where I am today to his advice, support, and (what I want to believe is diligently earned) trust.

I greatly appreciate the collaborative efforts and assistance of fellow Smart Structures Technology Lab members. The members of SSTL have the brightest minds I have ever had the privilege of working with and being in the group was a truly humbling experience. Particularly, I would like to acknowledge Zachary Treece, and Yasutaka (Yasu) Narazaki. Zach performed much of the initial work on miter gate gap detection. His initial efforts form the backbone of the work presented herein. Zach's support as the project transitioned from his to my hands laid the foundation for the success of this dissertation as a whole. Yasu provided valuable input on vision-based monitoring and invaluable assistance in obtaining the videos used for the research performed herein.

Much of the research herein would've been impossible without the valuable insight from the researchers, engineers and maintenance personnel from the US Army Corps of Engineers. Stuart

Foltz and Steve Sweeney have been invaluable resources in navigating USACE bureaucracy. Travis Fillmore has been an excellent collaborator and is an all-around great guy. In regards to this dissertation, Travis has helped immensely in the numerical modeling of lock gates, and has provided figures and verbiage for me to use to aid in the explanation of numerical modeling constraints and interactions. I would additionally like to acknowledge Quincy Alexander, Chris Lunderman, Chuck Ellison, Eric Johnson, Rob Kelsey, and Frank Salber. Their assistance came in many forms, from help with field tests to detailed information on structural behavior and design of lock gates.

Of course, it goes without saying that I would never be where I am without the unwavering love and support from my family. I must express how truly grateful I am to have amazing parents, Ron and Lori Eick. They, who had children at a young age and struggled at blue collar jobs to ensure that I had everything I would ever need, raised me up from an unassuming apartment on the south-side of Chicago to now obtaining a Ph.D. from one of the top programs in the world. I hope you see that this accomplishment is very much yours, too. I must acknowledge my very first teachers and friends (and enemies), my brother Ron Eick Jr., and my sister Kelly Pavloski. Everything I am, I owe to you guys.

There is, of course, the shy young woman I met at a bus stop in Yosemite National Park nearly 20 years ago, and now my wife of 15 years. Ever since I've known her, even well before the outbreak of COVID-19 and the accompanying spate of panic buying seen in the population, she has (for whatever reason) stockpiled daily essentials, "just in case". It should be noted, then, that the endless supply of toilet paper in my household is, in no small way, responsible for the success of this dissertation. To my wife Po, who has been with me through thick and thin, with whom I roughed it around the world and back, all jokes aside, I don't know what else I can say other than I love you. As we continue on our latest adventure in form of parenting our son Sage, I hope you see that this was worth it.

Finally, like the liner notes of a good punk rock album, this list would feel wholly incomplete without a sincere, explicit, and heartfelt thank you to Paul J. Slonskis. I wouldn't not [sic] want to also thank Joe Klochan. Through the years, their friendship has allowed me to never lose sight of who I am, where I'm from, and what truly matters. They are the providers of an infinitely valuable commodity, namely company amongst whom I can let loose and simply just be.

TABLE OF CONTENTS

Chapter 1. Introduction

Inland navigation of waterborne transportation refers to the movement of vessels and associated cargo on any intracontinental riverway. Inland navigation can refer to anything from the small, such as a small fishing boat, or to the very large such as ocean-going container ships on the Panama Canal. Generally speaking, inland riverways are too shallow to facilitate the transportation of large vessels; however, motivated by the efficiency and significant economic benefit of waterborne transportation, infrastructure is frequently constructed to increase the depth of water on riverways. The research presented in this dissertation focuses on this very economically important infrastructure, namely locks and dams. Emphasis is placed on the steel gates of the locks and dams which, as will be shown, are the weak links in inland navigation infrastructure systems. Inspection of these steel gates is shown to be challenging, expensive, and therefore often lacking; as a result, these steel gates are generally maintained in a reactive, rather than proactive, manner. That is, the steel gates are typically operated until something breaks, at which time a portion of the inland navigation system is shut down for emergency repairs. Indeed, the most common cause of the inability to transport goods on an inland navigation system is emergency maintenance of the steel gates of a lock or dam. To address this shortcoming, the research presented herein aims to develop a systematic approach to obtaining continuous, real-time, actionable information that the lock gate owners and operators can use to determine the condition of the structures they are tasked to maintain. This information can then be used to allocate maintenance resources and prevent extended unexpected closures of the inland navigation system by proactively addressing issues as they arise. Thus, the ultimate goal of the research presented herein is the development of methodologies to monitor and help prevent sudden failures and mitigate the occurrence of unexpected emergency repairs of the steel gates used in inland navigation infrastructure systems to keep traffic and goods moving to market.

To place the research presented herein in the proper technical perspective, an overview of inland navigation is presented in this chapter. Emphasis is given to the efficiency and significant economic importance of the system. Subsequently, the infrastructure of interest to this research is introduced, with focus given to the particular steel gates that are investigated herein, namely miter and Tainter gates. Next, an overview of Structural Health Monitoring (SHM) is provided. In the literature, very little work can be found on SHM of inland navigation infrastructure; nevertheless,

a discussion is provided on historical monitoring methods and other similar topics for inland navigation infrastructure. The efforts underway by the US Army Corps of Engineers (USACE) to implement SHM systems on their existing inland navigation infrastructure is discussed, and details are provided. Finally, a layout of the remainder of the dissertation is provided, which provides an overview of the specific work performed towards the development of an SHM system for inland navigation infrastructure.

1.1. Inland navigation systems

Inland navigation is an enterprise with global importance and impact. For example, in Europe, 40,000 km of navigable waterways are maintained (Inland Navigation Europe 2020). In China, the country with the largest inland navigation system, 126,300 km of inland riverways are navigable (Asia Development Bank 2016). The inland navigation system in the U.S. is comprised of 40,000 km of riverways that connect inland cities and businesses to major coastal ports. Figure 1.1 shows an overview of the inland navigation system in the U.S., where the yellow circles represent major inland cities, the cyan circles represent major costal ports, and the blue lines are the inland waterways that connect the two.

Figure 1.1 The inland navigation system in the U.S. (Institute for Water Resorces 2012).

In terms of economic importance in the U.S., towboats carrying barges along inland waterways are the vessels with highest priority. These towboats require a depth of water of at least 9 feet to navigate a river, which is generally not available. A typical towboat carrying 15 barges is shown

in Figure 1.2. To address the issue of generally shallow riverways, locks and dams are constructed to provide the necessary depth of water to facilitate efficient waterborne traffic. In the U.S., the organization primarily responsible for operating and maintaining the inland navigation system is the United States Army Corps of Engineers (USACE). The USACE operates and maintains 236 lock chambers at 191 lock sites on 41 US waterways (U.S. Army Corps of Engineers 2014a). A typical lock and dam site is shown in Figure 1.2, while an aerial view of the Greenup Lock and Dam on the Ohio River is shown in Figure 1.3, (this site is used extensively in the course of this research). The transverse-oriented portion of the structure in the image is the dam. The dam is what physically maintains the navigable depth of water in the river, and the elevation of the water on the upstream side of the dam will be significantly higher than on the downstream side of the dam. The differential in water elevation on either side of the dam requires a lock chamber to allow boats to traverse the dam. The portion of the structure along the axis of the river in Figure 1.3 shows a typical lock chamber, with a towboat carrying 11 barges waiting to enter.

Figure 1.2. Typical towboat carrying 15 barges through a lock site (U.S. Army Corps of Engineers n.d.).

Figure 1.3. The Greenup Lock and Dam site on the Ohio River (U.S. Army Corps of Engineers n.d.).

A lock, in the navigation sense, is effectively an elevator in a river. The lock is comprised of a long concrete chamber with a gate on each end. The gates, which are typically made of steel, work as the damming surface on the lock chamber, allowing the water level in the chamber to raise and lower as needed. Figure 1.4 shows the typical procedure of a vessel passing through a lock, with the lock gates represented as solid black rectangles. Figure 1.4-a shows the vessel entering the lock, with the water levels in the lock chamber equal to the downstream river water level, allowing the downstream gate to open. In Figure 1.4-b, the vessel enters the lock chamber, and both gates close allowing the chamber water levels to raise. Finally, in Figure 1.4-c, the water levels in the lock chamber match the upstream water level, allowing the upstream gate to open and the vessel to exit the lock.

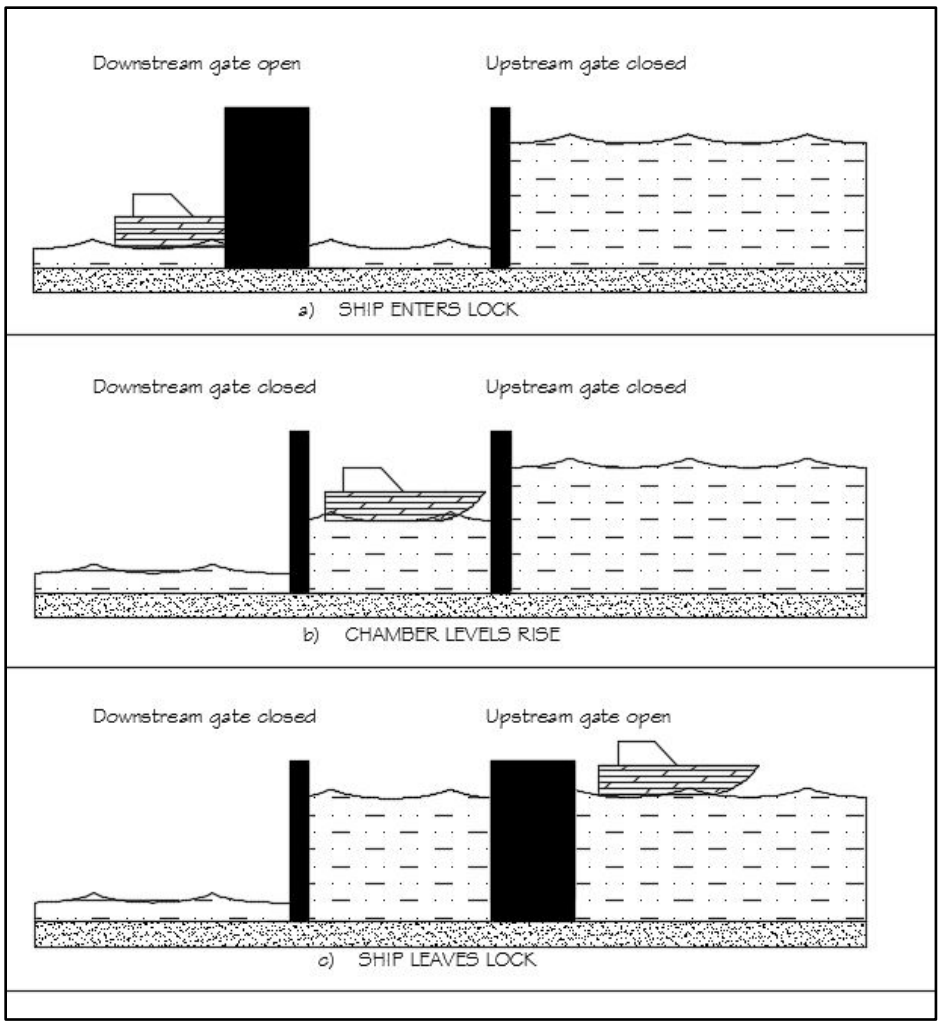

Figure 1.4. Typical vessel passage through a lock. a) Rear gate opens, vessel enters lock, b) both gates are closed and water levels in the chamber adjust. c) Forward gate opens and vessel leaves the lock.

Many types of lock and dam gates are used throughout the world; however, the research presented herein focuses on miter gates and Tainter gates. The focus on these particular gates is due to the fact that they are, by far, the most common gates found throughout the U.S. inland navigation system. Miter gates comprise over 90% of all lock gates in the U.S. They are characterized by their primary load carrying members and are classified as either vertically framed (using vertical steel girders) or horizontally framed (using horizontal steel girders). A miter gate consists of two leaves, which, when closed, are referred to as "mitered" due to the resemblance that the two leaves make to a miter joint that one might find in carpentry. Figure 1.5 shows a typical elevation view of an in-service miter gate in the mitered position and acting as a damming surface.

Figure 1.5. Horizontally framed miter gate at Lock 27 on the Mississippi River.

A Tainter gate is quite different from a miter gate. They are radial type gates that swing up and down, rather than open and closed. The damming surface on a Tainter gate resembles a circular arc, and each side swings about a central pivot point by means of hoisting or lifting chains. Unlike miter gates, Tainter gates are more commonly used on dams; however, there are documented instances of Tainter gates used as the damming surface of a lock chamber, such as the upstream gate at The Dalles Lock and Dam on the Columbia River in Oregon. A typical Tainter gate in-service is seen in Figure 1.6. For both miter and Tainter gates there are several components which are critical to the continued operability of the structure, and the behavior, design, and common issues of these structure is elaborated on in Chapter 2 of this dissertation.

Figure 1.6. Typical Tainter gate on a dam. (U.S. Army Corps of Engineers n.d.).

1.2. Efficiency and economic importance of inland navigation

The structures discussed above are complicated systems that require an immense amount of investment to operate and maintain; however, the efficiency and economic value of the infrastructure far outweighs the cost. Indeed, inland navigation systems are extremely efficient in transporting goods. For example, the typical method of transportation on the inland navigation system in the U.S. is via a towboat carrying 15 barges (generally referred to as a 15-barge tow, see Figure 1.2). As illustrated in Figure 1.7, one modern 15-barge tow on the Mississippi River is capable of transporting upwards of 26,000 tons of cargo, equivalent to 1050 semi-trucks or 240 rail cars (U.S. Army Corps of Engineers 2015). In terms of fuel efficiency, a barge can move one ton of goods 616 miles by using one gallon of fuel, whereas a train can move the same ton only 478 miles, and a semi-truck only 150 miles (St Paul District, US Army Corps of Engineers n.d.).

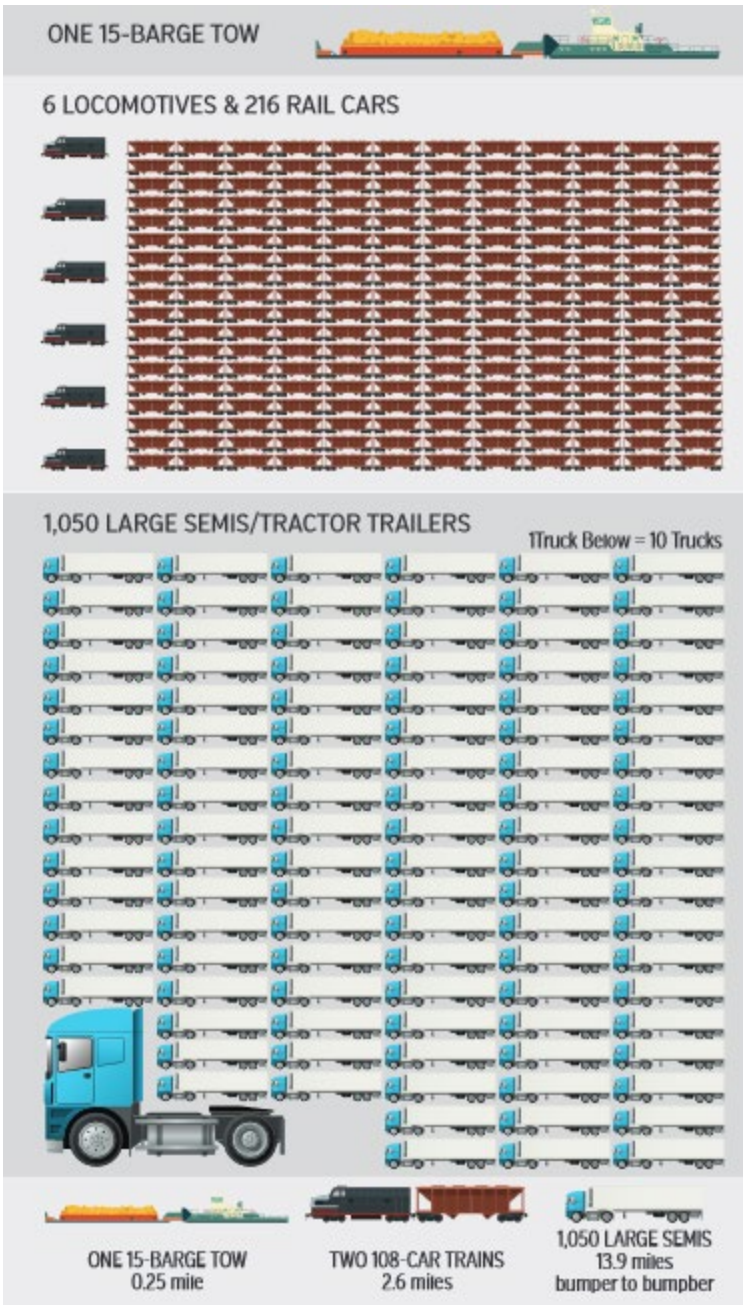

Figure 1.7. Equivalent units required for same capacity of cargo (St Paul District, US Army Corps of Engineers n.d.).

Moreover, inland navigation infrastructure is critical to the global economy, as it facilitates the transportation of trillions of dollars in goods annually. In Europe, over 540,000 metric tons of goods were shipped on inland waterways in 2018 (Eurostat 2019), while in China 3.5 billion metric tons of cargo was handled at river ports on inland waterways amounting to a 51% share of freight movement in 2014 (the most recent year with data available) (Asia Development Bank 2016). In the U.S., Figure 1.8 shows the amount of goods, in millions of tons, processed through the 10 most

used lock and dam sites in the year 2015 (most recent year with data available) (Kelley 2016). The most used site, Lock and dam 52, is the lock site on the Ohio River that is closest to the Mississippi River (it has since been replaced with a lock and dam site called Olmstead). At this one site alone, over 80 million tons of goods (in the form of corn, coal, etc.), passed through the lock, amounting to billions of dollars of commerce.

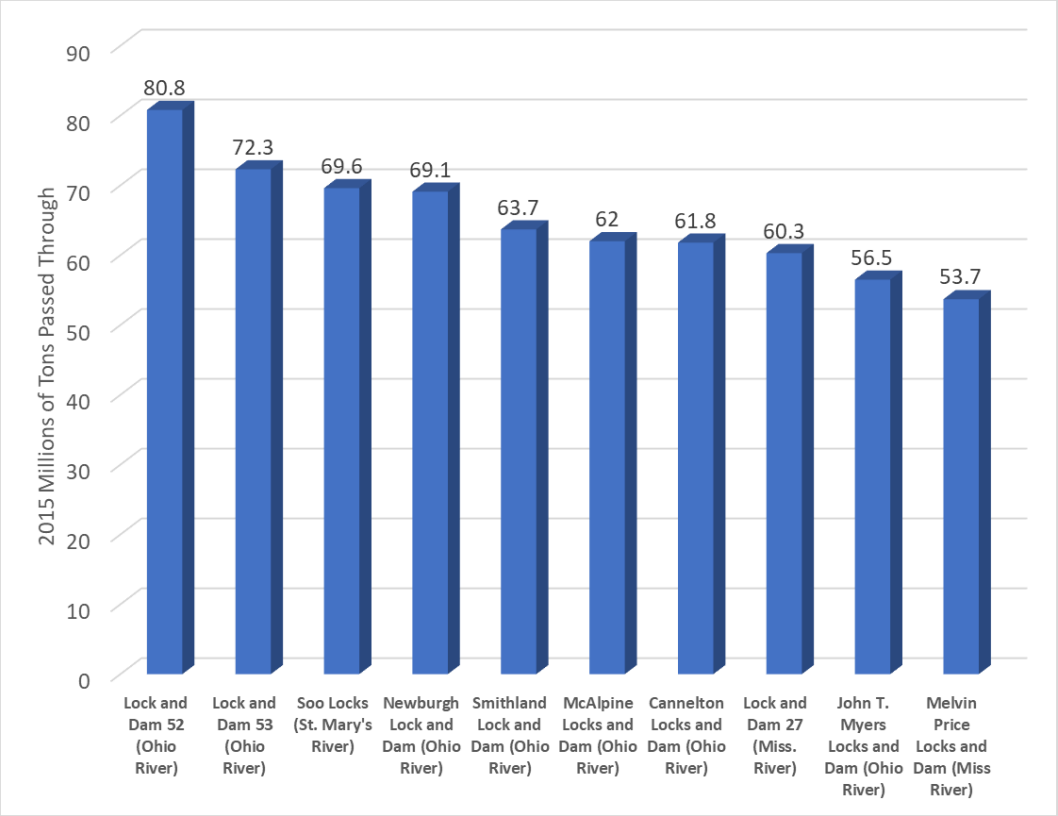

Figure 1.8. Millions of tons of goods processed through the 10 most used lock and dam sites in the U.S. in 2015 (Kelley 2016).

Given their economic importance, proper maintenance of locks and early detection of damage is crucial, because the unplanned closure of a lock site can have a ripple effect along an entire river. That is, closure of Lock 52 on the Ohio River for emergency repairs would stall traffic on the entire river, affecting businesses as far away as Pittsburg, which is over 900 miles away. Indeed, one estimate notes that the closure of a lock in the US, due to repairs or maintenance, would cost the US economy up to $3 million per day (Gillerman 2013). However, USACE must operate, maintain and repair these aging resources with an increasingly tight budget. USACE estimated that an investment of $13 billion dollars in inland waterways would be required between 2013 and 2020 to keep delays on these waterways from growing beyond their current level (U.S. Army Corps of Engineers 2015); however, only an estimated $7 billion dollars was budgeted

during this time (American Society of Civil Engineers 2013). Due to this shortfall in funding, inspection and maintenance of the Nation's locks is behind schedule. Consequently, unexpected failures and more extensive repairs are likely to occur with greater frequency in the future. Early evidence of failures due to delayed maintenance and inspection include the high profile failures at the Markland Lock and Dam in September of 2009 (Chapman 2010) (James and Zhang 1996)and the Chickamauga Lock and Dam in October of 2014 (Murray 2014) (Smith, et al. 2017).

While many components comprise the infrastructure necessary for the operation of an inland navigation system, the structural weak links in the system are the steel lock and dam gates. These gates are designed to swing open and closed several times a day; the cyclic nature of the loading on these gates makes them prone to fatigue cracking. Moreover, they are steel structures that sit in an aquatic environment subjected to extreme environmental variation, and so corrosion and freeze/thaw cycles are issues as well. A typical example of a lock gate mostly submerged in water and encased in ice is shown in Figure 1.9.

Figure 1.9. Miter gate mostly submerged and encased in ice (Mulherin and Haehnel 2003).

In the U.S., gate damage is the leading cause of downtime and unplanned closures for USACE controlled locks (U.S. Army Corps of Engineers 2014a). Several researchers have begun investigating retrofit options to extend the life of lock gates. Lozano, et al., (2017) investigate using prestressed carbon fiber reinforced polymer (CFRP) patches to mitigate fatigue crack

propagation in miter gates. Mahmoud, et al., (2018), test the CFRP patches in typical environments expected in miter gate operation. Soti (2014) and Riveros, et al., (2018) similarly investigate the use of non-steel, composite-type materials to mitigate fatigue and corrosion issues on miter gates. Camporese (2013) investigates an optimal design for the loads typical to miter gates. While retrofitting or redesigning lock gates is a promising solution to common issues, it is prohibitively expensive. Thus, monitoring the health of lock gates is of critical importance to maintaining the operability of the inland navigation system. Currently, monitoring of lock gates is primarily conducted by visual inspection; however, lock gates are generally mostly submerged in water that is usually excessively turbid, precluding the simple visual inspection. Thus, to get any kind of information on the condition of the gate, two common options are: 1) to send divers to perform an inspection or 2) to close the lock chamber and drain the water (typically referred to as "dewatering") to allow for visual inspection such as shown in Figure 1.10. Communications with the USACE indicate that the estimated cost of is on the order of US $1 Million for just a single dewatering (that is, not including any repairs). The high costs and downtime of the lock associated with such visual inspections leads to inspections being performed infrequently, typically once every five to ten years, with some lock site noting they have gone as long as 25 years without an inspection. Therefore, alternative methodologies for assessing lock gates, such as is offered by structural health monitoring (SHM), are being investigated and employed.

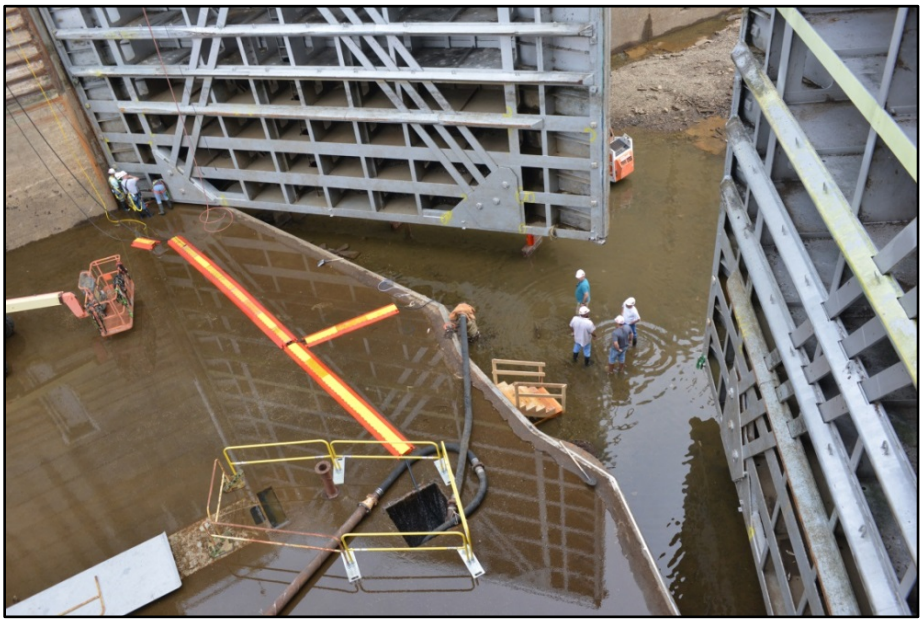

Figure 1.10. Typical inspection methodology: Drain the lock chamber and visually inspect the lock (Rankin 2014).

1.3. Structural Health Monitoring

Due to the need to efficiently allocate limited resources available for the maintenance and inspection of locks, structural health monitoring (SHM) systems have been considered to assist in establishing maintenance, repair, and replacement priorities for navigational locks. SHM is designed with the goal of moving away from a prescribed maintenance schedules to a system where maintenance decisions are made based on information gathered about the condition of the component from the SHM system. These systems are also expected to detect any impending failures before their occurrence, as well as operational problems that may present themselves.

SHM is traditionally defined as a process of detecting damage and characterizing the state of a structure by periodically observing the structure in the form collecting measurements from an installed sensor system. A damage sensitive feature is identified and extracted from the measurements, the statistics of which are analyzed to determine the health of the structure. The presence of damage in the structure will manifest itself as a change in the statistics of the damage sensitive feature. A successful structural health monitoring program can be seen as having the goal of answering the following four questions (Farrar and Worden 2012):

1. Is there damage?
2. Where is the damage?
3. How much damage is there?
4. How much longer can the structure be used safely?

To date, SHM has found limited application to lock gates. Greimann, et al., (1991) implemented a simple monitoring procedure on lock gates in 1990. In the study, data from the gate was manually recorded during inspections and compared to the expected performance of the gate. An empirical condition index was developed to use as a decision making tool. As data was not collected continuously, this study can be seen as a precursor to SHM of lock gates. Commander, et al., (1994) investigated detection of damage in miter gates by comparing strain measurements. The study was limited to types of damage that would lead to stiffness loss of structural members (e.g., cracks or corrosion), as the damage considered was simulated in a Finite Element Model (FEM) by reducing the stiffness of a member. The detection method relied heavily on manual inspection of data plots and on updating the associated FEM to match the damaged case. One of the metrics used in this study to detect damage is the correlation coefficient between monitored strain and the known undamaged strain collected via strain gages. McAllister, et al., (2001)

developed a reliability-based assessment method for existing miter gates calculating the probability of failure conditioned on detected flaw sizes. The study included uncertainty in strength, applied loads, flaw size, flaw detection, and flaw propagation. The goal was to provide an estimate of the remaining life of a miter gate, given some detected flaws. Estes, et al., (2004) implemented a Bayesian updating methodology to include data obtained in the field to reassess the reliability of a miter gate.

The USACE has invested heavily in an explicit SHM program for inland navigation systems termed the Structural Monitoring and Analysis in Real Time of Gates (SMART Gate) program (US Army Corps of Engineers 2016). The SMART Gate program was initially deployed at the Tainter gate at The Dalles Lock and Dam on the Columbia River, at the behest of the engineers on site. The system implemented at The Dalles consists of 176 gages measuring strain in structural members, temperature, water levels, and pressure on the gate. The data from these gages is uploaded to a web portal in real time to allow engineers and technicians to assess the performance of the structure. In late 2009, engineers noticed a marked change in the readings of some of the sensors, which led to the lock being shut down for an emergency inspection. The inspectors noticed substantial damage to the lower girders and the chamber wall, and emergency repairs were performed, preventing a catastrophic gate failure (Brinckman 2009). The success of the SMART Gate program in Oregon led the USACE to expand the monitoring campaign to include new lock and dam sites. The system is now employed on six gates in various locations as shown in Figure 1.11. Each of the sites have instrumented gates with upwards of 300 total sensors measuring strain, temperature, tilt, and water levels. Sampling rates range from $1/15^{th}$ to 50 Hertz; data is then uploaded to a database for processing. Currently, the SMART Gate system is little more than a data acquisition and storage system. Some work has been done to develop monitoring methodologies utilizing the SMART gate system. For example, Smith, et al., (2015) developed a method to detect a vessel impacting a lock gate by using accelerometers installed via SMART Gate. Alexander, et al., (2017) developed a tool to detect excessive friction in moving components of gates using strain gages. Leveraging the results from the research performed herein, Parno, et al., (2018) utilized Gaussian process regression to quantify the magnitude of reaction forces in the quoin boundary of miter gates based on strain gage data. More recently, and in tandem with the research performed herein, vision-based methods have been explored for application to lock gates. Narazaki, et al., (2019) investigated vision-based techniques to provide dense strain and

displacement measurements. The goal was to supplement the sparse strain information provided by strain gages by obtaining strain information from all points on a miter gate visible in a video frame. Hoskere, et al., (2019) investigated the use of a neural network classifier to identify damage from image of miter gates. However, for the most part, decision-making based on the incoming data requires manual review of the data by trained engineers and so, the system is currently of limited use.

Figure 1.11 Locations with SMART Gate instrumentation systems.

The goal of this research is to address the gap in knowledge in developing and utilizing SHM systems for navigation infrastructure. Critical scenarios affecting steel lock gates are identified as optimal targets for development of monitoring methodologies. The work discussed herein relies heavily on the USACE SMART Gate system, the data collected herein, and the particular gate designs and configurations used in the U.S.; however, the results are applicable to navigation infrastructure in general.

1.4. Layout of Dissertation

To understand the methodologies developed as part of this research effort, the necessary background on the particular structures investigated, namely miter and Tainter gates, is given in Chapter 2. The configuration and critical components of these gates are discussed in detail, as is standard design practices utilized in the U.S. for construction of these gates. Then, the expected

behavior of the gates due to typical loading scenarios is discussed, with emphasis given to expected load paths and states of stress under normal operating conditions. Knowing the expected behavior of the gates, the damage scenarios of critical interest to extending the useful life of these gates are discussed and are used as the motivation for the methodologies developed in this dissertation. These methodologies are 1) the detection of what's known as a quoin gap, 2) the quantification and localization of a quoin gap, 3) detection of loss of tension in a miter gate component known as the diagonals, and 4) detection of a phenomenon known as uneven hoisting of Tainter gates.

As an initial step in developing an SHM system for inland navigation infrastructure, finite element analysis (FEA) models were created to assist in developing the necessary understanding of the global behavior of the gate under normal operating conditions. Moreover, the FEA models allow the imposition of damage to the structure to investigate how the behavior of the structure changes in the presence of the damage that is of desire to detect. Chapter 3 of this dissertation provides information on the best practices to use when creating and using FEA models of miter and Tainter gates. Discussion topics include the selection of geometry and elements, mesh refinement, appropriately modeling boundary conditions, model validation and model updating. Two particular examples of FEA models used heavily in the course of this research are discussed at length, namely the models of the upstream miter gate at the Greenup Lock and Dam and the upstream Tainter lock gate at The Dalles Lock and Dam.

In Chapter 4, the methodology developed for detecting, locating, and quantifying what is known as a quoin gap for miter gates is discussed. The quoin gap is effectively a degradation of the boundary conditions of the miter gate which may lead to accelerated fatigue damage and a reduction in service life. The developed methodology utilizes readings from strain gages on a miter gate to monitor for changes in the load path of the miter gate that may indicate the presence of degradation in the boundary conditions. To address the environmental variability inherent in strain gage readings, a novel quantity is derived from the strain gage readings, termed "the slope", which is defined as the change in stress due to a corresponding change in lock chamber water levels. The slope is found to effectively remove environmental noise while still being sensitive to the presence of damage on the gate. To facilitate the detection of a quoin gap using the slope, the statistical method of Principal Component Analysis (PCA) is employed to combine the information from many strain gages into a damage index. Training data from the strain gages of an assumed healthy miter gate is used and processed with PCA to determine typical values of the damage index under

normal operating conditions. From the training data, a threshold is developed based on the statistics of the damage index. As new data is collected, the damage index is found and compared to the threshold. If it exceeds the threshold, it is assumed that a quoin gap is present on the structure. Validation of the approach is performed utilizing a combination of sensor data and the FEA model from the Greenup Lock and Dam.

Chapter 5 focuses on the vision-based methodology developed to monitor and detect changes in tension in the components of the miter gate known as the diagonals, which are long, slender beams that span the diagonal dimensions of the miter gate. The diagonals of a miter gate are necessary because the geometry of the gate is such that it will tend to twist torsionally due to its own weight. The diagonals of the gate are thus added and post-tensioned to counter-act the torsional twist, as well as to provide torsional stiffness to the gate as it swings through the water. Monitoring and maintaining the tension in the diagonals has been identified as a critical concern by miter gate owners and operators as a loss in tension will increase the likelihood of the gate being impacted by passing vessels. An increase in tension will lead to accelerated fatigue damage in the gate. To forgo the need for direct contact sensors to monitor the diagonals on miter gates, the methodology herein uses a vision-based method, whereby the Lukas-Kanade Optical-Flow technique is used to track the displacements of a vibrating diagonal from video. With the obtained displacements, frequency domain techniques are used to find the frequencies of vibration of the diagonal, from which the tension in the diagonal can be ascertained via beam theory. Particular challenges of the successfully implementation of this technique are the rigidity of the diagonals, appropriately modeling the boundary conditions of the diagonals, and the effects of submersion on the frequency of vibration of the diagonals; all of which are addressed. The methodology is then verified using video of the vibrating diagonals on the Greenup Lock and Dam, and a comparison of the calculated tension using the vision-based method with the tension measured using a load cell shows good agreement.

Chapter 6 focuses on the development of a methodology to detect what is known as uneven hoisting of Tainter gates. Tainter gates are designed to raise and lower through the water via cable or chains connected on each side of the gate. Under normal operating conditions, the gate is expected to raise and lower evenly on both sides so that there is no twist in the gate. When twisting occurs, unexpected stresses can occur throughout the gate which can accelerate fatigue damage and potentially lead to catastrophic failure of the gate. The initial goal of this study was to develop

a methodology to automatically detect uneven hoisting of the gate utilizing strain gage data from a continuous monitoring system. However, peculiarities in the incoming data compared to the expected behavior led to doubts regarding this approach. Three explanations for these differences seemed possible: the model of the gate was flawed, the sensors were unreliable, or the gate was actually already hoisting unevenly. To definitively diagnose the issues seen in the data, a short-term monitoring program was devised to use vibration measurements of the hoisting cables of the gate. Then, a frequency domain method was employed to estimate the force in the cables which provides an indication of the unevenness of the gate hoisting. Results indicate that, indeed, The Dalles Tainter gate regularly hoists unevenly and that the initial methodology for detecting uneven hoisting of the gate was effective.

Finally, Chapter 7 outlines the overall conclusions of the research performed throughout the preparation of this dissertation. Furthermore, future work is discussed in detail, with particular emphasis given to the desire to develop models to provide a probabilistic assessment of the remaining life of inland navigation infrastructure. The goal of the probabilistic assessment is to incorporate the knowledge of the state of the structure obtained from the SHM methodologies developed herein to inform the likelihood of failure of the structure occurring within a given time frame. Part of this future work is expected to involve physical testing to determine fatigue and fracture parameters for materials and weld details ubiquitous to miter gate configurations. Additionally, work on full-scale implementation of the methodologies developed herein is discussed with the preliminary implementation at one lock and dam on the Ohio River emphasized.

Chapter 2. Lock Gate Design, Behavior, and Critical Problems

As discussed in the previous chapter, the gates that comprise the damming surface of lock chambers are the weak link in the inland navigation system. These primarily steel structures are dynamic in nature (designed to swing open and closed) and are subjected to extremely adverse environments, as they are sitting in a river where air and water temperatures can fluctuate significantly throughout the year. Maintenance of lock gates is by far the leading cause of unplanned closures of lock and dam sites in the inland navigation system, and so, the primary focus of this research is on lock gates. There are many types of lock gates, but this research focuses on miter and Tainter gates. This section provides the necessary background to understand the behavior of lock gates and the motivation for the methodologies developed as part of this research. The function and design of the components of lock gates investigated as part of this research are discussed. Focus is given to the quoin and diagonals of miter gates, as well as the hoisting mechanism of Tainter gates.

2.1. Miter Gates

Miter gates are the most common lock gate type found at USACE lock and dam sites (U.S. Army Corps of Engineers 2015). Characterized by their primary load carrying members, miter gates are designated as either "vertically framed" or "horizontally framed" based on the respective orientation of the steel girders that comprise the gate. Horizontally framed miter gates are typically used in locations that require a large "lift" in the lock chamber; that is, locations where the difference in typical water elevation on either side of the lock chamber is relatively large (e.g., greater than 6.0 m or 20 ft.). Figure 2.1 shows one leaf of a horizontally framed miter gate hanging from a crane prior to installation in the field. The yellow members on the structure, which are fiber-reinforced polymer fenders, are attached to the namesake horizontal girders, while the vertically oriented diaphragms between the horizontal girders are added to simply provide stability. Vertically framed gates are typically used for locations where a relatively short lift is required in the lock chamber of say, 1.5 m to 3.0 m (5 to 10 ft.). Vertically framed miter gates are generally much shorter than horizontally framed miter gates, but equally as wide, to facilitate the transportation of similarly sized vessels. Figure 2.2 shows a vertically framed miter gate leaf awaiting installation in the field. In the figures shown, the horizontally framed gate is about 65 feet tall, while the vertically framed gate is about 20 feet tall. Vertically framed gates are particularly

common at lock sites on the Upper Mississippi River, while horizontally framed gates are used throughout the rest of the contiguous U.S. For the research performed herein, focus is given to horizontally framed miter gates, as they are more common. Thus, henceforth any reference to "miter gate" can be assumed to be referring to horizontally framed miter gates.

Figure 2.1. Horizontally framed Miter gate being installed in the field.

Figure 2.2. Vertically framed miter gate being installed in the field.

A miter gate consists of two leaves which, when closed, are referred to as "mitered" and act as a dam, holding back the water on the upstream side of the gate. The gate's leaves rest on a ball and socket joint at their base, known as the pintle, and are further secured by a gudgeon hinge and anchors at the top, shown in Figure 2.3. The gates are operated (opened and closed) by a strut arm that connects the gate to operating machinery on the lock chamber wall.

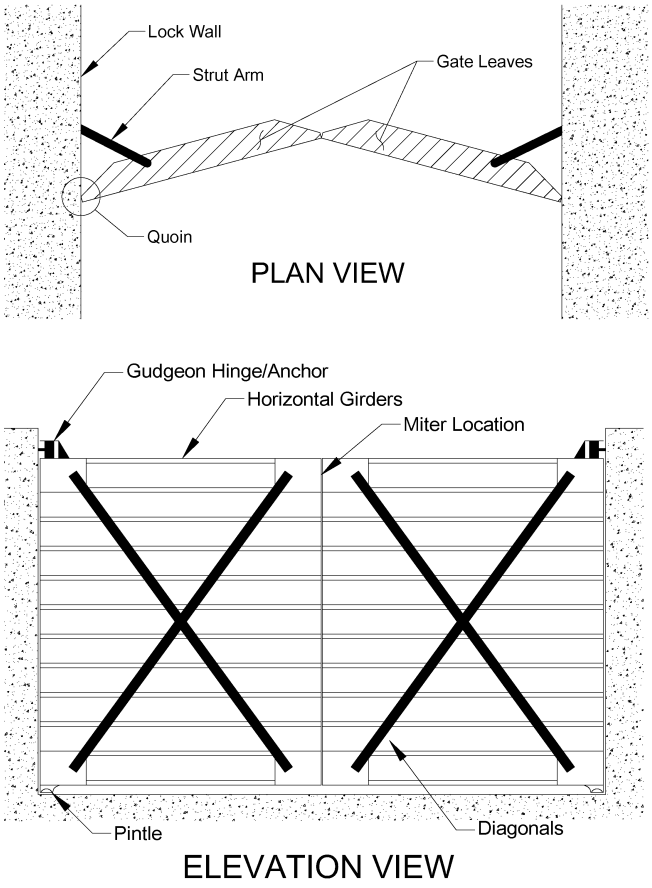

Figure 2.3. Miter gate schematic.

Design of miter gates in the U.S. is typically governed by the USACE engineering manual (EM) 1110-2-2703 (U.S. Army Corps of Engineers 1994) (herein referred to as simply "the EM") and the more recent engineering technical letter (ETL) 1110-2-584 (U.S. Army Corps of Engineers 2014b). The more recent World Association for Waterborne Transport Infrastructure (more commonly referred to by its historical name, the Permanent International Association of Navigation Congresses, or, PIANC) report on miter gate design (PIANC 2017) provides an

international perspective. Both documents give general recommendations on block shapes and installation procedures, an overview of which will be presented here.

The primary loads considered in miter gate design are the gravity loads, operating machinery loads, vessel impact loads, and hydrostatic loads. Other loads frequently considered are what are called hydro-temporal or hydrodynamic loading (e.g., wave action) and seismic loads, which are both generally negligible in comparison to the aforementioned primary loads. For the sake of understanding the research presented herein, having an understanding of the gravity, operating machinery, and hydrostatic load cases is sufficient. The gravity loads on the gate are typically considered for a miter gate in an open and hanging configuration; these loads are used primarily for the design of the components that support the gate, namely the upper gudgeon anchorages and lower pintle. Figure 2.4 shows an overview of a typical hanging gate load and associated reactions. The weight of the gate, which often incorporates an assumed amount of mud, ice, and debris, causes an overturning moment on the gate which must be resisted by the upper anchorage and lower pintle.

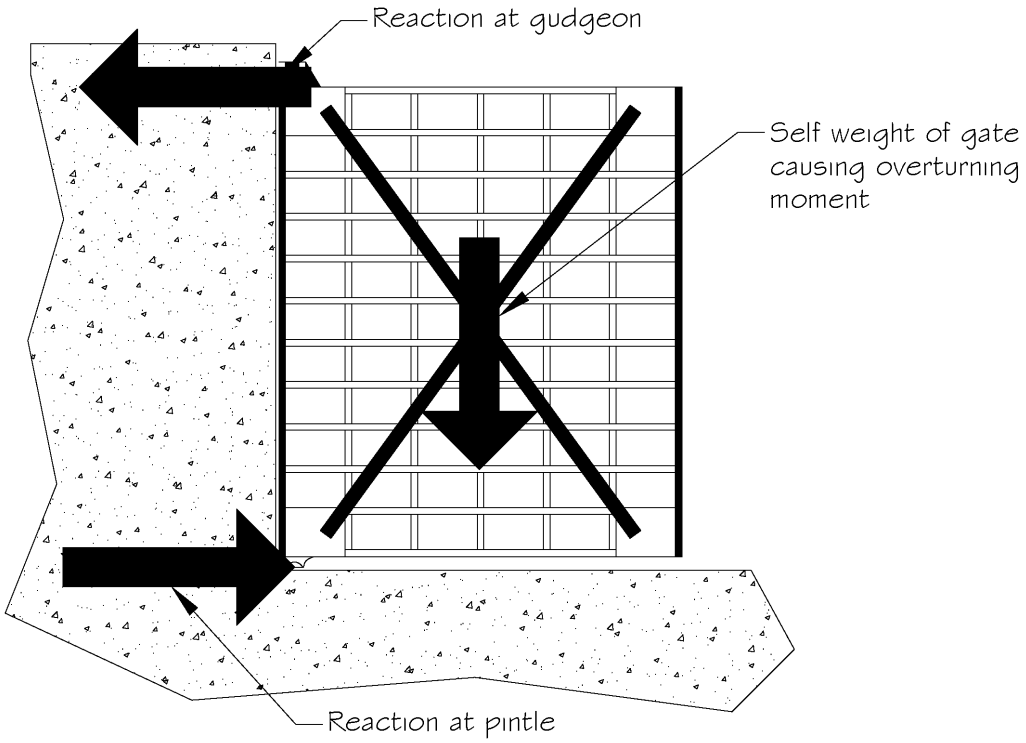

Figure 2.4. Loading on an open miter gate due to gravity loads.

For the operating machinery load, the critical load case that is considered for miter gate component design is the case where the gate meets an obstruction as it is swinging open or closed. This loading scenario is represented in Figure 2.5. In this loading scenario, the movement of the gate is assumed to be blocked, and the strut arm that opens and closes the gate is inducing a significant torsional load on the gate. The strut-arm in the figure is represented by the black dot at the top of the gate, and labeled as such, in the revised dissertation. The primary interest of this loading scenario to this research is its use in designing the diagonal steel members of the miter gate (represented by solid black diagonal lines in Figure 2.5). As will be explained in greater detail later, the diagonals are added specifically to add torsional stiffness to the gate and to provide resistance to the type of loading depicted in Figure 2.5.

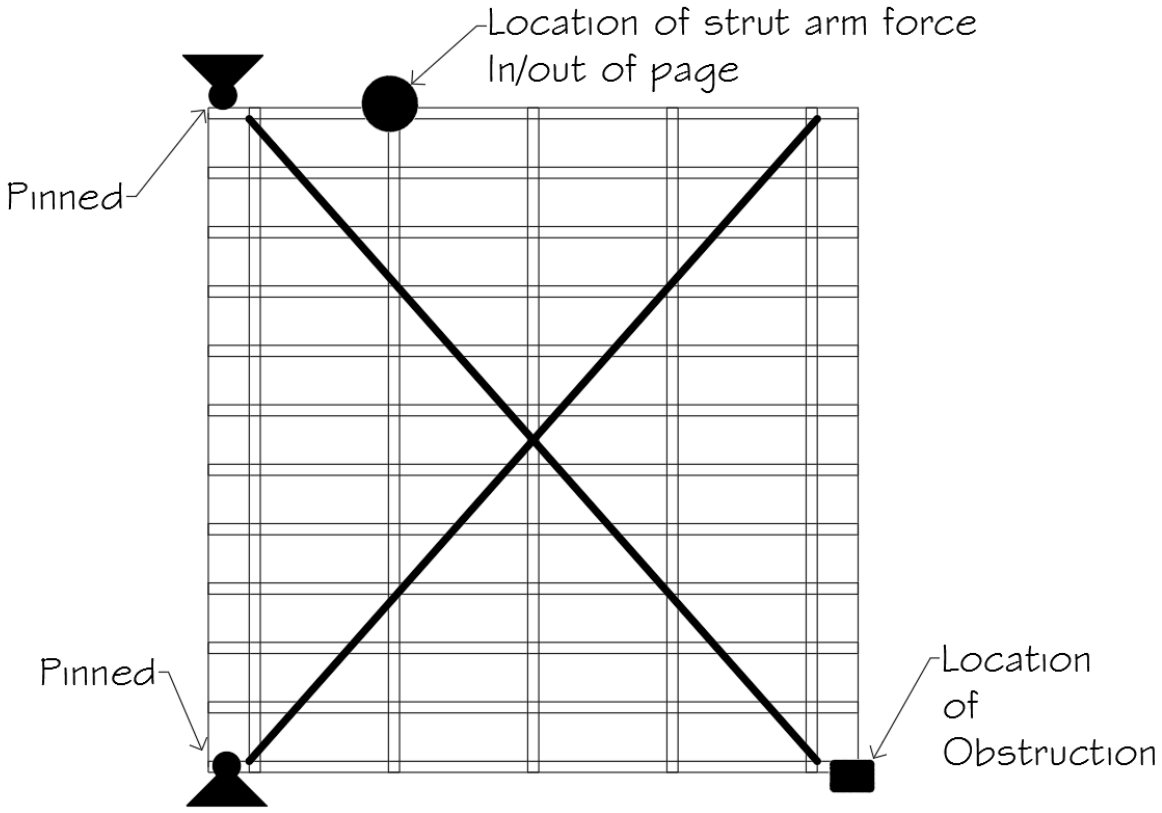

Figure 2.5.Location of critical operating load on a miter gate.

Hydrostatic loads on a miter gate are only considered when the gate is closed and acting as the damming surface for the lock chamber. The boundary conditions at the gate/wall interface (also known as the quoin) are such that, under normal operating conditions, the hydrostatic load is

intended to thrust the gate into continuous bearing against the lock chamber wall. Similarly, when fully mitered and in contact, the two leaves of the gate continuously bear on each other along their heights. These boundary conditions result in three-hinged arch behavior of the gates in their closed position. When the water level in the lock chamber differs from the water level outside the chamber, hydrostatic load is placed on the gate as seen in Figure 2.6-a. Under normal operating conditions, the boundary conditions dictate that no moment is present at the ends of the gates, and the entire load transfers as axial compression into the wall of the lock chamber. A schematic of the load transfer mechanism is provided in Figure 2.6-b. Maintaining continuous contact in the quoin of a miter gate is one of the most critical issues in miter gate maintenance, as described next.

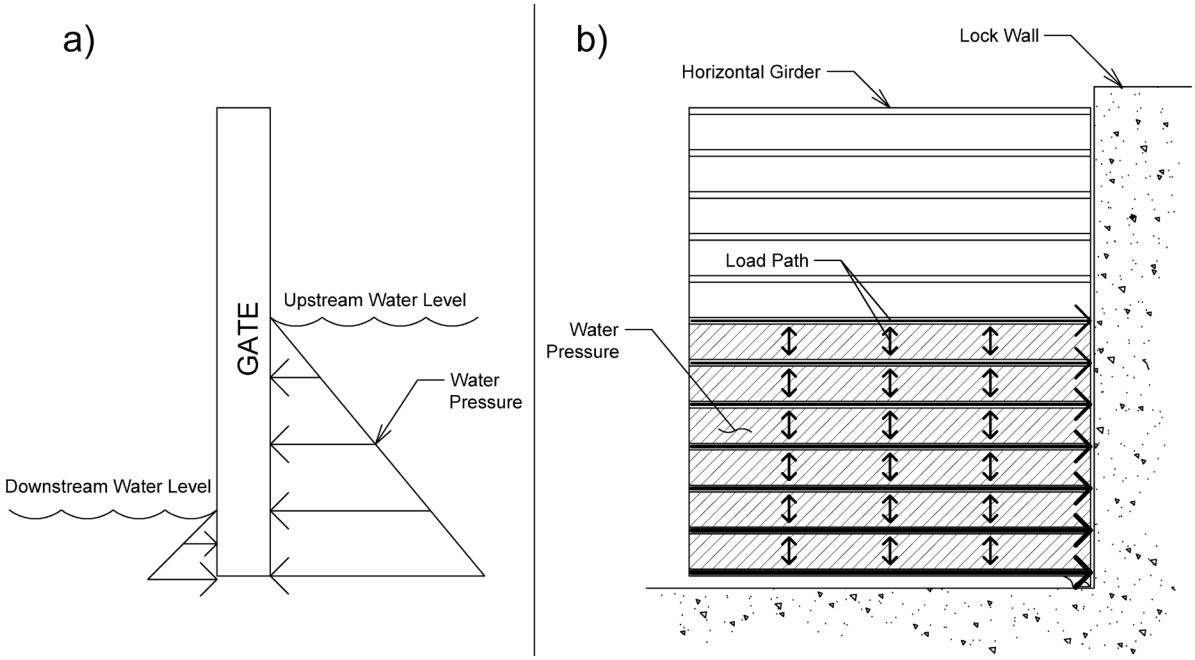

Figure 2.6. a) Load scenario for lock gate. b) Load transfer through girders to wall.

2.1.1. Design of and function of miter gate quoin

As mentioned, the hydrostatic load on a miter gate is intended to flow through the girders of the gate and thrust into the lock chamber wall through axial compression in the region of the gate known as the quoin. Miter gate construction involves the fabrication and installation of contact blocks that are effectively a buffer between the concrete chamber wall, and the gate itself. The EM notes that the contact blocks serve two functions. First, contact blocks facilitate an even distribution of the intended thrusting load from the gate into the lock chamber wall. Second, they act as a seal between the gate and the wall, preventing water leakage into the lock chamber. Generally, contact blocks are solid steel elements with dimensions on the order of 7.6-10.1 cm

(3.0–4.0 in.) thick and 20.3-25.4 cm (8–10 in.) wide. Contact blocks are intended to span the entire height of the gate around 18.0-21.3 m (60-70 ft.), but for constructability purposes, they are allowed to be fabricated in large, individual pieces that are then spliced together.

Contact blocks in the United States are flat on the backside to facilitate load transfer to the gate, and they are convex on the side that would contact the wall, allowing for contact at a very small point and facilitating the gate's swing action. This geometry is seen in the cross-sectional plan view of a contact block in Figure 2.7.

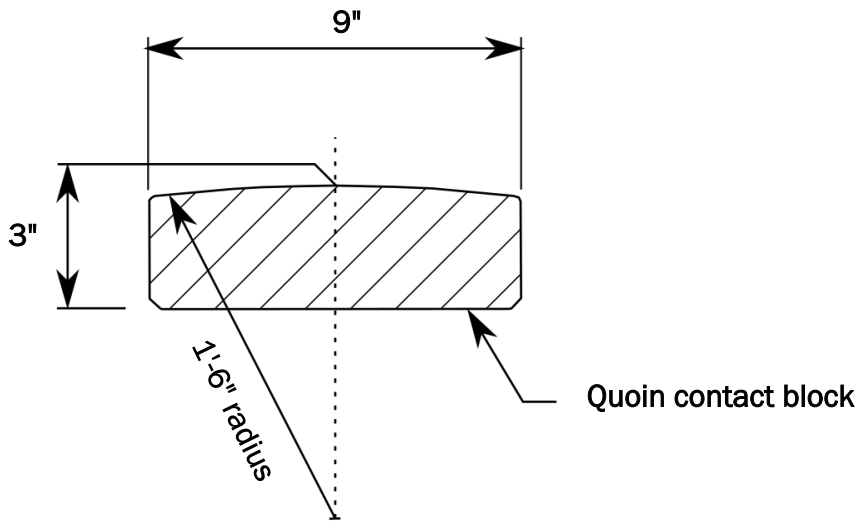

Figure 2.7. Typical quoin block cross-section.

Because of fabrication irregularities and potential warping of the large contact blocks, a procedure is generally followed to allow adjustment of the contact blocks and ensure continuous contact along the height of the quoin. A typical adjustment strategy is to apply a pair of push and pull screws along the height of the block, as noted in the EM (U.S. Army Corps of Engineers 1994). Figure 2.8 shows a plan view of the quoin-block end of a girder, highlighting the typical bolt arrangement for the quoin block. As seen, one bolt is generally threaded into the contact block that is used to pull the block towards the gate. Opposite the threaded bolt, there is typically a cap screw that is used to push the block toward the lock chamber wall. A typical layout for these push-pull screws is to apply them every 2 ft. along the height of the quoin. The threaded pull bolts serve the additional function of physically attaching the block to the gate; however, the need for adjustability dictates the requirement of a gap between the contact block and the gate. To further

ensure the even distribution of contact pressure from the contact block into the end plate of the gate, epoxy or molten zinc is added in this small gap (Foltz, et al. 2015). The small gap and epoxy filler location are shown in Figure 2.8. During installation, the quoin block is fully adjusted by using the push-pull screws so that contact is present to within the desired tolerances, then the backing material is added. Internationally, there is a push to utilize only small, intermittent contact block pieces along the height of the quoin. The intermittent pieces would increase flexibility in the quoin region, aid in initial adjustments, and greatly simplify replacement if a portion of the quoin block were damaged (Daniel 2000) (Eick, et al. 2019).

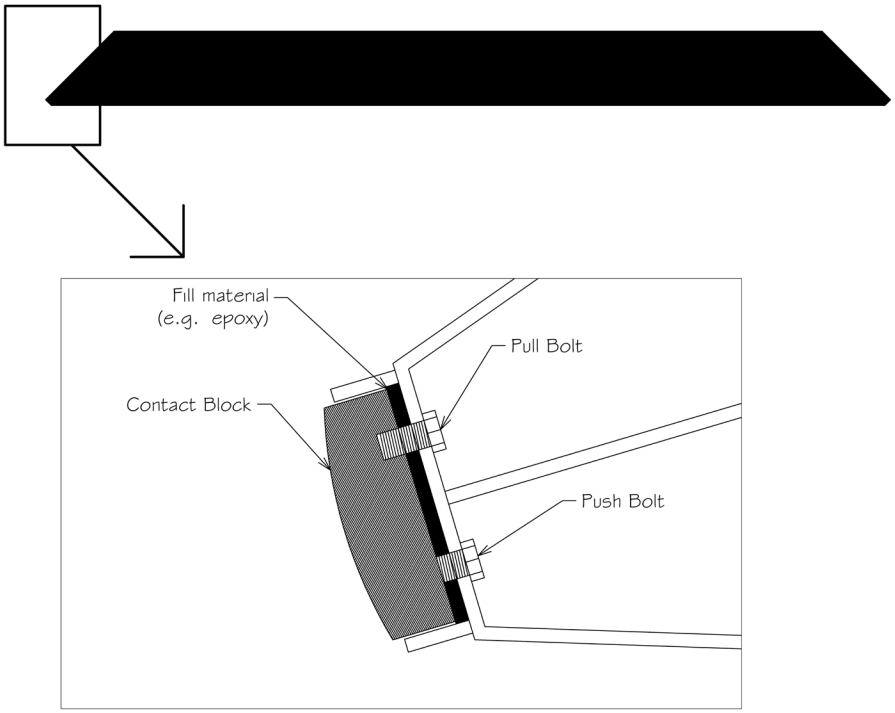

Figure 2.8. Push and pull bolts as adjustment mechanism of quoin blocks.

2.1.2. Issues with miter gate quoin

As mentioned above, the hydrostatic load applied to a closed miter gate is intended to be transferred into the concrete lock chamber wall through continuous bearing along the height of the gate in the quoin. However, over the life of the gate, it is common that gaps in the bearing surface of the quoin form, or indeed are initially present due to improper initial quoin adjustment (U.S. Army Corps of Engineers 2008). A gap changes the load path of the gate, forcing loads to

redistribute, resulting in higher forces and stresses in other parts of the gate. Figure 2.9 shows a representation of a gap in the quoin of a miter gate. Here, the girder immediately next to the gate is no longer able to carry load into the lock chamber wall due to lack of contact. Accordingly, the load that would be carried by the out-of-contact girder must now flow through the other nearby girders that are still in contact. Figure 2.10-a shows the quoin region of an in-service miter gate with a quoin gap, with the gate and concrete wall highlighted. Figure 2.10-b shows a zoomed view of the region of the gap in the quoin. Here, the field engineers hold a measuring stick to identify the out-of-plumbness of the quoin in this region, and noted that the gap appears to be one-half inch wide.

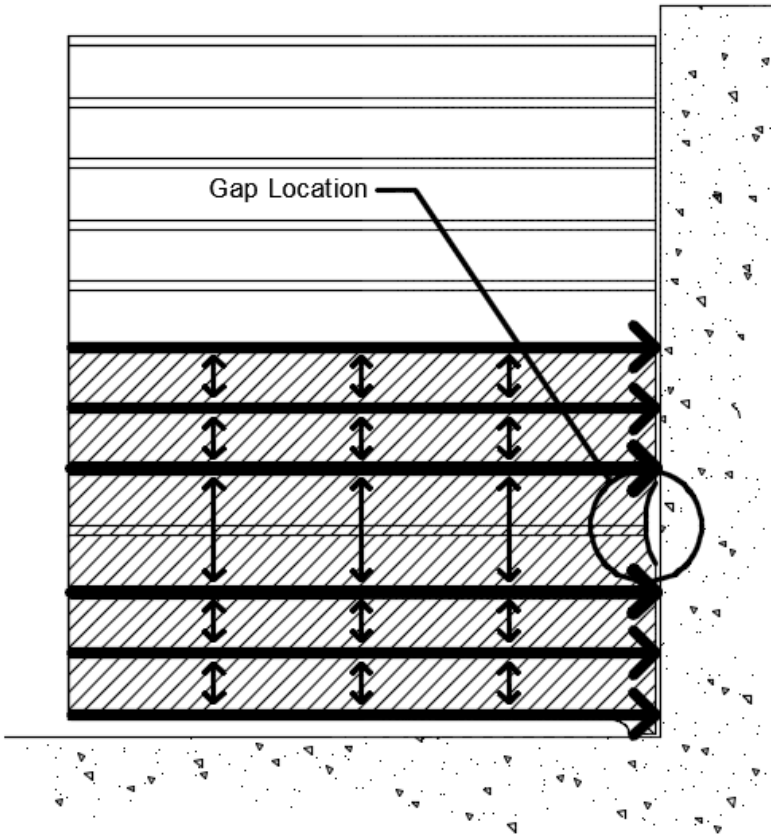

Figure 2.9. Gap in the quoin region, causing a redistribution of stress throughout the gate.

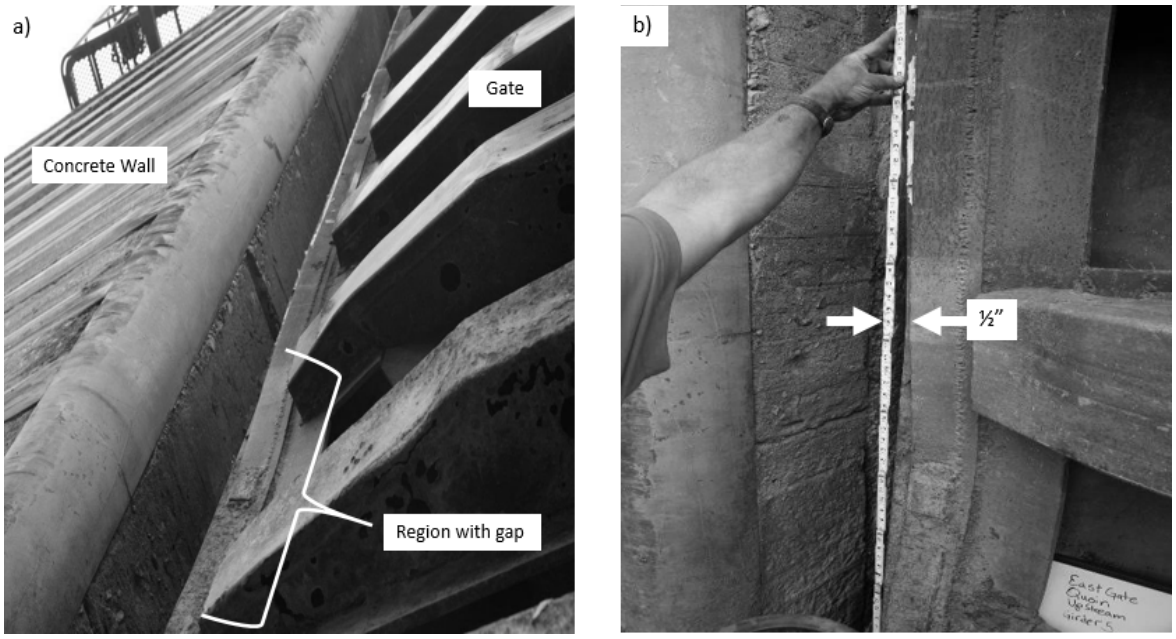

Figure 2.10. a) View of quoin region of a miter gate with a gap in the quoin b) zoom of gap region, showing that this portion of the quoin is warped ½ inch.

The higher stresses in miter gate components due to the presence of a quoin gap become problematic, especially in the pintle region, which is prone to fatigue damage. Figure 2.11 shows an extreme case of a quoin gap where an entire section of the quoin contact block fell off the miter gate at the Meldahl miter gate. The missing section of the quoin block led to complete lack of contact in the quoin region of the gate and thus most of the hydrostatic load was forced to flow into the pintle region of the gate. Figure 2.12 shows the extensive cracking caused in the pintle region of this miter gate due to the redistribution of forces caused be the lack of quoin contact.

Figure 2.11. Meldahl miter gate, with section of quoin block missing.

Figure 2.12. Pintle region of Meldahl miter gate with extensive cracking due to lack of quoin contact.

The USACE has identified the formation of quoin gaps as a critical problem in lifecycle maintenance of miter gates. Accordingly, quoin gaps are one of the key detection targets of the USACE SMART Gate system. Thus, a significant portion of this dissertation is devoted to developing methodologies to utilize strain gages to detect the presence, location, and magnitude of gaps in miter gate quoins, as will be described in detail in Chapter 4.

2.1.3. Design and Function of Miter Gate Diagonals

As discussed in the previous section regarding the torsional loads induced by miter gate operating machinery, miter gates have large, steel diagonal members that are tensioned and span the full diagonal dimension of the gate. To understand the function of these diagonal members (herein simply termed “diagonals”), it helps to understand that the miter gate cross section resembles a deep, channel-like section (see Figure 2.13-a). This particular geometry is such that there is an eccentricity between the shear center and the center of gravity, which will cause the gate to torsionally deflect under its own weight (Figure 2.13-b) (Boresi and Schmidt 2003). To counteract the torsional deflection, the diagonals are added to the gate and tensioned (Figure 2.13-

c). Additionally, in the design phase of a miter-gate, the torsional stiffness of the miter gate is assumed to be small enough to be neglected. In other words, a miter gate subjected to a torsional moment is assumed to deflect in an extreme manner. Diagonals are thus added to provide some degree of torsional stiffness to the gate. The idea is that, as the gate swings through the water, the diagonals will resist the torsional moment caused by the operating machinery or other torsional loads. The diagonals are tensioned because of their extreme slenderness ratio. That is, the least radius of gyration of a miter diagonal is so small compared to the length of the diagonal, that miter gate diagonals have effectively no compressive capacity. The tensioning of the diagonals allows the resistance of compressive-type loads until the point of decompression of the diagonal. For additional information on the behavior of steel structures subjected to torsion, the reader is directed to the guide to steel torsion analysis and design by AISC (American Institute of Steel Construction 1997).

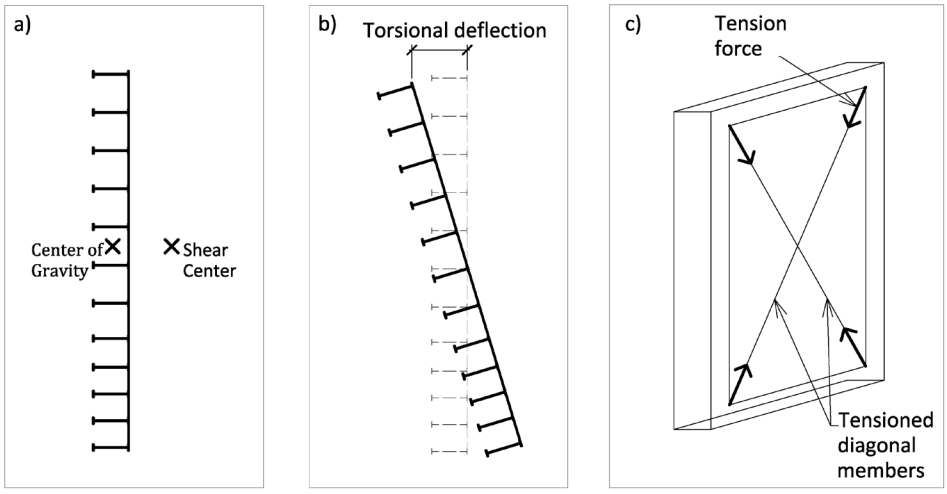

Figure 2.13. a) Typical cross-section of miter gate. b) Isometric view of torsional deflection of a miter gate due to self-weight, c) Tensioned diagonal members to counteract torsional deflection.

Diagonals on a miter gate are generally termed “positive” or “negative”, where a positive diagonal is one in which an increase in tension will cause the top of the miter gate to torsionally deflect upstream. A negative diagonal is then the opposite case. Typically, the positive diagonal spans from the top corner near the gudgeon anchor to the opposite bottom corner of the gate. The negative diagonal spans from the bottom corner near the pintle to the opposite top corner of the gate. The diagonals are typically offset from the other components of the miter gate, and from other diagonals, by several inches. There are rare exceptions to the typical design of diagonals that

freely span the entire diagonal dimension of the miter gate. In some instances, the diagonal are intermittently welded to the girders of the gate. In these instances, the intermittent span lengths of the diagonals are such that the diagonals will have some compressive capacity and will likely not need to be pretensioned. The EM offers guidance concerning torsion in miter gates and presents a method that a structural designer can use to determine the size of the diagonals and the amount of post-tensioning to be put into the diagonals. The guidance provided in the EM is largely based around two nearly identical academic theses, one being a PhD thesis written by Shermer (Shermer 1951) in 1951, and the other a thesis written by Hoffman in 1944 (Hoffman 1944). The design of the diagonals is then performed such that they satisfy two design requirements. First, they must be tensioned so that the gate hangs plumb under its own weight. Second, they must not lose tension as the gate swings through the water. For the second criteria, the operating machinery load on an obstructed miter gate is typically the governing load case. Formally, for each diagonal, the pretension in the diagonal σ_0 should be selected such that:

$$0ksi < \sigma_0 + \Delta\sigma < F_y \tag{2.1}$$

where $\Delta\sigma$ is the change in stress in a diagonal due to any torsional load on a miter gate, and F_y is the yield stress of the diagonal. Here, both positive and negative changes in stress need to be considered. Then, for the gate to hang plumb, the following equation must be satisfied:

$$P_{\mathrm{DL}} x_{\mathrm{DL}} y_{\mathrm{DL}} - \sum_{i=1}^{n} \pm 2\sigma_{0_i} A_{\mathrm{d}_i} \cos(\psi_i)\, h_{\mathrm{p}_i} d_{\mathrm{g}} = 0 \tag{2.2}$$

where the subscript "DL" refers to the dead load of the gate, the subscript *i* refers to the *i*th diagonal, A_{d_i} refers to the cross sectional area of the *i*th diagonal, and +/- refers to negative and positive diagonals, n is the number of diagonals on the gate. The other variables are geometric properties of a miter gate and torsional load: $h_p$is the height of the diagonal panel, d_g is the depth of the gate and ψ is the angle of the diagonal, each of which is represented in Figure 2.14. , P represents the torsional load due to self-weight, x, is the distance of the gravity of the load to the

pinned boundary condition of the gate, and y is the eccentricity of the load with respect to the shear center. These are pictorially represented in Figure 2.15.

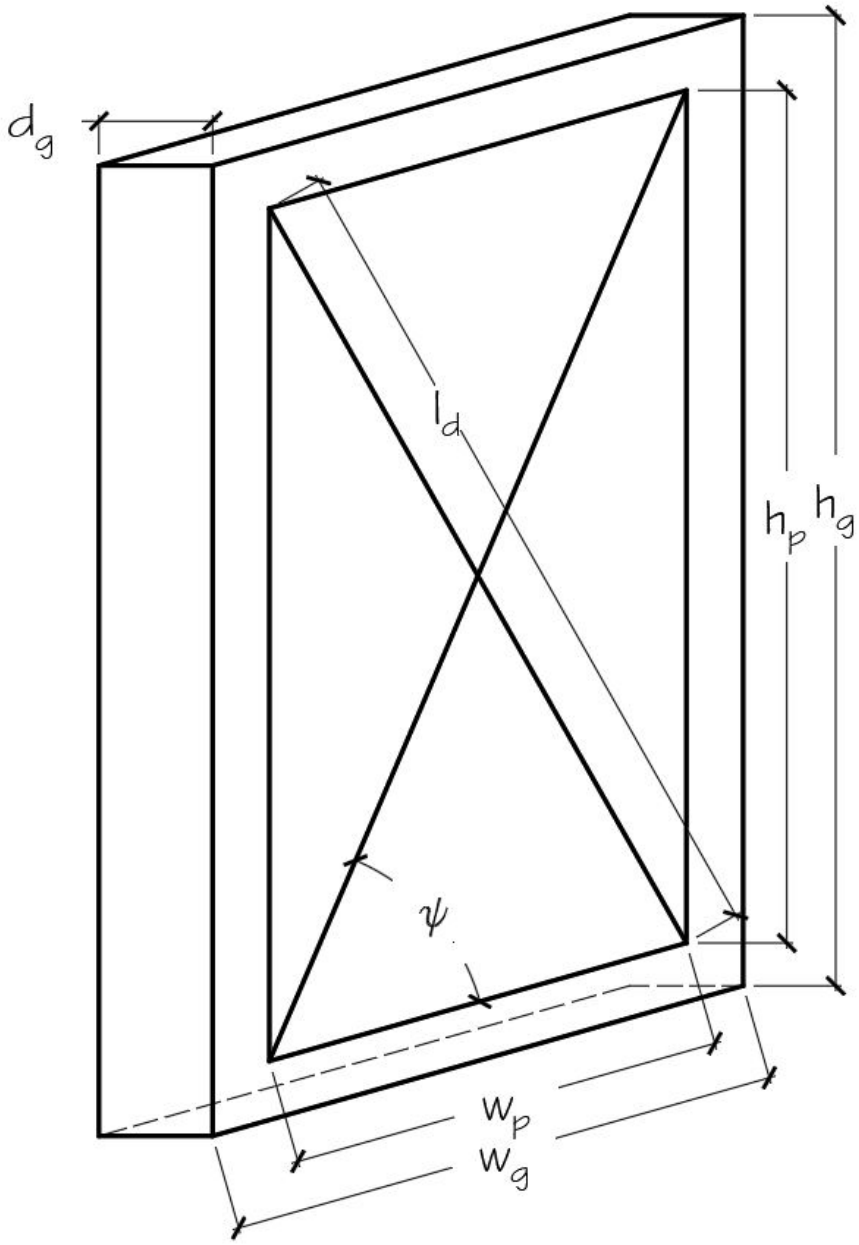

Figure 2.14. Geometric properties of a miter gate used in diagonal design.

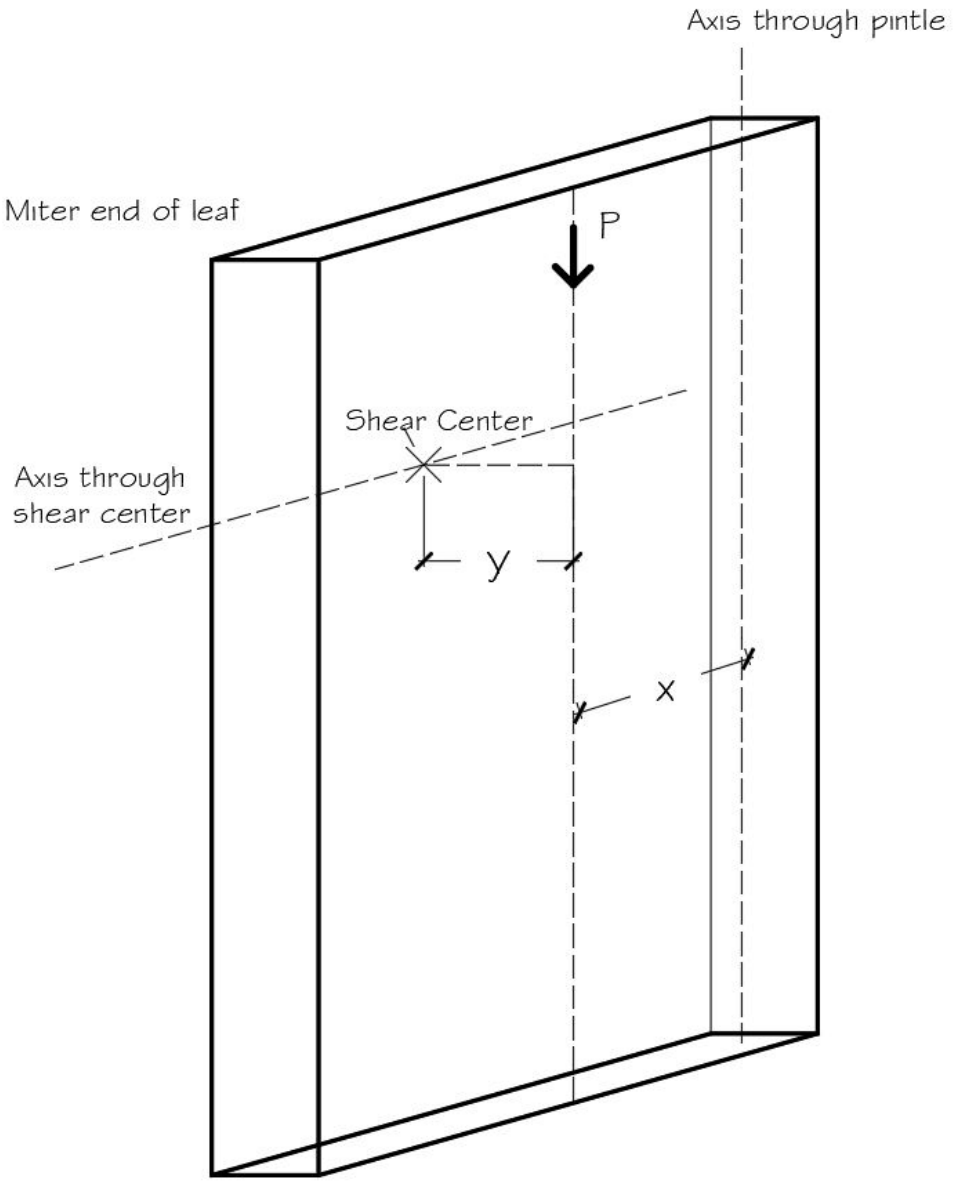

Figure 2.15. Information required for location of torsional load for miter gate diagonal design.

The exact location of x_{DL} and y_{DL} would require an extensive numerical model of the individual gate. In this study, utilizing the distance from the shear center to the centerline of the girders is sufficiently accurate for the location y_{DL}. Similarly, simply using the horizontal distance from the pintle to the midpoint of the gate is sufficiently accurate for x_{DL}. Note that the pretension in the diagonals that will satisfy the design requirements is not unique. The suggested approach for the designer, then, is to select a value of σ_0 that satisfies equation (2.1) and then calculate the other value of σ_0 such that equations (2.1) and (2.2) are satisfied simultaneously. The designer should iterate until the smallest value of tension that satisfies the requirements is found.

Maintaining an appropriate value of tension in the diagonal members is of critical importance to both the serviceability and the fatigue life of the gate. If the tension is lost in the diagonals, the gate will lose torsional stiffness and potentially lean into the lock chamber when open, thus increasing the likelihood of vessels impacting the gate when passing. If there is too much tension in the diagonals, then overstressing and accelerated fatigue damage becomes a concern (Riveros, et al., 2017). The USACE has identified monitoring of diagonal tension as a key desirable feature of an SHM system for miter gates. Accordingly, a significant portion of this dissertation is devoted to developing a methodology to remotely monitor the tension in miter gate diagonals using non-contact, vision-based sensing methods, as discussed in Chapter 5 of this dissertation.

2.2. Tainter Gates

Tainter gates, named after their designer Jeremiah Burnham Tainter, are common water control structures used at dams throughout the world (Sehgal 1996). Tainter gates are radial type structure that, unlike miter gates (which swing horizontally open and close) swing up and down via ropes or chains. Most Tainter gates work as flood-control dam spillway gates (Abela 2017), or as the water-depth control structure on the dam portion of a lock and dam. A series of Tainter gates installed on the dam portion of a lock and dam are shown in Figure 2.16. In the U.S., the vast majority of lock and dam sites utilize a Tainter gate configuration similar to that shown in Figure 2.16, with some locations having many more Tainter gates than shown in the figure. Accordingly, Tainter gates are very common and critical infrastructure to inland navigation.

Figure 2.16. Series of Tainter gates at the dam portion of a lock and dam.

The research presented herein on Tainter gates focuses on the upstream gate on the lock chamber of The Dalles Lock and Dam on the Columbia River in the U.S. Focus on this particular Tainter gate is due to the fact that it is instrumented with an SHM system as part of the USACE SMART Gate system. The Tainter gate at The Dalles is a lock gate, rather than a dam gate. That is, The Dalles lock Tainter gate works as the damming surface to allow the water levels in the lock chamber to change. Then, for a vessel to pass by the Tainter gate, the gate swings down into the lock chamber and the vessel passes over it. Figure 2.17 shows a schematic of how The Dalles Tainter gate operates, where (a) shows the gate closed and acting as a damming surface, while (b) shows the gate lowered allowing a vessel to pass over. Figure 2.18 shows the Tainter lock gate at The Dalles in operation, close, and acting as the damming surface to the lock chamber. The function of The Dalles Tainter gate is different than the typical spillway Tainter gate, which raises up to allow water to flow underneath. Aside from this difference, the design and function of The Dalles Tainter lock gate is similar to other Tainter gates in general.

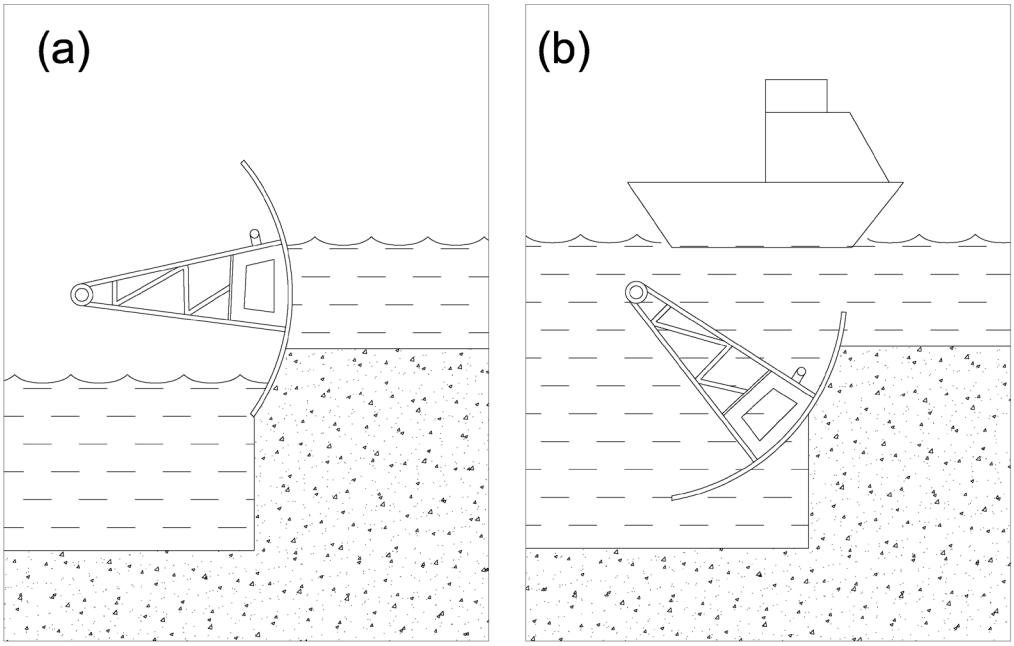

Figure 2.17. Operation of The Dalles Tainter Lock gate with a) the gate closed and acting as the damming surface and b) the gate lowers to allow the passage of a vessel.

Figure 2.18. The Dalles Tainter gate, closed and acting as the damming surface of the lock chamber.

As mentioned previously, Tainter gates are radial gates that resemble a circular sector consisting of two truss-like strut arms that support a skin plate that comprises the chord of the sector and acts as the damming surface. At the center of the circular sector, and at one end of the strut arms, is a trunnion pin which acts as a pivot point about which the Tainter gate rotates. At the other end of the strut arms are lifting lugs to which the hoisting cables that raise and lower the gate are attached. Figure 2.19 shows an isometric schematic of a Tainter gate, with important components labeled.

Design of Tainter gates in the US is largely governed by EM-1110-2-2702 (U.S. Army Corps of Engineers 2000), “Design of Spillway Tainter Gates”. The section in the lock gate engineering manual for lock type Tainter gates directs the reader to the spillway gate design manual (U.S. Army Corps of Engineers 1994). The typical loads considered for Tainter gate design are gravity loads (including ice and mud), hydrostatic loads, operating machinery loads, and friction loads. The hydrostatic loads are again are only considered for the gate in the closed position. A schematic of the loading on a Tainter gate in the closed position is shown in Figure 2.20.

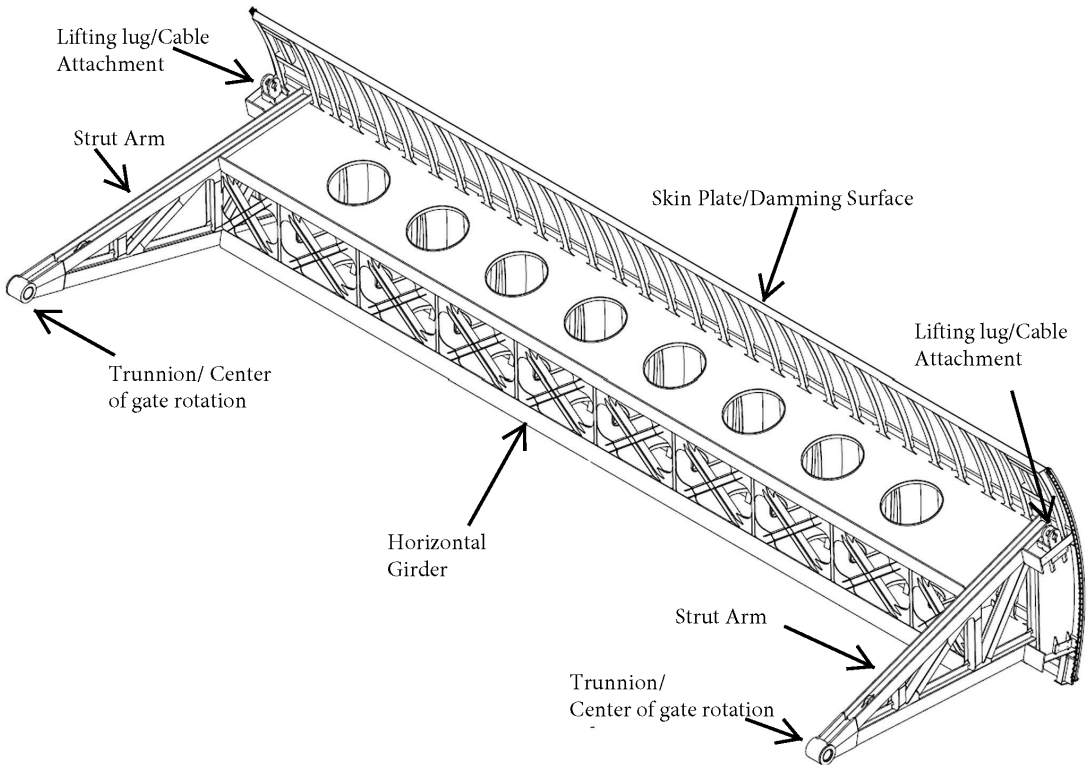

Figure 2.19. Isometric schematic of The Dalles Tainter gate.

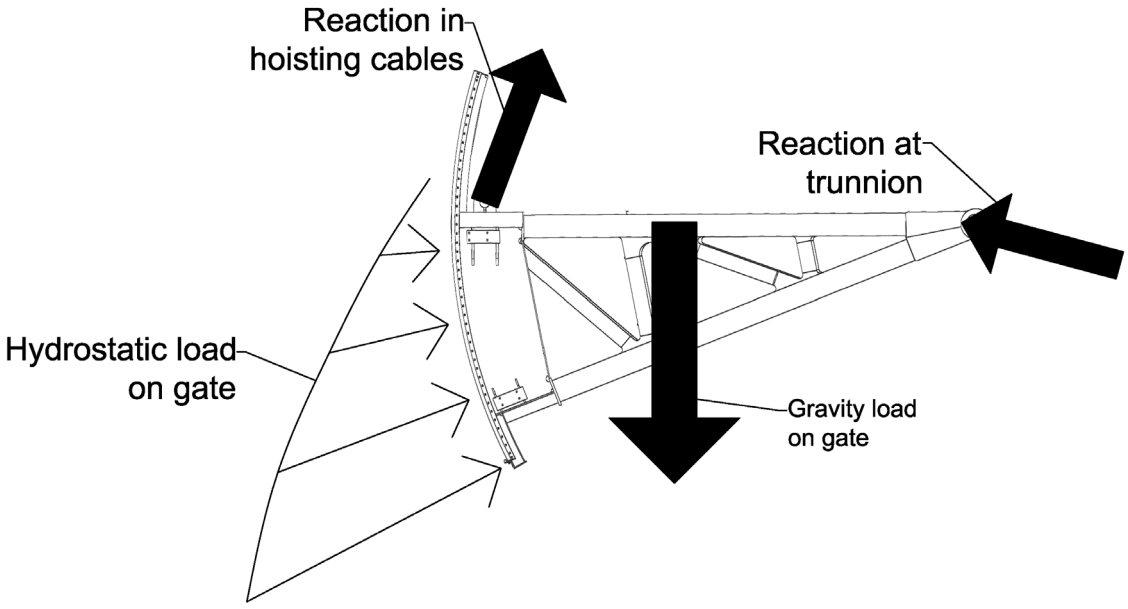

Figure 2.20. Tainter gate under hydrostatic load.

The gravity loads on the gate, as well as the operating machinery loads and potential friction in the trunnion are only considered when the gate is moving. For the sake of the research presented herein, this loading scenario is of critical interest. As the gate raises or lowers, the operating machinery induces a load through the hoisting cable of the gate, which is transferred through the lifting lugs into the gate itself. For a properly designed gate, the loads in the hoisting cables on each side of the gate should be approximately equal. Additionally, as the gate raises and lowers about the trunnion pin, friction in the trunnion needs to be considered. The loading scenario of a moving Tainter gate is shown in Figure 2.21

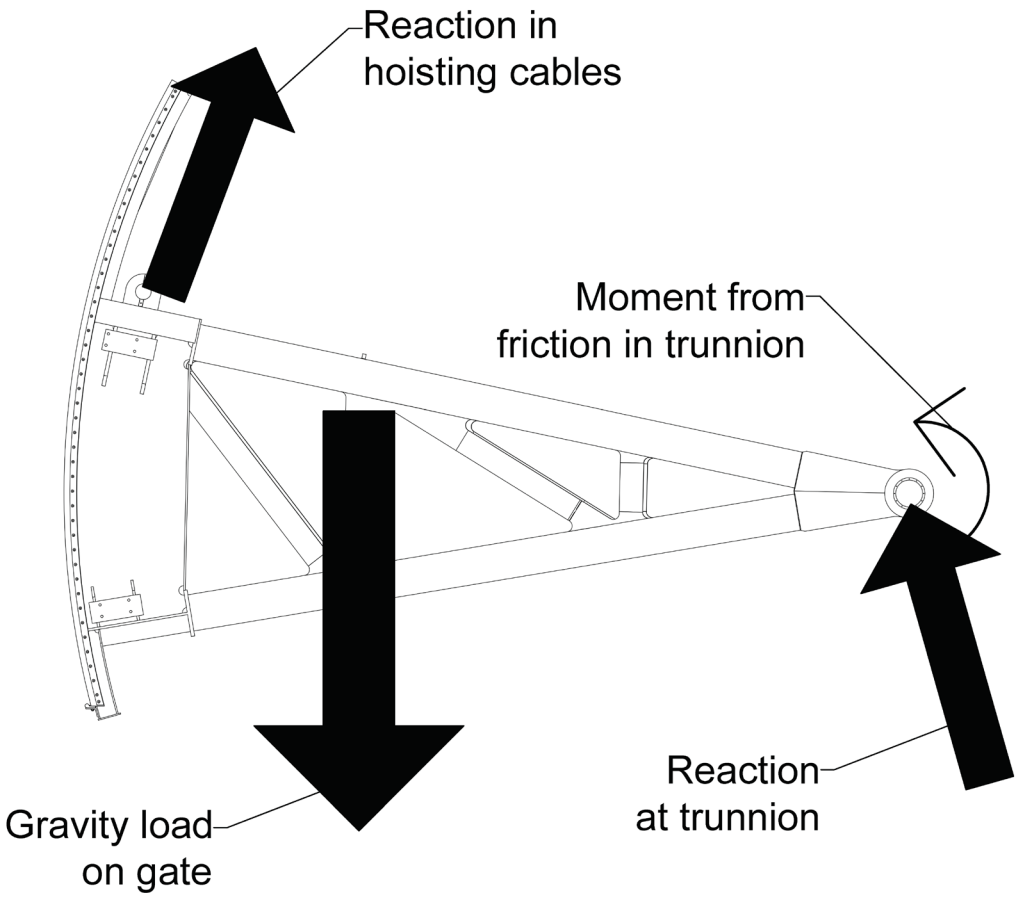

Figure 2.21. Tainter gate under operating loads.

2.2.1. Design and issues with Tainter gate trunnions and operating equipment

The trunnion of a Tainter gate is a critical component with an entire section in the appropriate engineering manual dedicated to its design. A great deal of components are needed to be carefully designed based on expected loadings and degradation modes, many of which are labeled in Figure

2.22. An explicit discussion of the design of all the components of a Tainter gate trunnion is beyond the scope of this dissertation.

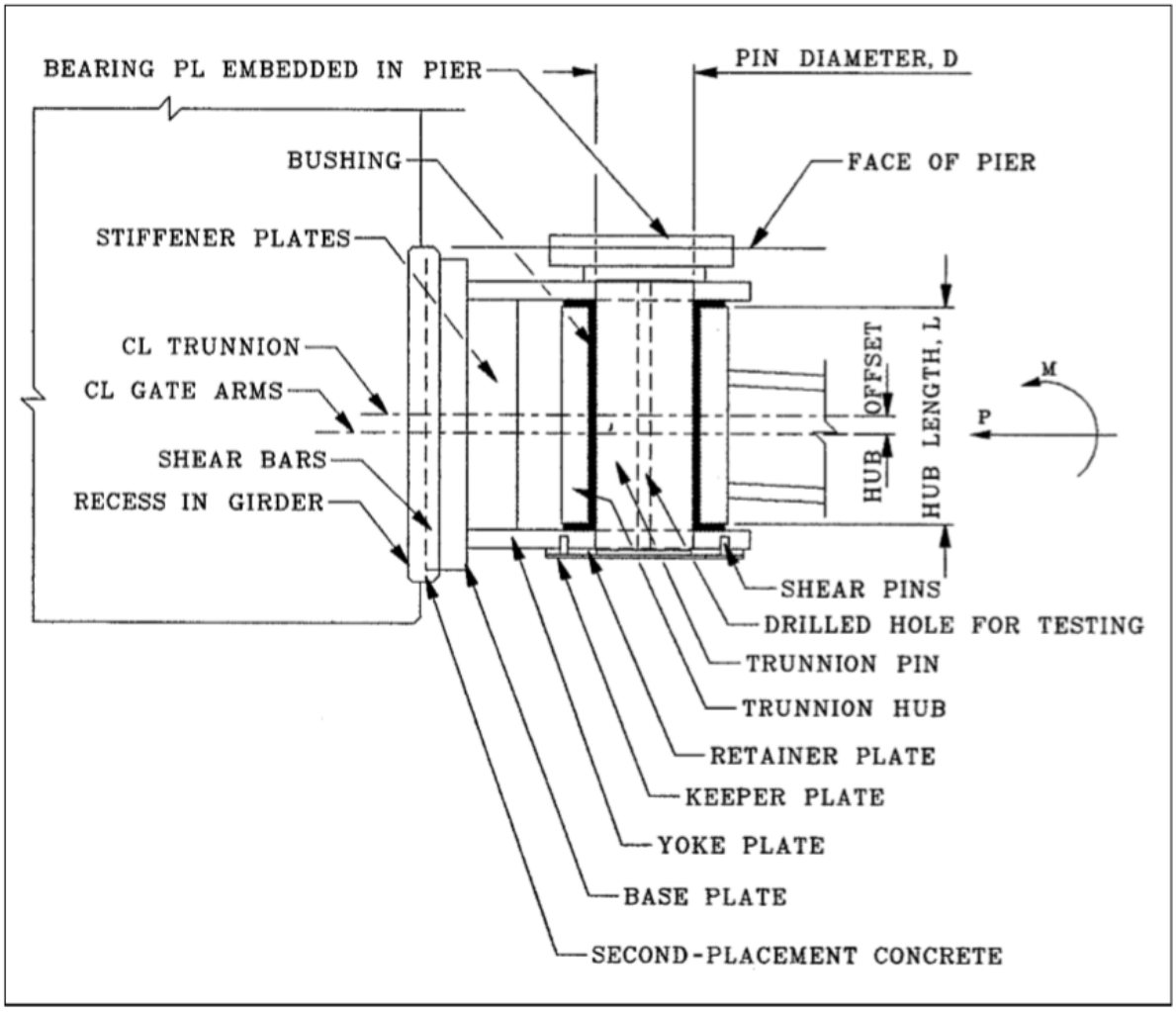

Figure 2.22. Structural components of a Tainter gate Trunnion (U.S. Army Corps of Engineers 2000).

Understanding that the degradation of the trunnion and an associated increase in friction are critical issues to Tainter gate operation is sufficient for the sake of the research presented herein, because these issues may lead to skewed raising and lowering of the Tainter gate, which can cause structural stability issues of the gate and ultimately failure. Indeed, the failure of the Tainter gate at the Folsom dam (Figure 2.23) has been attributed to excessive friction caused by corrosion of the trunnion, which in turn led to uneven hoisting of the gate, and ultimately structural failure.

Figure 2.23.Failure of Folsom dam Tainter gate due to excessive trunnion friction, uneven hoisting, and buckled strut arms (U.S. Army Corps of Engineers n.d.).

To address the potential for uneven hoisting of a Tainter gate, the hoisting drums that raise and lower the gate may be designed such that the drum on one side of the gate is the "master" cylinder, and the drum on the other side of the gate is the "slave" cylinder. This configuration is the design employed at the Tainter lock gate at The Dalles Lock and Dam. The master-slave relationship is such that one drum is designed to rotate at a constant speed, while the other drum is designed to run at a varying speed to prevent skew in the gate. A rotary encoder is used such that, as soon as a difference of one encoder count is detected between the two drums, the slave drum adjusts speed to even the gate. As will be seen in this dissertation, the master/slave drum relationship may not fully address uneven hoisting, as it may not take into consideration the elasticity of the hoisting cables.

Trunnion friction and uneven hoisting of Tainter gates have been identified by the USACE as critical detection targets for SHM systems of Tainter gates. Alexander, et al., (2017) have developed a method of utilizing strain gages to obtain an indication of the magnitude of trunnion friction present on a Tainter gate. Accordingly, Chapter 6 of this dissertation is dedicated to a case study on the apparent uneven hoisting of the Tainter lock gate at The Dalles, and appropriate

methodologies for detecting that phenomenon, whether caused by trunnion friction, malfunctioning operating equipment, or otherwise.

2.3. Summary

This section presented the critical background necessary to understand the SHM methodologies developed as part of this research. The behavior and design philosophies of miter and Tainter gates were discussed, with particular emphasis given to the components and degradation modes that form the basis of the research presented in the remainder of this dissertation. Critical SHM detection targets, as identified by the USACE, were noted and discussed: Miter gate quoin gaps, inappropriate tension of miter gate diagonals, and uneven hoisting of Tainter gates. The development of methodologies to monitor for these three phenomena forms the remainder of this dissertation, with the initial step of development being the creation of appropriate numerical models, as discussed in the next chapter.

Chapter 3. Finite Element Modeling of Lock Gates

In this chapter, the efforts regarding the creation, validation, and use of finite element models is discussed in the context of the research performed herein. For structural health monitoring, finite element analysis (FEA) models of a structure are utilized for two primary purposes: 1) to obtain a greater understanding of the expected behavior of the undamaged structure to be monitored and 2) to determine how damage to the structure affects the quantities that are measurable with the SHM system. Several researchers have utilized FEA models for the analysis of lock gates. Hartman, et al., (1987), published several reports on the detailed analysis of miter gates using FEA. Their reports were published in the 1980s, and so, the computational resources available dictated that their models were poor representations of actual miter gate behavior. Riveros, et al., (2017) have utilized numerical models to investigate the optimal pretension to apply to miter gate diagonals. Eick, et al., (2019) leverage FEA models to investigate the feasibility of existing miter gates to withstand the changes in stress caused by utilizing intermittent quoin blocks

To understand modeling of lock gates, Sections 3.1 through 3.6 of this chapter first outlines best practices to consider when modeling lock gates. Appropriate modeling of the geometry of miter gates is discussed. Then, the modeling of the boundary conditions of various load cases of miter gates is discussed in detail, as is the appropriate loading to apply. Critical constraints and interactions between miter gate components, such as explicitly modeling contact between the quoin and the lock chamber wall, are discussed. Mesh selection and refinement, as well as validation of the model with field data are examined. Finally, specific examples of the best practices are discussed in sections 3.7 and 3.8 by introducing the models of the Greenup miter gate and the Tainter gate at The Dalles. Both structures are instrumented as part of the USACE SMART Gate system, and the FEA models are created and utilized to inform the development of the SHM methodologies that are the subject matter of this research. For all FEA modeling in this dissertation, the commercial software Abaqus is used, and so, the topics discussed herein are presented in the context of the Abaqus software. For specific details of the Abaqus-specific terminology utilized in this chapter, the reader is directed to documentation for the software (Dassault Systems 2017). For general details on FEA, the reader is directed to any textbook on the subject, such as that by Fish and Belytschko (2007).

3.1. Modeling lock gate geometry

A lock gate is typically constructed of welded, thin steel plates. The plates that comprise a lock gate are generally much wider and/or longer than they are thick, and so, on a global scale, their behavior is expected to be primarily plane stress and plate bending. Accordingly, the vast majority of a lock gate's geometry lends itself well to the use of 3D shell elements. This is particularly true for situations where global behavior is of interest, such as deflections of the lock gate due to an applied load or obtaining an indication of the stress field of the global lock gate due to external loads. In the analyses performed in this dissertation, linear, 4-node quadrilateral shell elements are utilized to represent the vast majority of the geometry of lock gates.

Figure 3.1 shows a screen capture of a miter gate modeled using almost entirely shells (with exceptions noted for the diagonals, anchor arms, and quoin block, as described below). The model is of the Greenup miter gate used extensively in this dissertation. For global behavior of the miter gate, this model has been shown to provide adequate results. It is constructed almost entirely of linear, reduced-integration, quadrilateral shell elements denoted "S4R" in the Abaqus commercial software. Where the complicated geometry provides difficulty in meshing, linear 3-node triangular elements are used, denoted as "S3" elements in Abaqus.

The connectivity of the steel plates comprising a lock gate can be problematic to model explicitly using FEA. For global behavior investigation of a lock gate, it is generally sufficient to abstain from explicitly modeling welds or other connections throughout the gate. Indeed, the explicit modeling of every weld on a lock gate would be excessively time consuming. Instead, all welded connections within the lock gate are simply modeled as rigid. To elaborate, generally no constraints or other connectivity methods are used in the model, rather, welds are modeled as shells simply sharing nodes. In the Abaqus commercial software, this is simply performed by modeling the entire lock gate as a single part, and extruding shells out of other shells, which ensures that all lock gate plates are connected.

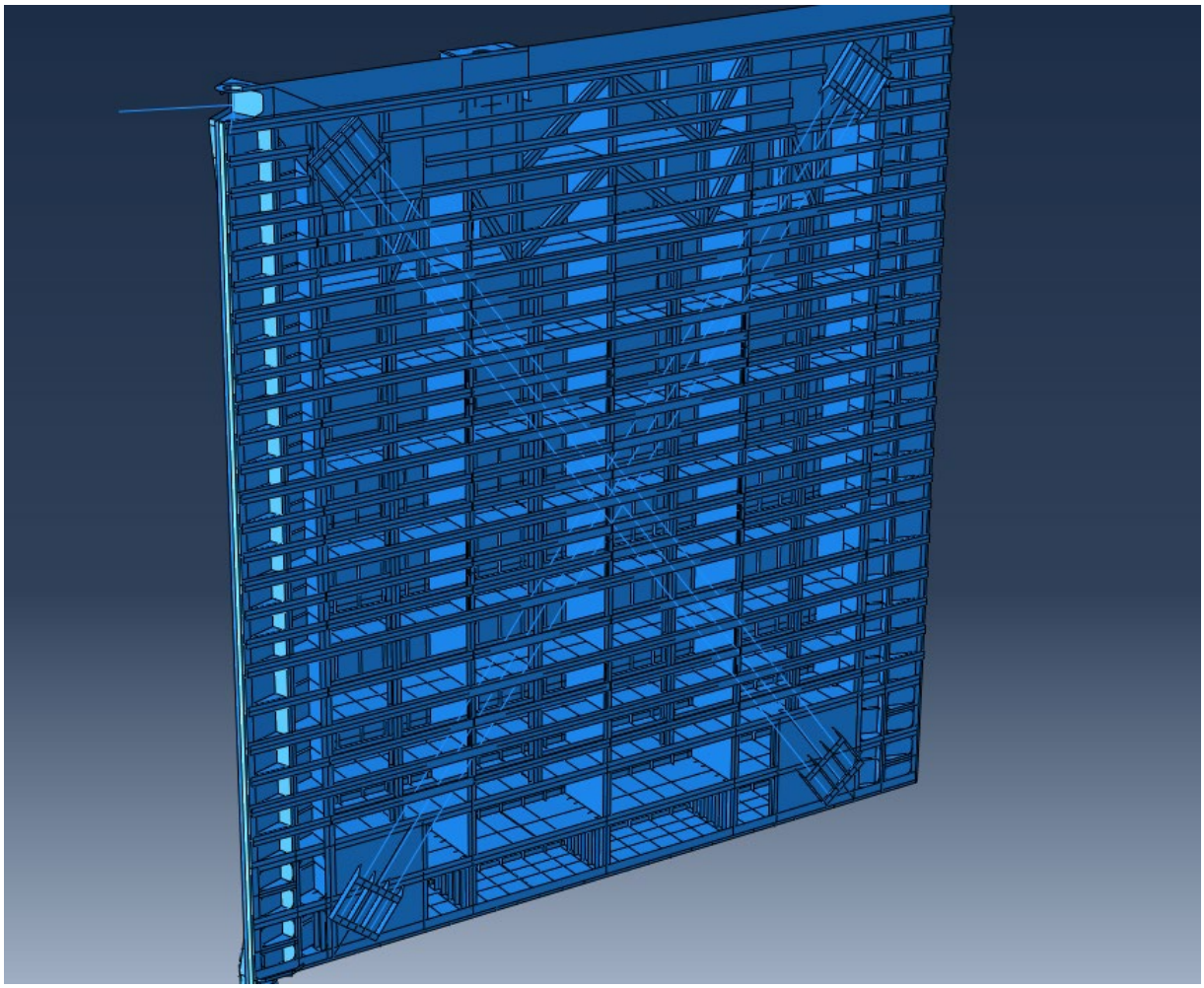

Figure 3.1. Greenup miter gate modeled with shells (geometry only).

The method described above for modeling steel plates as shells, and welds as rigid connections can produce erroneous results in the model, particularly at regions with intersecting plates. As an example, consider a fillet-welded cruciform joint that is typical to a lock gate as shown in Figure 3.2. The geometry of the fillet-welded region is quite a bit more complicated than shells allow to represent, and the interaction between the plates and the welds is very complex in the region immediately surrounding the weld. The typical method of modeling the connection of the plates in this region (as rigid connections with shared nodes) effectively models the connectivity of the region as an infinitely thin line along the center-line of the welded region, as shown on the right in Figure 3.2. The simplification of the weld with shell elements is unable to capture the post-weld residual stress distribution and deformations (Petric, et al. 2014).

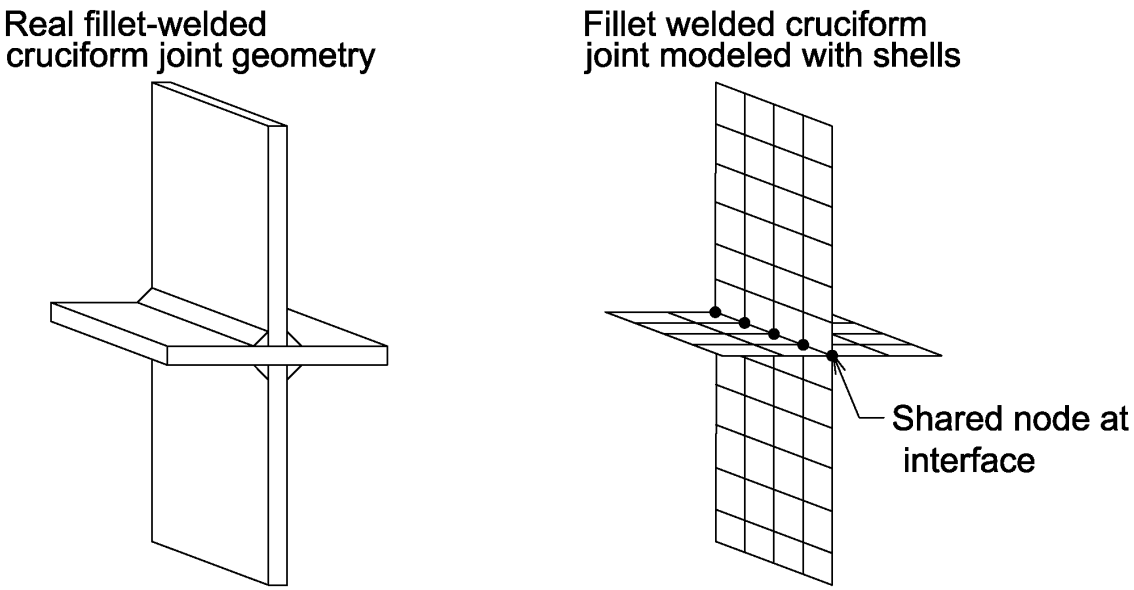

Figure 3.2. Actual geometry of a weld vs. shell representation.

Accurately modeling stresses at or very near welds or other similar connection is better performed with use of solid elements (D. Kim 2003). As an example, the geometry shown in Figure 3.2 was modeled in the Abaqus software using both shells and solids. The geometry was simply pulled at the edges of the plates to apply a load. In the solid model, a quarter inch fillet weld was explicitly modeled at all four locations of weld shown in Figure 3.2. The resulting von Mises stress field for the shell and solid models are shown in Figure 3.3 and Figure 3.4 respectively. As seen, the shell model is unable to capture the complicated stress distribution in the region of the weld, and results very near the weld should not be trusted. The solid model, which provides a much more realistic representation of the weld, provides results which are expected to be much closer to reality for the weld under the applied load.

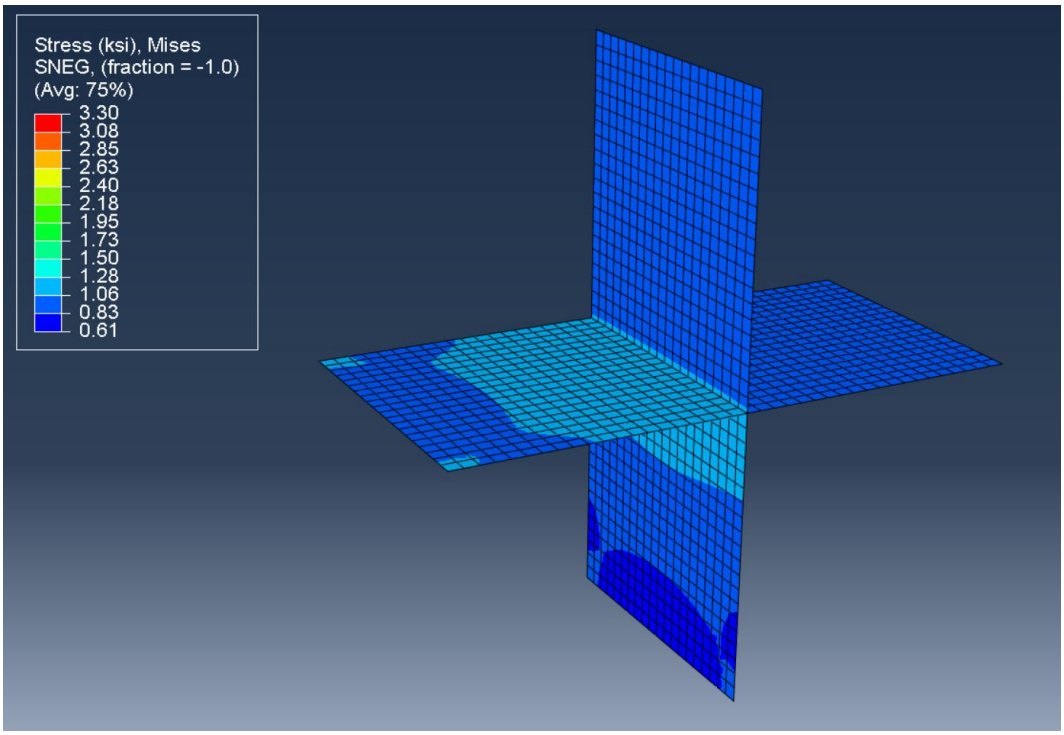

Figure 3.3. Weld represented by shells.

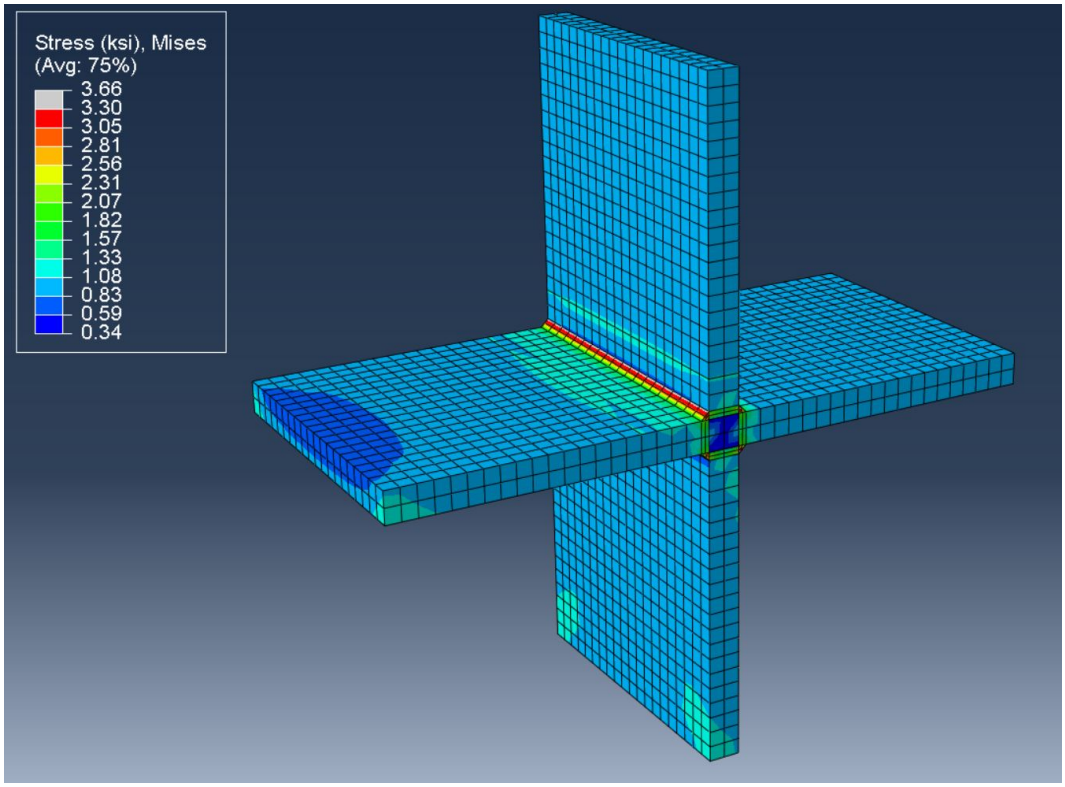

Figure 3.4. Weld represented by solids.

Several components of miter gates are most-appropriately modeled using beam type elements. Beams are particularly well suited for modeling of miter gate diagonals, anchor arms, and strut arms, but can be extended to any long, slender member with behavior well represented by beam theory. Generally, beam-like components utilize linear, 2-node beam elements. The model shown in Figure 3.1 utilizes two node linear beam elements denoted as “B31” in the Abaqus software to model the diagonals and anchor arms. The gudgeon pin and strut arm pins are also modeled using beams, with an example of the gudgeon pin and anchor arms modeled as beams shown in Figure 3.5. Care should be taken when inputting the geometry for beams to accurately capture any connectivity present on the gate. For example, many miter gate diagonals can be accurately modeled as rigidly connected to the miter gate, in which case, having a beam simply share a node with a miter gate shell is sufficient to model the connectivity. In other cases, such as the anchor arms or gudgeon pin, rotation or movement may be allowed between connected components. In these cases, the beams should not be modeled as sharing a node; rather, they should be slightly offset from the point of connectivity and connected using an appropriate constraint, as described in section 3.4.

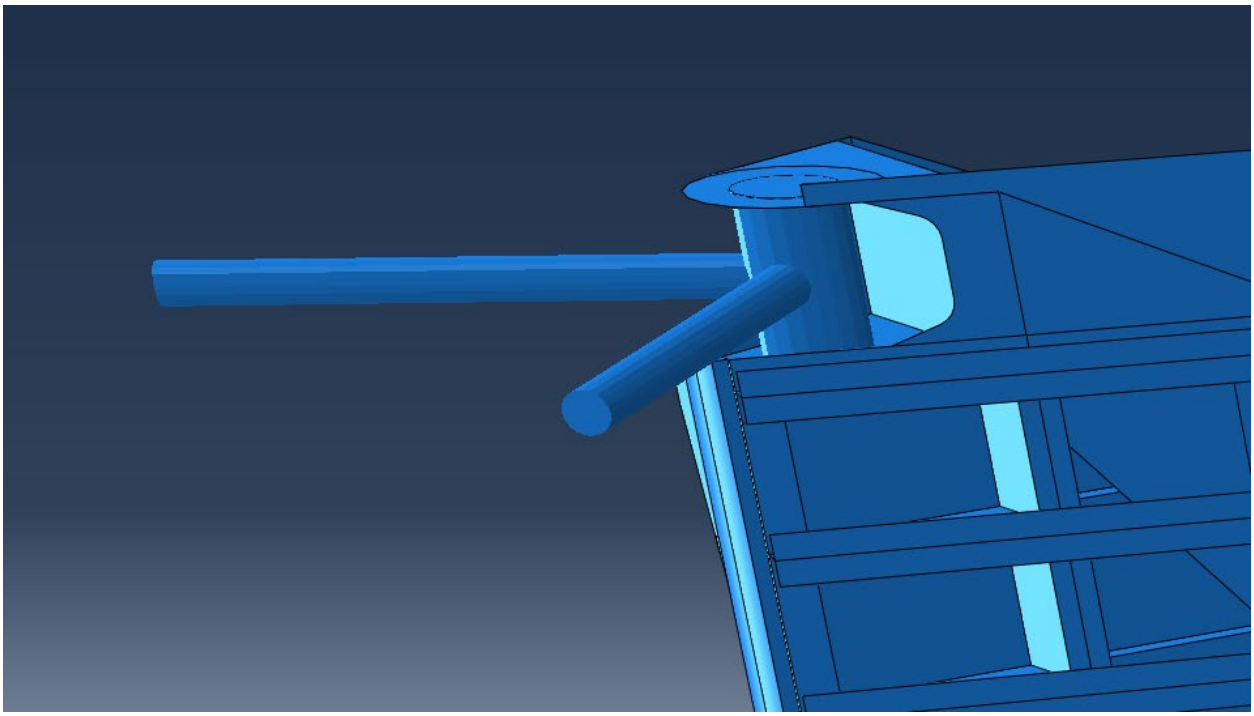

Figure 3.5 Beams used for the anchor arms and gudgeon pin.

Solid geometry is used in a limited fashion when modeling miter gates and is typically only used when a specific component is well represented by solids, or when a detailed local analysis of a particular portion of the miter gate is desired. When utilizing solids in a miter gate model comprised mostly of shells, the modeler should take note that shells and solids are not generally compatible. That is, they cannot share nodes due to incompatible degrees-of-freedom, and so shell-to-solid coupling interaction would need to be utilized in these scenarios (Sellitto, et al. 2011). Another option is to construct any solids and shells as different parts and studiously employ tie constraints, as discussed later in this dissertation.

Typically, linear 8-node hexahedral elements are utilized for solid-type geometry in miter-gate analysis. In the Abaqus software, C3D8R elements are typically used. Two locations where solids have been used with success is in modeling the quoin contact block and performing detailed local analysis of the pintle. The quoin contact block is a very thick steel beam that is intended to serve as a contact-like boundary condition between the gate and the lock chamber wall, shown in Figure 3.6. Several modelers have forgone explicitly modeling the quoin contact block, and have simply utilized the region of the gate where the block would connect to as a contact surface. However, for analysis where the results immediately near the contact block are of interest, it was seen that not explicitly modeling the contact block as a solid piece led to an unrealistic distribution of load to the miter gate girders. Accordingly, for analysis where the location near a contact block is of particular interest, the contact block should be explicitly modeled using solids, similar to that seen in Figure 3.6, which shows the contact block used for the same Greenup miter gate model shown in Figure 3.1. In this case, the solid block is connected to the rest of the gate via a tie constraint.

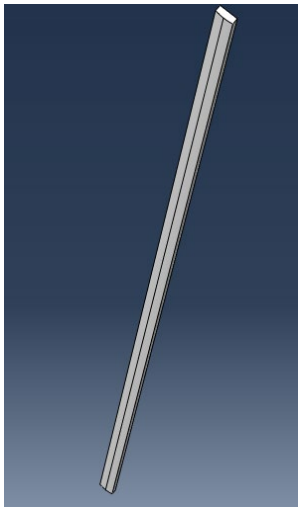

Figure 3.6. Contact block modeled using solid elements for the Greenup lock gate model.

3.2. Modeling lock gate material properties

Miter gate material properties are addressed in a relatively straightforward fashion. Effectively, the modeler simply applies the appropriate values for the density, elastic behavior, etc. The most critical aspect to consider when inputting the properties is to ensure unit consistency. That is, if the geometry of the model is defined in inches, and loads are defined in kips, then all material properties need to be consistent to these units. Throughout this dissertation, models are created using the imperial system of units utilizing kips, inches. Thus, the density of steel (for example) is input as approximately $7.35 \times 10^{-7} \frac{kips*s^2}{in^4}$.

There are some unique aspects to miter gate material properties that may not be obvious and should be considered by a modeler. For example, if contact between the quoin and the lock chamber wall is being explicitly modeled, the modeler should take care to accurately represent the lock chamber wall with appropriate concrete material properties. As found by Hoskere, et al., (2019) a small wall-quoin piece (modeled as steel) with a rigid boundary condition provides too much stiffness to the region, causing a slight overestimation of stress in regions near the quoin. For most practical purposes, this appears to be a minimal issue that can be ignored.

Additional attention should be given to the miter gate diagonals. These long, slender members can provide erroneous results in situations where it is of interest to model a miter gate with un-tensioned diagonals, or situations where the diagonals are expected to go slack. Effectively, the diagonals are tension-only members due to their large slenderness ratio. Using linear analysis, and modeling the diagonals as beams, the analysis will be unable to capture the buckling of the diagonals in compression (which, due to their slenderness, will happen as soon as they are in compression). Rather, the linear analysis will treat the beams equally stiff in compression as in tension. If possible, the diagonals can be modeled as tension-only; however, through the course of this study, tension only diagonals have been found to lead to an unstable model. As soon as the diagonals are placed in compression, they will infinitely deform, and equilibrium cannot be obtained. One approach to alleviate the instability is to superimpose a beam with very little compressive stiffness over the diagonal and constrain the two pieces or to define a material property with very little compressive stiffness. For many of the load cases of importance to an engineer, the miter gate diagonals are not engaged, and so this will be of no concern. The primary load case where this is of concern is the scenario where the miter gate is opening or closing and is obstructed at the bottom corner of the miter block, as described in Chapter 2.

3.3. Modeling miter gate geometric properties

The most critical concern when modeling the geometric properties of a lock gate are locations with beams of varying cross-sections and locations with multiple plates welded on top of each other. The most critical location of beams with varying cross-section requiring accurate modeling is the anchorage link arms on miter gates. There are several approaches that a modeler may take to represent these components. If the varying cross-section can be well represented by a mathematical function of the length of the beam, it is generally possible to incorporate this directly into an FEA code. Another option is to manually discretize the beam into many small parts, and assign each discretized representation an average cross-section for the region. The approach taken herein is to assign an equivalent stiffness to the beam. This approach is likely to be significantly less time intensive than other options.

To assign an equivalent stiffness, the beam with varying cross-section is thought of as a set of springs in series. The equivalent stiffness, k_{eq}, is then given by:

$$\frac{1}{k_{\text{eq}}} = \frac{1}{k_1} + \frac{1}{k_2} \ldots + \frac{1}{k_n} \tag{3.1}$$

where k_i is the stiffness of the i^{th} beam and n is the number of discretized beam segments considered. A question to consider then is what beam stiffness should be considered (e.g., axial, flexural, torsional). The authors herein consider the stiffness corresponding to the behavior the is expected to dominate the component. For example, miter gate anchorage link arms are expected to behave primarily as axial load members, and so, the axial beam stiffness is used, where, all other properties being equal, the cross-sectional area defines the axial stiffness.

Frequently for miter gates, there are locations with multiple plates welded at a single joint. Care must be taken when modeling these joints so that the thickness and placement of all components is accurately captured. To understand the issue, consider a shell model of a simple I-beam as in Figure 3.7, which considers a 25-inch deep I-beam with 12” flanges, all of which are 1.0” thick. Often times, the modeler may be given outer dimensions of the geometry, as shown in Figure 3.7. By simply inputting these outer dimensions into the preprocessing software, the modeled beam will inaccurately depict the geometry of the beam, as seen in Figure 3.8-a. Without offsetting the shell centroids, the beam will be modeled as 26 inches deep, as seen in Figure 3.8-b. Moreover, the top and bottom half-inch of the modeled web will encroach into the flanges, effectively doubling the amount of material in these locations. Even if the centroids of the flanges

are offset as in Figure 3.8-c, the depth of the beam will be correct but the web and flanges will still overlap, leading to an increased moment of inertia. To more accurately model the beam, the modeler should subtract the thickness of the flanges from the outside dimension of the depth of the beam, and use the resulting dimension to model the web (in this case, 23 inches). While the definition in the preprocessor will appear to model a beam that is one inch too shallow (Figure 3.9-a), offsetting the shell centroids will provide the appropriate depth of the full beam, as seen in Figure 3.9-b. Additionally, the flanges and webs will not intersect, leading to an appropriate moment of inertia. Note that for miter gates, typically all outer dimensions are equal, while flange thicknesses and web widths may vary. Thus, accurately modeling the depth of all beams of a miter gate, as described above, may lead to nodal mismatches, and so, the small changes in stiffness introduced by additional modeled material may need to be allowed to facilitate feasibly modeling the whole structure.

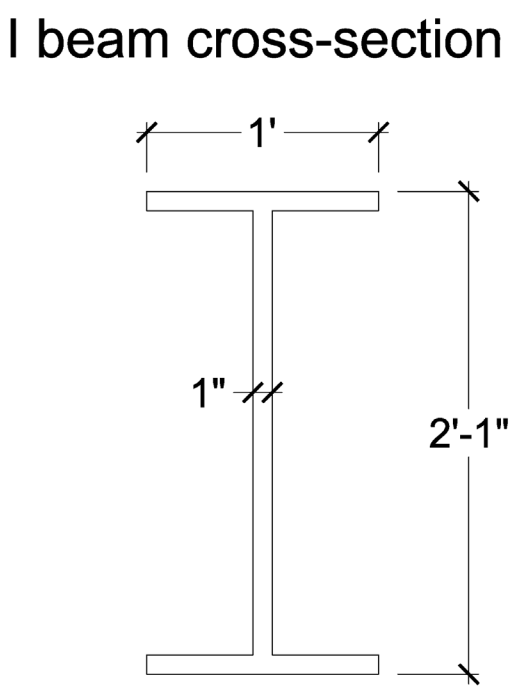

Figure 3.7. I-beam to be modeled as shells.

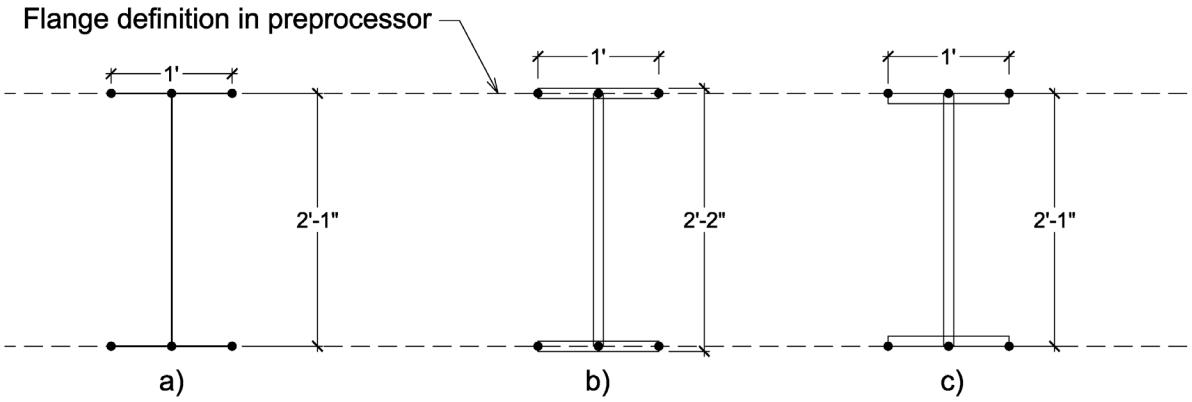

Figure 3.8. a) Definition of beam that leads to inaccurate representation. b) No shell offsets defined, beam is too deep and some shells overlap. c) With shell offsets, web and flanges significantly overlap leading to more mass of the beam and higher moment of inertia.

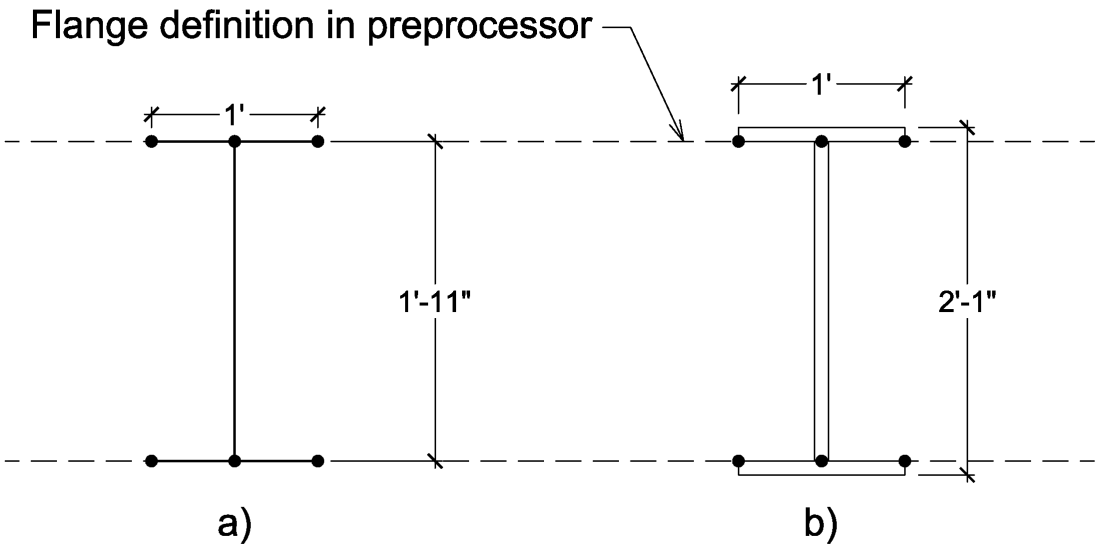

Figure 3.9 a) beam definition that allows for accurate representation. b) Shell offsets appropriately defined, beam is correct depth with correct moment of inertia.

An additional scenario that should be considered is an instance where multiple plates are welded on top of each other on the physical structure. This is a common occurrence on miter gates, particularly on the flanges of horizontal girders. For example, the skin plate of the miter gate frequently covers and is welded to the upstream flange of the horizontal girders. A simple representation of a configuration similar to the flange/skin-plate connection is shown in Figure 3.10-a, which shows two beams connected with a cover plate. The geometric representation of this

configuration for a shell-based model is shown in Figure 3.10-b. To capture the regions where the cover plate overlaps the beam flanges, a shell is assigned with thickness equal to the sum of the thicknesses of the individual plates. Care should be taken because if shell offsets are not considered, the plates will likely not align correctly, as in Figure 3.10-c, which may lead to an incorrect stiffness of the model. Figure 3.10-d shows the shell representation with appropriate thicknesses and offsets assigned so that the stiffness of the configuration is adequately captured.

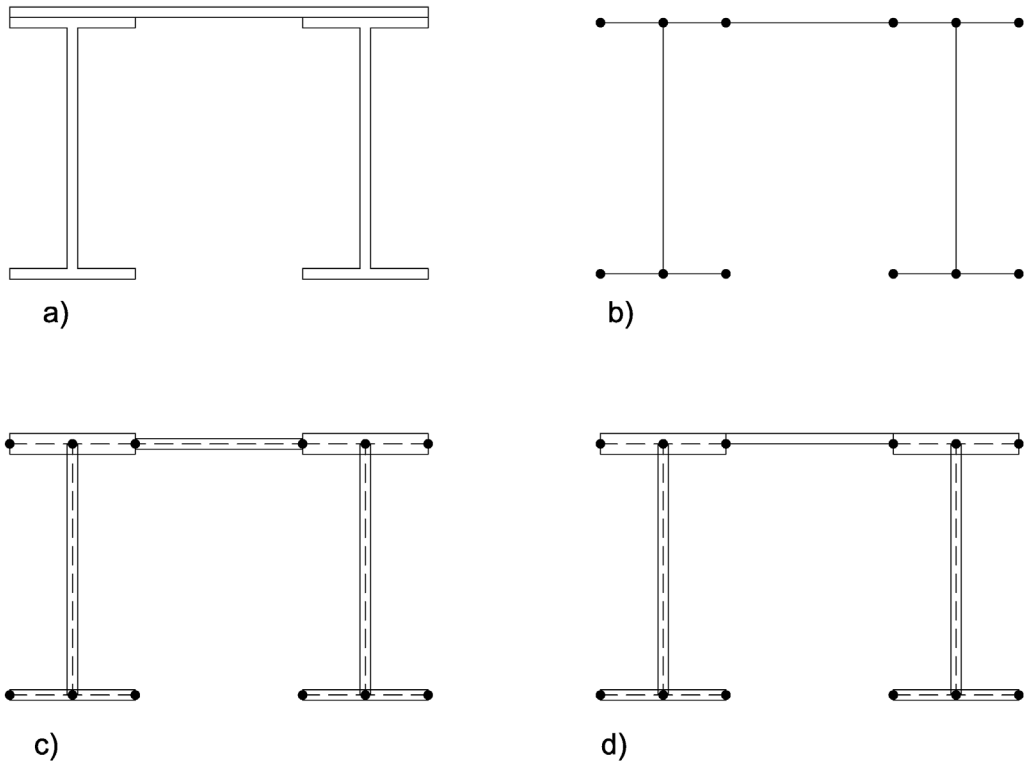

Figure 3.10. Modeling beams with cover plates. a) A schematic of a beam with a cover plate. b) The representation of the beam with a cover plate in a shell-based numerical model, c) 3D representation of shell model with offsets incorrectly defined at shell midpoint. d) 3D representation with appropriate thicknesses and offsets defined.

3.4. Constraints and interactions

Lock gates have many locations with complicated interactions, the accurate modeling of which is necessary to represent the behavior of the gate. Of particular concern are the pintle, the quoin, and the gudgeon of miter gates. To accurately capture the behavior of these regions, various constraints and interaction definitions are utilized in the analysis. Of particular use to miter gate modeling are what are known in Abaqus as multi-point constraints (MPC) and tie constraints. MPCs are utilized to couple the degrees-of-freedom (DOFs) of some nodes (termed slave nodes) in the analysis to the DOFs of one particular node (termed the control point). In Abaqus, there are

many options for MPCs, the appropriate choice of which depends on which DOFs are to be coupled. For the analysis performed in this dissertation, link-type MPCs are utilized, which provide a pinned, rigid link between the slave nodes and the control point. An MPC link maintains the norm of the distance between two nodes, and so, the nodes are free to rotate with respect to each other.

Examples where link-type MPCs are used in the model are the gudgeon, the strut arm connector, and the pintle. Recall from section 2.1 that the gudgeon is the upper hinge on the miter gate. The gudgeon consists of two anchorages, a pin, and a gudgeon hood. The contact between the anchorages, pin, and gudgeon hood can be challenging to model using FEA, so an MPC link-type constraint is used, as seen in Figure 3.11. In the model, the gudgeon pin top and bottom act as the control points for the gudgeon assembly. Then, the steel plates that the gudgeon pin passes through are constrained to the control points as slave nodes by using the MPC-link constraint. This means that the top and bottom of the pin shown in Figure 3.11 (where the label "MPC Link" is shown) can rotate freely about the pin plates represented by the red circles, but translational motion will be all the components will be coupled.

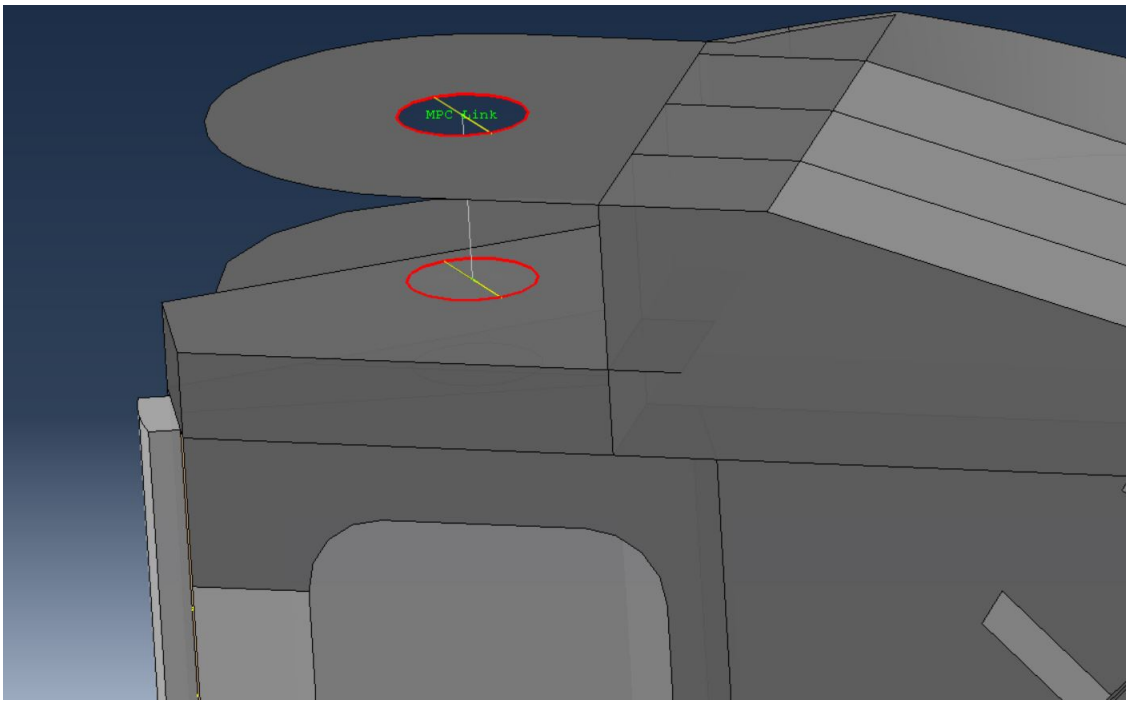

Figure 3.11. Gudgeon multi-point constraint.

The strut arm is the piston that physically opens and closes the miter gate. This opening and closing action induces a force on the gate, in the location noted in Figure 2.5. The strut arm

connects to a pin that is in turn connected to the gate. A multi-point constraint is used to model the interaction between the strut arm pin and the steel plates on the gate, as shown in Figure 3.12. The strut arm constraint is very similar to the constraint used to model the gudgeon. Rather than anchorage beams connecting to the strut, a boundary condition is applied to the strut to restrain movement in the direction of the strut arm, as would be expected in the field. The pin that connects the gate in the strut arm is modeled similarly to the gudgeon pin, and the plates to which the pin passes through are constrained to the top and bottom of the pin using MPC link constraints. This allows the strut-arm pin to rotate freely about the plates.

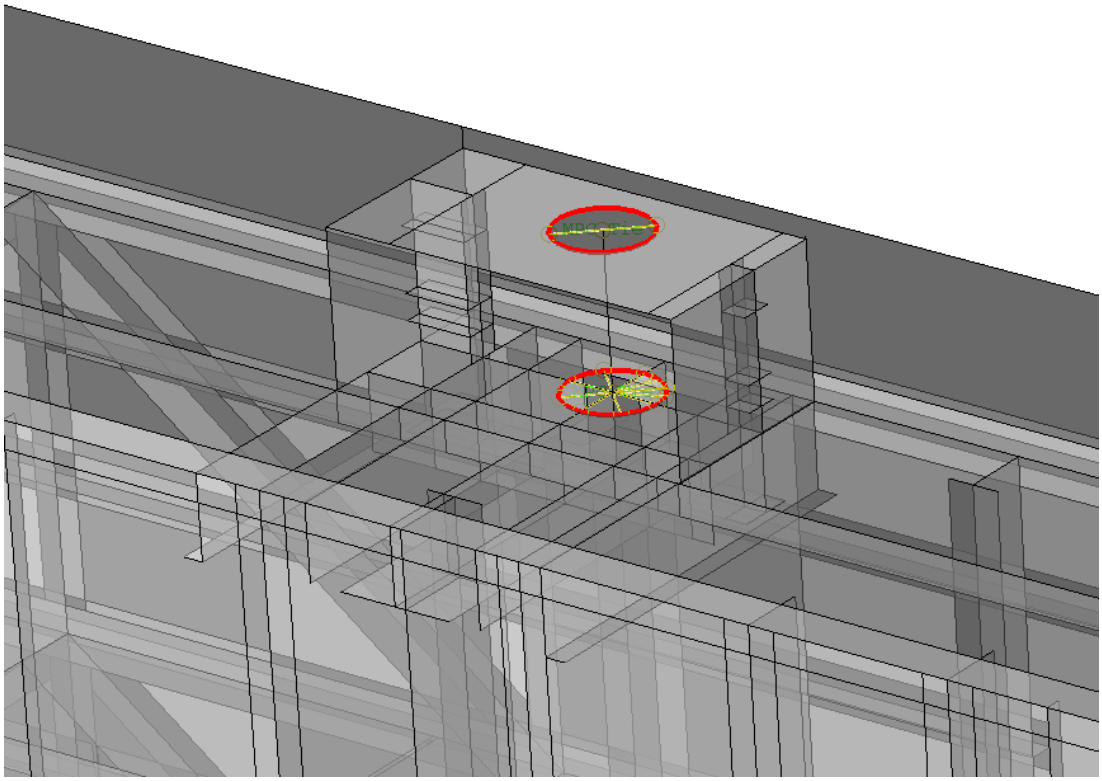

Figure 3.12. Strut multi-point constraint.

The pintle of a miter gate, as discussed in section 2.1, has complicated behavior with a large cup-like steel component on the miter gate rotating freely over a ball connected to the lock chamber floor. To simplify this interaction, while still accurately capturing the behavior, the "cup" portion of the pintle is modeled accurately and connected to the gate, as seen in red in Figure 3.13. The ball portion of the pintle is typically modeled as a beam spanning from the center of the cup to a location coincident with the center of the ball on the physical gate (note, in Figure 3.13, the position of the center of the ball is offset for visualization purposes). This modeling of the ball is simply

utilized to provide some connectivity of the gate to the point about which it rotates. Then, to simulate the rotation of the pintle, a link-type MPC is utilized where the bottom of the beam is used as the control point and the entire interior surface of the cup is selected as the slave nodes. This single MPC allows the pintle to rotate as expected in the field.

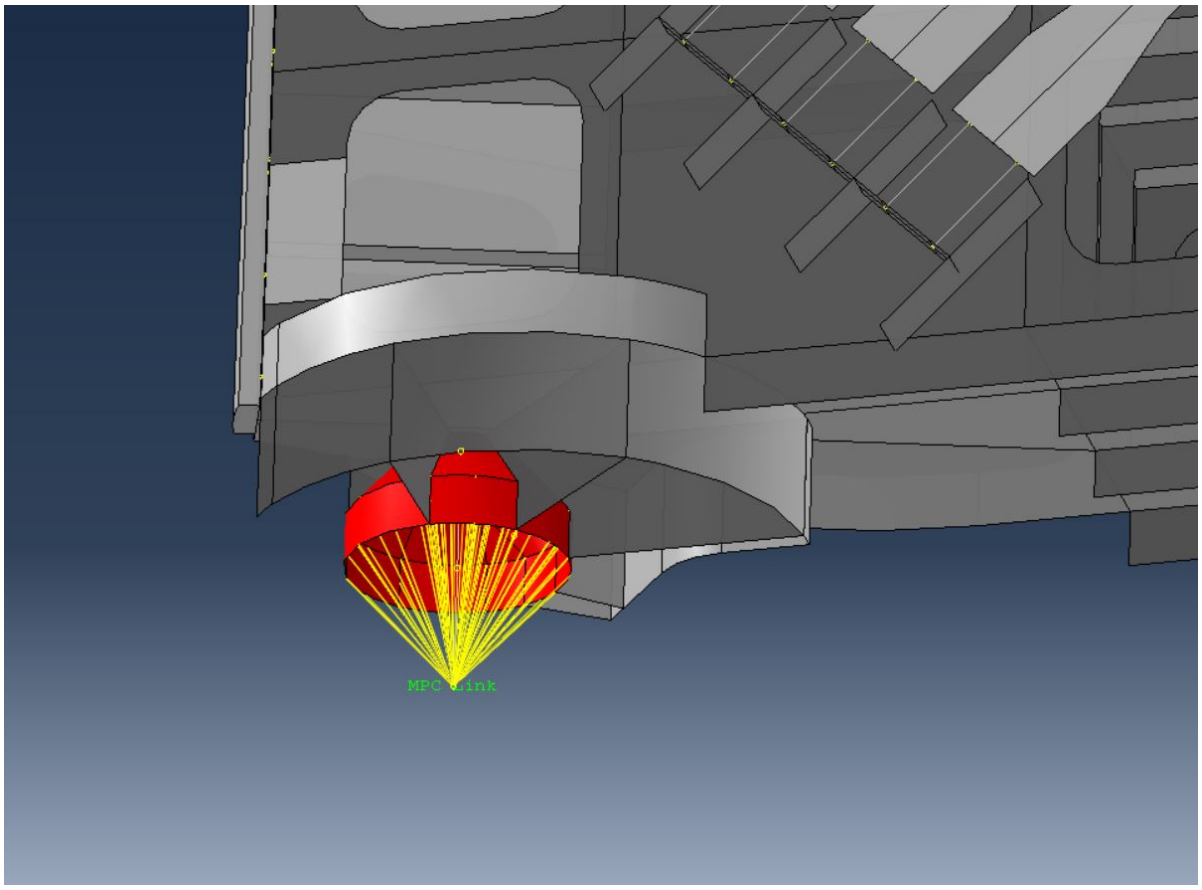

Figure 3.13. Pintle multi-point constraint.

In section 2.1.1, the contact block used in the quoin and miter regions of miter gates was discussed. As mentioned in section 3.1, the contact blocks are best modeled as separate, solid parts that need to be connected to the rest of the model of the gate. The connection is done via a tie constraint. Figure 3.14 shows the quoin contact block tied to the miter gate end plate, with the red field and yellow circles representing the tie constraint. The tie constraint constrains the translation and rotational movements of the back surface of the contact block to the outer surface of the quoin region of the gate. Similarly, the miter contact block is tied to the miter end plate.

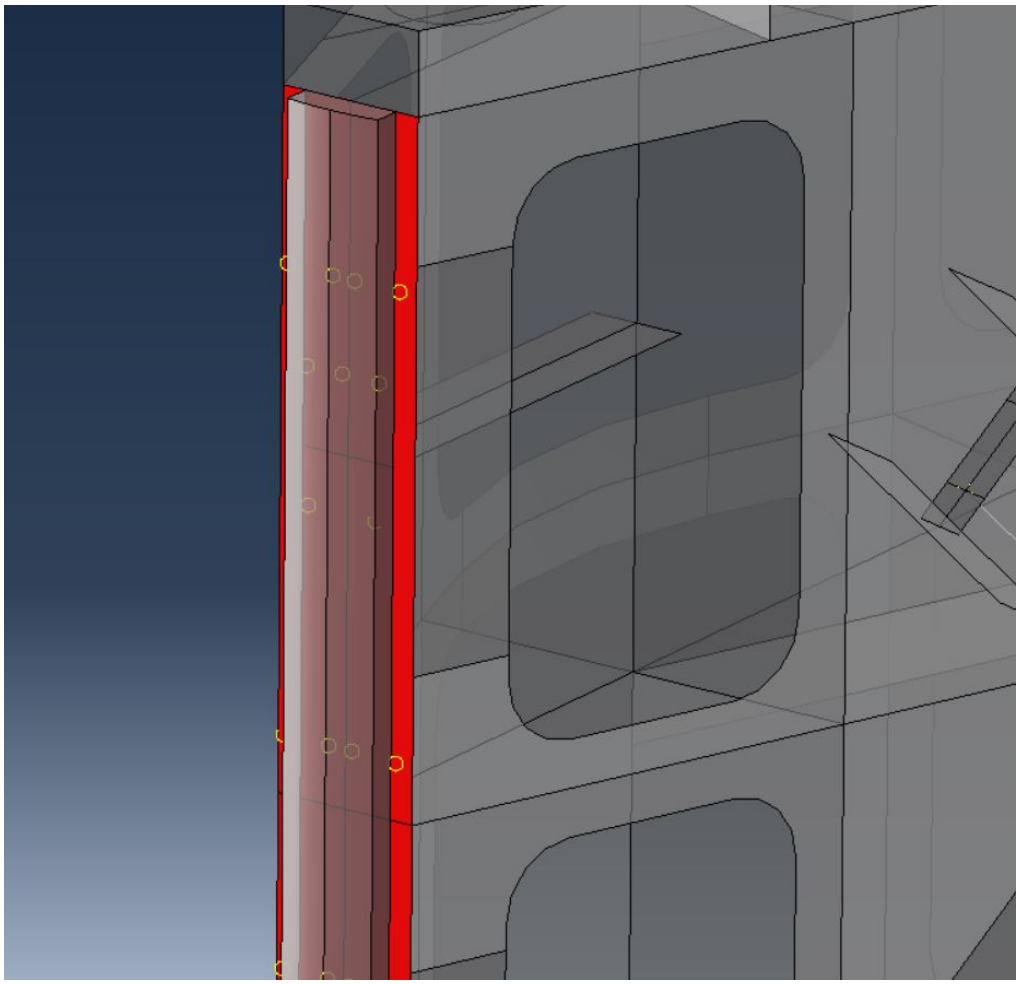

Figure 3.14. Quoin block tied to the end plate of the miter gate.

3.5. Mesh discretization and selection

To ensure that the mesh utilized in the numerical model is sufficiently refined, a discretization study is performed. For FEA, as the mesh becomes more and more refined, it is assumed that the solution approaches the theoretical exact solution (NASA 2008). However, a more refined mesh will demand more computational resources. Thus, a trade-off must be made between a computationally efficient model and a sufficiently accurate model. The most efficient method of determining how refined a mesh should be is to investigate the solution of a series of FEA with increasingly refined meshes. The solution from the most refined mesh is used as the benchmark to compare the other solutions. For the research performed herein, the meshes are considered sufficiently refined when the percentage difference from the most refined mesh is less than one percent. Specific examples of mesh refinement studies are given in the examples in sections 3.7 and 3.8.

3.6. Validation and model updating

When possible, and after a refined mesh is found, the lock gate model should be validated against existing data to ensure that the behavior of the model sufficiently represents the behavior of the physical gate. For the research performed in this study, the primary data of interest for model validation is strain gage data collected as part of the SMART Gate system from USACE. However, data outside the SMART Gate system may be of interest as well. For example, when miter gate diagonals are tensioned in the field, engineers occasionally collect survey data on the torsional deflection of the gate due to tensioning of the diagonals. This data is excellent for verification of the torsional stiffness of the miter gate and to validate the mass of the model. Unfortunately, for the models utilized as part of this study, this survey data does not exist, and so, only the SMART Gate strain data is utilized.

For a miter gate, validation is best performed by simulating a loading event on the gate and comparing the change in strain in the model to the change in strain on the physical gate subjected to the same load in the field. For the Greenup model in this study, this type of validation is performed, as explained in detail below. For a Tainter gate, the primary value of interest is strain in the strut arm while the gate is raising and lowering. Thus, validation is performed by comparing the simulated change in strain in the strut arms due to a change in gate position of the model to a similar scenario on the physical gate. This is performed for The Dalles Tainter gate, as explained in detail below. These validation steps are used to inform shortcomings in the model to allow updating appropriately. For the case of the Greenup miter gate, the validation step highlighted that the upper girders of the gate are likely not in contact with the quoin, and so, the model was updated appropriately. For The Dalles Tainter gate, the validation step highlighted that there is likely an issue with the raising and lowering of the gate, and motivated further testing in the field to validate that the gate was operating abnormally. The validation and updating steps for the two models utilized in this research are explained in detail in their respective sections below.

3.7. The Upstream miter gate at the Greenup Lock and Dam

The upstream miter gate at the Greenup lock and dam is a horizontally framed miter consisting of twelve horizontal girders and five vertical diaphragms. The gate stands at 62.75 feet tall, from the centerline of the top girder to the centerline of the bottom girder, and is 61.5 feet wide from the point of contact at the quoin to the point of contact at the miter. The gate was modeled utilizing the best practices, as described previously in the chapter. The primary use of this model throughout

this dissertation is in modeling the gate under hydrostatic load, and in modeling the degradation in the quoin region of the gate. The model is as shown in Figure 3.1, and consists primarily of shell-type geometry, with exceptions being the quoin contact block, the anchorages, and the diagonals, which are modeled as described above.

The miter gate at Greenup was modeled primarily due to the fact that it is instrumented as part of the USACE SMART Gate system. A map of the instrumentation was provided by the USACE and is shown in Figure 3.15. The labeling system is such that "S" refers to strain gage, "LC" refers to load cell, and "RTD" refers to resistance temperature detector. Not shown in Figure 3.15 are four strain gages on each the second, sixth, tenth, eleventh, and twelfth girders. Of primary interest to the studies performed in this dissertation are the strain gages. Accordingly, the FEA model of the Greenup gate was partitioned such that small squares were placed at location corresponding to the locations of strain gages on the physical gate. These partitions facilitate the collection of data at the location of strain gages to validate the model and test for convergence of the solution. These partitions are shown as red squares superimposed on the gate in Figure 3.16.

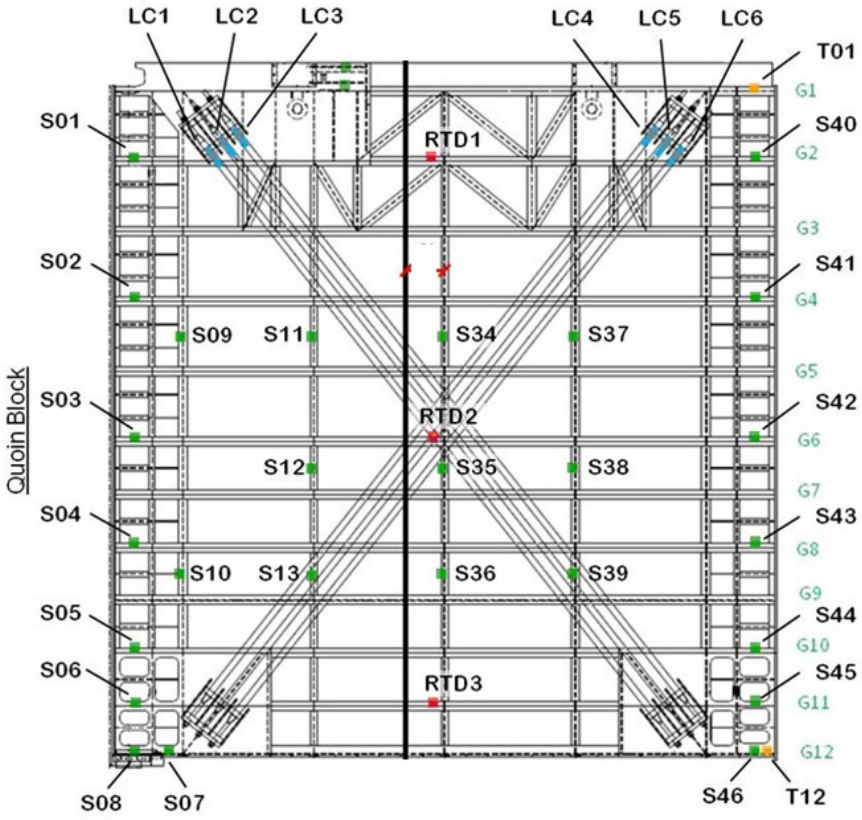

Figure 3.15. Sensor map for Greenup miter gate.

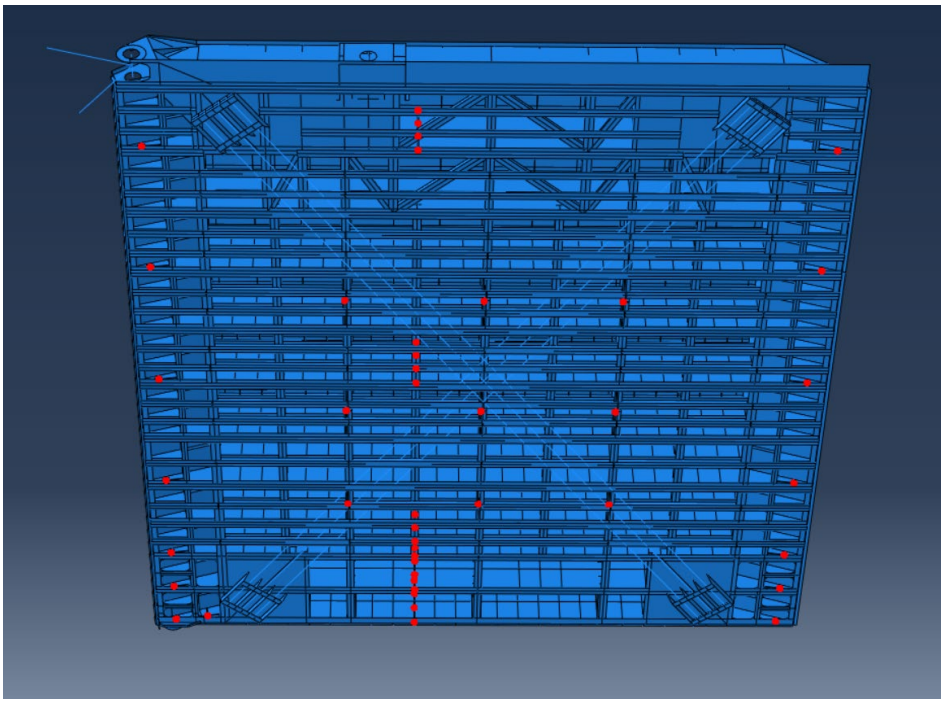

Figure 3.16. Partitions (red squares) in the geometry representing locations with strain gages.

3.7.1. Constraints and boundary conditions

The Greenup miter gate model follows the general best practices laid out in the previous section regarding constraints used for the pintle, gudgeon, and strut arms. Additionally, tie constraints are used to connect a solid contact block in the quoin with the appropriate region on the gate. As for loads and boundary conditions, the primary load scenario of interest to the Greenup miter gate is that when the gate is closed and subjected to a hydrostatic pressure from the differing water levels on either side of the gate. The boundary conditions for this loading scenario are such that the anchor arms at the top of the gate and the pintle at the bottom of the gate are pinned. Explicitly simulating contact between two leaves of the gate in the miter region is prohibitively demanding from a computational perspective and typically leads to solution convergence issues. For computational efficiency, each leaf of the gate is modeled assuming symmetry with the other leaf of the gate and the contact interaction between the two leaves is simulated by simply using a line of rollers along the height of the miter contact block. An outline of the idealized boundary conditions that can be considered for a miter gate under hydrostatic load is shown in Figure 3.17. Strictly speaking, the quoin region of the gate also has non-linear contact-like behavior; however, for many simulations, this contact can be well represented by rollers in the quoin region, as seen in Figure 3.17.

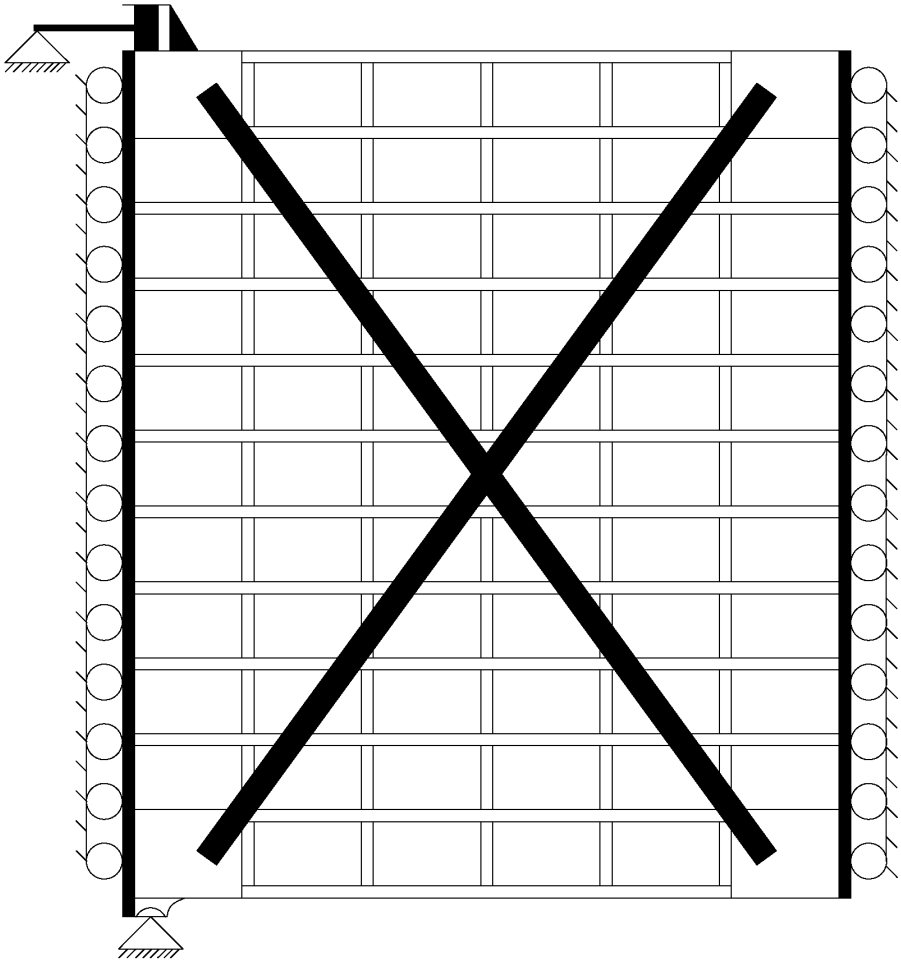

Figure 3.17. Idealized boundary conditions on the Greenup miter gate model.

For many simulations, it has been found that simplifying the non-linear contact behavior in the quoin by simply considering a line of rollers along the height of the quoin is sufficient. However, the miter gate quoin gap detection algorithm developed as part of this dissertation explicitly considers contact between the quoin and a solid block modeled to simulate the lock chamber wall. Contact is used in this scenario to allow for regions of the quoin next to the gap to potentially come into contact under load, or allow regions away from the gap to separate. Note, it was found in this dissertation that only a very small portion of a quoin gap will close due to the extreme stiffness of the quoin region of the gate. Thus, even for quoin gap modeling, it is likely adequate to consider the simplified boundary condition of rollers along the quoin, with the gap being represented as a portion of the quoin without rollers applied.

3.7.2. Mesh discretization study for Greenup

As mentioned above, the primary use of this model is in modeling the gate under hydrostatic load and modeling the degradation of the quoin region of the gate. Accordingly, the locations corresponding to strain gages in the quoin of the gate are investigated for convergence of the solution. As an exact solution is not obtainable for this model, convergence is deemed to be obtained when the solution of the model changes less than 1 percent from one refinement step to the next. Some background information and approaches on mesh convergence can be found in the literature (NASA 2008). The models investigated had meshes comprised of 112k, 159k, 285k, 636k, 815k, 1.11 million and 2.50 million elements. For each refinement step, the von Mises stress is recorded at each strain gage in the quoin region of the gate (gages S01 to S08 in Figure 3.15). A typical convergence plot is shown in Figure 3.18. From the results of this discretization study, it is deemed that the mesh comprised of 815,000 elements is sufficiently converged, with the note that local refinement is required around the pintle region of the gate. Note, for a model of this size, it is difficult to obtain monotonic convergence using the Abaqus software. One of the requirements of monotonic convergence is that the mesh in each refinement step must contain the nodes from previous refinement steps in their original position (Lepi 1998). In Abaqus, refining the mesh entails deleting the original mesh, defining a smaller approximate element size, and then constructing an entirely new mesh. Maintaining all nodes in their original positions is not possible in this procedure. Nevertheless, the change in stress in successive refinements shown in Figure 3.18 is sufficiently small for the purposes of the research performed herein. The final mesh, after local refinements, contains 919,500 elements, of which 3208 are linear beam elements, 49846 are linear triangular shell elements, 843,586 are linear quadrilateral shell elements, and 22,850 are linear hexahedral brick elements. The selected mesh is shown in Figure 3.19.

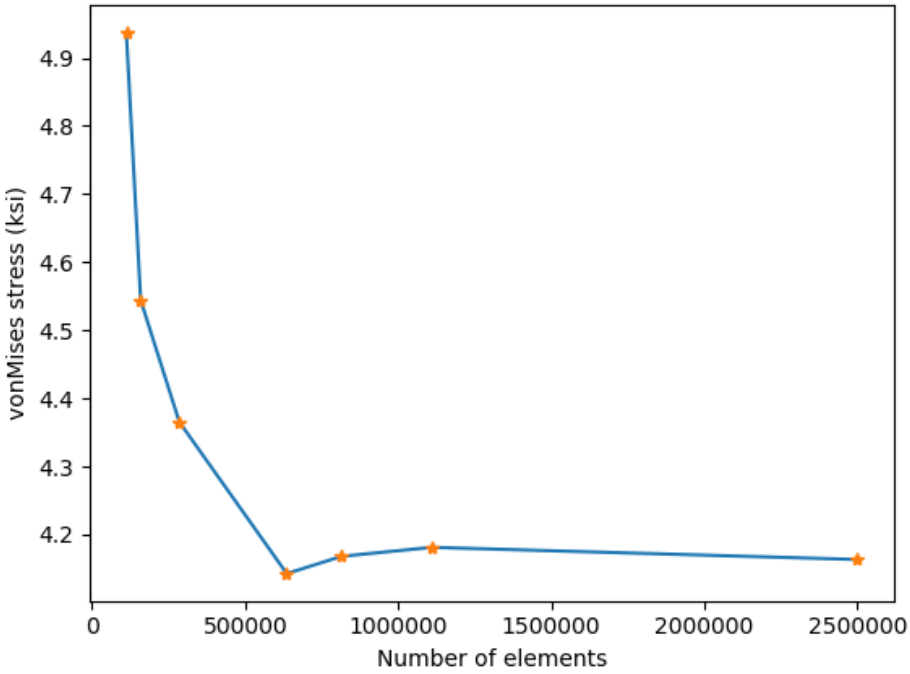

Figure 3.18. Convergence behavior of von Mises stress at strain gage S03.

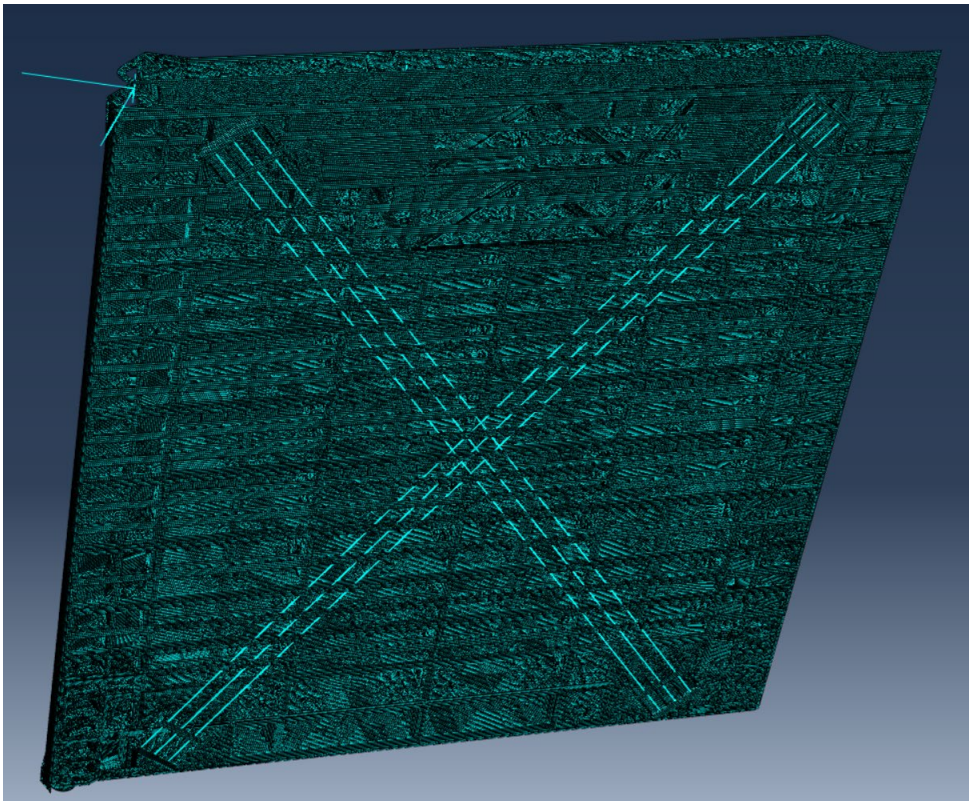

Figure 3.19. Mesh of Greenup gate.

3.7.3. Model Validation

To validate the Greenup model, the model was run to simulate a typical lock event where the chamber water levels are decreasing. Again, this model is primarily intended to be used to determine the change in strain associated with deteriorating boundary conditions in the bottom portion of the quoin, and so, this region is of primary interest to validate. The upstream gate at Greenup is modeled, and so, a water pressure coinciding with the upstream water level was placed on the skin plate of the gate. Here, the upstream water level was assumed to be 46 feet, as listed in the structural drawings of the gate. Then, a water pressure in the opposite direction was placed on the gate and simulations were run at 2-foot increments to simulate the change in strain on the gate due to changing water levels in the lock chamber. Then, the SMART Gate database is queried, and several loading scenarios are extracted for the Greenup miter gate with similar changes in chamber water levels, and the Abaqus results are compared to the SMART Gate strains. Figure 3.20 shows the change in strain for strain gage locations in the quoin region near the bottom of the gate. Note, the strain gage denotation is that same as that shown in Figure 3.15. In Figure 3.20, the red line represents the strain measured in Abaqus, while the black lines are the strains from corresponding lock events measured via SMART Gate. The comparison is generally good, except gage S04 appears to have too little compression, while gage S07 appears to have too much compression. This is demonstrated by how negative the results are, in that, a more negative strain value indicates higher compression. These results suggest that the region of the quoin immediately next to girder S07 may not be in contact and some girders above the girder containing S04 may not be in contact. This is reasonable as the anchor arms at the top of the gate are extremely stiff, and would prevent any movement if the upper portion of the gate into the chamber wall. Similarly, the tolerances of the pintle, where gage S07 is located, are extremely tight, and so the very bottom of the quoin block is likely not to be in contact. The boundary conditions are adjusted accordingly, and results of the updated model are shown in Figure 3.21.

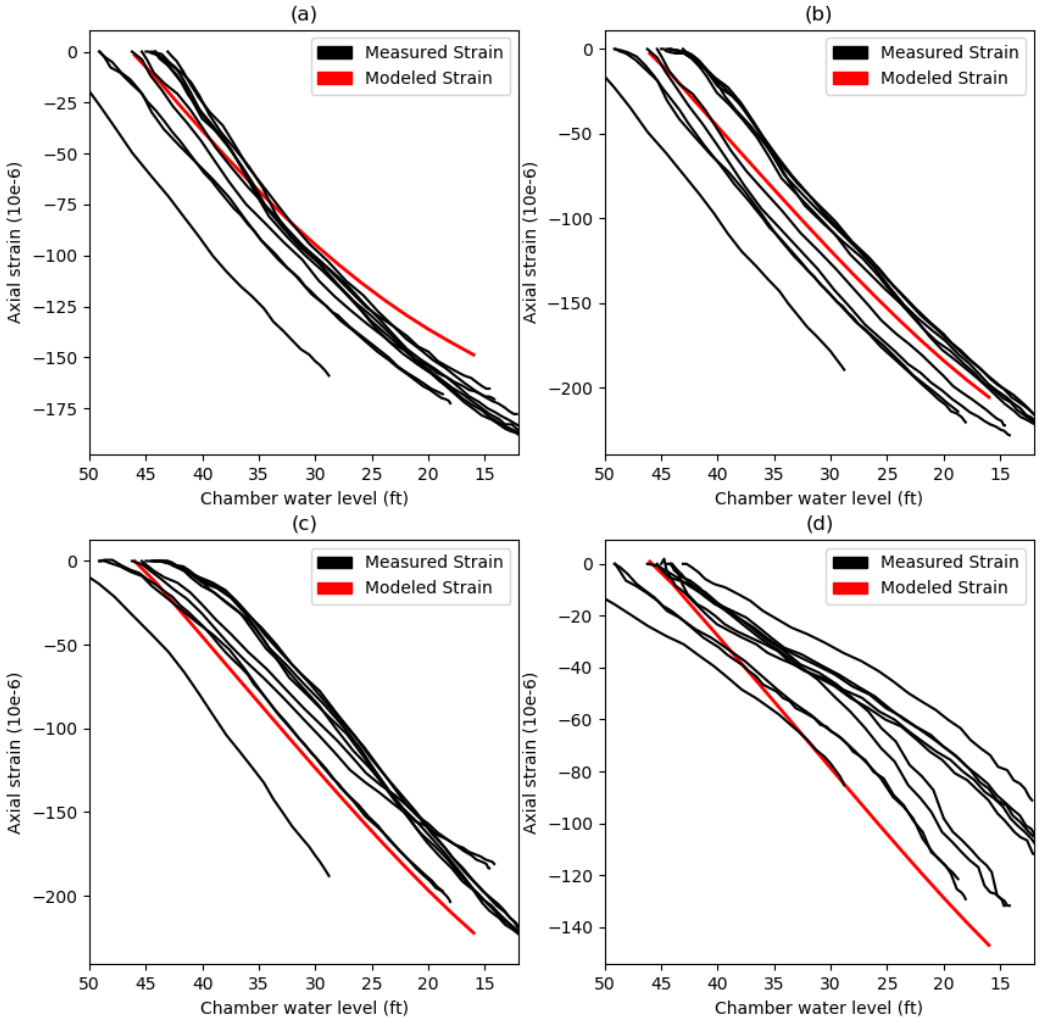

Figure 3.20. Bottom girders showing good agreement with measured data. a) Strain on girder 8, gage S-04, modeled strain slightly less compression than measured strain. b) Strain on girder 10, gage S-05, showing good agreement, c) Strain on Girder 11, gage S-06, showing good agreement, d) Strain on Girder 12, gage S-07, modeled strain slightly more compression than measured

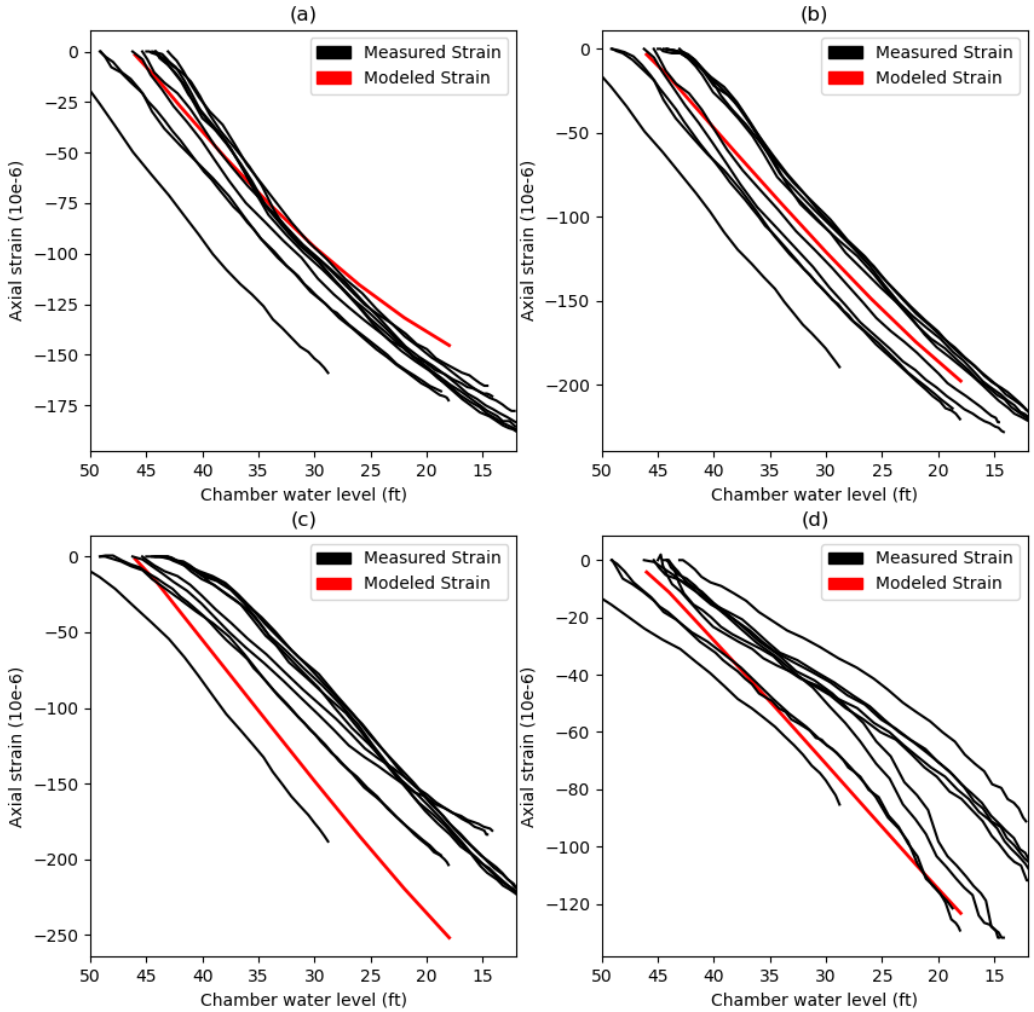

Figure 3.21. Updated validation plots after adjusting quoin boundary conditions. a) Strain on girder 8, gage S-04, largely unchanged. b) Strain on girder 10, gage S-05, largely unchanged, c) Strain on girder 11, gage S-06, slightly increased compression, but still within measured readings, d) Strain on girder 12, gage S-07, shows superior agreement

3.8. The upstream Tainter lock gate at The Dalles Lock and Dam

The upstream lock gate at The Dalles Lock and Dam is a Tainter gate that is 91 feet wide with a skin plate that has a radius of curvature of 30 feet. The gate was modeled using the best practices, as outlined above. To save time and computational demand, symmetry of the gate is exploited and only half the gate is modeled, with the modeled half shown in Figure 3.22. For any simulations where the gate is behaving symmetrically, this model is sufficient. For simulations of asymmetric behavior, such as uneven hoisting, the geometry is mirrored and two halves are tied together at the middle.

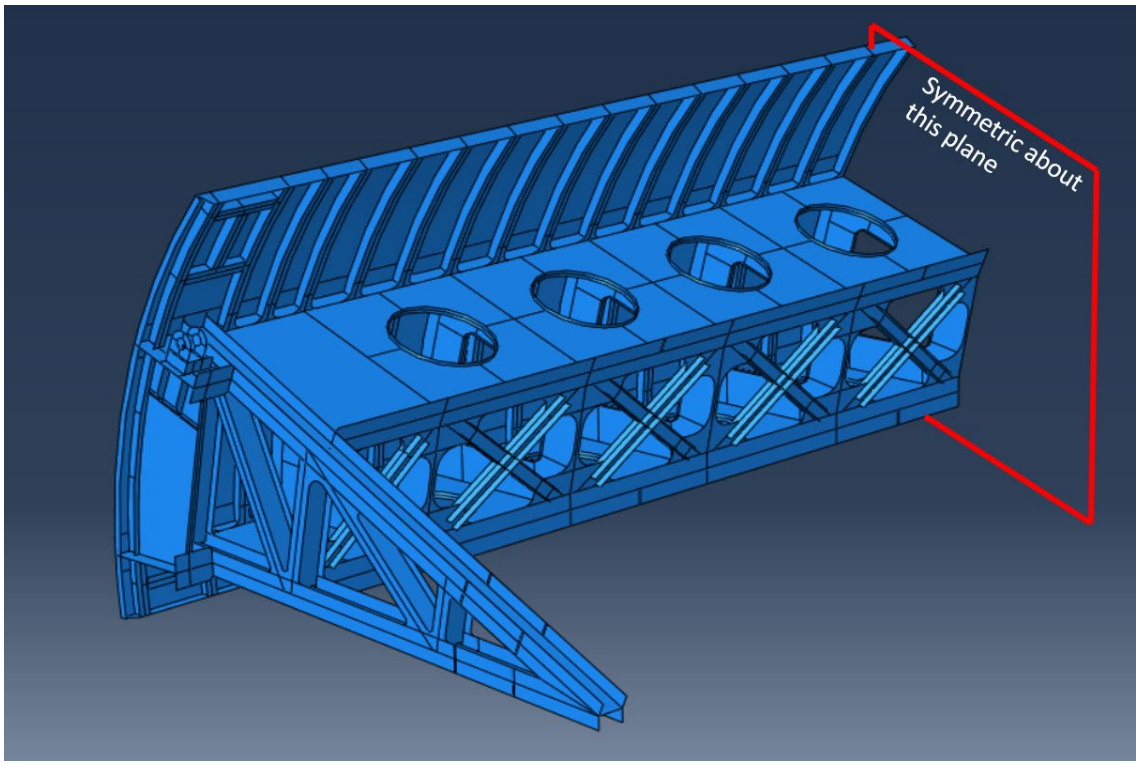

Figure 3.22. Modeled half of The Dalles Tainter gate exploiting gate symmetry.

This gate was selected to be modeled because the physical gate has instrumentation installed as part of the SMART Gate program. The primary use of this model is to determine the change in strain in the strut-arm portion of the gate caused by uneven hoisting; therefore, for the research performed as part of this dissertation, the strain gages on the strut arm of the gate and the tilt meter that measure rotation of the gate are of primary interest. The location of the strain gages of interest on the physical gate are shown in a schematic in Figure 3.23. Similar to the Greenup miter gate model, The Dalles Tainter gate model was partitioned with one-inch squares in locations corresponding to the location of strain gages on the physical gate. These partitions facilitate inspection of strain in the strain gage locations to compare results from the model with strain gage readings in the field.

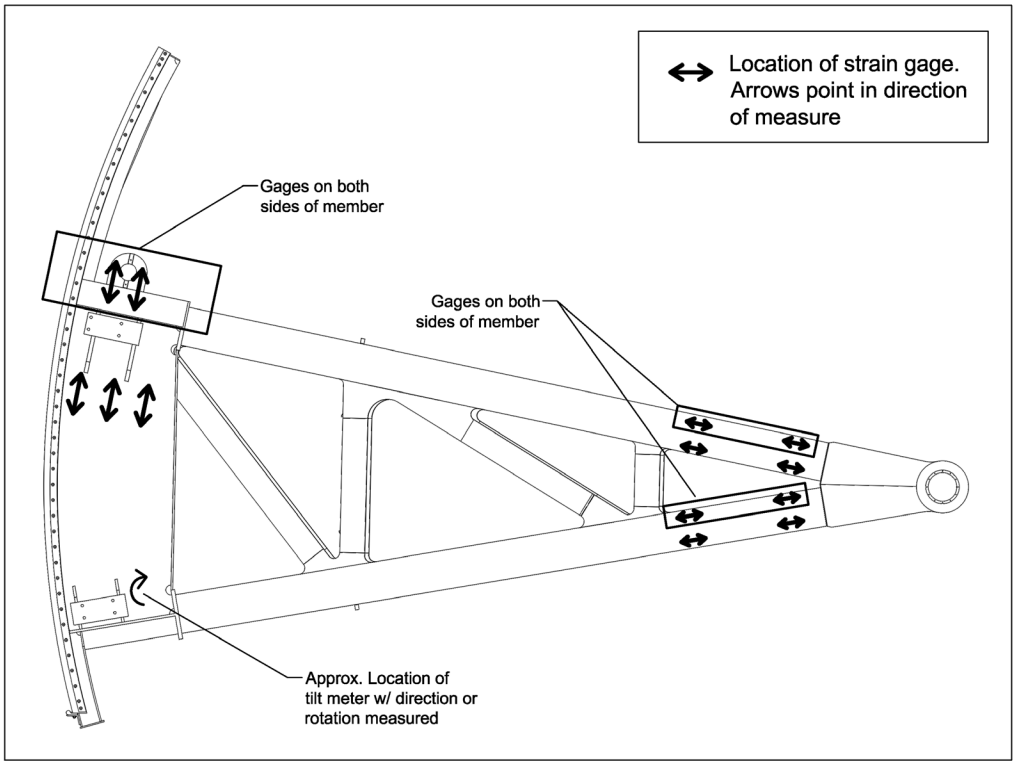

Figure 3.23. Location of strain gages on strut arm of The Dalles Tainter gate.

3.8.1. Constraints, loads and boundary conditions

To model the gate hoisting, two sets of boundary conditions are used. For the evenly hoisting case, the gate is expected to behave symmetrically, and so, symmetric boundary conditions are used on the plane of symmetry, as shown in Figure 3.24. The other boundary conditions are a roller on the lifting lug preventing motion in the direction of the hoisting cables and a restraint at the trunnion only allowing rotation about an axis passing through the trunnion. The only loads acting on the gate while it is hoisting are gravity and friction in the trunnion. For the simulations performed herein, static analysis is performed and friction is assumed negligible; thus, the only load considered is gravity. Rather than dynamically modeling the gate hoisting, individual static steps are used to simulate the gate position as it hoists. Then, the gravity load applied to the gate and the direction of the roller of the lifting lug are rotated to the appropriate direction based on the geometry of the gate. The lifting lug itself is modeled as two plates, which in the field would be connected via a pin, and so the two plates are coupled together so they rotate and translate in the same fashion.

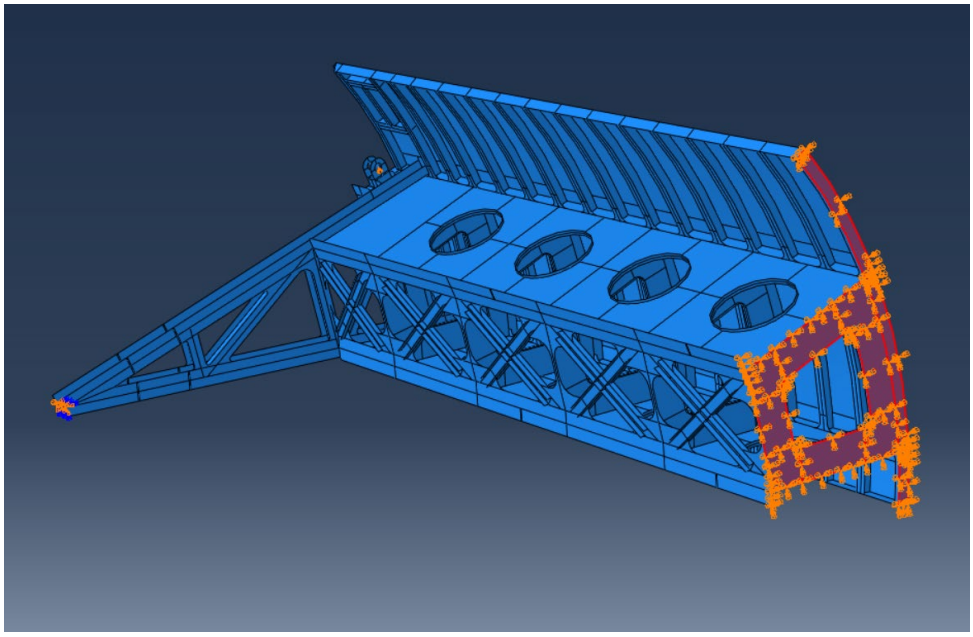

Figure 3.24. Plane of symmetry, indicated by red highlighting, to which symmetric boundary conditions are applied to The Dalles Tainter gate FEA model.

For the asymmetric case where uneven hoisting is considered, the other half of the model is explicitly added by mirroring the existing half and connecting the two parts together via a tie constraint. To model uneven hoisting, one lug has a roller boundary condition placed on it as in the symmetric case, and the other lug has a point load in the direction of the cables. Varying the magnitude of the point load will vary the extent of unevenness in the hoisting. All other loads and boundary conditions are the same.

3.8.2. Mesh discretization study

This model will be used to determine the change in strain in the strut arm due to uneven hoisting. Accordingly, the modeled strain at locations corresponding to strain gages on the strut arm of the physical gate are investigated for convergence of the solution. As an exact solution is not obtainable for this model, convergence is deemed to be obtained when the solution of the model changes less than 1 percent from one refinement step to the next. The models investigated had meshes comprised of 58k, 82k, 131k, 170k, 226k, 334k and 512k elements. For each refinement step, the von Mises stress is recorded at each strain gage in the strut arm region of the gate as shown in Figure 3.23. A typical convergence plot is shown in Figure 3.25. As with the mesh of the Greenup miter gate, due to the method of remeshing necessary in Abaqus, it is not possible to ensure monotonic convergence of the mesh. This is because the requirement that all nodes from less refined meshes are maintain in their original positions in future refinements (Lepi

1998) cannot be practically implemented in Abaqus. Nevertheless, from the results of this discretization study, it is deemed that the mesh comprised of 226k elements is sufficiently converged; however, as the model runs very quickly even with 512k elements, the most refined mesh is selected for analysis, of 99.6% are linear quadrilateral S4R elements, while the remaining elements are linear triangular S3 elements. The final mesh, with the mirror part tied to the modeled part, is shown in Figure 3.26.

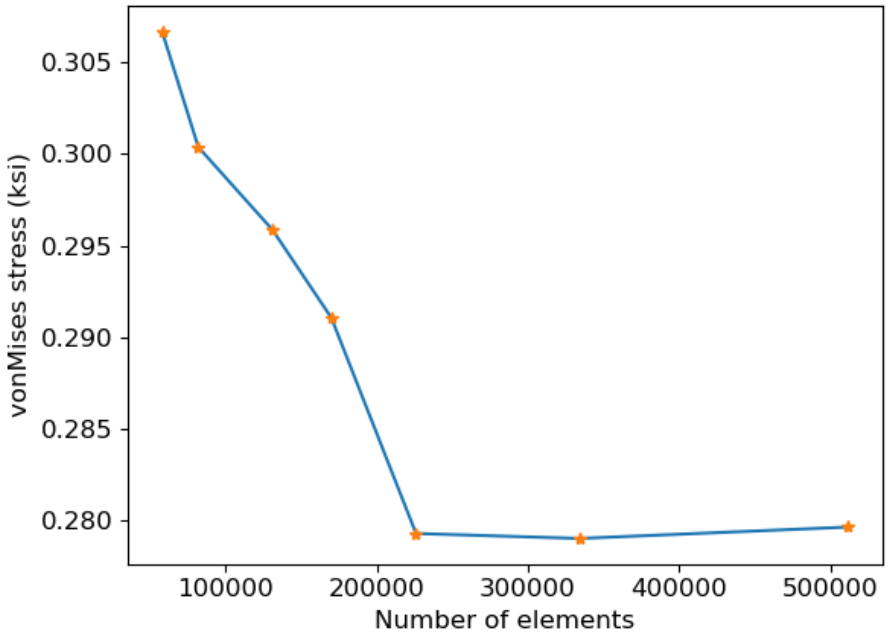

Figure 3.25. Convergence behavior of von Mises stress at location of model corresponding to physical strain gage on The Dalles FEA Model.

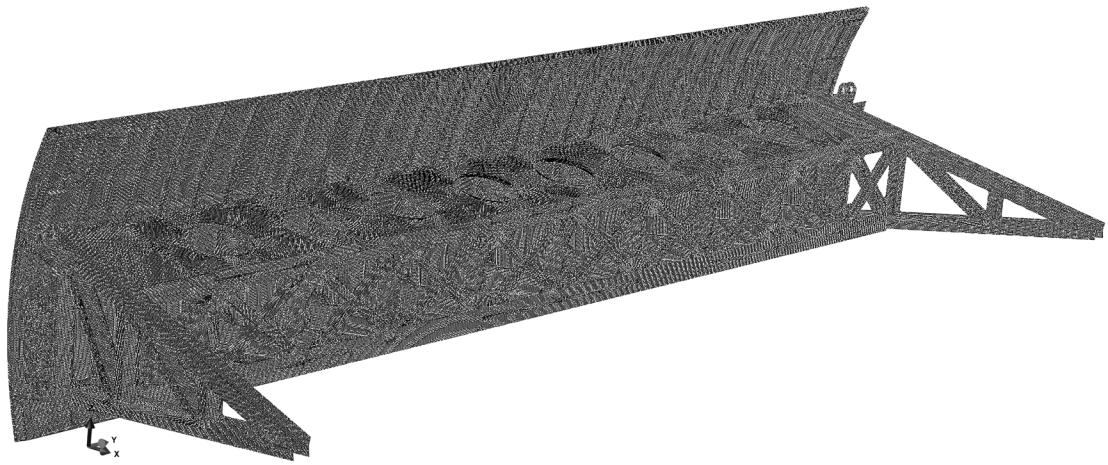

Figure 3.26. Full mesh of the Dalles Tainter gate.

3.8.3. Model validation

To validate the model, the symmetrically hoisting gate was simulated, and the strains were extracted at locations corresponding to strain gages on the physical gate. The SMART Gate database was then queried to find strain readings from the strain gages for times when the gate was hoisting. For model validation, the strains from the FEA model are compared visually to the strains from the SMART Gate data and shown in Figure 3.27. The strut arms on the physical gate are denoted "north" and "south" due to their respective orientation with each other, and are represented by the black and light blue lines, respectively. For a symmetrically hoisting gate, the gages on the north and south strut arms should have similar readings. As seen in Figure 3.27, there appears to be asymmetry in the SMART Gate data. While only one hoisting event is shown, the results were consistent across all event investigated and suggests that the gate is already hoisting unevenly.

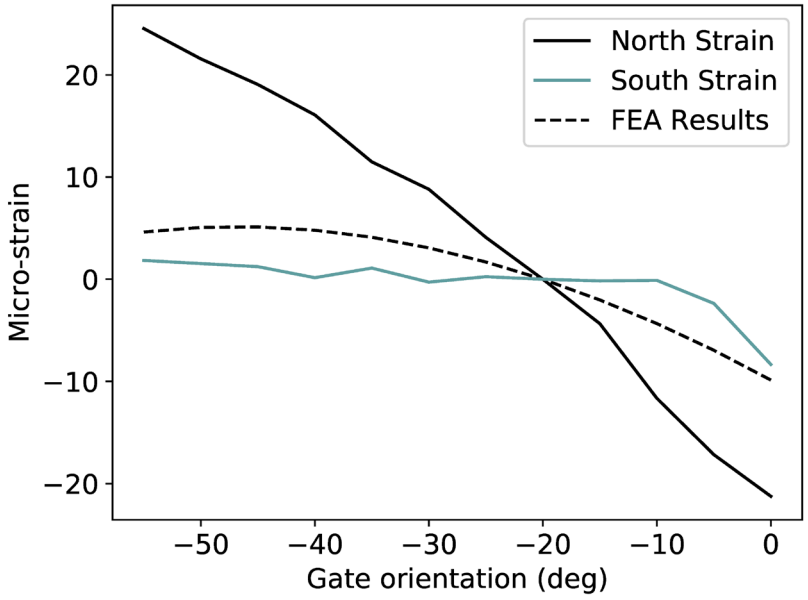

Figure 3.27. Strain comparison of FEA model and SMART Gate data.

To test the theory that the gate is already hoisting unevenly, an asymmetric loading scenario was simulated as explained in subsection 3.8.1. The magnitude of the point load simulating uneven hoisting was arbitrarily selected, and the simulation was run. The results were extracted and again compared to the physical data. As this is an asymmetric simulation, results are now shown for the FEA model on both strut arms, and the comparison is seen in Figure 3.28, where the solid lines represent SMART Gate data. As seen, when uneven hoisting is considered, the comparison is superior. These results are somewhat alarming, as it suggests that the Tainter gate is already

hoisting unevenly, which is a critical scenario addressed later in this dissertation. Thus, these results motivate the field-testing and data exploration performed in Chapter 6 of this dissertation.

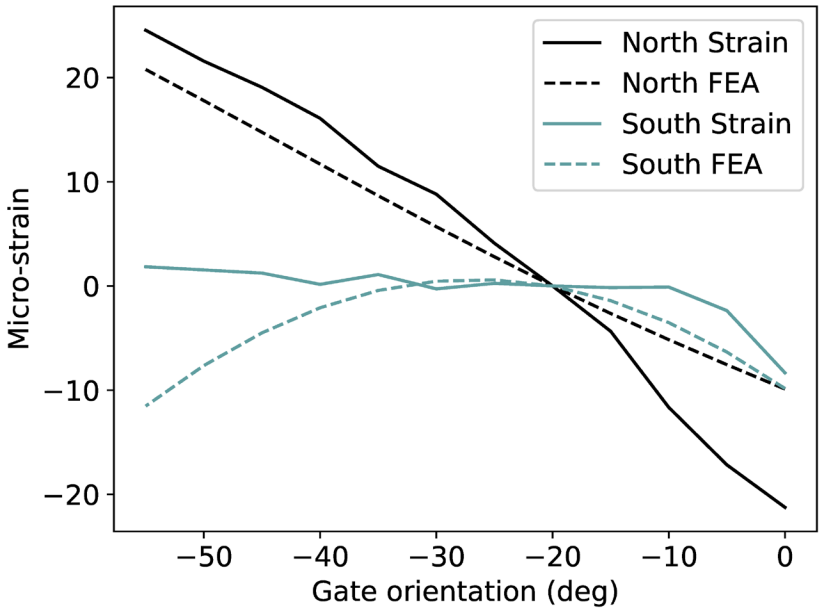

Figure 3.28. Comparison of FEA strain with SMART Gate strain, considering uneven hoisting.

3.9. Conclusions

This chapter outlined the work performed to create FEA models of lock gates. The models are created as a first step towards developing an SHM system for navigation infrastructure. This chapter first outlined best practices for numerical modeling of lock gates, focusing on miter and Tainter gates. Topics discussed are best approached to modeling geometry, boundary conditions, loads, and constraints to aid modeling complicated component geometry. Selection of a sufficiently refined mesh and model validation in the presence of field data are then discussed. The best practices are then highlighted by means of example models leveraged heavily in this dissertation, namely the FEA models of the miter gate at Greenup and the Tainter gate at The Dalles.

The FEA models discussed in this chapter allow a detailed investigation into the expected behavior of lock gates subjected to the various loading scenarios expected on site. Moreover, FEA models allow the simulation of damage to the structure to determine how the behavior of the structure subsequently changes. In this way, the FEA models provide detailed information as to which sensors of an SHM system are sensitive to different types of damage, allowing development of decision-making tools.

Chapter 4. Detection of miter gate quoin gaps using principal component analysis [1]

This chapter focuses on the methodology developed as part of this dissertation to utilize strain gage data to automatically detect the presence of quoin gaps in miter gates. As discussed in Chapter 2 of this dissertation, under normal operating conditions, the hydrostatic load on a closed miter gate is intended to transfer to the lock chamber wall via axial compression through the girders of the gate. The interface between the gate and the wall, known as the quoin, is intended to provide a continuous bearing surface along the height of the gate so that all loaded girders transfer the compressive load into the wall, as seen in Figure 4.1-(a). Due to normal wear, vessel impact, or inappropriate initial adjustment of the quoin block (as explained in Chapter 2), a gap forms in the bearing surface of the quoin, as seen in Figure 4.1-(b). When gaps form, the girders immediately next to the gap are no long able to transfer load into the lock chamber wall, and so, the load distributes to other girders still in contact with the wall. The load redistribution is problematic as it can lead to increases in stress in critical lock components and accelerate fatigue damage, and so, early detection of gaps in quoin blocks is of critical concern to lock operators and maintenance personnel.

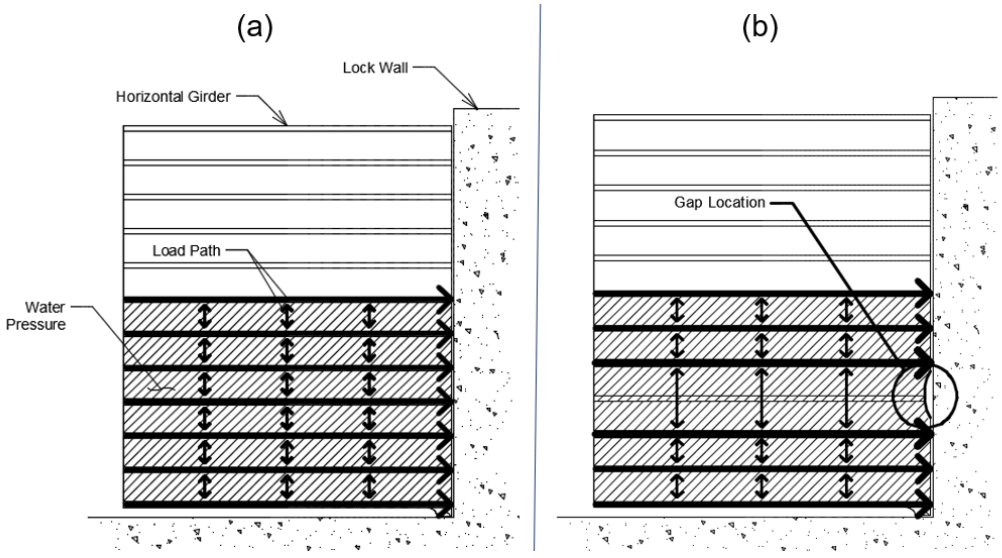

Figure 4.1. (a) Load path of miter gate with continuous quoin contact (b) load path with gap in the quoin.

[1] Much of the work in this chapter has been published in the Structural Control and Health Monitoring journal (Eick, Treece, et al. 2018): Eick, BA; Treece, ZR; Spencer Jr., BF; Smith, MD; Sweeney, S; Alexander, QG; Foltz SD; "Automated damage detection in miter gates of navigation locks", *Struct Control Health Monit.* 2018 25e2053. Its reuse in this dissertation is in accordance with the binding copyright agreement.

In this chapter, the challenges with using strain to monitor for the presence of damage are first discussed, motivating the need for a more robust feature that is sensitive to the presence of a quoin gap. The rate of change of the strain in a girder with respect to an increase in load (herein termed the slope) is found to be an appropriate feature as it is insensitive to changes in strain caused by environmental changes while still being sensitive to the presence of a gap. Moreover, the slope greatly reduces the amount of data that needs to be analyzed. Next, the method used for statistical analysis of the data, namely principal component analysis (PCA) is discusses. Using PCA, a damage index (DI) of monitored data is calculated and compared with data from the structure operating in a known undamaged state. If the DI exceeds a defined threshold, damage is said to likely be present. To demonstrate the efficacy of the proposed method, a combination of measured strain data and FEA model results are utilized and it is shown that the proposed method readily detects gaps in the quoin of a miter gate.

4.1. Strain gages for gap detection

This chapter will leverage the upstream miter gate at the Greenup Lock and Dam site due to the fact that it has a continuous monitoring system installed with strain gages that will be utilized for the detection of a quoin gap. See section 3.7 of this dissertation for details on the strain gages installed at Greenup. For the problem of gap detection, the redistribution of load caused by a gap will be manifested as measurable changes in strain; therefore, the most useful information from the available sensors is strain. However, the strain response is only informative when a hydraulic load is on the gate. Figure 4.2 shows typical strain and chamber water level time histories superimposed on the same plot for April 24th, 2014 at the Greenup Lock and Dam site. The dashed line represents the water levels, cycling between approximately 29 and 55 feet, as seen on the left y-axis. The solid line represents the strain time series, cycling between approximately -350 and -690 micro-strain. The x-axis represents time. Note, this is an upstream miter gate, and so the gate is only damming water (and thus under pressure load) when the water levels in the chamber lower. That is, the water level on the upstream side of the gate is always at the high water mark, while the downstream side of the gate faces the lock chamber, and so lower water levels in the lock chamber lead to a differential water pressure on the two sides of the gate. For the strain gage investigated here, the response due to the differential water pressure is compressive in nature, and so the strain gets more negative as the water levels in the lock chamber decrease. For this day at Greenup, seven so-called “lockages” occurred, where the chamber water levels cycled through emptying and

filling. When the water level in the chamber changes, the load on the gate and the strain change accordingly. Filling or emptying the lock chamber has a nominal duration of about 10 minutes, with the entire lockage lasting approximately 30 minutes. Outside of lockage events, the change in strain is minimal; therefore, long periods exist in the data record where the strain gages provide little useful information.

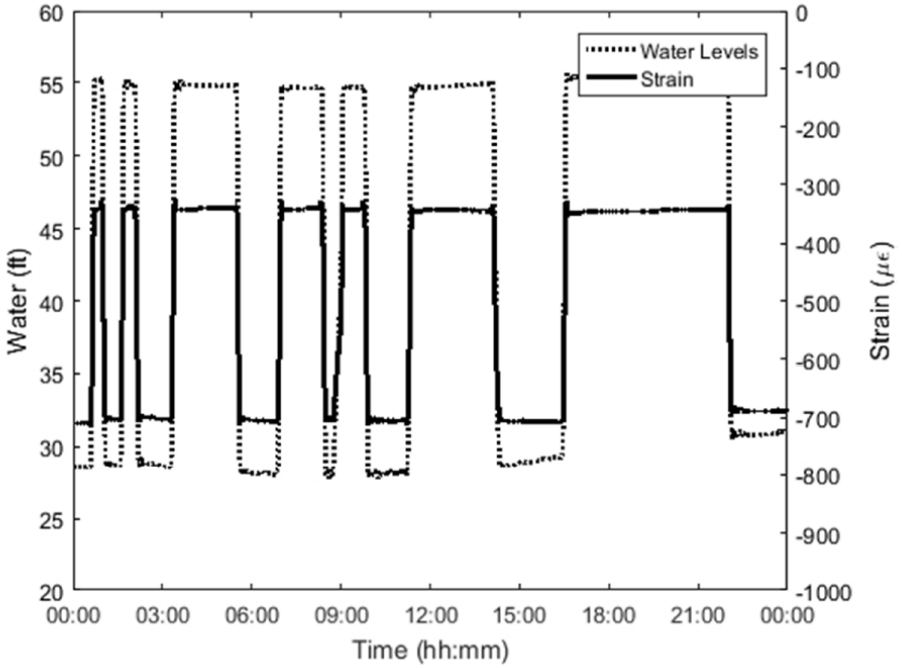

Figure 4.2. Typical strain values and water levels for one day at Greenup Lock and Dam.

Throughout the year, the undamaged strain response varies due to a variety of seasonal and environmental factors. Figure 4.3 shows the strain response at one gage location on a lock gate over a six-month duration. Note that as temperatures increase toward the summer months, the ambient strain measured by the gages increases, leading to a higher apparent strain response at this location on the gate. Additionally, the strain response in a girder is proportional to the load applied on the gate; the strain response is therefore dependent on the difference between the upstream and downstream water levels. These water levels can vary significantly through the year. For example, the region in Figure 4.3 for late February shows the strain response during a flood, when the upstream and downstream water levels are nearly equal. During this time, the strain response of the gage is nearly zero. The remaining variation in the absolute strain response can be shown to be highly correlated to the difference in upstream and downstream water levels, which fluctuates

greatly throughout the year due to snowmelt and quantity of rain. These environmental variables greatly increase the difficulty of assessing whether the change in the strain response is due to damage or merely seasonal variation. Moreover, many statistical methods used for SHM require the data to be stationary, meaning that the statistical parameters such as mean and standard deviation are time invariant (Farrar and Worden 2012). The clearly variable mean value and apparently fluctuating variance of the strain seen in Figure 4.3 leads the strain data from this gage to be classified as nonstationary.

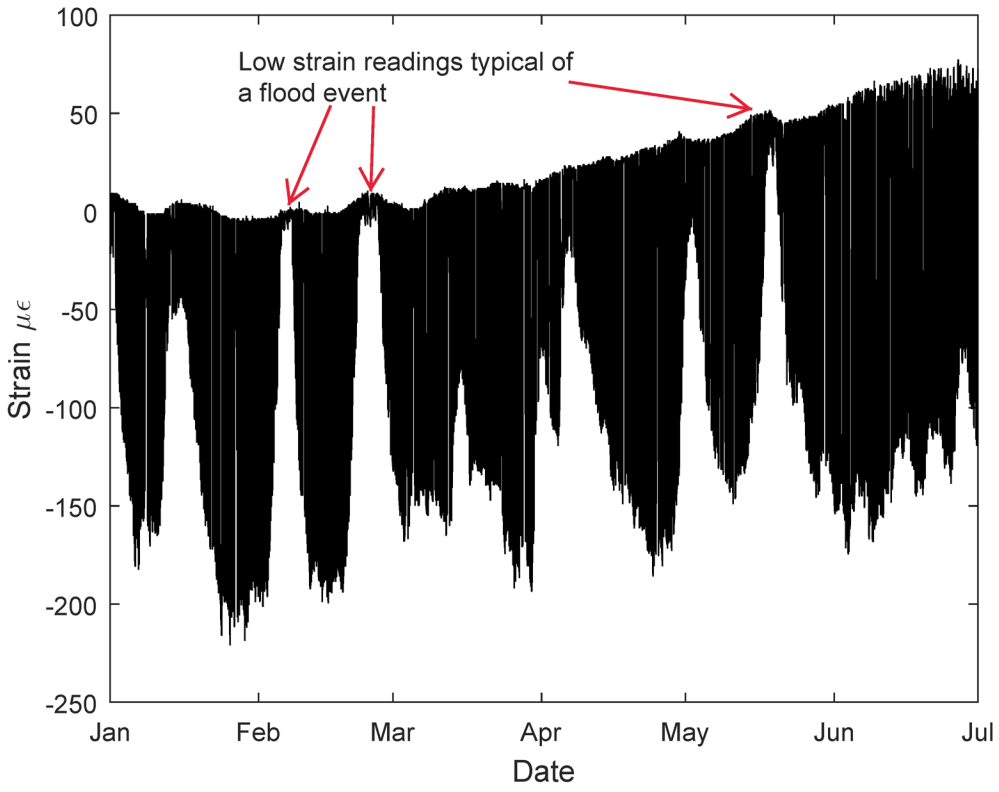

Figure 4.3. Strain measurements for six months at Greenup, with flood periods highlighted.

4.1.1. Slope as a damage sensitive feature

As seen in Figure 4.2 during filling and emptying of the lock chamber, the strain response of the strain gage changed in a manner almost identical to the water level. The similarity between the two series plotted in Figure 4.2 suggests that strain and water levels are highly correlated. Indeed, the correlation coefficient between the strain and water levels in Figure 4.2 was found to be 0.9995, suggesting a nearly perfect linear relationship between the two. Similar correlation was found across many gages at multiple lock sites. Recall that the load transfer mechanism for the gate to

the chamber wall is primarily axial compression through the girders. The load on the gate is related directly to the difference in water levels on either side of the gate, and these loads are well within the elastic range; therefore, the linear relationship between strain and water levels seen in many of the gages is reasonable. The linear relationship between strain and water levels is illustrated by plotting the strain response from Figure 4.2 versus the corresponding water levels in the lock chamber and is shown in Figure 4.4. Where Figure 4.2 shows the separate, but similar time histories of both strain and water, Figure 4.4 plots the strain versus the water level, with strain on the y-axis and water level on the x-axis. Each long diagonal line in Figure 4.4 correspond to a fill or empty event and the cluster of data at either end of the diagonal lines corresponds to the long periods of time when nothing is happening in the lock chamber, and the water levels remain nearly constant. The upstream gate is instrumented at Greenup, which means when the chamber water level decreases, the gate is damming the higher water level on the upstream side causing a net hydrostatic load to be placed on the gate. As seen in Figure 4.4, when the Greenup chamber water level decreases, the girder is compressed, and the strain gets lower in a corresponding linear fashion. This linear behavior was seen for many of the gages across multiple gates where instrumentation is installed. Notable locations that were lacking such linear behavior were any locations in which the gage was not aligned in the girder's axial direction, and some gages near the pintle region of the gate, where the load path is too complex to expect linear behavior. The data from gages with non-linear behavior was not used for this study.

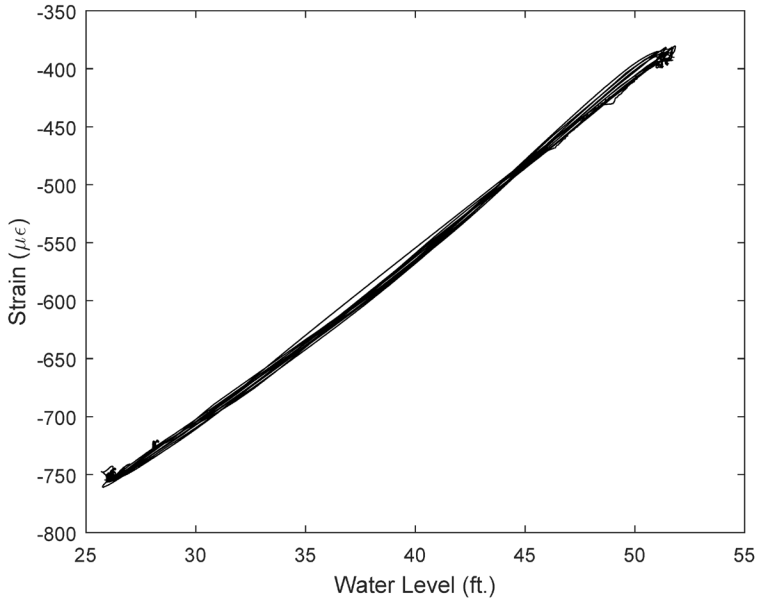

Figure 4.4. Strain response at one gage showing linearity with respect to water levels.

For the gages where linear behavior was observed, the consistency of that behavior with respect to water levels suggests that the rate of change of strain with respect to water levels should be nearly constant for every fill or empty event at that gage, and so the rate of change is investigated as a potential damage sensitive feature. Accordingly, the strain and water level data for fill and empty events is extracted from the data record using algorithms developed in Matlab (2015). The strain is then regressed onto the chamber water levels and an ordinary least squares (OLS) line is fit to the data (Ang and Tang 2007). The slope of the OLS line is the single metric that is proposed as the damage sensitive feature that contains information about the gate behavior during lockage events; the intercept of the OLS line contains information on the constant offsets caused by noise in the system or environmental variables such as temperature or river depth and is discarded. The typical strain-vs-water level behavior for one fill event for a strain gage, and the OLS fits, are shown in Figure 4.5. For this particular event in which the data was extracted, the downstream water level (the low point of the chamber level) was around 32 feet, and the upstream level (the high point of the chamber level) was around 50 feet. The points marked by 'X' are the raw data points for the event, and the solid line is the OLS fit. Note, the strain in Figure 4.5 was not adjusted for mean offset, and so the values are all positive. Nevertheless, as the water levels decrease, the strain response for this gage shows a decrease in the value, suggesting this location of the gate experiences a compressive-type force when subjected to differential water pressure. The apparent goodness-of-fit of the line of least squares seen in Figure 4.5 is typical for all the gages and events investigated. The slopes from the selected gages are thus extracted for the period under investigation and formed into a new time series. Henceforth within this chapter of the dissertation, any further reference to the term "slope" can be considered in reference to the slopes extracted from the OLS fit.

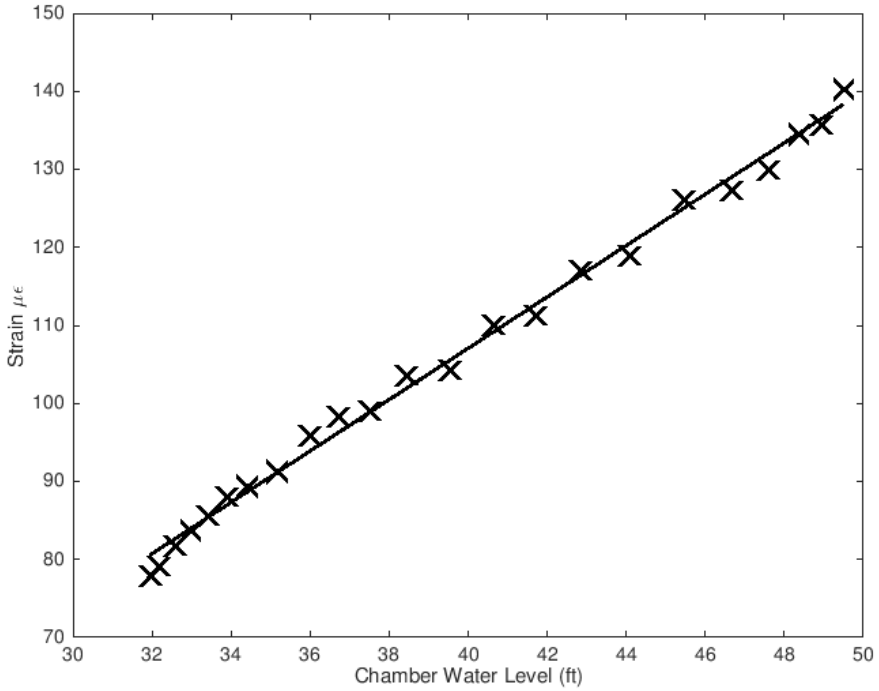

Figure 4.5. Data from fill event at Greenup with OLS fit.

4.1.2. Data cleansing

After inspection of the data, several instances were found where the strain gage data was deemed unreliable. The major example of unreliable data was during a downstream flood event, when little difference was present between the upstream and downstream water levels. This led to a negligible load being placed on the gate and, thus, a change in strain on the order of the magnitude of the noise in the system. Figure 4.6 shows the strain and water levels recorded for one such flood event that occurred on February 23rd, 2014. The y-axis on the left represents the water levels in the lock chamber, while the y-axis on the right represents the strain extracted at a strain gage. The x-axis represents the time of day. Figure 4.6 illuminates the noise in the strain signal, and the difficulty in differentiating between noise in the signal and a true change in strain. Accordingly, the slope extraction algorithm in Matlab (2015) was changed such that chamber fill or empty events with the water level changing less than five feet were ignored.

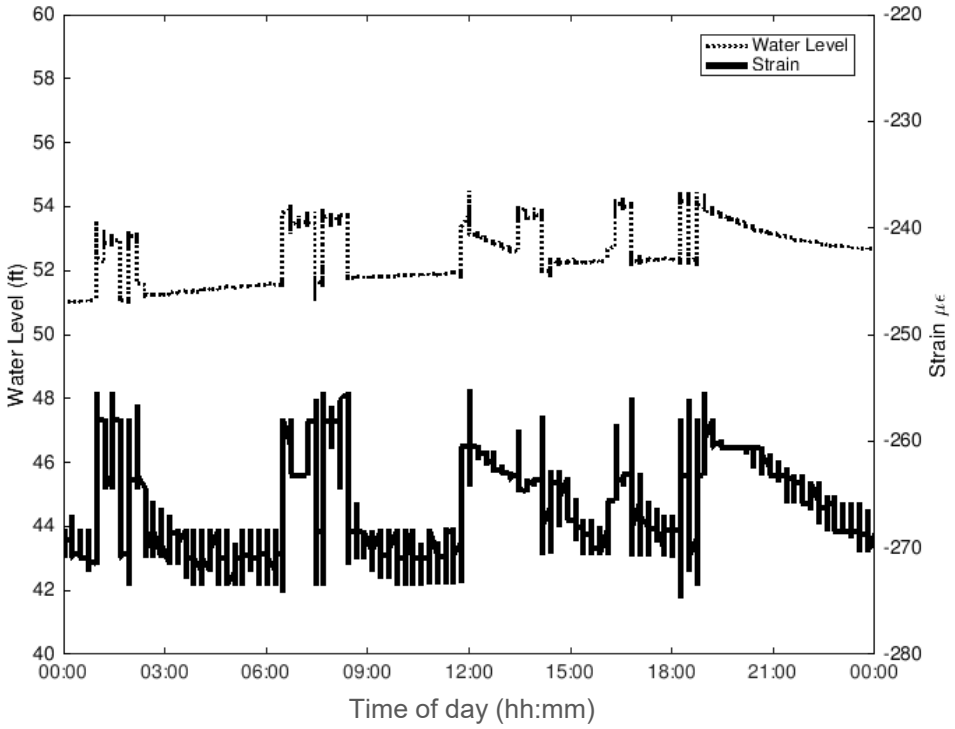

Figure 4.6. Zoom of typical strain and water levels for a flood at Greenup, showing noisy signal.

Other clearly anomalous events occurred when, for instance, the data logger shut off in the middle of a fill event, causing all the gages to zero, and leading to an apparent significantly different slope value. To facilitate automation of removal of unreliable outliers in the data, the data was run through an algorithm that removed any points that were more than four standard deviations away from the mean of the data, provided there were not consecutive observations of such behavior. Figure 4.7-a shows three months of uncleansed data from a strain gage on the Greenup lock gate, with the circles signifying points slated for removal by the four-sigma algorithm. The circled points were investigated and were found to be justifiably removable due to obvious issues with the data collection system such as sudden, one-off spikes in the data record, thereby validating the four-sigma cleansing algorithm which was then applied to all data. Figure 4.7-b shows the same slopes, now cleansed with justifiable anomalous outliers removed.

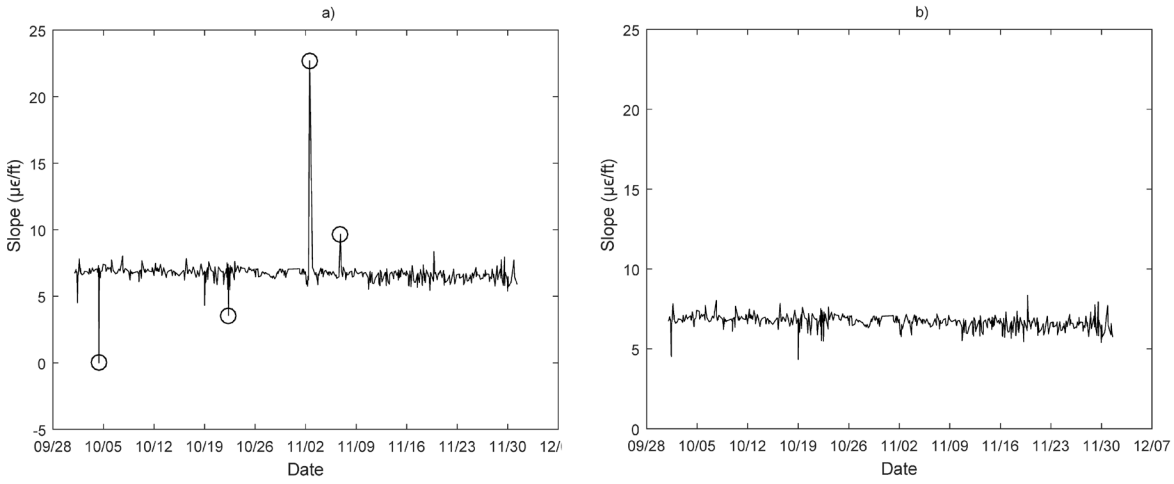

Figure 4.7 a) Slope time series with significant outliers. b) Cleansed slope time series with outliers removed.

Using the cleansed slope data as the damage sensitive feature significantly reduced the number of data points to be analyzed. At Greenup, the data is sampled every 15 seconds; so, 5760 strain samples are taken every day for every gage on a gate. If only 10 empty and 10 fill events occur in the chamber in a day, the 5760 points are reduced to 20, making data analysis more computationally efficient. Critically, in the presence of a gate/wall gap, the slope is expected to change in a similar manner as the strain. Moreover, the slope time series, in marked contrast to the raw strain data in Figure 4.3, have a nearly constant mean value and low, near constant variance. To further illustrate this point, a slope time series showing nearly two years of data is plotted to investigate any long-term trends, and is shown in Figure 4.8. The slopes in Figure 4.8 were extracted and cleansed as previously describe for the period from March 2013 through the end of December 2014. As seen, the series remains consistent throughout this period. The apparent consistency supports the idea that the slopes form a time series that can be well approximated as stationary and can be employed as a damage sensitive feature for automated detection of gaps at the gate-wall interface of miter gates on navigation locks.

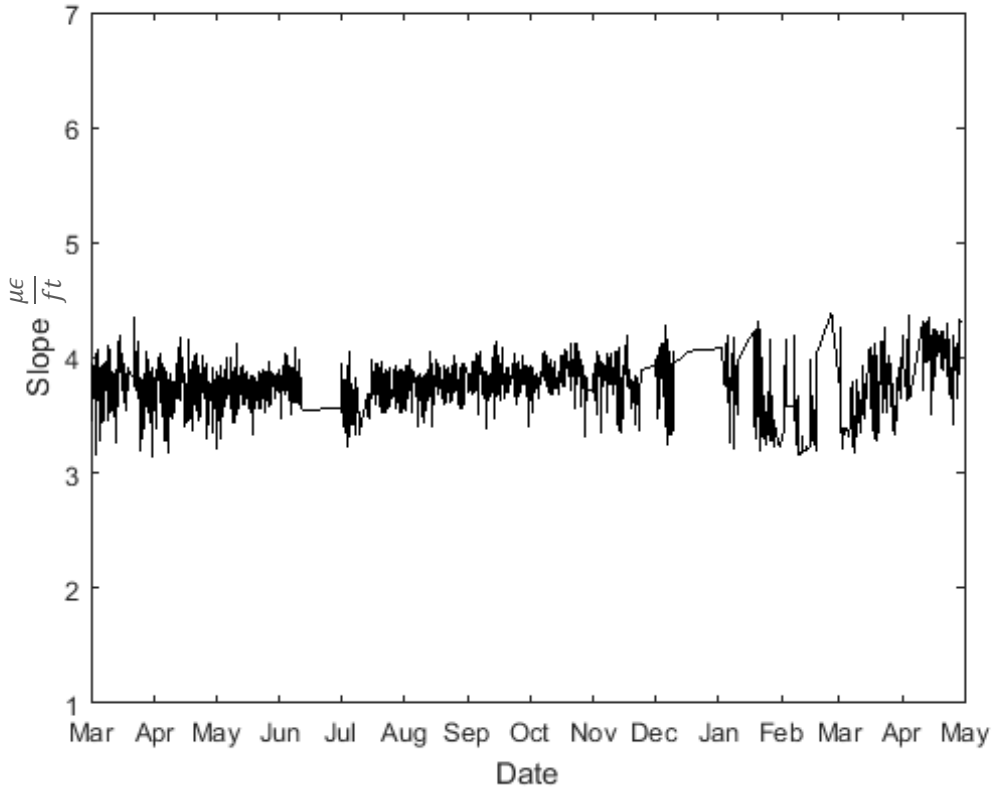

Figure 4.8. Slope time series for seventeen months of data for a gage at Greenup.

4.2. Damage Detection Strategy

The strain gage response and the associated slope data at locations near a gap will be affected by the redistribution of load caused by a gap. Given that the slope data is well approximated as a stationary time series, a gap detection methodology that analyzes individual slope time series (e.g., similar to statistical process control charts) could be considered. Because anomalous behavior from one strain gage may be insufficient to indicate damage is present, and the location of a gap is unknown, analysis of many individual slope time series in a region would be required to assess whether a gap is present. Automating this process could result in a very cumbersome and unreliable algorithm.

As an alternative, the principle component analysis (PCA) method can combine data from multiple measurements into a single time series that can be used for damage detection, and provide an assessment of the region of interest in the gate rather than the localized assessment provided by one time series. For example, Figueiredo, et al., (2009) provide a common access Matlab script to use PCA on various data sets for damage detection. Cross (2012) applies PCA to the detection of

a hole drilled in a steel plate using thermal spectral lines. Santos, et al., (2015) used PCA as a data normalization tool to remove environmental effects from vibration data. Thus, PCA will be employed in this research to develop a single metric combining information from multiple strain gages for use in assessment of the presence of gaps at the gate-quoin interface.

PCA is an orthogonal transformation of a set of *n* possibly correlated random variables or time series, to a set of *n* linearly uncorrelated variables known as the principal components of the data (Joliffe 2002). The PCA transformation is derived from the eigenvectors of the covariance matrix, where each eigenvector represents a "direction" of the data describing a certain percentage of the variance in the data. The first step to using the PCA method for SHM is to create a matrix, **X**, of the data from *n* sensors in the SHM system, consisting of *m* observations, such that

$$\mathbf{X} = \begin{bmatrix} x_{t_1}^{(1)} & x_{t_2}^{(1)} & \dots & x_{t_m}^{(1)} \\ x_{t_1}^{(2)} & x_{t_2}^{(2)} & \dots & x_{t_m}^{(2)} \\ \vdots & \vdots & \vdots & \vdots \\ x_{t_1}^{(n)} & x_{t_2}^{(n)} & \dots & x_{t_m}^{(n)} \end{bmatrix}_{n \times m} \tag{4.1}$$

where $x_{t_j}^{(\mathrm{i})}$ is the data from the i^{th} sensor collected at the j^{th} observation in time *t*. For the study herein, **X** is a matrix consisting of slope values. The $n \times n$ square covariance matrix of the data is found and spectrally decomposed to find *n* eigenvectors and eigenvalues. The percentage of the variance explained in a given principal direction can be determined as the ratio of the corresponding eigenvalue, λ_i, divided by the sum of the eigenvalues. That is

$$\%explained_i = \frac{\lambda_i}{\sum_{j=1}^{n} \lambda_j} \times 100\,. \tag{4.2}$$

A percentage of desired variance to maintain in the system is selected. Typically, it is desirable to maintain as much of the variance in the system as possible. Then, the *d* eigenvectors that correspond to the eigenvalues that sum to the desired retained variance (also known as the loadings) are stored, and the data is projected onto these eigenvectors forming an $m \times d$ dimensionally reduced matrix. A residual matrix, **E**, is found by projecting the reduced data matrix

back onto the original coordinates and subtracting the projection from the original data matrix. Concisely, **E** is found as:

$$\mathbf{E} = \mathbf{X} - (\mathbf{X}\mathbf{U_d})\mathbf{U_d^T} \tag{4.3}$$

where **X** is the data matrix, and $\mathbf{U_d}$ is the matrix of retained eigenvectors. Each point in time of the residual can then be seen as an $n \times 1$ vector of observations, $\boldsymbol{e^{(t)}}$. To form a single time series to monitor for damage, the magnitude of each vector is found. Formally, the damage index, *DI*(*t*), is found as

$$DI(t) = \left\|\boldsymbol{e^{(t)}}\right\| \tag{4.4}$$

where $t = 1, 2, \ldots m$. So called "training data" from the known undamaged is first utilized and the damage index is found via PCA. The damage index of the training data is used to find a threshold against which a damage index of testing data from the structure in an unknown condition is compared. The choice of threshold is critical, in that, too large a threshold will cause the process to be too insensitive and yield multiple false negatives, and too small a threshold will yield multiple false positives. The threshold should be seen as a parameter to be adjusted based on specific requirements of the monitoring system, such as the magnitude of damage that is deemed critical, and the acceptable error rate. For the research performed herein, two approaches to threshold selection are investigated. One approach is a threshold value of three standard deviations (3σ) from the mean value of the damage index, similar to a threshold used by typical control charts. The other approach is that used by Santos, et al., (2015) of setting the threshold value at 95% cut-off value over the trained DI. The two approaches offer different levels of sensitivity to the algorithm, with the 3- σ approach being more sensitive. The preferred threshold between the two choices is discussed in the conclusions

To monitor for damage, the same PCA process is repeated for data from the structure with an unknown condition; however, the damage index for the monitored data is found by projecting the data onto the same eigenvectors found using the training data, and taking the magnitude as in Eq. (3.1). If the structure is still operating under similar conditions as when the training data was collected, the damage index will be very small; however, if a significant change in the structure

occurs, such as changes due to damage, the damage index should be significantly larger. To further reduce the probability of false positives using this method, an indication of damage is said to be present only when consecutive observations above the threshold are recorded. The number of consecutive observations above the threshold needed to indicate damage will be dependent on the actual rate of threshold exceedance in the training data and what is deemed an acceptable false alarm rate. The correlation between successive points in the damage index, $DI(t)$ is on the order of 0.05, indicating that each observation is nearly uncorrelated with the previous one. For the study at hand, the lack of correlation is assumed to imply independence of successive observations; therefore, the observations above the threshold are modeled as a binomial process. For a binomial process, the probability that each of the next q observations is above the threshold is simply

$$P(X = q) = p^q \tag{4.5}$$

where p is the probability that the data exceeds the threshold and X is the number of observations that exceed the threshold. p is found from the training data by dividing the number of times the trained damage index exceeds the threshold by the total number of points in the damage index. For an acceptable false alarm rate, $R_{\text{acceptable}}$, the number of minimum consecutive observations required to indicate damage and minimize the potential for false alarms is given by:

$$q \geq \frac{\ln\left(R_{\text{acceptable}}\right)}{\ln(p)}. \tag{4.6}$$

For more information regarding the PCA method, see Jolliffe (2002) or Hastie, et al., (2009). Additionally, concise overview of PCA directly applicable to SHM application can be found in Santos, et al., (2015).

4.3. Validation for Greenup Lock and Dam

To determine the effectiveness of the slope as a damage sensitive feature, a case study was performed using miter gates at Greenup Lock and Dam. This site was chosen because the SHM instrumentation was installed on a new gate in 2011, and the data was expected to be representative of an undamaged lock gate. The lock gate at Greenup is a horizontally framed miter gate, consisting of 12 horizontal girders spaced vertically at an average of six feet apart. The sensors at Greenup

are located on both leaves of the upstream gate. The instrumentation on the gate consists of 115 strain gages, 8 temperature sensors, 4 pressure transducers (to measure water levels), and a number of tilt meters and load sensors not used in this study.

4.3.1. Instrumentation

The strain gages used are 350 ohm, full-bridge, HiTec temperature-compensated gages, model HBWF-35-125-6-150GP-NT. While the strain gages are compensated for temperature, the thermal sensitivity of the gages has not been completely removed. The gages are placed primarily on every other girder, with each of the bottom three girders instrumented. There is a gage near the quoin, a gage near the miter, and four gages at mid-span to allow assessment of bending moments. Gages at the ends of the girders are located on the neutral axis of the girder. Two of the mid-span gages are located near the neutral axis, and the other two are located near either flange. A number of gages are also located on the vertical strut members of the gate, but are not used for this study. The temperature sensors are HiTec model TSW-00-D-150GP-RTD and are distributed across the gate and near the data logger. The pressure transducers are Campbell Scientific model CS450-L150-SA-2-9-NC and are intended to measure the upstream, downstream, and lock chamber water levels. The sensors are all connected to a Campbell Scientific data logger model CR1000-ST-SW-NC. The data from each sensor is sampled every 15 seconds and is uploaded to a database. Figure 4.9 shows an elevation view of one leaf of the Greenup gate; girders are numbered from top to bottom, and the gages used in this study are labelled as shown in the figure. Note that girders on miter gates are oriented horizontally, with their flanges running parallel to the gate's height.

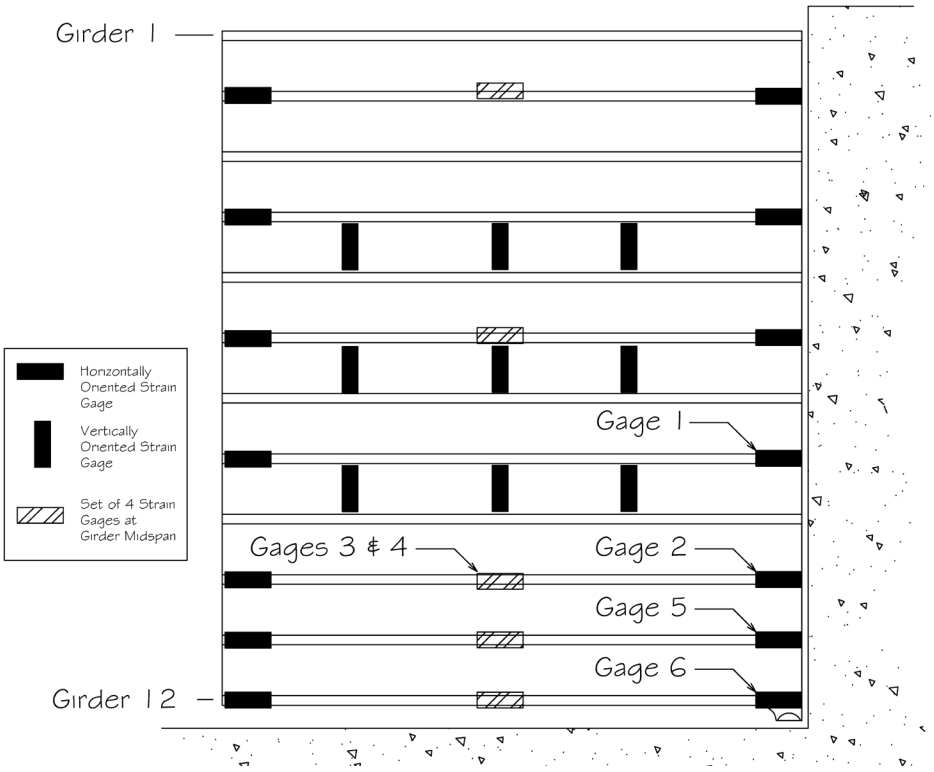

Figure 4.9. Elevation view of Greenup gate leaf with strain gage map.

The selection of gages for use in this study was narrowed down to choices that would exhibit both a strong response under load and likely be affected by the presence of a gap. Girders near the bottom of the gate will carry more load than those near the top. Therefore, gages on girders near the bottom of the gate are considered. Furthermore, the gap will be in the quoin, and thus gages near the quoin are affected the most. Accordingly, the final gages included in the study are those located near the bottom of the gate, and either at mid-span on the girder, or near the quoin. In total, six gages were included in the study. Table 4.1 shows the gage numbers used with a brief description of their locations. It is expected that gages in the quoin region of the gate will be sensitive to the presence of a gap in the quoin; however, gages at mid-span of the girders are sufficiently far away from the quoin that they are expected to be insensitive to the presence of the gap. The inclusion of the gages 3 and 4 are to show that including relatively insensitive gages in the PCA algorithm still yields acceptable results. The locations of these particular mid-span gages were the furthest from the modeled gaps while still being located within the region of interest investigated on the gate, and so they are expected to be the least sensitive to the presence of the gap. Ten months of data from the gages in Table 4.1 was extracted and used to validate the proposed methodology.

Table 4.1. Gage naming convention.

Gage Number	Location Description
1	Girder 8, near the quoin
2	Girder 10, near the quoin
3	Girder 10, mid-span
4	Girder 10, mid-span
5	Girder 11, near the quoin
6	Girder 12, near the quoin

4.3.2. PCA training and monitoring a healthy structure

The data from the Greenup site was processed, the slopes were extracted, and PCA was applied. The data from May 2014 through September 2014 was used as the training data, and consists of 1,002 data points. The eigenvectors of the covariance matrix of the training data were found and stored. For six individual time series, there will be six total eigenvectors. To compare the sensitivity of the PCA method to the amount of variance retained in the system, two PCA scenarios are considered as outlined in Table 4.2.

Table 4.2. PCA cases considered.

PCA Case	Variance Retained	Description
1	92%	Use three eigenvectors corresponding to 3 highest eigenvalues
2	98%	Use all but the eigenvector corresponding to the smallest eigenvalue

The residual of the training data was found for the two scenarios identified (92% variance and 98% variance), and the norm taken, as in Eq. (4.4). The 3σ and the Santos' 95% cutoff thresholds were identified for each case. The damage index for the testing data outside the training period, from October 2014 through March 2015 was determined using the same eigenvectors previously found for the training period. The testing data consists of 1,026 observations. As noted previously, this data is expected to be representative of an undamaged lock gate, and therefore, the damage index is inspected for Type I errors (that is, false indication of damage). The damage index at each point in time is plotted as a bar graph. The plots for scenario 1 and scenario 2 are shown in Figure

4.10 and Figure 4.11, respectively. The horizontal dotted lines represent the thresholds for damage detection, and the vertical line represents the end of the training period.

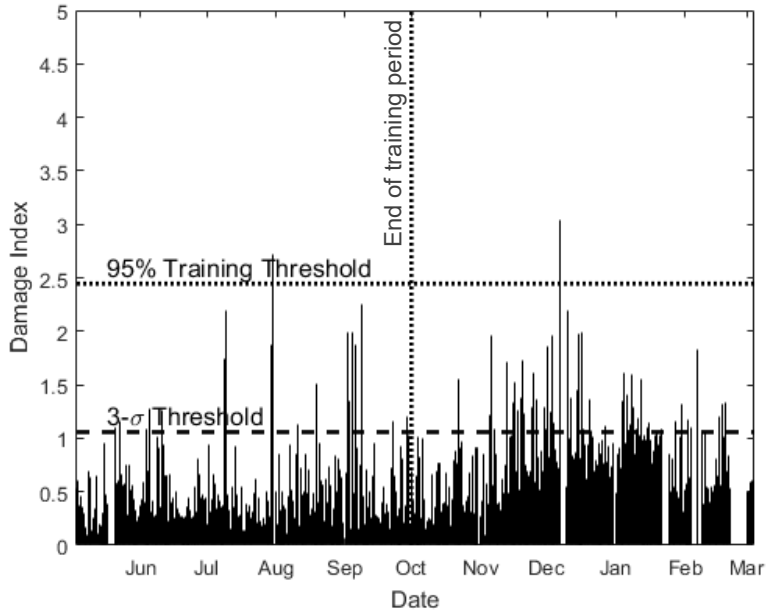

Figure 4.10. Plot of PCA damage index for undamaged case with 92% variance retained.

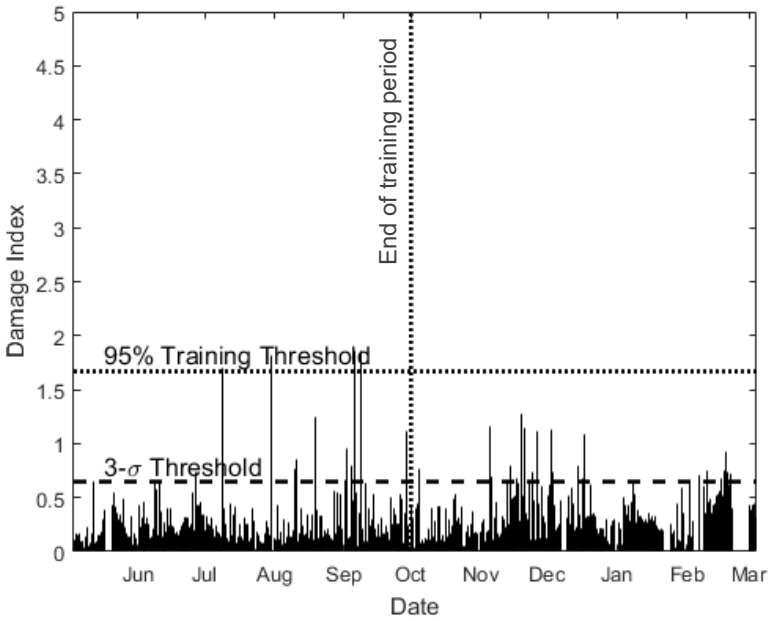

Figure 4.11. Plot of PCA damage index for undamaged case with 98% variance retained.

Recall the damage will be indicated when consecutive observations above the threshold are observed. If the number of consecutive observations required to indicate damage is equal to two,

several consecutive observations above the threshold are observed for Case 1 for the 3σ threshold. However, none are observed for the 95% threshold. For Case 2, there are two occurrence of consecutive observations for the 3σ threshold: one in early November and one in early December. If the number of consecutive observations above the threshold required is three, a false positive never occurs. An apparent seasonal variation in the damage index is noted in Figure 4.10, with a clear increase in the variability of the DI between November and February. Note that Figure 4.10 represents the residual of the PCA model with only 92% of the variance retained. In contrast, when 98% of the variance is retained, as shown in Figure 4.11, this trend is distinctly absent. Indeed, the residuals shown in Figure 4.10 are expected to be larger than the residual in Figure 4.11. For the proposed damage detection strategy, scenario 2 (i.e., retaining 98% of the variance) is recommended.

To formalize the probability of false alarms, the percentage of exceedance is found from the data. For this data, there were 27 observations above the threshold and a total of 1026 testing samples, yielding a probability of exceedance of 0.0263. In order for a binomial distribution to be valid, the observations in the data must be independent. To test this the correlation coefficient was found between the damage index, and the same damage index shifted one point in time. The data consisted of 2,028 points, so the correlation was found between a time series consisting of [DI(1),DI(2) ,…DI(2027)] and a time series consisting of [DI(2),DI(3) ,…DI(2028)], resulting in a correlation coefficient of 0.07. This supports the conjecture that the observations in the damage index are uncorrelated, and it is thus assumed that the observations are independent. The probability of a false alarm is then calculated by Eq. (4.6) and seen in Table 4.3. For detecting gaps in a miter gate, the false alarm rate provided by two consecutive observations is adequate to provide an acceptable trade-off between sensitivity and significance of the algorithm.

Table 4.3. Probability of false positives for two and three consecutive observations for 98% variance case.

No. of consecutive observations for damage indication	**Probability of occurrence**	**False Alarm rate**
2	0.000692	1 in 1446 events
3	1.82×10^{-4}	1 in 54,971 events

As seen, the PCA damage index is a good feature for monitoring the healthy state of the structure, as the occurrence of false positives is small for two consecutive observations, and highly

improbable for three observations. If an average of ten lockages per day occurs, the use of two consecutive observations to indicate damage would be expected to yield a false alarm once every five months for this gate. For three consecutive observations, a false alarm would be expected once every 15 years. If the Santos threshold is used, false positives are effectively eliminated.

4.3.3. Simulated damage

To fully characterize the effectiveness of PCA, damage was simulated in an FEA model and superimposed on the measured data. This simulated damage is then run through the PCA algorithm to check the efficacy of the proposed approach. The Abaqus finite element model of the Greenup miter gate, as described in Chapter 3 of this dissertation, is used to simulate damage. Locations in the FEA model that corresponded to the physical strain gage locations were selected for investigation. The strain at these locations was investigated for the undamaged case and the simulated damaged cases. Damage, in the form of a gate/wall gap, was simulated by imposing a change in the boundary conditions in the model at the quoin near the pintle region. A schematic representing the location and reference dimensions for the gap is shown in Figure 4.12. Table 4.4 shows the dimensions used for the two damage cases considered.

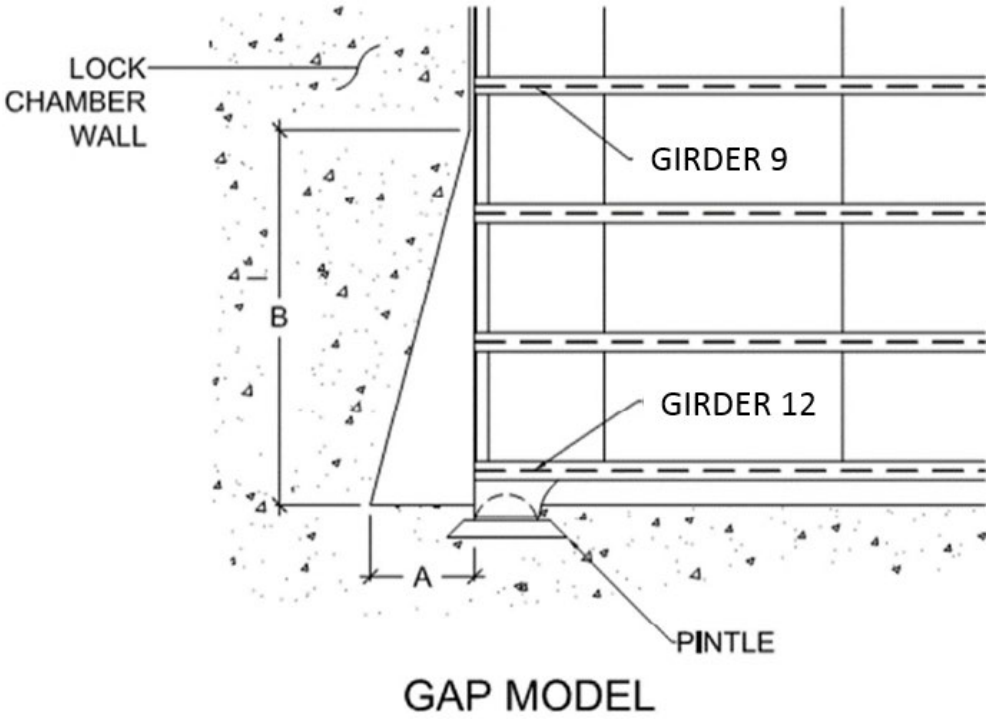

Figure 4.12. Elevation view of pintle area with gap dimension.

Table 4.4. Simulated gap dimensions.

Damage Case	"A" Dimension	"B" Dimension
D1 (Small Gap)	1/8 inch	7 feet
D2 (Large Gap)	1/4 inch	15 feet.

A typical lock-chamber emptying event was simulated in Abaqus using 16 separate differential head scenarios consisting of hydrostatic pressure on both sides of the gate. The upstream water level was simulated with a constant hydrostatic load corresponding to a water level of 46 feet above the lock floor. The downstream water was simulated by a hydrostatic pressure corresponding to a water level varying between 46 and 14 feet at 2-foot intervals. The values for water levels were taken from discussions with USACE personnel as to what typical water levels at Greenup are. A schematic showing the physical meaning of the differential head is shown in Figure 4.13.

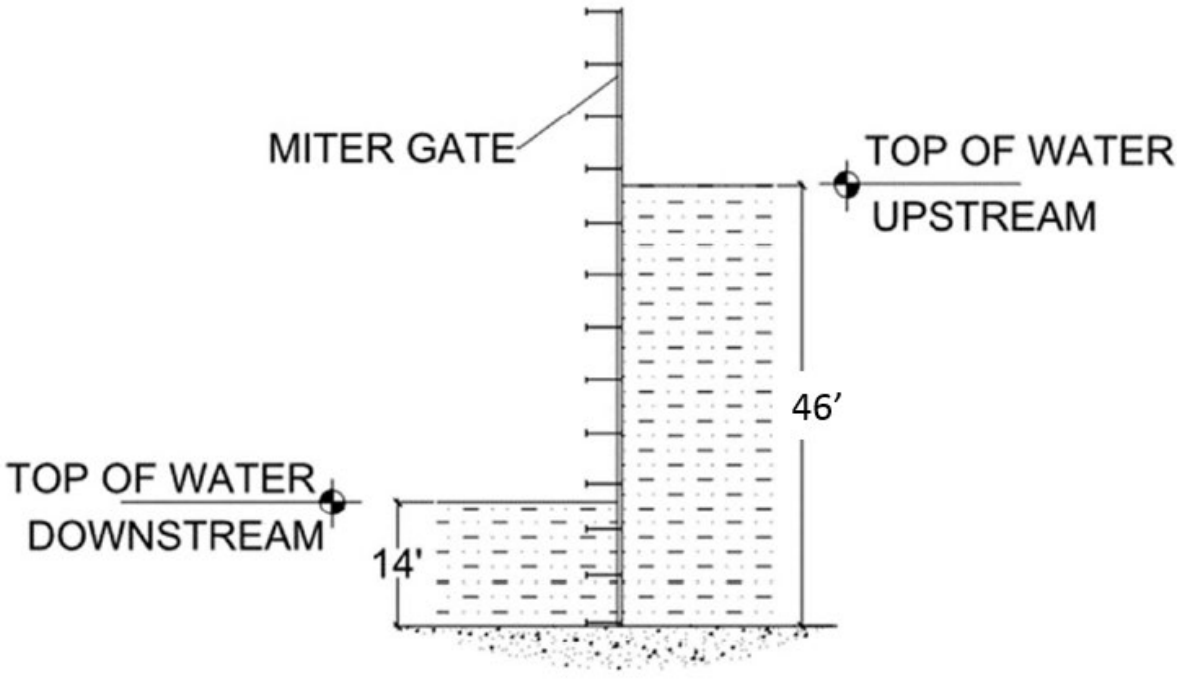

Figure 4.13. Representation of differential head.

For the two cases, the Abaqus model was manually inspected and the strain at each location of interest was recorded. As mentioned previously, the strain in the system is well approximated to behave linearly with respect to the water levels allowing linear interpolation of strain at various

water levels. Accordingly, the reader can assume that the strain at 46 feet is zero at all gages. The strain for the undamaged and two damage scenarios is recorded in Table 4.5. Table 4.6 shows the corresponding slopes and percentage of change for each slope as calculated from the Abaqus simulation. Figure 4.14 shows the recorded strain values taken from the Abaqus model, plotted versus the simulated chamber water level for Gage 6, and illuminates the apparent change in the slope of the strain-vs-water relationship when damage is introduced.

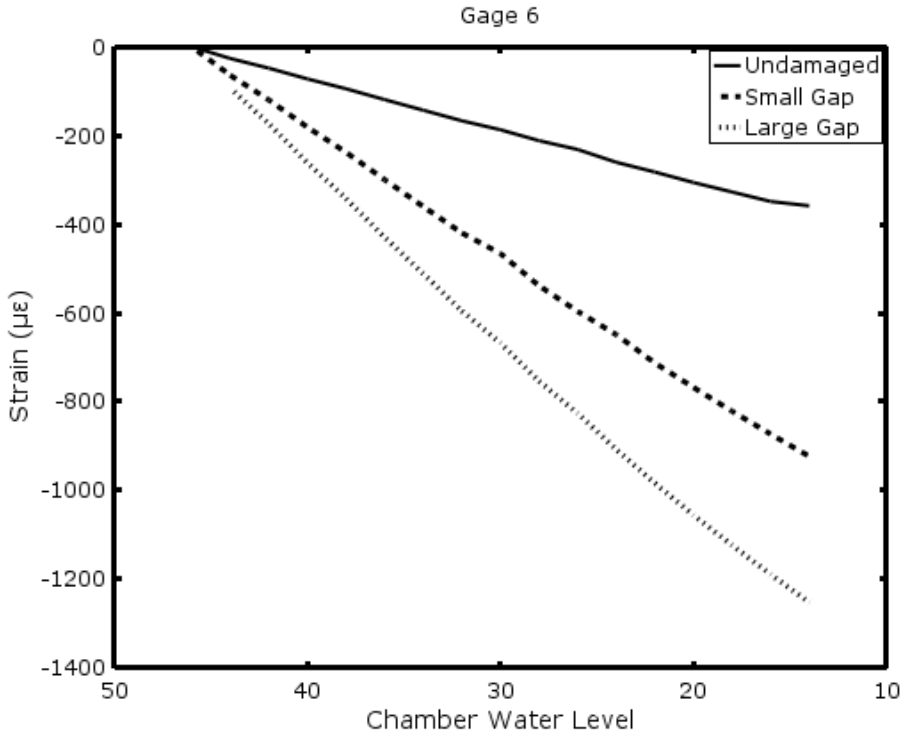

Figure 4.14. Strain from Abaqus simulations showing undamaged, small gap, and large gap cases for Gage 6.

Table 4.5. Strain values taken from Abaqus for upstream water level of 46 feet.

Gage Number	Undamaged Strain x 10^{-6}	Small Gap Strain x 10^{-6}	Large Gap Strain x 10^{-6}
1	-226	-246	-325
2	-256	-329	-76
3	-431	-420	-405
4	-246	-269	-244
5	-269	-115	-78
6	-285	-923	-1252

Table 4.6. Slopes calculated from Abaqus results.

Gage Number	Undamaged Slope	Small Gap Slope	Large Gap Slope	Percent Change Small Gap	Percent Change Large Gap
1	7.06	7.69	10.16	8.92%	43.9%
2	8.00	10.3	2.38	28.8%	-70.3%
3	13.5	13.1	12.6	-3.05%	-3.81%
4	7.68	8.41	7.63	9.51%	-0.65%
5	8.41	3.59	2.43	-57.3%	-71.1%
6	8.91	28.8	39.1	223%	338%

Strain values from Abaqus were recorded for only one particular chamber-draining event with 16 differential head scenarios; however, infinitely many differential head scenarios are possible in practice. Thus, a systematic method was developed to superimpose the damaged strain onto the measured data in Matlab. Imposing the change in response on the strain, as opposed to the slope, was performed to test the slope extraction algorithm's performance when presented with changing strain, and to further demonstrate the capability of the use of the slope to remove environmental noise. Because the difference in strain occurs approximately linearly with respect to water level, a linear relationship for the change in strain based on water levels was developed. That is, for a particular change in water level for the undamaged gate, the strain gages will show a particular linear change in strain, e.g.:

$$\Delta\epsilon_u = m_u h_{water} + b_u \tag{4.7}$$

Where m is the slope of the line, h_{water} is the height of water in the lock chamber, and b is the intercept of the linear relationship. Subscript u here refers to "undamaged". In the presence of damage, the slope of that linear response changes, and the response can now be expressed as:

$$\Delta\epsilon_d = m_d h_{water} + b_d \tag{4.8}$$

Where the subscript d here refers to "damaged". Taking the difference of the two responses also yields a linear response, namely:

$$\Delta\epsilon_d - \Delta\epsilon_u = (m_d - m_u)h_{water} + (b_d - b_u) \quad (4.9)$$

The difference in slope, $m_d - m_u$, is found from the numerical model. For all cases, damaged or undamaged, the change in strain when the water level is at its highest point is zero, because the gate is not under load. Using this information, the change in intercept is found. For example, consider gage number 1. For the large damage case, the difference in slope between undamaged and damaged cases from Table 4.6 is 3.1 $\frac{\mu\epsilon}{ft}$.Knowing the range in high water level used for simulation was 46 ft., the intercept of the line was taken as the negative of this slope times 46 feet. Thus for gage 1, the linear relationship between difference in damaged strain and water levels was found to be

$$\Delta\epsilon = 3.1\frac{\mu\epsilon}{ft}h_{water} - 142\mu\epsilon\,. \quad (4.10)$$

This formula is then use to superimpose the damage onto measured strain extracted from the instrumentation system. Similar formulas were developed for all strain gages considered in this study. These formulas for the Greenup Lock and Dam assume the upstream water levels are nearly constant at 46 feet, which, from the data, is a reasonable assumption. For other gates, the water level at which the change in strains will be zero will need to be individually investigated, and may vary significantly from event-to-event; however, this variation will only affect the intercept of the formula developed. For lock gates with significantly varying water levels, a new intercept would need to be calculated for every event.

4.3.4. Damage detection

Damage was systematically added to the measured data. Eq. (4.10) is specific to gage 1, and a similar linear relationship was developed for all other gages for both damage scenarios and implemented on the measured data as described previously. The process was repeated considering the four cases; two damage scenarios with each considering the two difference percentages of variance to maintain. The two damage scenarios presented here will be a sudden-small and sudden-large gap, with simulated dimensions as listed in Table 4.4. To test the damage detection sensitivity, the changes in strain caused from the gap were superimposed on the measured data. The eigenvectors found from applying PCA on the training data were used and the two cases for damage simulation were tested. Recall that the training period is from May 2014 through

September 2014, and so, any damage simulation takes place from October 2014 through March 2015. For the sudden formation of a gap, the data was left undamaged until December 1st, when the full extent of change in strain was implemented on the measured data.

4.3.5. Damage Case D1. Sudden-Small Gap.

For case D1, the change in strain caused by the small gap was imposed on the measured data suddenly and at full intensity on December 1st. Figure 4.15 shows the results for retaining 92% of the variance in the system. The results for retaining 98% of the variance in the PCA algorithm are shown in Figure 4.16. In the plots, the dotted vertical line represents when training the algorithm stopped, and the dashed vertical line represents when damage was introduced. The horizontal lines represent the thresholds above which damage will be indicated.

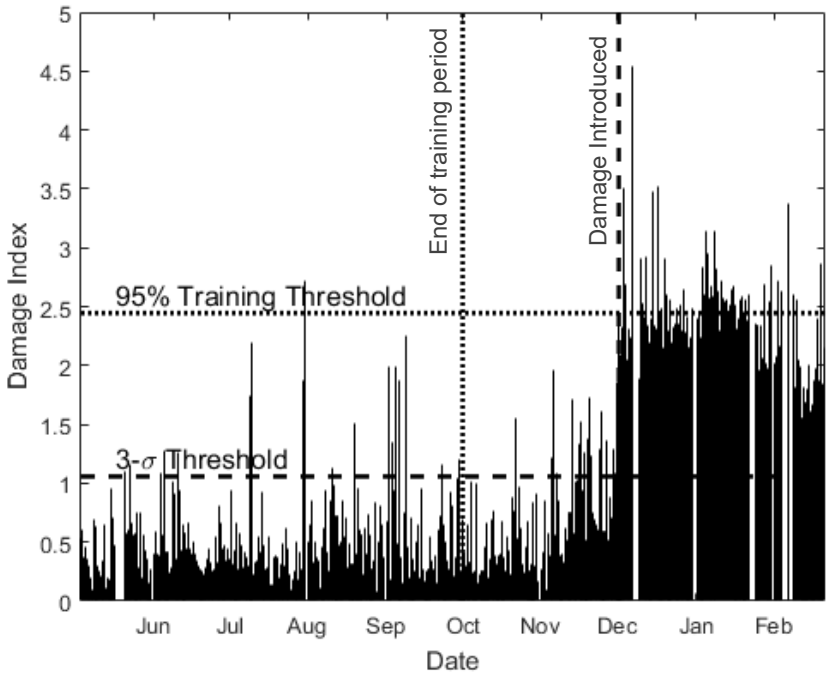

Figure 4.15 PCA damage index for small-sudden gap and 92% variance.

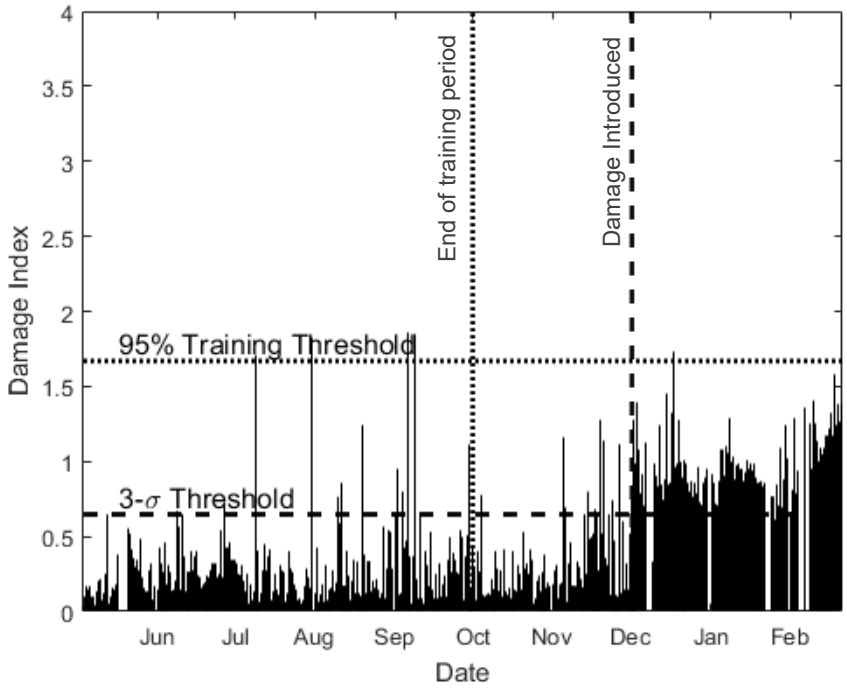

Figure 4.16. PCA damage index for small-sudden gap and 98% variance.

For the 92% variance case shown in Figure 4.15, several false positives occur after the training period but prior to the introduction of damage if the 3σ threshold is selected (as similarly seen in Figure 4.10). After damage is introduced, the 3σ threshold readily detects the presence of damage with no false negatives. For the 95% threshold, multiple indications of the presence of damage are observed, however, numerous false negatives are also present. When 98% of the variance is retained (Figure 4.16), one false positive is seen in early November prior to the introduction of damage in the if the 3σ threshold is used (as similarly seen in Figure 4.11).When damage is introduced, the 3σ threshold readily detects damage, with one false negative seen at the end of January. The Santos 95% threshold is too insensitive to detect damage in this case.

4.3.6. Damage Case D2. Sudden-large gap.

Case D2 is identical to case D1 with the exception that the damage that is suddenly imposed corresponds to the simulated large gap. The results using 92% variance are shown in Figure 4.17. The results using 98% variance are shown in Figure 4.18. Both figures show that the large gap is detected readily by the damage index. Prior to damage introduction, the false positives identical to those seen in case D1 are observed. After damage is introduced, no false negatives are observed. As seen in Figure 4.18, a very sensitive threshold is unnecessary to detect the larger gap, as both

threshold choices readily identify the presence of damage. In both damage cases (D1 and D2), retaining 92% of the variance in the PCA formulation leads to a more sensitive damage index, but also leads to an unacceptably high rate of false positives.

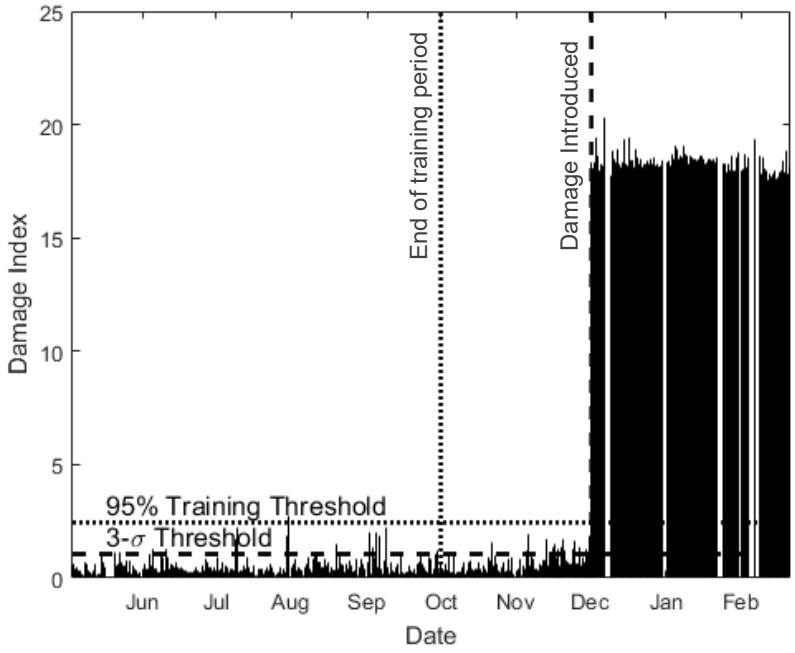

Figure 4.17 PCA damage index for large, sudden gap and 92% variance.

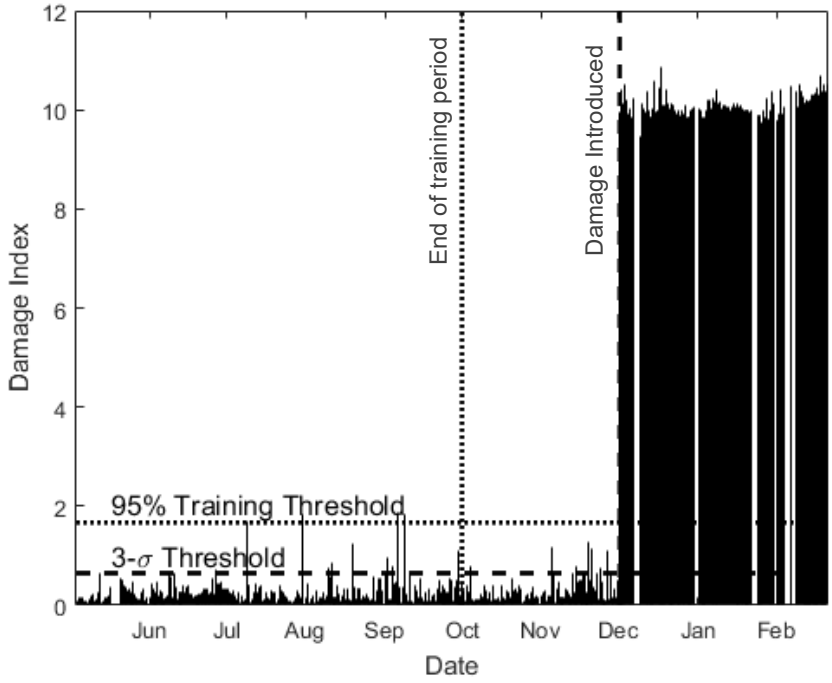

Figure 4.18. PCA damage index for large, sudden gap and 98% variance.

4.4. Conclusions

This chapter presents the efforts undertaken as part of this dissertation to develop a method to utilize strain gages to automatically detect the presence of gaps forming in the bearing surface of miter gate quoins. First, challenges were identified with using raw strain as a feature for gap detection: namely, strain is highly sensitive to environmental noise, and the strain gage data on miter gates is subjected to long period of inactivity. This chapter then proposed a new damage sensitive feature for detecting gaps at the quoin; namely, the rate of change of strain data with respect to the water level in the gate chamber, or slope. The time series comprised of slope data was shown to be nominally stationary and independent of temperature effects. Moreover, the slope time series has significantly less samples than the strain time series, reducing computation time. The slope as a damage sensitive feature has since been used in future studies of strain as a damage indicator, such as that by Hoskere, et al. (2019). The slope was then extracted for a selection of appropriate sensors, and finally PCA was applied as the method of statistical analysis of the data and finding a damage index to detect damage. The results demonstrate the efficacy of the proposed method for detecting even small gaps at the gate/quoin interface.

The data investigated was from Greenup miter gate, discussed at length in previous chapters of this dissertation. The date was sampled from late spring 2014 through late winter of 2015. In this time period, the gate would have been subject to very wide ranging temperature and other environmental variables. This study has shown that using the slope data for damage detection in conjunction with PCA allows for continuous, automated monitoring through wide ranging environmental conditions, with no additional input required from the user. The damage index used is sensitive to the presence of a gap. The sensitivity of the algorithm is dependent on the amount of variance retained in the system when training the eigenvectors. Among the two training schemes tested, the 92% variance (that is, using the eigenvectors corresponding to the directions with the three highest variances) was more sensitive to the presence of damage than the 98% variance (using all but the eigenvector that describes the least variance), but the 92% variance case was found to be too noisy, leading to an unacceptably high rate of false positives. Equally important is that the proposed method works well in monitoring the gate in the absence of damage. For the 98% variance case, no false positives are shown when damage was not imposed on the gate with the requirements of three consecutive observations above the threshold, and false positives are all but eliminated when the threshold is set larger.

Individual observations of exceedance of a sensitive threshold occasionally occur and need to be addressed. This highlights the fact that the threshold should be viewed as a parameter to be tuned based on a qualitative assessment of what "critical" damage is. To illustrate the sensitivity of the proposed method to the selection of a threshold, two possible threshold values were investigated, a 3σ threshold similar to industrial control charts, and a 95% cutoff threshold used by Santos, et al., (2015). The 95% cutoff threshold was unable to detect the small damage case, but was had few false positives. It is the authors' opinion that the 95% cutoff threshold is more than adequate to detect the level of damage likely critical to lock-gate operations. A different method to address false positives would be to increase the number of consecutive observations required above the threshold to be considered an indication of damage. For this study, there was never a false positive consisting of more than three consecutive observations if 98% of the variance is retained in the PCA algorithm.

The results have shown that the approach presented in this chapter provides an effective method for detecting gaps in miter gates. The PCA approach is easily automated and, once set up, requires no additional input from a user. Similar approaches are expected to be useful for detecting other types of damage in miter gates.

Chapter 5. Non-contact, vision-based monitoring of tension in miter gate diagonals[2]

This chapter discusses the method developed in this research to leverage displacement records of a vibrating miter gate diagonal obtained via a non-contact, vision-based approach to monitor the tension in miter gate diagonals. Recall from Chapter 2 that miter gates have large, steel diagonal members that are tensioned and span the full diagonal dimension of the gate. The geometry of a miter gate is such that there is an eccentricity between the shear center and the center of gravity, which will cause the gate to torsionally deflect under its own weight. To counteract the torsional deflection, the diagonals are added to the gate and tensioned. Maintaining the appropriate tension in the diagonals is critical to maximizing the useful life of a miter gate. Diagonals with insufficient tension will cause the gate to lean into the lock chamber when the gate is open, thereby increasing the likelihood of a vessel impacting the gate. Diagonals with excessive tension will lead to accelerated fatigue damage. Thus, as part of this dissertation, it was critical to develop an efficient and effective method to monitor the tension in miter gate diagonals.

In this chapter, the challenges of monitoring tension in miter gate diagonals are first discussed. Then, the dynamics of miter gate diagonals and the effects of partial submersion on the dynamics of the diagonal are explored. The water surrounding a diagonal is found to be sufficiently modeled by considering added mass to the beam. Next, the use of the approximate assumed-modes method to find a relationship between extent of submersion, the frequency of vibration, and the tensile stress in the diagonal is discussed. The proposed vision-based method utilizing Lukas-Kanade optical flow is then introduced. The experimental setup used to validate both the vision-based method and the model accounting for partial submersion is described and the results of the experimental validation are presented. Finally, the proposed approach is validated using video of the vibrating diagonals of an in-service miter gate instrumented with load cells. The results of the field validation show excellent agreement between the tension calculated using the proposed method and the tension recorded by the load cell installed on the diagonal.

[2] Some of the work presented herein has been previously published in proceedings of the 12th International Workshop on Structural Health Monitoring (Eick, Narazaki, et al. 2019): Eick, Brian; Narazaki, Yasutaka; Smith, Matthew; Spencer Jr., Billie F, "Monitoring post-tensioned miter gate diagonals using vision-based vibration measurements", Proceedings, 12th International Workshop on Structural Health Monitoring, 09/10/19, Stanford

5.1. Challenges with monitoring tension in miter gate diagonals

Utilizing traditional contact sensors such as strain gages to monitor the stress in the diagonals would be straightforward, but expensive, as the infrastructure to acquire, process, and store the data does not exist on the vast majority of lock and dam sites. Moreover, installing strain gages on already tensioned diagonals without knowledge of the initial tension value would not provide any information other than future changes or differences in tensile stress. Vibration monitoring is promising, such as the procedure outlined by Cho, et al., (2010)for cables on cable-stayed bridges; however, it is challenging to access the diagonals on a miter gate without getting in a boat, rappelling from the lock gate, or closing the site and draining the water from the lock chamber. To circumvent the expense and difficulty of accessing the diagonals, a non-contact, vision-based method to monitor the tension in the diagonals is developed.

The goal of the developed methodology is for a lock operator or maintenance technician to monitor the tension from the lock chamber wall with nothing more than an inexpensive camera and the software/scripts developed herein. The developed methodology utilizes a method known as optical flow to track the displacements of a vibrating diagonal from a video. A frequency domain method is then used to determine the frequency of vibration of the diagonal from the measured displacement record, and the tension is found via beam theory. However, partial submersion of the diagonals in water, which is expected in the field, will lead to a decreased frequency of vibration in the diagonals and a measurement of tension below the true value. Exact calculations of the tension in a partially submerged diagonal are difficult to obtain. An approximate method must be used to accurately measure the tension in the diagonals given a frequency of vibration while accounting for the effects of partial submersion.

5.2. Dynamics of miter gate diagonals

As mentioned above, vibration-based tension monitoring of structural components is attractive (Rytter 1993), and has been employed in numerous studies, with a strong focus on monitoring the cables of cable-stayed bridges (Cho, et al. 2010). Unlike the cables on a cable-stayed bridge where flexural rigidity is often neglected (Irvine 1981), the diagonals investigated in this study are represented as Euler-Bernoulli beams. To this end, the relationship between the absolute tension in a vibrating beam and the frequency of the beam must be found. In addition, the diagonals on a miter gate are not subjected to idealized boundary conditions. The boundary conditions for the diagonals under investigation are not strictly pinned and are expected to provide

some moment resistance to the ends of the beam. Moreover, the two ends of the diagonal are expected to have slightly asymmetrical boundary conditions. The general solution to the equation of motion of a tensioned, prismatic beam, regardless of boundary conditions, is given in generalized non-dimensional form as follows

$$v(\bar{x}) = C_1 \cosh(\alpha_1 \bar{x}) + C_2 \sinh(\alpha_1 \bar{x}) + C_3 \cos(\alpha_2 \bar{x}) + C_4 \sin(\alpha_2 \bar{x}) \tag{5.1}$$

where

$$\alpha_1 = \left(\frac{k^2}{2} + \sqrt{\frac{k^4}{4} + \beta^4} \right)^{\frac{1}{2}}, \tag{5.2}$$

$$\alpha_2 = \left(-\frac{k^2}{2} + \sqrt{\frac{k^4}{4} + \beta^4} \right)^{\frac{1}{2}}, \tag{5.3}$$

$$k = \sqrt{\frac{PL^2}{EI}}, \tag{5.4}$$

$$\beta = L \left(\frac{\mu \omega^2}{EI} \right)^{\frac{1}{4}}, \text{and} \tag{5.5}$$

$$\bar{x} = \frac{x}{L}. \tag{5.6}$$

In the equations above, E is the beam's modulus of elasticity, L is the length of the beam, I in the moment of inertia of the beam in the direction of vibration, x is the location on the beam from the datum, μ is the mass per unit length of the beam, P is the axial tensile load in force unit, and ω is the frequency of vibration. C_n are constants of integration that are determined using the boundary conditions of the problem. Generally speaking, the characteristic equation of the beam is found by solving for the constants of integration, which is done by taking the determinate of the matrix that consists of the coefficients for the unknowns based on the boundary conditions. Particular solutions of Eq. (5.1) for typical Dirichlet boundary conditions are readily available in the

literature, such as the compilation by Shaker (1975). In the course of this study, it was found that miter gate diagonals that utilize super-nut style connectors are most appropriately modeled as fixed-pinned, in which case, the characteristic equation of the beam is as given by

$$\alpha_1 \cosh \alpha_1 \sin \alpha_2 - \alpha_2 \sinh \alpha_1 \cos \alpha_2 = 0. \tag{5.7}$$

For a pinned-pinned beam, the characteristic equation is given by

$$\sin \alpha_2 = 0. \tag{5.8}$$

With the characteristic equation in hand, the tension in the beam can be determined if the geometry, material properties, and frequency of vibration are known. The appropriate modeling of boundary conditions of the diagonal may be critical to the ability to accurately determine the tension given a frequency of vibration. The relationship provided in Eq. (5.7) has been found appropriate for the diagonals investigated in this study. Other relationships may need to be investigated for diagonals whose design significantly differs from those investigated in this study. From a design perspective, the diagonals are assumed to be tension-only, axial-load members; vibration of the diagonals is not explicitly considered. The diagonal specimens used in this study mimic those diagonals that use super-nut type tensioning systems, which are common on newly installed gates along the Ohio River and elsewhere. However, standards for connecting the diagonals to the miter gate do not exist, and so the end fixity of the diagonal will need to be determined on-site on a case-by-case basis.

An additional challenge to vibration-based tension monitoring of miter gate diagonals is that, unlike the cables of a bridge (which have round cross-sections with uniform moment of inertia in all orientations), the miter gate diagonals investigated in this study are mostly comprised of narrow rectangular cross-sections with an aspect ratio on the order of 8:1. Thus, miter gate diagonals have a weak and strong bending axis, which leads to different vibration frequencies in different directions. Care must be taken when referring to the frequencies of vibration of the diagonals, and for this study, the authors are primarily seeking to measure the weak axis frequencies. The amplitudes in the weak axis are expected to be higher and the frequencies lower. Note, the weak axis of motion is likely to be out-of-plane of the miter gate, but this would depend on the

configuration of the diagonals. Differentiating between the two axes of motion is critical because if the strong axis frequency is measured but the weak axis moment of inertia is used in Eq. (5.7), the calculated tension will be overestimated. Additionally, the miter gate diagonals investigated in the study have varying cross sections at the ends of the diagonals, where the diagonal tapers from a rounded cross-section with comparatively large moment of inertia to a rectangular cross-section with comparatively small moment of inertia in the weak axis direction. This additional bending stiffness at the ends of the diagonal is significant, as there is a bending moment expected at the fixed-end of a fixed-pinned beam. An exact solution to Eq. (5.7) for a non-prismatic beam would be intractable, and so an approximate method is utilized as part of this study, as explained in the next section.

5.3. Effects of submersion on miter gate diagonal dynamics

A particular challenge to vibration-based monitoring of miter-gate diagonals is that they are subjected to varying amounts of submersion in water. Figure 5.1-a shows an elevation view of a typical miter gate, while Figure 5.1-b shows the typical in-situ partially submerged condition of a miter gate. Draining, or "dewatering" a lock chamber requires specialized infrastructure to be put in place and is thus very expensive. Accordingly, dewaterings are only performed infrequently for routine maintenance once every five to ten years, or for emergency repairs to prevent catastrophic failure of the gate. Generally speaking, the diagonals on a miter gate will be partially submerged for the vast majority of their life.

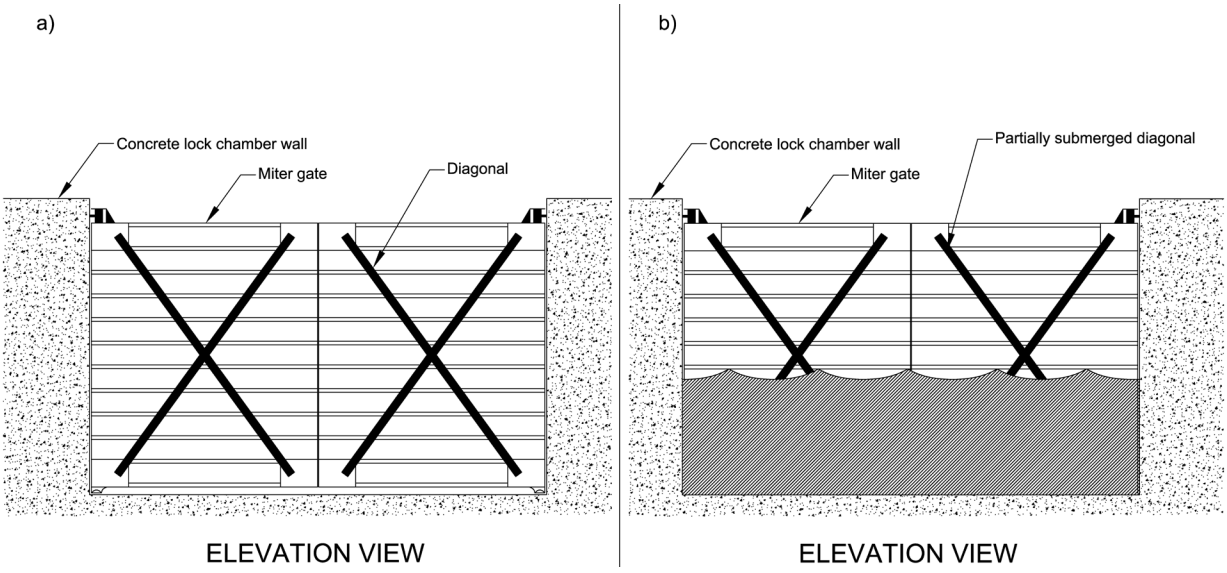

Figure 5.1. (a) Elevation view of miter gates with diagonals. b) Typical condition of the miter gate, partially submerged in water

The partially submerged nature of a miter gate diagonal makes it a fluid-structure interaction system. Fluid-structure interaction systems consist of a structure moving through a fluid, a volume of which must be displaced to allow the structure to move. For simplicity, consider an illustrative example of a single-degree-of-freedom (SDOF) structure. In the fluid-structure interaction system, the structure itself has some stiffness (k_s), mass (m_s), and damping (c_s). The fluid also has some stiffness (k_a), mass (m_a), and damping (c_a). The subscript a is used here for "added", in that the values from the fluid are thought of as added to the structure. The formulation of the equation of motion for an SDOF fluid structure interaction system then takes the form of (Kaneko, et al. 2014)

$$(m_s + m_a)\ddot{x} + (c_s + c_a)\dot{x} + (k_s + k_a)x = f \tag{5.9}$$

where f is an external force to the system. Chen (1985) notes that, for a structure moving through an ideal fluid (i.e., incompressible and inviscid), the primary effect of the submersion is to add mass, and so Eq.(5.9) can be simplified to

$$(m_s + m_a)\ddot{x} + c_s\dot{x} + k_s x = f. \tag{5.10}$$

The experimental analysis performed herein shows that, for determining the effects of submersion on the fundamental frequency of vibration of a beam, the simplification provided in Eq. (5.10) produces excellent results. The value of added mass can be determined analytically and is related to the properties of the fluid and the geometry of the structure, which dictates the volume of water displaced when the structure moves through the fluid. Tabulated values of added mass for common geometries are available in the literature, such as in Kaneko, et al., (2014). For this study, the geometry of the diagonals closely resembles a thin plate in two cases studied and a rectangular prism in one case. The value of added mass per unit length of a thin plate of width 2a is given by

$$\mu_{a\_plate} = \rho_{water}\pi a^2. \tag{5.11}$$

The value of added mass for a rectangular prism of width 2a and depth 2b is dependent on the aspect ratio of the cross section, b/a. As will be seen the rectangular geometry used in this study has an aspect ratio of 0.57. Using the table available in Kaneko, et al., (2014) and linearly

interpolating, the value of added mass per unit length for the rectangular prism used in this study is given by

$$\mu_{a\_rectangle} = 1.38\rho_{water}\pi a^2. \tag{5.12}$$

If the beam is fully submerged in water, then Eq. (5.7) can be directly used to find the relationship between the frequency of vibration and tension, with the only change occurring in β defined in Eq. (5.5). Incorporating the added mass term, β is defined as

$$\beta = L\left(\frac{(\mu + \mu_a)\omega^2}{EI}\right)^{\frac{1}{4}}. \tag{5.13}$$

The diagonals on a miter gate, being partially submerged, must be modeled as piecewise beams with two distinct sections. The first section has a length, L_w, corresponding to the submerged part of the beam and has a mass per unit length of the steel plus the added mass per unit length due to water. The other section has length corresponding to the unsubmerged length of the beam and mass per unit length of steel only. On both sections of the beam, all other geometric and material properties are the same. The beam model for a partially submerged diagonal for the pinned-pinned case is shown in Figure 5.2.

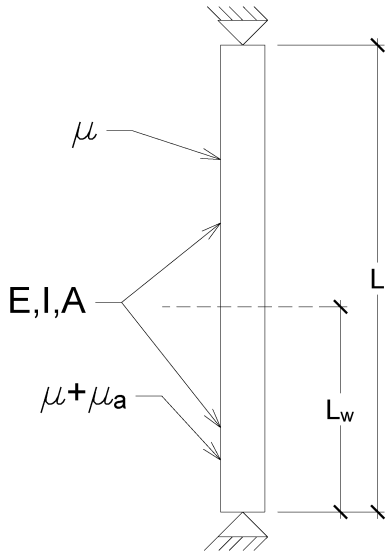

Figure 5.2. Piecewise beam model of partially submerged miter gate diagonal

The relatively simple adjustment to the continuous beam model of adding mass to a portion of the beam leads to a complicated closed-form relationship between the tension in the beam and the frequency of vibration. For the beam shown in Figure 5.2 the characteristic equation of the beam is given by the determinate of the matrix below.

$$\begin{bmatrix} \sinh(\alpha_{1a}\frac{L_w}{L}) & \sin(\alpha_{2a}\frac{L_w}{L}) & -\cosh(\alpha_{1b}\frac{L_w}{L}) & -\sinh(\alpha_{1b}\frac{L_w}{L}) & -\cos(\alpha_{2b}\frac{L_w}{L}) & -\sin(\alpha_{2b}\frac{L_w}{L}) \\ \alpha_{1a}\cosh(\alpha_{1a}\frac{L_w}{L}) & \alpha_{2a}\cos(\alpha_{2a}\frac{L_w}{L}) & -\alpha_{1b}\sinh(\alpha_{1b}\frac{L_w}{L}) & -\alpha_{1b}\cosh\alpha_{1b}\frac{L_w}{L} & \alpha_{2b}\sin(\alpha_{2b}\frac{L_w}{L}) & -\alpha_{2b}\cos(\alpha_{2b}\frac{L_w}{L}) \\ \alpha_{1a}^2\sinh(\alpha_{1a}\frac{L_w}{L}) & -\alpha_{2a}^2\sin\alpha_{2a}\frac{L_w}{L} & -\alpha_{1b}^2\cosh\alpha_{1b}\frac{L_w}{L} & -\alpha_{1b}^2\sinh\alpha_{1b}\frac{L_w}{L} & \alpha_{2b}^2\cos\alpha_{2b}\frac{L_w}{L} & \alpha_{2b}^2\sin\alpha_{2b}\frac{L_w}{L} \\ \alpha_{1a}^3\cosh\alpha_{1a}\frac{L_w}{L} & -\alpha_{2a}^3\cos\alpha_{2a}\frac{L_w}{L} & -\alpha_{1b}^3\sinh\alpha_{1b}\frac{L_w}{L} & -\alpha_{1b}^3\sinh\alpha_{1b}\frac{L_w}{L} & -\alpha_{2b}^3\sin\alpha_{2b}\frac{L_w}{L} & \alpha_{2b}^3\cos\alpha_{2b}\frac{L_w}{L} \\ 0 & 0 & \cosh(\alpha_{1b}) & \sinh(\alpha_{1b}) & \cos(\alpha_{2b}) & \sin(\alpha_{2b}) \\ 0 & 0 & \alpha_{1b}^2\cosh\alpha_{1b} & \alpha_{1b}^2\sinh\alpha_{1b} & \alpha_{2b}^2\cos\alpha_{2b} & \alpha_{2b}^2\sin\alpha_{2b} \end{bmatrix} \tag{5.14}$$

where α_1 and α_2 are as described in (5.2) and (5.3), but the subscripts *a* and *b* refer to using the appropriate material and geometric properties of the bottom and top sections of the beam, respectively, as shown in Figure 5.2. The determinate can be explicitly found using appropriate symbolic math software; however, determining the tension given a specified measured frequency of the beam is not possible in closed form and must be done numerically.

Because of the ease of implementation and computational efficiency, the assumed modes method (Craig and Kurdila 2006) is employed to model the submerged beam. For the assumed modes method, admissible shape functions must be selected for the *n* modes to be estimated. Here, we refer to the i^{th} shape function as ψ_i. An admissible shape function is one that satisfies the geometric boundary conditions of the beam and is twice differentiable. For this study, the beam is modeled as fixed-pinned, and so the shape functions must satisfy $\psi_i(0) = 0, \psi_i(L) = 0, \psi_i'(0) = 0$, and $\psi_i'(L) \neq 0$, where the "prime" subscript denotes the derivative of the shape function with respect to the dimension along the length of the beam, *x*. As can be shown, Eq. (5.15) is an admissible shape function for every i^{th} mode of vibration of a fixed-pinned beam and is thus used in this study.

$$\psi_i(x) = x\sin\left(\frac{i\pi x}{L}\right). \tag{5.15}$$

For miter gate diagonals with connection details that differ significantly from the multi-jackbolt tensioning nuts used in this study, the boundary conditions should be rigorously explored and an assumed mode shape that satisfies the boundary conditions of the particular diagonal should be used. It is worth noting that for typical miter gate diagonals, the slenderness ratios are significantly larger than the scale model specimens used in this study, and it is likely that boundary conditions will have less of an impact on the behavior of the diagonals. The need to accurately capture the boundary conditions of an in-service diagonals is the subject of future work. Then, to estimate the frequencies of vibration, a number of mode shapes are considered to get converged results for the frequencies of vibration. For this study, 25 modes are found to be sufficient. To determine the frequencies of vibration using the assumed modes method, the eigenvalue problem is solved such that:

$$\det\left(\left(\left[K_{stiff}\right]+\left[K_{geom}\right]\right)-\omega^2\left(\left[M_{beam}\right]+\left[M_{added}\right]\right)\right)=0 \tag{5.16}$$

where $\left[K_{stiff}\right]$ is the bending stiffness matrix of the beam, $\left[K_{geom}\right]$ is the geometric stiffness matrix of the beam, $[M_{beam}]$ is the mass matrix of the beam, and $[M_{added}]$ is the added mass matrix of the beam. Note, the damping of the beam itself is assumed to be negligible and as stated previously, the results from Chen (1985) are first explored by only considering the added mass of the water. The *i*, *j* component of each of these matrices is found by

$$K_{stiff_{i,j}}=\int_0^L EI(x)\psi_i''(x)\psi_j''(x)dx\,, \tag{5.17}$$

$$K_{geom_{i.j}}=\int_0^L P\psi_i'(x)\psi_j'(x)dx\,, \tag{5.18}$$

$$M_{beam_{i,j}}=\int_0^L \mu\psi_i(x)\psi_j(x)dx\ \text{, and} \tag{5.19}$$

$$M_{added_{i,j}}=\int_0^{L_w} \mu_a\psi_i(x)\psi_j(x)dx\,. \tag{5.20}$$

This proposed approximate method utilizing the assumed-modes approach is leveraged herein to analytically relate the extent of submersion of a diagonal to the axial tension and frequency of vibration of the diagonal. To use this approximate method in a field setting, the frequency of vibration must be obtained, as described below.

5.4. Vision-based methodology for measuring frequency of diagonals

Obtaining the frequencies of vibration of diagonals to use in Eq. (5.7) would be straight-forward using accelerometers; however, accessing the diagonal members to install accelerometers would either require closing the lock site and draining the water, using a boat, or specialized personnel rappelling from the side of the gate. Either case is difficult, dangerous, and expensive; therefore, this study investigates the use of non-contact sensing utilizing computer vision methods, namely Lucas-Kanade optical flow (Lucas and Kanade 1981). Vision-based structural health monitoring (SHM) is a growing field (Spencer, et al. 2019) (Ye, et al. 2016) (Song, et al. 2014). A lot of recent work in vision-based SHM is aimed at damage identification such as detecting concrete cracks (Yamaguchi and Hashimoto 2010) or corrosion in steel (Ahuja and Shukla 2017). There has also been recent work on utilizing vision-based methods for monitoring vibration characteristics of civil structures and for detecting tension in structural components. Ribeiro, et al., (2014) developed a vision-based method of monitoring dynamic bridge displacements. Kim, et al., (2013) (2017), successfully demonstrated utilizing a template-matching algorithm, along with subpixel interpolation to monitor the vibration of cables on a suspension bridge and cable stayed bridges. Feng, et al., (2016) (2017) utilize a similar approach to monitor the cables of cable-stayed bridges, and they compare their results to a gradient-based template matching algorithm, and find the gradient-based method to be superior. For this study, the proposed approach employs an optical flow algorithm that directly solves for the apparent velocities of pixels between sequential frames of a video by assuming that the spatial intensities of local regions of the frames of a video are approximately constant (Beauchemin and Barron 1995). The optical flow algorithm aims to solve the following equation for the apparent image velocity, V (Horn and Schnuck 1981):

$$I_x V_x + I_y V_y = -I_t \tag{5.21}$$

where I_x, I_y, I_t are the partial derivatives of the image intensity with respect to x, y, and t (note the variable assignments are different in Horn and Schnuck (1981)). This study utilizes the Lucas-

Kanade method of solving Eq. (5.21) for V_x and V_y, which takes a least squares approach to the problem. A small patch of n pixels is defined centered on the pixel of interest, and all pixels within the patch are assumed to have the same velocity. The specifics of the solution can be found in the literature (Lucas and Kanade 1981), with the results of the apparent velocity of pixels within the patch shown in Eq.(5.22) and Eq. (5.23).

$$V_x = \frac{\sum_{\mathrm{i}=1}^{\mathrm{n}} I_{x_i} I_{y_i} \sum_{i=1}^{n} I_{y_i} I_{t_i} - \sum_{\mathrm{i}=1}^{\mathrm{n}} I_{y_i}^2 \sum_{\mathrm{i}=1}^{\mathrm{n}} I_x I_t}{\sum_{\mathrm{i}=1}^{\mathrm{n}} I_{x_i}^2 I_{y_i}^2 - \left(\sum_i^n I_{x_i} I_{y_i}\right)^2}, \text{and} \tag{5.22}$$

$$V_y = \frac{\sum_{i=1}^{n} I_{x_i} I_{y_i} \sum_{i=1}^{n} I_{x_i} I_{t_i} - \sum_{i=1}^{n} I_{x_i}^2 \sum_{i=1}^{n} I_y I_t}{\sum_{i=1}^{n} I_{x_i}^2 I_{y_i}^2 - \left(\sum_i^n I_{x_i} I_{y_i}\right)^2}. \tag{5.23}$$

where i refers to the i^{th} pixel of the patch of n pixels. The Lucas-Kanade method can be used to track points of interest in a video, since a displacement record in pixels can be readily obtained from the apparent velocity. From the displacement record, the frequencies of vibration are found by means of a fast-Fourier transform (FFT), and then Eq.(5.7) is solved for T. Vision-based methods, such as optical flow, are particularly useful in tracking displacements that are in-plane of the field-of-view of the camera. This presents a challenge for miter-gate diagonals since typical diagonals are oriented such that their vibration response will be dominated by displacement that is out-of-plane of the miter gate. Due to the configuration of miter gates and lock chambers, camera will need to be offset by some angle other than perpendicular to the direction of vibration of the diagonal. Thus, video can only be readily obtained such that only some component of the vibration of the diagonal is in-plane of the field-of-view of the camera. Accordingly, the amount to which a camera can be offset from the direction of vibration and still facilitate optical flow-based displacement tracking must be investigated.

Further, Typical to vision-based methods, satisfactory performance of optical-flow requires sufficient lighting, good contrast in the image, and a sharp gradient in image intensity of the tracked feature. Adequate conditions for the use of vision-based monitoring may be challenging in the field, where environmental conditions such as inclement weather may impede obtaining video of sufficient quality. The power of using optical flow for monitoring of miter gate diagonals is that the proposed method is not intended, nor needed, to be used for continuous monitoring. Insufficient

or excessive tension in the diagonals is not likely to pose an immediate threat of catastrophic failure of the miter gate; rather, the effects will be of a gradual, cumulative nature. That is, inappropriately tensioned diagonals may, for instance, accelerate fatigue damage when excessively tensioned, or increase the likelihood of vessel impact to the miter gate when insufficiently tensioned. Accordingly, the proposed methodology is intended to be utilized periodically, with temporarily placed commercial-off-the-shelf (COTS) cameras (cameras on a tripod near the miter gate). An acceptable monitoring period is expected to be monthly and can be adjusted if significant changes in diagonal tension are found. Thus, the field engineer utilizing the methodology can simply wait for sufficient lighting, or use an artificial light source if necessary (e.g., a flood light, which is typically available at a lock and dam site), and then capture the video.

Another issue with vision-based methods is noise, in the form of incidental camera movement, which will manifest itself as motion of the structure. The researchers here take a similar approach for noise removal as outlined by Kim and Kim (2013) and Luo, et al., (2018) of tracking a stationary reference point in the same frame. The results from the tracked stationary point are then subtracted from the results of the tracked pixel on the vibrating beam. Kim and Kim (2013) suggest subtracting the time domain results to remove noise. For the optical flow method, noise is not equivalently tracked for all features in a frame. The predicted motion of a feature from optical flow is largely dependent of the gradient of the intensity in the region of the frame near the tracked feature, and so, small deviations in the calculated displacement occur and are not equivalent from feature to feature. The authors of this study find better results by removing noise in the frequency domain by subtracting frequency domain results. Additionally, as drift may be present in the displacement signal, a high-pass filter is used to remove the low frequency noise caused by signal drift.

To test the efficacy of the proposed approach on miter gate diagonals, testing was performed of scale-model diagonals subjected to different excitations. Both accelerometer readings and video of the vibrating beams were taken. The Lucas-Kanade method is implemented on the video by utilizing the OpenCV library in Python (Bradski 2019) and as outlined by Mordvintsev and Abid (2013). The method proposed herein is a human-in-the-loop (HITL) approach. As mentioned previously, the use of the proposed approach will be periodic in nature, using temporarily placed cameras, which will require some action by a field engineer to place cameras, record video, and transfer data. Much of the literature of vision-based monitoring focuses

on methodologies that utilize automated feature extraction. The methodology herein is one in which the features to be tracked are manually selected by the engineer. This small additional required input comes at the benefit of a greatly simplified approach and effectively eliminates the possibility of tracking the motion of the wrong miter gate component or some feature not on the miter gate. Moreover, because only the fundamental frequency is required to obtain the tension estimate, only tracking a single point of the diagonal is further justified, not unlike using an accelerometer.

To facilitate the video processing, a script was written in Python wherein a user defines a point to track on the tensioned diagonal in a video frame and the script outputs the displacements record (in pixels) of the point of interest. For optical flow to work successfully, the tracked region of the diagonal should have a high gradient in image intensity seen in the frames of the video. What this means in practice is that an engineer should select a point on the edge of the diagonal to track. As seen in the images of miter gates provided in Chapter 2, the depth of the miter gate tends to create good contrast between the diagonal, and the region of the miter gate behind the diagonal leading to a high gradient of image intensity at the edges of the diagonal. A patch size of 15 x 15 pixels was used in the algorithm with acceptable results. An FFT is performed on both the accelerometer data and the displacement record obtained from the Lucas-Kanade method, and the fundamental frequencies are found and used to calculate the tension in the beam, which is compared to the known value measured by strain gages. As the weak-axis vibrations are expected to have higher vibration amplitudes, this study investigates the ability of the Lucas-Kanade method to detect weak-axis vibration at different camera angles, camera distances, and at varying amplitudes of vibration. Of importance is to determine if the optical flow method can differentiate between the weak axis and strong axis vibrations when both directions are visible to the camera. Similarly, it is critical to determine if the optical flow method can accurately track the displacements of low amplitude vibration at relatively far distances, which would be a scenario seen in the field. The authors show herein that the optical flow method is able to match the vibration measured by an accelerometer, even for low amplitude vibrations and when the camera is offset from the direction of vibration and at a relatively far distance. The optical flow approach performs particularly well when a zoom lens is utilized. The experimental validation of the proposed method is explained in the following chapter.

5.5. Experimental setup

As mentioned above, the efficacy of the vision based method is tested by means of scale model specimens in a laboratory setting. The scale-model diagonals were setup to be vertically oriented in a lab and placed in a submersion tank that was constructed consisting of stacked, welded 208 liter (55 gallon) drums with their bottoms removed. The submersion tank facilitated exciting the diagonals by means of flowing water by simply filling the tank with a hose, as well as testing the effects of submersion on the vibrating frequency of the specimens. The geometry of the scale-model diagonals used for this test were constrained by the size of the laboratory facilities and a desire to mimic the behavior of the typical miter gate diagonals as closely as possible. That is, it was desirable to have diagonals that would be expected to have relatively low frequencies of vibration when subjected to a tensile stress of around 172 MPa (25 ksi), as in the field. Three diagonal cross-sections were tested, all having the same cross-sectional area, with the rectangular cross-section dimensions of each specimen listed in Table 5.1. The geometry of the diagonal specimens is typical of diagonals in the field that use the super-nut style tensioning system, which is common, but not exclusive, among U.S. miter gates. Thus, results regarding calculated tension should be considered limited to diagonals with similar geometries given the dependency of calculated tension on the boundary conditions, which are assumed to be fixed-pinned in this study. This assumption of boundary conditions is an idealization, allowing for the use of the closed-form relationship of Eq. (5.7) and for the determination of an appropriate shape function for use in the approximate assumed modes method. The hex-nut end of the test specimen is not strictly fixed, and the super-nut end is not strictly pinned, and so, this assumption will lead to small errors in tension estimates. The three different geometries provide some insight into the uncertain boundary conditions of the diagonals, but the geometry of the beam has little effect on the results of the vision-based method to accurately capture the frequency of vibration of a diagonal. The height of the strong-wall to which the beams were attached limited the length of the beams such that the connection-to-connection length was set at 6.10 m (20.0 ft.). Tensioning the beam was performed as in the field by using a Nord-lock Superbolt multi-jackbolt tensioning nut. Stress in the beam is assumed to be primarily due to axial tension due to the super-nut; however, bending and shear stresses may be present due to small misalignments and incidental twists in the beam, which is equally likely to be experienced in the field. These additional stresses, if present, will not be captured by the strain gages, and will lead to further deviations between measured tension and

calculated tension using Eq. (5.7). As in the field, the use of the Superbolt tensioning nut requires a round threaded rod on both ends of the beam, and so the cross section of the beam was tapered over a length of 25.4 cm (10.0 in.) from a round beam with a diameter of 3.8cm (1.5 in.) to the rectangular cross-section. The dimensions of test specimens are shown in Figure 5.3 and listed in Table 5.1. Figure 5.3-a) shows a plan view of the test specimen highlighting the wider face of the rectangular cross section. Figure 5.3-b) shows the plan view that highlights the narrower face of the rectangular cross section and is essentially Figure 5.3-a) rotated 90 degrees about the axis passing through the length of the specimen. A labeled schematic of the experimental test setup is shown in Figure 5.4, while an image of the actual setup in the lab is shown in Figure 5.5.

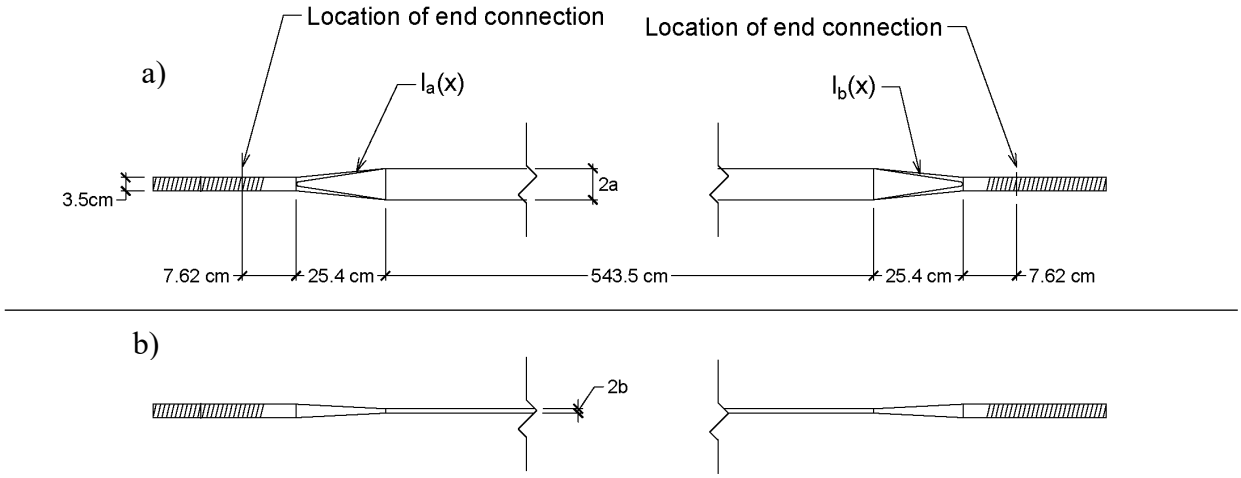

Figure 5.3. Scale model diagonal specimens used in this test. a) Plan view showing the wide face of the rectangular cross-section. b) Plan view showing the narrower face of the rectangular cross-section

Table 5.1. Scale model diagonal specimens.

Name	**Cross sectional dimensions**
Specimen 1	a=8.89 cm (3.50 in), b=0.32 cm (0.13 in)
Specimen 2	a=4.45 cm (1,75 in), b=0.64cm (0.25 in)
Specimen 3	a=2.22 cm (0.88 in), b= 1.27 cm (0.5 in)

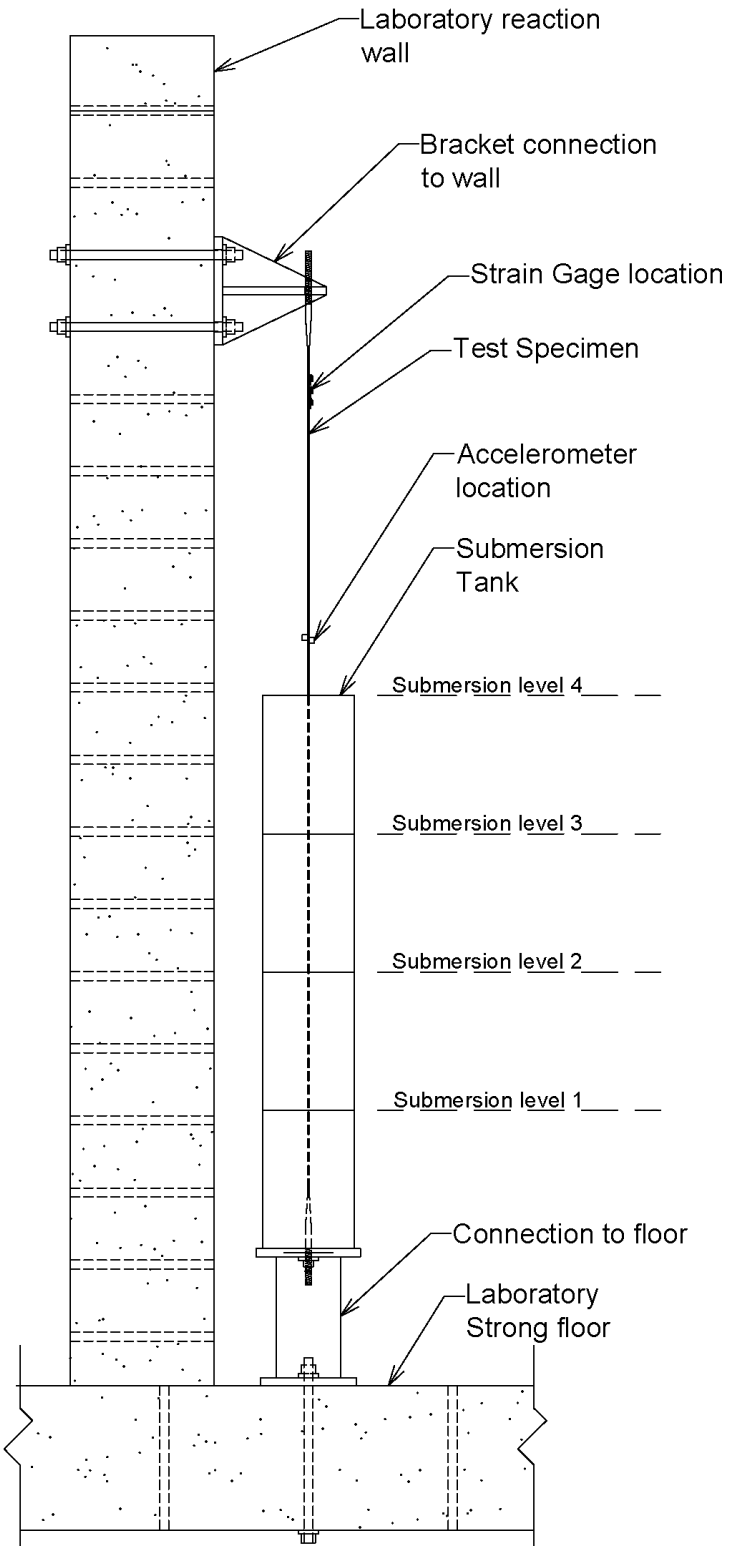

Figure 5.4. Schematic of test setup.

Figure 5.5. Test setup in the lab.

To validate the vision-based approach, the test consists of taking video of the vibrating beam from three different angles with the goal being to simulate a person taking video of a vibrating miter-gate diagonal from the lock chamber wall, and to test the effects of the angle of the camera with respect to the direction of vibration. The direction of motion of primary interest is that in the weak axis of the diagonal, and a camera placed at some angle other than perpendicular to the weak axis direction will see a reduced amplitude of motion in this direction. The three camera angles considered herein will provide some indication of the efficacy of the proposed approach at angles where the weak-axis motion of the diagonal will be partially out-of-plane of the frames of the

video. The camera positions for the lab test were limited by locations in the laboratory with unobstructed views of the test specimen, and the positions are defined with respect to the direction of weak-axis vibration. These camera-placement limitations will not be present in the field, where columns and other laboratory fixtures are not present. The layout of the laboratory is such that, as the angle of the camera increased, so did the distance of the camera. It was not possible to test all camera angles at the same distance, and so, there are coupled effects of distance and angle of the camera. Camera positions 1, 2 and 3 were setup to be at 0, 45 and 65 degrees from the weak axis vibration direction respectively. The respective distances of the three camera positions are 4.20 m, 5.93 m and 9.78 m. A schematic of the camera setup is shown in Figure 5.6.

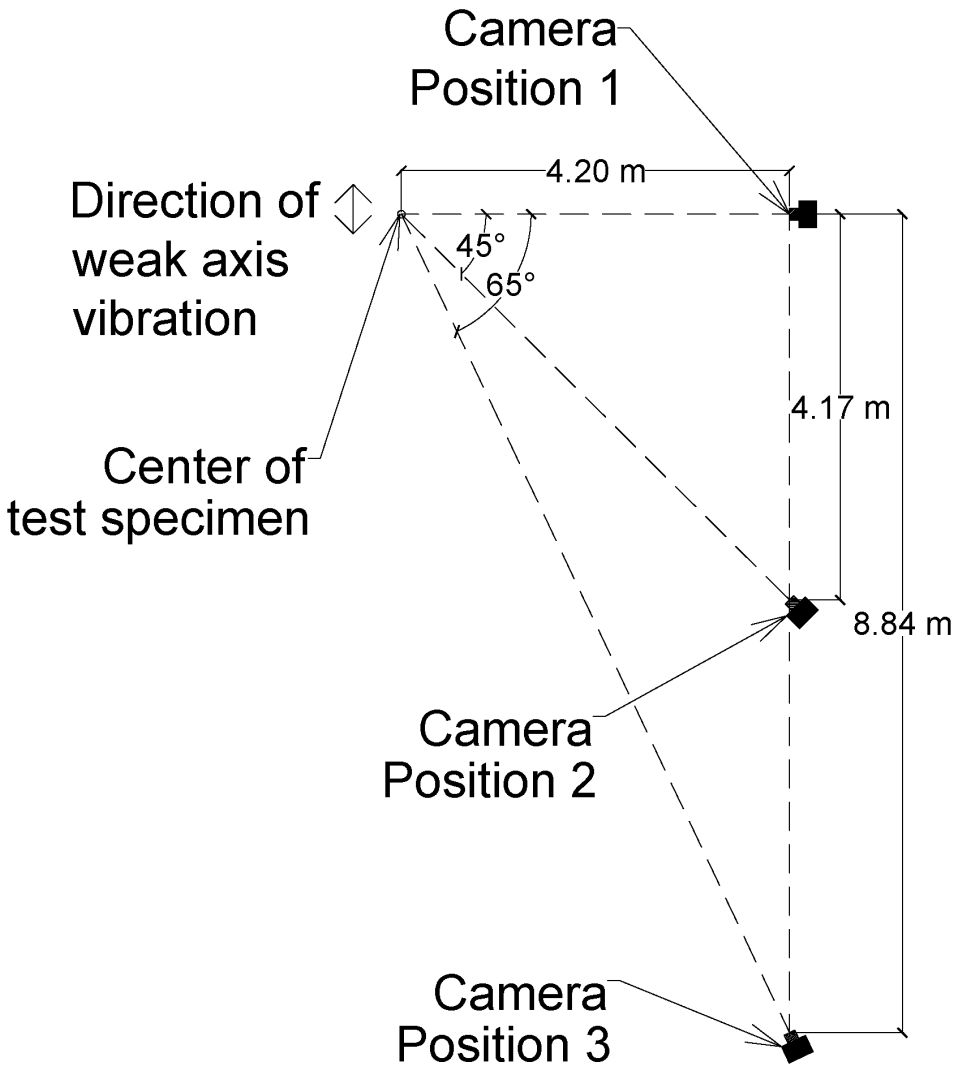

Figure 5.6. Camera positions utilized in this study.

The camera utilized in the study is a consumer-grade, commercial-off-the-shelf Nikon D3300. The Nikon D3300 has video resolution of 1080p 60 frames per second (fps) with a focal length of 55mm. For vision-based methods, the frame rate is analogous to the sampling rate of, for example, an accelerometer. Thus, the Nyquist frequency (which is the maximum measurable frequency) is one-half the frame rate). For the cameras used in this study, with a frame rate of 60 fps, the associated Nyquist frequency is 30 Hz. This frame rate can readily capture the fundamental frequency of the test specimens, which is expected to be in the range of 10 to 12 Hz. Moreover, typical miter gate diagonals will have a frequency of less than 10 Hz, and so a camera with a similar frame rate will provide adequate results. For tests with low amplitude ambient vibration, results were improved by utilizing a zoom lens. For this test, the zoom lens was an AF-S NIKKOR 70-200mm f/2.8G ED VR II with the focal length set to 200mm. To obtain reference vibration measurements, two PCB 353-B33 piezoelectric accelerometers were attached to the beam via magnets and were sampled at 256 Hz via an m+p VibPilot DAQ. The accelerometers only measure vibration in the weak-axis direction. To measure the amount of tension in the beam, three strain gages were applied to the center of the beam, and an average strain value was recorded for each test. At the time of testing, the beam was tensioned with a target strain 860 microstrain, corresponding to 172 MPa (25 ksi), which is a typical value of tensioning used in the field. Then, the camera was setup at each of the three positions, and the beam was excited first using the hammer impact and then using flowing water as previously described to simulate ambient vibration. The hammer impact tests resemble an impulsive load that will ideally excite all the modes of vibration with equal energy (Avitabile 2017), with the note that it is important to ensure that the impact is not applied to a modal zero. For the hammer impact tests, the location of the impact was just above the submersion chamber, which is more than halfway up the beam. Having the impact location offset from exactly mid-span was done to increase the likelihood of exciting the even numbered modes of the beam. That is, for a pinned-pinned beam, even numbered modes will have zero displacement (a modal zero) at the mid-point of the beam.

5.6. Efficacy of vision-based monitoring

The first step of the scale-model tests is to determine whether or not the vision-based method can successfully measure the frequency of vibration of a vibrating miter gate diagonal. Accordingly, the primary results of interest here are comparing the frequency of vibration obtained from the vision-based method to those obtained from accelerometers. However, tension in the

beams will be calculated using (5.7), ignoring any effects of submersion in water and assuming the diagonal is prismatic, highlighting the errors introduced by these simplifications. Results for the tests are first shown for the hammer impact test, and then for the tests with ambient vibration. For all tests, results will show the FFT of the displacement signal obtained from optical flow superimposed on the FFT of the accelerometer data. The FFTs are all normalized to plot them on the same scale, and so, the amplitude of the FFTs shown in the plots is not relevant. In each case, the signals from the accelerometer and the displacement measured form the vision-based method are de-trended to remove DC offsets. In all cases, 1 minute of data is processed for a frequency resolution of 1/60 Hz. For the hammer impact test, the tension values are calculated and compared to the reference value. For the ambient vibration method, the strain gages unfortunately stopped working, and so, only the frequencies of vibration can be compared. It is noted that for all results, most of the FFT for the accelerometer is trimmed along the x-axis for clarity, so that the vision-based method (with a Nyquist frequency of 30 Hz) is on the same scale as the accelerometer (with a Nyquist frequency of 128 Hz).

5.6.1. Hammer Impact Results

For the hammer impact tests, a video frame at each position is shown in Figure 5.7, with the manually selected tracked points using optical flow highlighted with red dot and white arrow. Note, as mentioned previously, successful implementation of optical flow requires a high gradient of image intensity, and so a point on the edge of the diagonal is selected in all cases. Note that the frames in Figure 5.7 have been cropped for space constraints. For brevity, only the results from the test of specimen A are plotted here, but all results are tabulated in Table 5.2. For an idea of the intensity of the acceleration caused by the hammer impacts, the acceleration time history for the hammer impact test of Specimen A at position 1 is shown in Figure 5.8-(a) while the displacement record obtained from the vision-based method is shown in Figure 5.8-(b). Note, for optical flow, the extracted displacements can be converted to length units using known dimensions of object visible in the field-of-view of the camera. For this study, it is not necessary to determine the magnitude of displacement since only the frequency of vibration is desired. Accordingly, the displacements obtained from optical flow are left in terms of pixels. The FFT plots for the tests of Specimen A at each camera position are shown in Figure 5.9, where the light-blue line represents the frequency content from the vision-based method, while the black line represents the frequency content from the accelerometers. Note, the amplitude spectrums for the superimposed FFTs were

normalized by dividing the values by the standard deviation so the two spectra would have similar scales and to facilitate visualization. Thus, the units on the y-axis of the spectra are arbitrary.

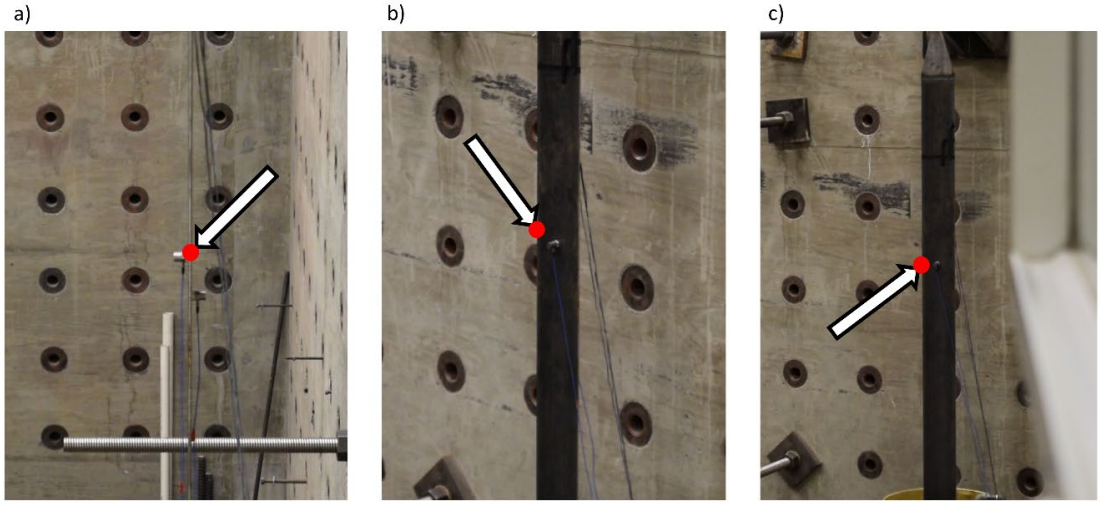

Figure 5.7 Camera field of view of specimen A at a) position 1 b) position 2 and c) position 3. Tracked points indicated with arrows.

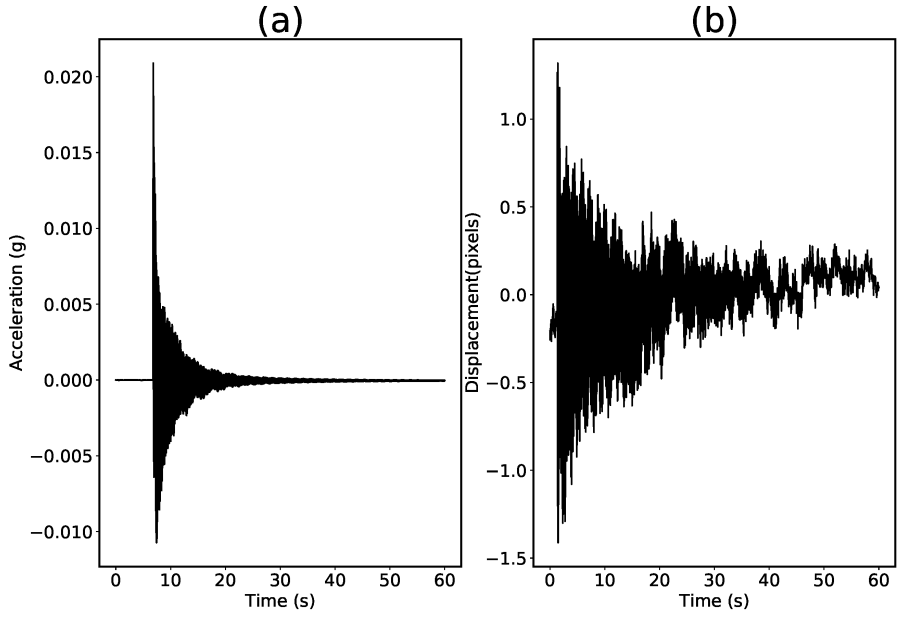

Figure 5.8. (a) Acceleration record from accelerometer and (b) displacements from optical-flow for hammer impact test at camera position 1 on specimen A.

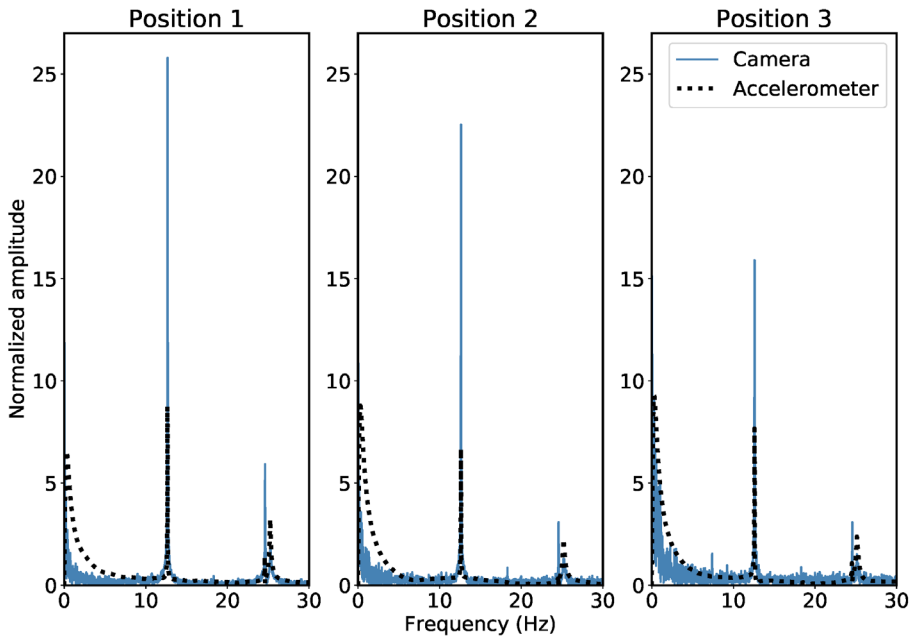

Figure 5.9. FFTs for hammer impact test of specimen A.

Table 5.2 Hammer Impact Results.

Specimen	Position	Fundamental Frequency Accelerometer (Hz)	Fundamental Frequency Optical Flow (Hz)	Reference Tension MPa (ksi)	Tension Eq. (5.7) MPa (ksi)
A	1	12.65	12.66	167.6 (24.31)	183.2 (26.57)
	2	12.62	12.63	166.8 (24.19)	182.3 (26.44)
	3	12.58	12.60	166.3 (24.12)	181.4 (26.31)
B	1	12.96	12.98	168.2 (24.39)	188.9 (27.40)
	2	12.93	12.95	167.2 (24.25)	188.0 (27.27)
	3	12.90	12.93	166.6 (24.16)	187.5 (27.19)
C	1	12.82	12.82	170.5 (24.73)	173.5 (25.16)
	2	12.78	12.80	170.4 (24.71)	173.1 (25.10)
	3	12.77	12.78	169.3 (24.55)	172.4 (25.01)

As seen in Figure 5.9 and Table 5.2, for all specimens, the frequencies obtained using the optical flow method closely match the values obtained from the accelerometers. The maximum error between the two frequency values is found for the test of Specimen B at position 3, with an

error of 0.23%. Using Eq.(5.7) to find the tension from the measured frequencies, there is an error in the estimated tension values for specimen A of about 9%, specimen B of 12%, and Specimen C of about 2%. The discrepancy is the result of the fact that Eq. (5.7) assumes a prismatic section, and is addressed in section 5.7. The larger error seen in specimen B may be caused by incidental bending, torsion, or differences in the end connectivity which are difficult to exactly match from specimen to specimen, all of which may be expected in the field. Nevertheless, the difference between recorded tension and calculated tension is acceptable for this application.

The results show that for high amplitude vibration, the angle of the camera has little effect on the ability to determine the frequencies of vibration. However, as the camera gets further away, the signal to noise ratio for the vision-based technique gets smaller until at position 3 (9.78m away from the specimen) the amplitude of vibration at the fundamental frequency is of a similar magnitude to the low frequency noise that is also captured. To eliminate some of the noise in the signal, the researchers take the approach as described earlier by subtracting the amplitude spectrum of a tracked stationary point. Note, subtracting two amplitude spectra has the possibility of generating negative amplitude values, and so, only positive values are inspected. The amplitude spectrum of the test performed at position 3 with the noise signal subtracted is shown in Figure 5.10. As seen, when compared to the results for position 3 in Figure 5.9, this simple subtraction technique has largely eliminated the low frequency noise.

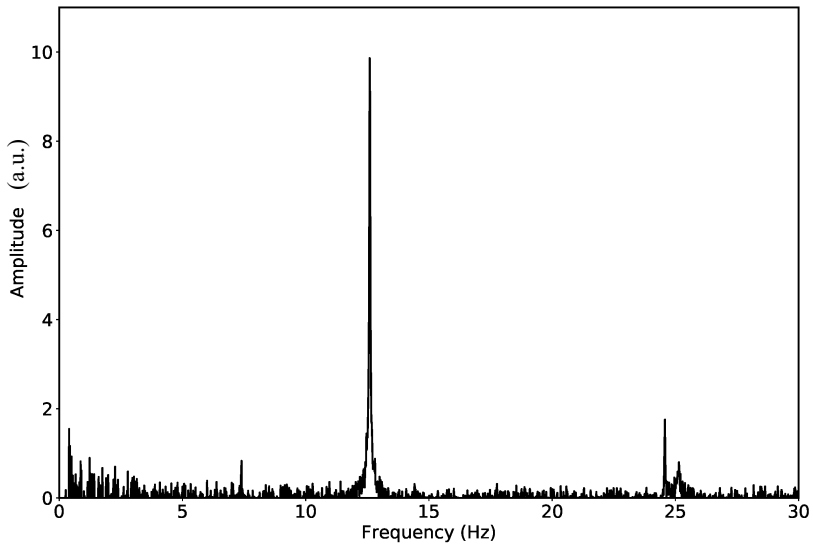

Figure 5.10 Noise removed from vision-based FFT of Specimen A at camera position 3 by subtracting out stationary signal.

5.6.2. Ambient Vibration Results without zoom lens

For the test with ambient vibration, the field of view and tracked points of the cameras is similar to that seen in Figure 5.7. The accelerometer time history and the displacement record obtained from optical flow are shown in Figure 5.11-(a) and (b) respectively, providing an indication of the intensity of vibration. As mentioned above, the strain gages on the test specimen stopped working when the ambient vibration tests were performed. Thus, the purpose of the ambient vibration tests is to determine whether or not the vision-based method is capable tracking motions with very small amplitude such as may be expected in the field. For the ambient vibration tests, only specimen A was tested, as it has an acceptably high difference between the strong-axis and weak-axis moments of inertia. This difference will allow the investigation into whether or not the vision-based method can distinguish between the strong and weak axis vibrations for camera angles where both directions are visible. The FFTs for the ambient vibration tests are shown in Figure 5.12, normalized as before by dividing the standard deviation.

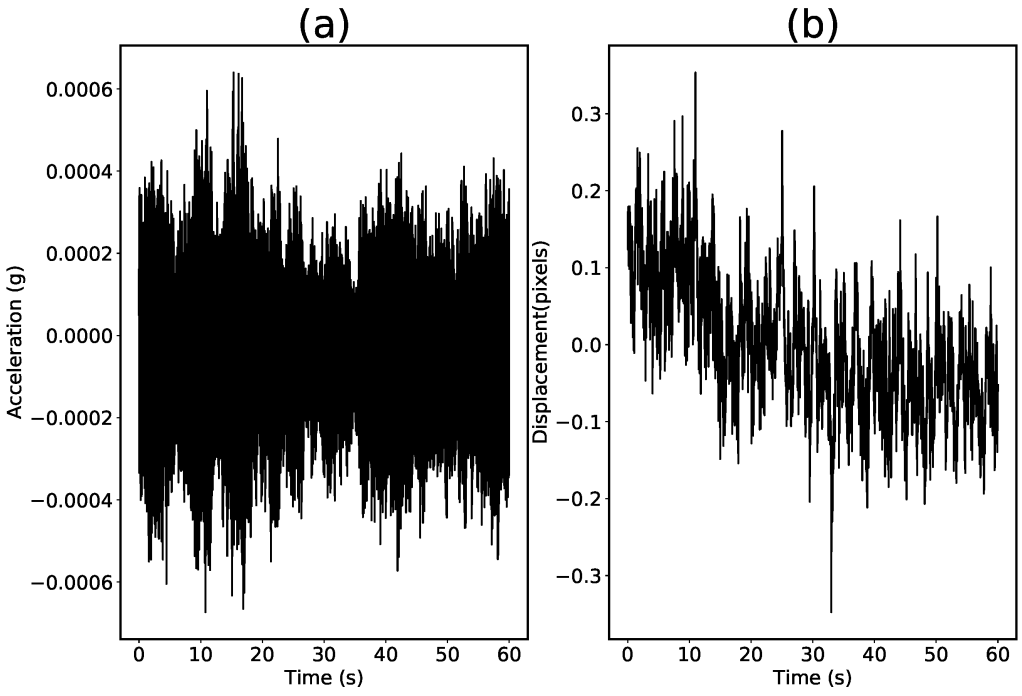

Figure 5.11. (a) Acceleration record from accelerometer and (b) displacement from optical flow for ambient vibration test of specimen A at position 1.

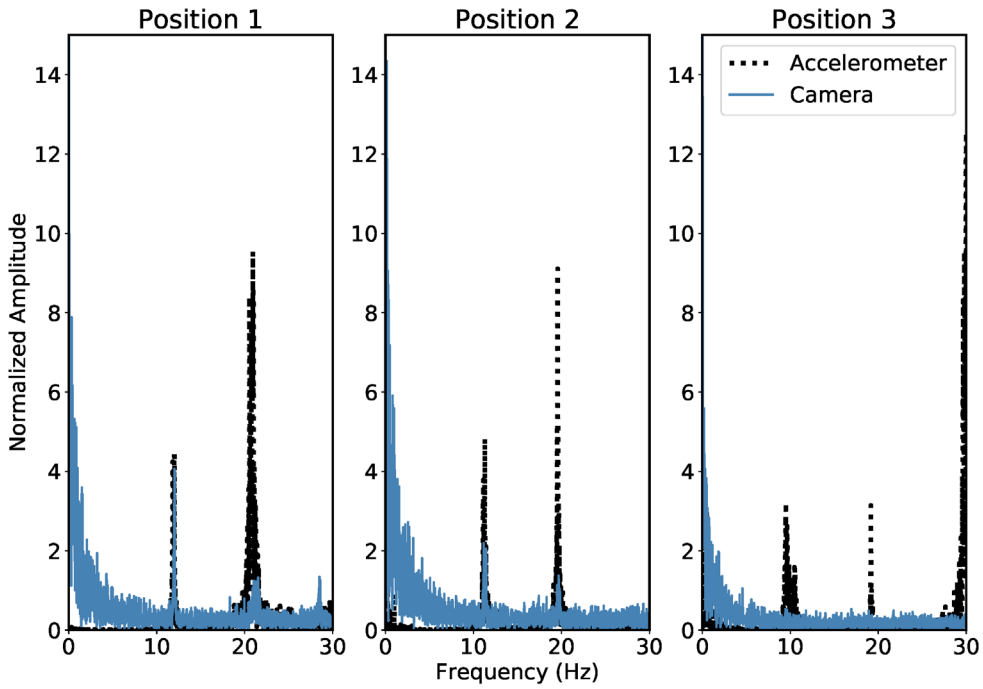

Figure 5.12. FFTs of ambient vibration tests.

As seen, even with the very low amplitude vibration the vision-based method performs well in Position 1 and Position 2, with an estimated fundamental frequency nearly identical to that estimate using accelerometers. At an angle of 65 degrees and a distance of 9.78m (position 3), the vision-based method is unable to detect the frequencies of vibration using ambient excitation. Using the estimated fundamental frequency from position 1 of 11.9 Hz, the tension in the beam is estimated to be 161.3 MPa (23.4 ksi) for a fixed-pinned beam. Utilizing the estimated tension in the beam, the strong-axis frequency of vibration is expected to be on the order of 21.3 Hz, and so, strong-axis vibration was not detected in any of the tests. The peaks near 20 Hz are the second harmonics of the weak-axis vibration, as corroborated by the accelerometer.

Recall that the ambient vibration is induced by means of filling the submersion chamber that surrounds the diagonal specimen with water. The results from this test show that, as the water used for ambient excitation filled the submersion chamber from the test at position 1 to the test at position 3, the frequency of vibration of the beam was seen to decrease (refer to the steadily decreasing frequency of vibration in Figure 5.12 from position 1 to position 3). Moreover, there is a notable decrease in frequency as compared to the hammer test results shown in Figure 5.9. This change is due to the fact that the hammer tests were performed when the submersion chamber was

empty, whereas the ambient vibration tests were performed when the submersion chamber was between one quarter and half full. Accounting for the effects of submersion is addressed in section 5.7.

5.6.3. Ambient vibration with zoom lens

The same ambient vibration tests as above were performed with the camera utilizing the zoom lens. The field of view as seen from the camera at each position is shown in Figure 5.13, with the manually selected tracked points highlighted by white arrows. Note again the selection of points on the edge of the diagonal to facilitate successful implementation of optical flow. The FFTs for the three positions are shown in Figure 5.14, normalized as before. For all three positions, the zoom lens facilitates readily capturing the fundamental frequency. It is noted that the vibration of the camera was a much bigger factor when utilizing the zoom lens, and all the records have significant frequency content around 18 Hz. This 18 Hz frequency is found to be vibration from the camera because, tracking a known stationary point on the laboratory strong-wall at position 2, for instance, the FFT shows large frequency content near 18 Hz (Figure 5.15-(a)) which must be due to camera movement. Removing this noise signal from the camera has proven challenging. Utilizing the authors' preferred method of subtracting the FFT shown in Figure 5.15-(a) from that shown in Figure 5.14, the results are seen in Figure 5.15-(b), with the frequency content at around 18 Hz not completely removed. Figure 5.15-(c) shows the results of subtracting the displacement record as suggested by Kim and Kim (2013) and Luo, et al., (2018) with inferior results. In as much as a human is required in the loop for this methodology to choose a location of interest to track, it is sufficient to manually inspect the frequency content of a tracked stationary point to determine what frequencies to ignore. Recall from the previous section that the strong-axis vibration is expected to be on the order of 21.3 Hz. The frequency content near 21 Hz at Position 1 cannot be the strong axis frequency content because a) it is captured also by the accelerometers which do not measure in the strong-axis direction and b), the strong axis direction of vibration is not visible to the camera in position 1. Therefore, again, the strong axis frequencies are not detected in these tests. To quantitatively assess the performance of optical flow, double integration was performed on the acceleration record shown in Figure 5.11-a. The typical peak-to-peak displacement of the diagonal specimen subjected to ambient vibrations was on the order of 1.2 cm (0.5 in). At an angle of 65 degrees, an image resolution of 1080p and a zoom lens with a focal length of 200mm, optical flow performed well.

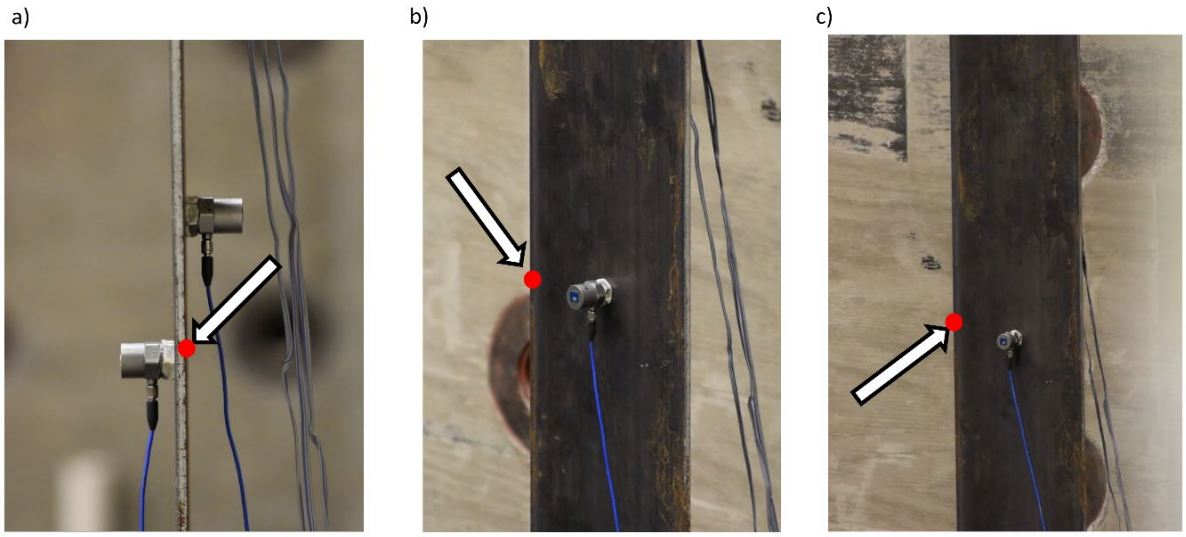

Figure 5.13. Field of view of the camera with zoom lens at (a) position 1, (b) position 2, and (c) position 3.

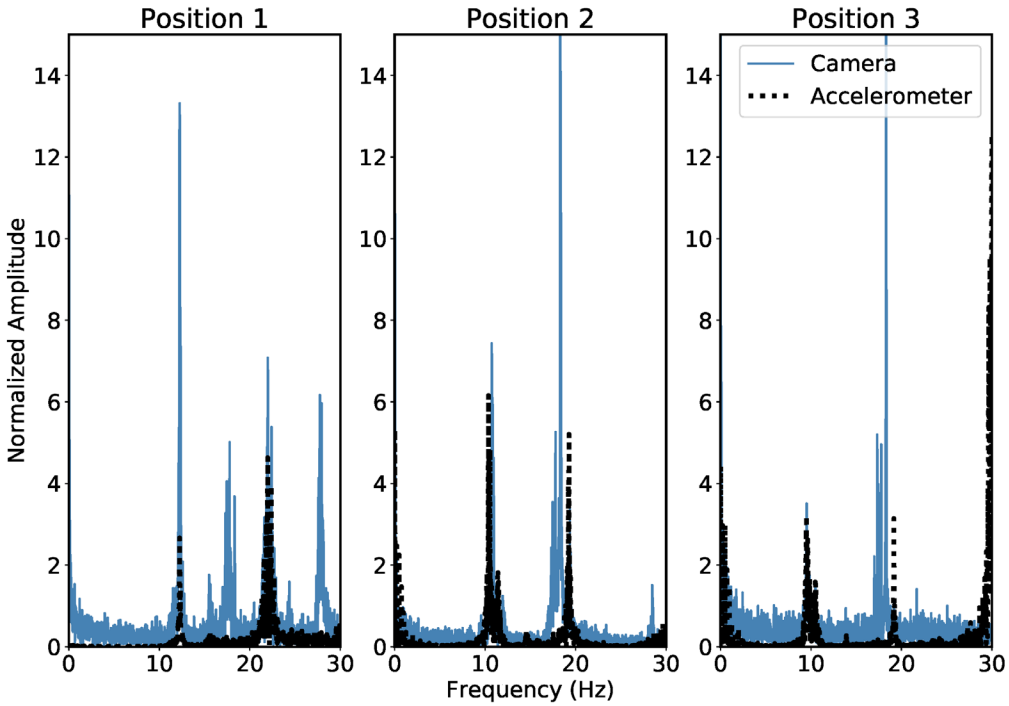

Figure 5.14. FFTs for zoom lens with ambient vibration.

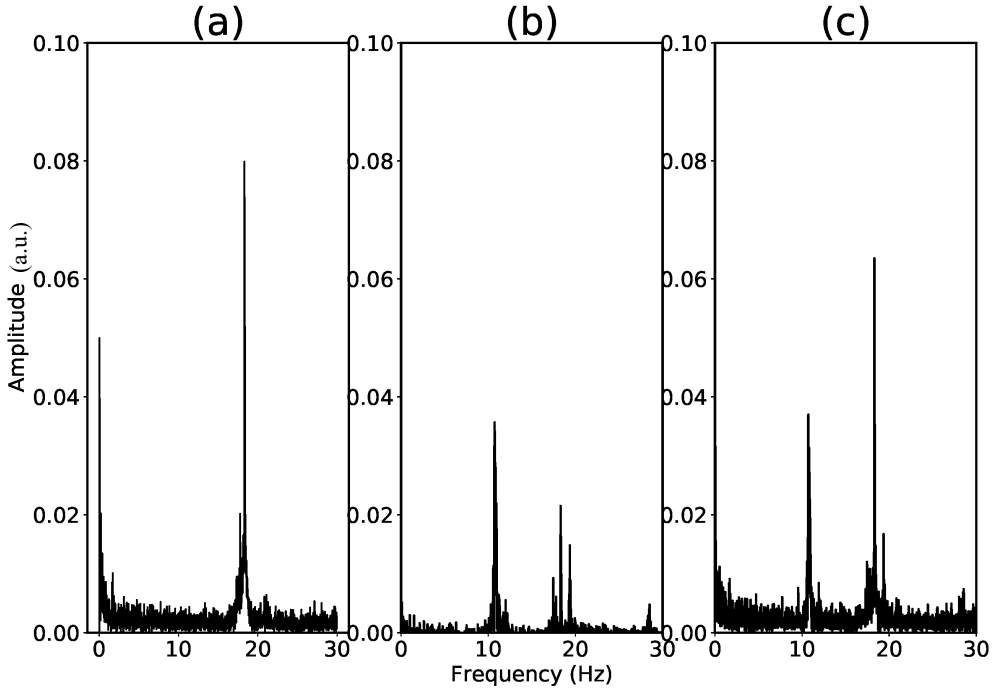

Figure 5.15 (a) Frequency content of tracked stationary point using zoom lens (b) noise removal of FFT by subtracting frequency amplitude and (c) subtracting displacement records for position 2.

Experimental results using the vision-based approach show excellent agreement between the frequencies of vibration measured via optical flow, and those obtained using accelerometers. Results were exceptional, even when the camera was far away and the diagonal was subjected to low amplitude vibration caused by flowing water, particularly when a zoom lens was utilized. However, tension values shown in Table 5.2 highlight the need to explicitly consider the non-prismatic nature of the beams. Moreover, the decrease in frequency between the results shown in Figure 5.9 (for an unsubmerged beam) and results shown in Figure 5.12 (for a partially submerged beam with the same tension) highlight the need to explicitly consider the effects of partial submersion of the frequency of vibration of the diagonals. Thus, the next step is to validate the approximate approach described in section 5.3 to modeling partial submersion of miter gate diagonals.

5.7. Validation of partial submersion model

The next step in the experimental analysis was to validate the approximate method of modeling the effect of partial submersion of pretensioned miter gate diagonals. Validation is performed by exciting the partially submerged diagonals and measuring the frequency of vibration with the

attached accelerometers. Then using the approximate assumed modes method, an iterative inverse approach was utilized to determine the tension in the diagonal given the known length over which the diagonal was submerged and the measured frequency of vibration. The reference tension, as measured by the installed strain gages, was recorded and compared to the calculated tension. Over the course of testing at certain levels of submersion, exciting the lower modes with a hammer impact proved difficult; using a small rope tied near the center of the specimen and plucking the specimen provided best results. Each specimen was tested at five different tension levels as listed in Table 5.3. For each level of stress, the beam was submerged to five different levels as listed in Table 5.3 and noted in Figure 5.4. Thus, a total of 25 tests were performed for each of the three specimens. For simplicity, the height of the individual 55 gallon drums was used as a marker for each level of submersion, with each drum being approximately 83.8 cm (33 in.) tall. When testing, the expected fundamental frequency of vibration for all tests is not expected to exceed 14 Hz, and so a sampling frequency of 256 Hz was selected for the accelerometers, which will allow for the measurement of several harmonics for each test. To obtain the frequencies of vibration, a fast Fourier-transform (FFT) is performed on the recorded acceleration record, and peaks in the record are manually selected.

Table 5.3 Tensile stress and water heights used to verify model of partial submersion.

Tensile stress levels, kN (kips)	38.92, 77.84 116.77 155.69 194.6 (8.75, 17.5, 26.25, 35.0, 43.75)
Height of water, cm (in.)	83.8, 167.6, 251.5, 335.3 (33, 66, 99, 132)

For each test, up to the first five frequencies of vibration are extracted from the FFT of the acceleration record. Note that in several instances, the frequencies of a particular harmonic of the beam's vibration are difficult to determine from the FFT, possibly due to the frequency of that harmonic nearly resonating with the frequency of vibration of the global test setup. In other instances, the amplitude of a particular harmonic is quite small, likely due to the placement of the accelerometer near the node for that mode of vibration. An example of an FFT displaying both of these characteristics (closely spaced peaks, and very low amplitude peak), is shown in Figure 5.16, which is the amplitude spectrum from the accelerometer data for specimen 1 at 137.9 MPa (20 ksi) stress and with 335.3 cm (132 in.) of water. Note, as accelerometer data is used for Figure 5.16,

the full range of data up to the Nyquist frequency of 127.5 Hz is shown. The numbers in the plot correspond to the frequency of the n^{th} mode of vibration, as determined by a peak-picking algorithm. In this case, several closely spaced peaks are seen near where the second mode is expected. Similarly, the amplitude for the peak near where the fifth mode is expected is very small. Accordingly, for this test, the second and fifth modes cannot be determined and are marked as N/A.

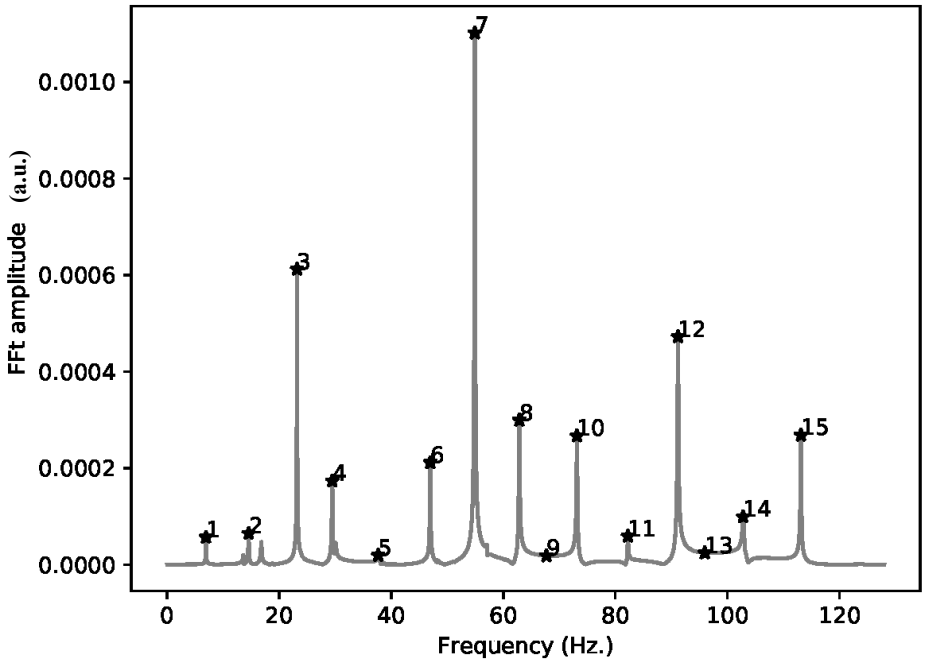

Figure 5.16. Amplitude spectrum of accelerometer data for test specimen 1 at 137.9 MPa (20 ksi) and 335.3cm (132 in) of water.

To validate the notion that added mass is the primary driver for a change in the frequency of vibration, the extracted frequencies from the experimental data are compared to the frequencies calculated using the proposed approach. Note, for specimens 1 and 2, the added mass used in Eq. (5.20) is the value for a thin plate (Eq. (5.11)). For specimen 3, the aspect ratio of the cross-section is a rectangular prism, and so the added mass from Eq. (5.12) is used. For all specimens, the bending stiffness varies across the length of the bar due to the changing cross section, as seen in Figure 5.3. Taking the left end connection shown in Figure 5.3 as the datum, each specimen is comprised of the following: a circular cross-section from 0 cm to 7.62 cm; a tapered region with varying cross section from 7.62 cm to 33.0 cm; a constant rectangular cross section from 33.0 cm to 576.5 cm; a tapered region with varying cross-section from 576.5 to 601.9 cm; a constant circular cross section from 601.9 cm to 609.5 cm. The moments of inertia from the regions with

constant cross section are readily obtained from the dimensions in Table 5.1. The moments of inertia for the tapered sections, labeled $I_a(x)$ and $I_b(x)$ in Figure 5.3, are functions of the position on the beam, *x,* and thus need to be incorporated into the integral in Eq.(5.17). Approximate functions describing $I_a(x)$ and $I_b(x)$ with respect to the datum previously described are listed in Table 5.4.

Table 5.4 Functions describing the varying moment of inertia of the tapered section for the test specimens.

Specimen	Functions of $I_a(x)$ and $I_b(x)$ (x in cm)
1	$I_a(x) = \frac{1}{12}(0.567x - 0.966\ cm)(-0.107x + 4.178cm)^3$ $I_b(x) = \frac{1}{12}(-0.567x + 345.112\ cm)(0.107x - 61.225cm)^3$
2	$I_a(x) = \frac{1}{12}(0.217x + 1.701\ cm)(-0.082\ x + 3.987\ cm)^3$ $I_b(x) = \frac{1}{12}(-0.217x + 134.419\ cm)(0.082x - 46.175\ cm)^3$
3	$I_a(x) = \frac{1}{12}(0.043x + 3.035\ cm)(-0.032x + 3.606\ cm)^3$ $I_b(x) = \frac{1}{12}(-0.043x + 29.072\ cm)(0.032x - 16.076\ cm)^3$

A key component in the assumed modes method is to ensure that the solution obtained is sufficiently converged. That is, the frequency of vibration obtained via assumed modes will always be higher than the true value. As more modes are considered in the analysis, the calculated frequency will converge to the true value from above. Thus, it is critical to ensure that an adequate number of modes is considered such that the solution is sufficiently converged. For this study, the convergence behavior of the approximate method is visually inspected by plotting the solution of the eigenvalue problem versus the number of modes considered in the problem formulation. For most of the test scenarios considered, the solution appears to converge rapidly, after less than 10 modes. Figure 5.17 shows the convergence behavior of the first three modes of specimen one when subjected to 155.69 kN (35 kips) tension and submersion of 251.5 cm (99 in), with the rapid convergence of the solution apparent. For the scenarios of the specimens subjected to 38.92 kN (8.75 kips), the convergence of the solution is less rapid. This is highlighted in Figure 5.18, which shown the convergence behavior of the first three modes for specimen 1 subjected to 38.92 kN

(8.75 kips) of tension and 83.8 cm (33 in) of submersion. For all cases, applying the proposed approximate method by considering 20 modes in the problem formulation produced sufficiently converged results.

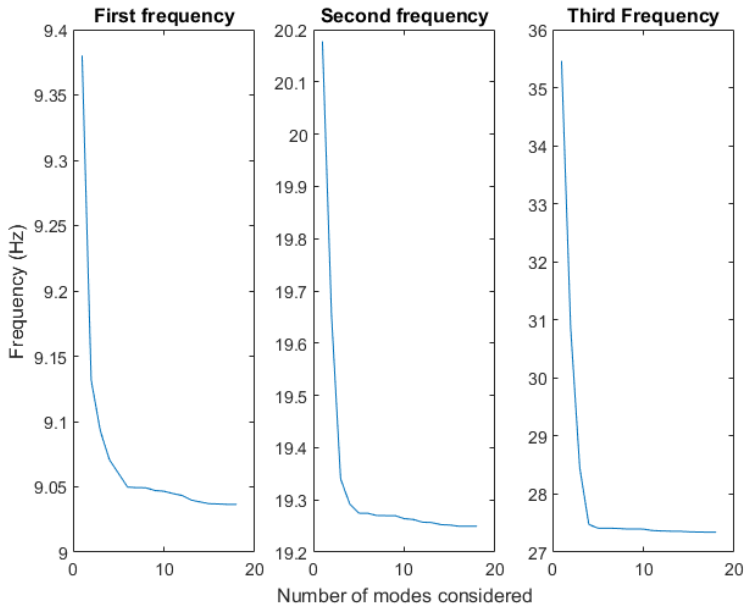

Figure 5.17. Convergence behavior of first three modes for specimen 1 with 155.69 kN (35 kips) tension and submersion of 251.5 cm (99 in).

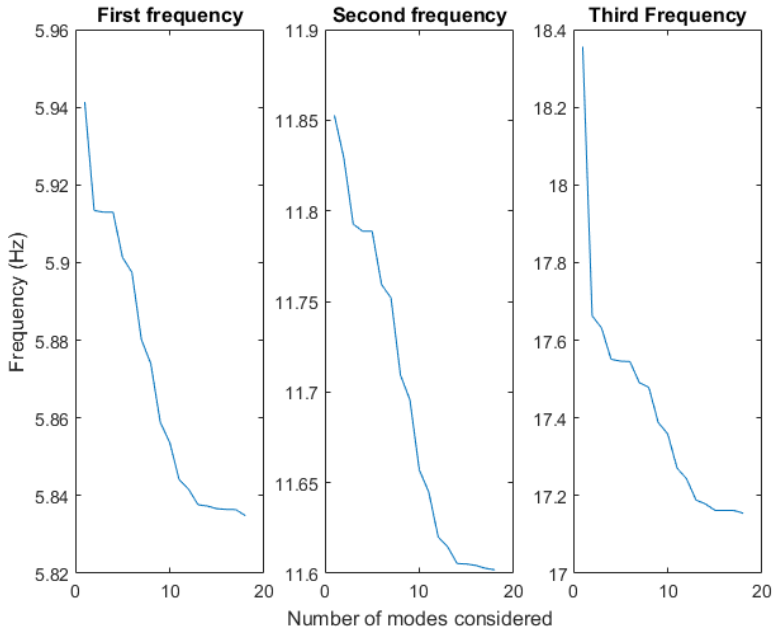

Figure 5.18. Convergence behavior of first three modes for specimen 1 at 38.92 kN (8.75 kips) and 83.8 cm (33 in) of submersion.

Twenty modes were considered and the frequencies of vibration were calculated for all the scenarios tested in the lab. Figure 5.19 through Figure 5.21 show a comparison between the calculated frequencies from the proposed method and the experimentally measured frequencies. In the plots, the *x*-axis represents the calculated frequencies using the method of assumed modes, while the *y*-axis represents the experimentally measured frequencies. A line is also provided on each plot for ready comparison; if the proposed method considering added mass does a good job of explaining the effects of submersion on the frequencies, then all points on the plots should lie near the y=x line. In each of the figures, the individual plots show the comparison for all levels of submersion for one level of pretension, with the levels of submersion represented by different point markers. The first five modes for each level of submersion are plotted simultaneously. Markers on the plot lying along a y =0 line are those locations where a particular frequency could not be determined from the measured data, such as for the previously described scenario for the test of specimen 1 at 137.9 MPa (20 ksi) and 335.3 cm (132 in) of water.

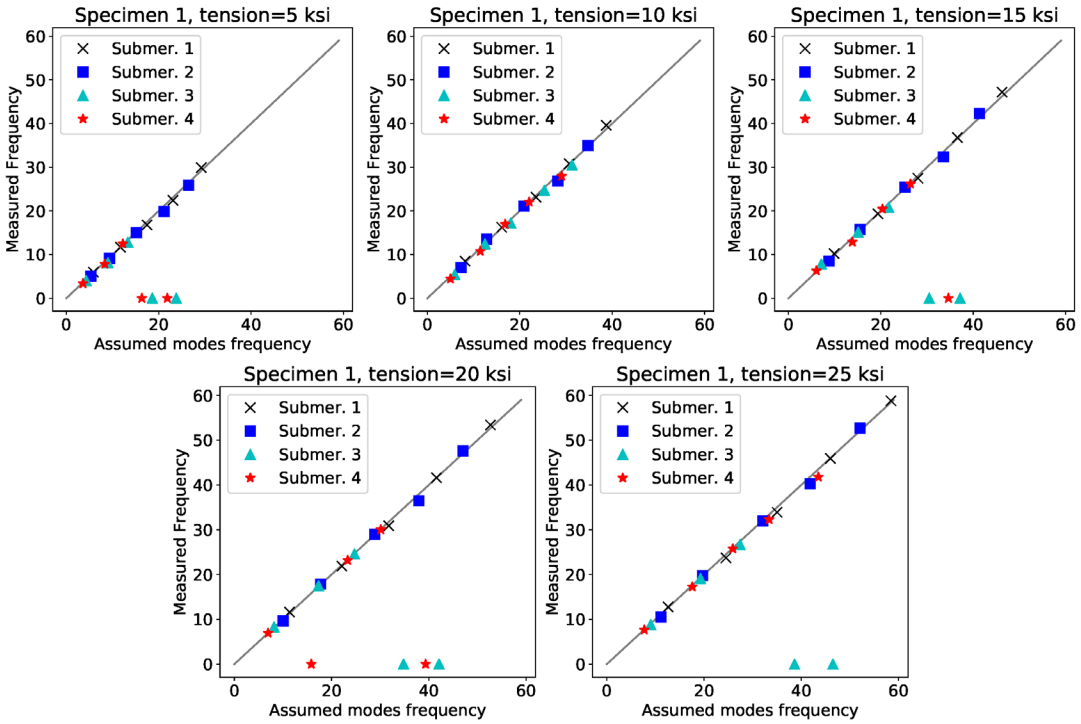

Figure 5.19. Comparison of first five frequencies of vibration for specimen 1. Each plot is specimen 1 and a specific tension value. Different markers represent levels of submersion

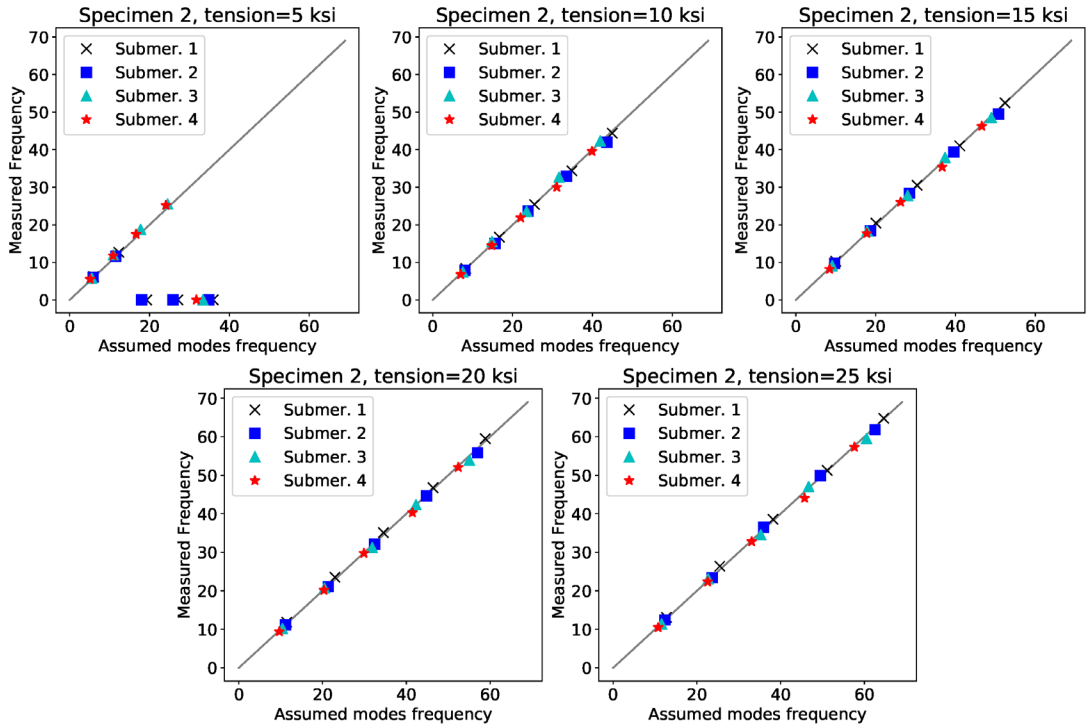

Figure 5.20. Comparison of first five frequencies for specimen 2. Each plot is of specimen 2 at a specific tension value. Different markers represent levels of submersion.

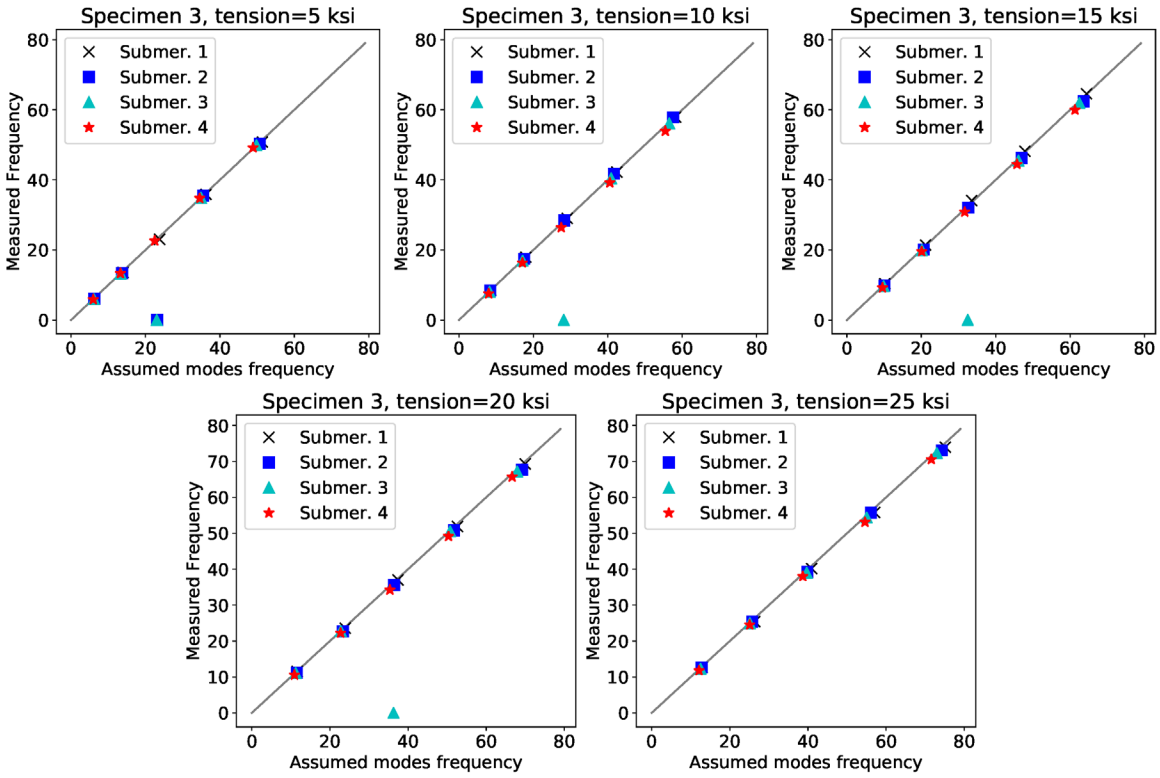

Figure 5.21. Comparison of first five frequencies for specimen 3. Each plot is for specimen 3 at different tension values. Different markers represent levels of submersion.

As seen in the figures, considering only the added mass due to the presence of water adequately describes the effects of submersion on the fundamental frequency. That is, the estimated frequency using the assumed modes shape matches very closely to the measured frequency. Note that similar results were found by considering a simplified geometry over the tapered region of the diagonal specimen where half of the tapered region was assumed to be comprised of the circular cross-section and the other half was assumed to be comprised of the rectangular cross-section. This simplification came with the benefit of significantly increased computational time of the integrals necessary for determining the bending stiffness matrix. For field operations, the small increase in accuracy gained by accurately modeling the tapered region of diagonals with similar geometry may not be worth the increased computational effort.

While the results for the frequency comparison is promising, the primary interest of this study is to be able to measure the tension in a partially submerged miter gate diagonal by measuring only the diagonal dimensions, submerged length, and fundamental frequency of vibration. To find the tension given the measured parameters, and iterative inverse approach is used where the frequencies of vibration for a range of tension values given the submerged length are calculated. Then, the tension that corresponds to the calculated frequency that is nearest to the measured frequency for a given submersion length is used as the tension in the diagonal. This is performed for all test specimens and the reference tension values obtained via the strain gages are plotted versus the calculated tension using the proposed method in Figure 5.22. The results of the proposed approach are typically within 5% of the measured value. The notable exception with less than ideal results is Specimen 1 for the tests with a target tension of 116 MPa.

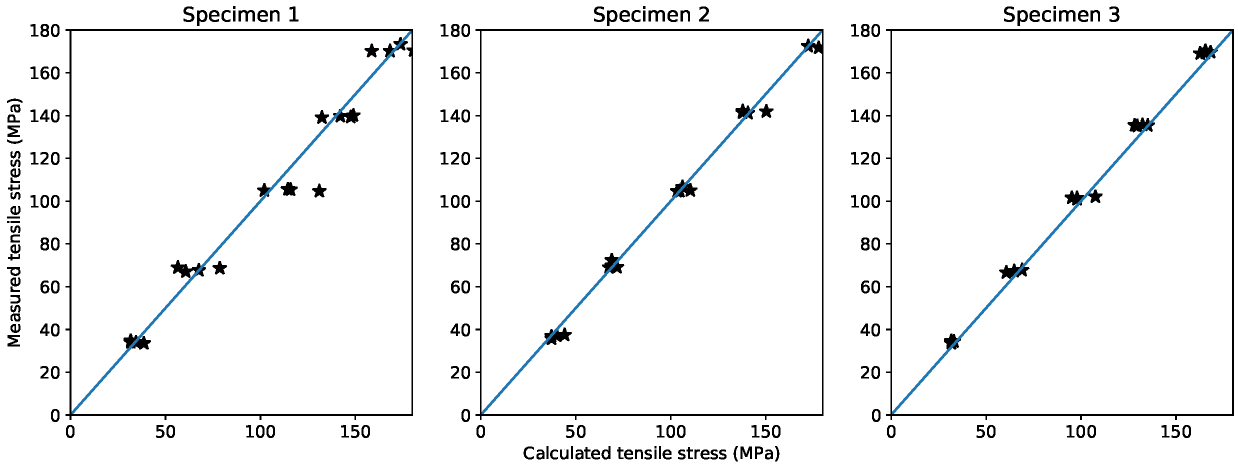

Figure 5.22. Comparison of measured tension and calculated tension for test specimens.

5.8. Field Validation

To test the efficacy of the proposed approach in the field, as well as validate the vision-based method, video was taken of the diagonals of the Greenup Lock and Dam miter gate while the gate was in operation. The miter gate at Greenup is the miter gate in the SMART Gate system with functioning load cells to monitor the tension in the diagonals, allowing the comparison of results found via the proposed approach with readings from the load cell. The same camera used in the lab was used in the field, and the camera was placed on a tripod on the lock chamber wall and pointed at the diagonals with a zoom lens. Figure 5.23-(b) shows the field-of-view of the camera in the field test, with the location of the field of view on the gate noted in Figure 5.23-(a).

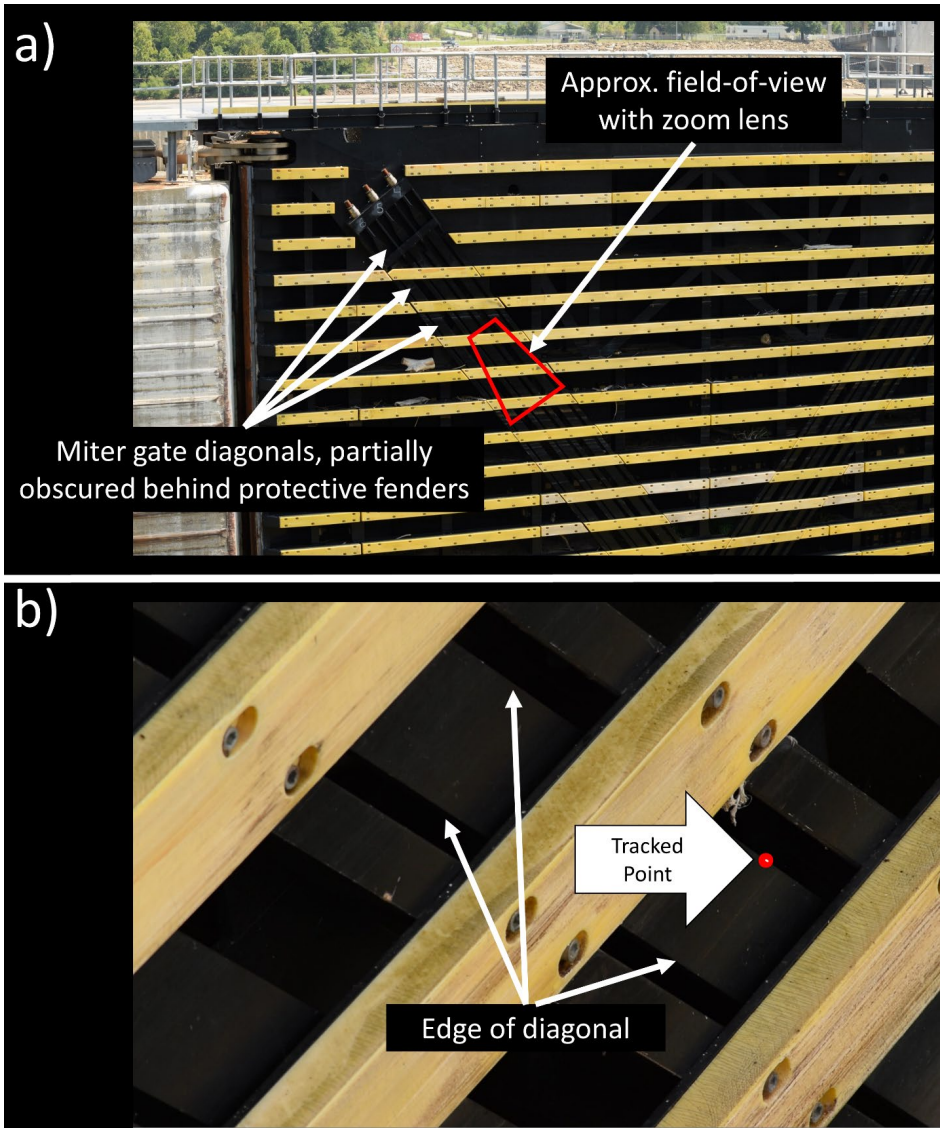

Figure 5.23. a) The Greenup miter gate on the day video was captured. b) The field-of-view of the camera placed on the lock chamber wall.

For the vision-based method to be effective, the best results were obtained as the gate swung closed and immediately after the two leaves of the gate came in contact with each other. This small impact provided adequate excitation to the diagonals for the optical flow method to track. The vision-based approach was applied to the captured video and the raw displacement record as tracked by optical flow is shown in Figure 5.24-(a), normalized by subtracting the mean. A high-pass Butterworth filter was applied to the displacement signal with a cutoff frequency of 1.0 Hz, and the filtered displacement record is shown in Figure 5.24-(b). An FFT was applied to the filtered displacement record to determine the frequencies of vibration. The resulting fundamental frequency is found to be 2.7 Hz, as shown in Figure 5.25, while the second peak of 6.3 Hz is a reasonable value for the second harmonic of the beam.

The Greenup diagonals are 22.5 m (886.5 in.) in length, with a cross section of 17.8 cm X 3.18 cm (7.0 in. X 1.25 in). As one of the newer gates on the Ohio River, the diagonals utilize the same super-nut jackbolt connections as those tested in the lab, and so fixed-pinned boundary conditions are assumed. Using the proposed method with the measured vibration frequency of 2.7 Hz, and a measured length of submersion of 556 in, the tensile load is determined to be 895.2 kN (201.25 kips). The load cell on the diagonals at the time of testing read 862.9 kN (194 kips), resulting in an error of 3.7% for the proposed method. Note, using beam theory and ignoring the effects of submersion on the frequency of vibration, the tension in the diagonals is calculated to be 630.5 kN (141.75 kips), for an error of 26.9%. It is particular interesting to note the poor contrast between the diagonals seen in Figure 5.23-(b) and the rest of the miter gate. That is, the diagonal whose displacement is tracked has a color that is very similar to the rest of the gate. Even with these relatively poor conditions, the vision-based method performed adequately.

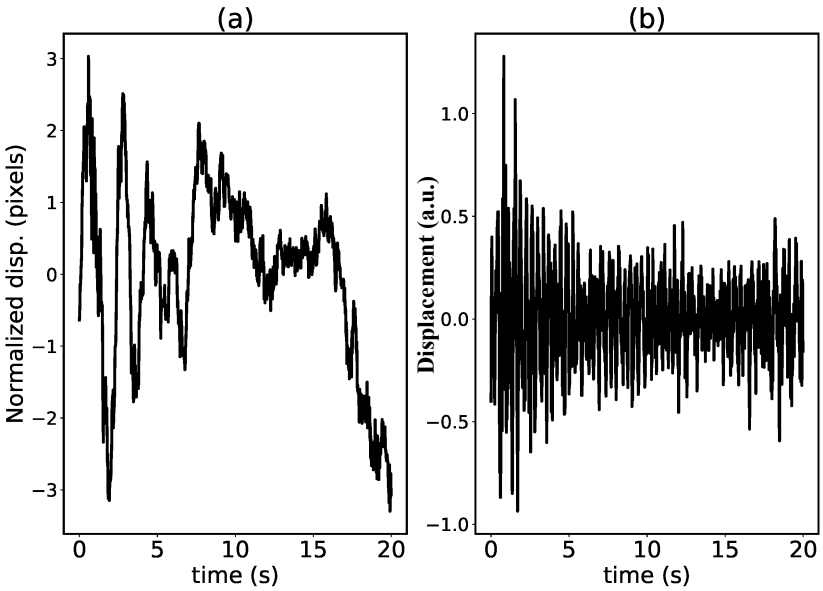

Figure 5.24. a) Raw displacement of tracked point of Greenup diagonal. b) Filtered displacement of tracked point.

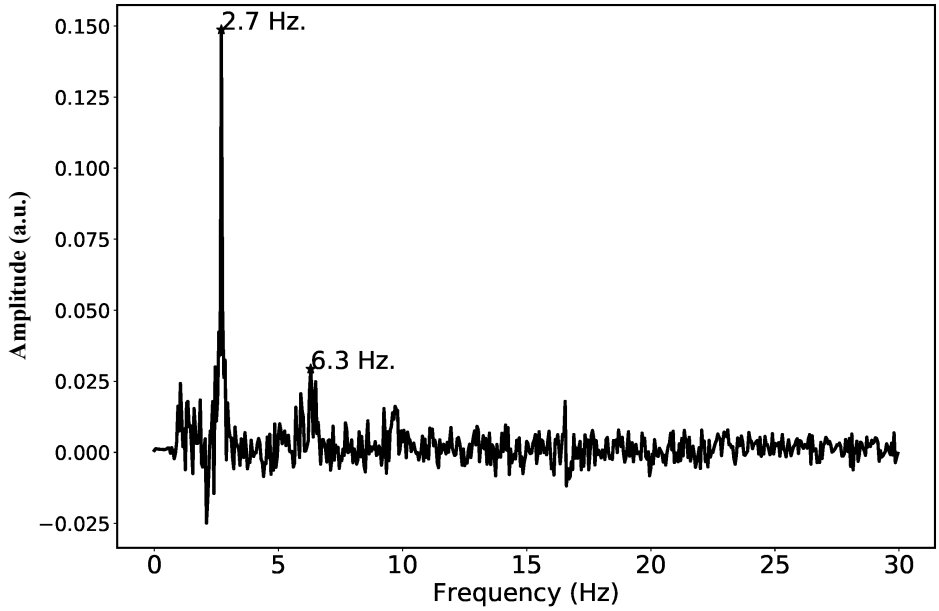

Figure 5.25. FFT of displacement of Greenup diagonal.

5.9. Conclusions

Diagonals are components of miter gates that are pretensioned to overcome the torsional twist of the gate due to the eccentricity between the self-weight of the gate and the shear center. Maintaining an appropriate level of tension in the diagonals is critical to extending the useful life of the gate, as inappropriately tensioned diagonals can lead to accelerated fatigue damage or increased likelihood of vessel impacts. Currently, there is no method used to regularly monitor the

tension in miter gate diagonals. Vibration-based methods to monitor the tension are attractive, but the nature of the diagonals poses difficulties: the diagonals are difficult to access, they are generally partially submerged, and they are generally not prismatic. This study investigates the use of a vision-based method utilizing Lucas-Kanade optical flow as a non-contact, virtual sensor to indirectly monitor the tension in the diagonals of miter gates. The vision-based approach will overcome the difficulty in accessing the diagonals by allowing a user to measure the tension in the diagonals via video of the vibrating diagonal taken from the lock chamber wall. To address the effects of partial submersion, it is found that the water surrounding the diagonal can be modeled as added mass to the diagonal. Then, the approximate assumed modes method is used to determine a relationship between the frequency of vibration of the diagonals, the tension in the diagonal, and the length over which the diagonal is submerged. The vision-based method, and the approximate method of modeling the effects of partial submersion, are validated by both scale model experiments and field-based measurements of the diagonals of an in-service miter gate.

For the vision-based method, the proposed approach is a human-in-the-loop method expected to be performed periodically wherein points to be tracked are manually selected by the user. The periodic nature of the measurements addresses typical limitations of vision-based methodologies in that the user can simply wait for acceptable lighting conditions. For successful implementation, the user should select a point on the diagonal along the edge, as this will have an acceptably high image intensity gradient. Miter gate diagonals are rectangular sections with notably different weak and strong axis frequencies of vibration. The authors demonstrate the ability of optical flow to track the weak-axis vibrations of scale model miter gate diagonal at various camera angles and distances. When the amplitude of vibration is relatively high, the vision-based method performs very well, even at relatively far distances. When the amplitude of vibration is relatively low, the vision-based method struggles when offset from the direction of vibration, and placed at a far distance; however, when a zoom lens is utilized, the optical flow method is readily able to determine the frequencies of vibration from all positions tested, even for low amplitude vibrations. Quantitatively, the camera place at the sharpest angle of 65 degrees, at a distance of 9.8m, an image resolution of 1080p, and a zoom lens with a focal length of 200mm, optical flow was able to track displacements on the order of 1.2cm, which correspond to the smallest displacements measured in this study. The authors found that, for positions where the strong-axis vibration would be readily visible to the camera, it was not detected which simplifies determining the tension in the beam, as

it is easier to interpret the FFT results. For ambient vibration tests, noise was a persistent issue, especially when a zoom lens is utilized. Noise reduction techniques consistent with the literature were utilized; however, the authors found better success by subtracting the amplitude spectrum of the stationary point from the amplitude spectrum of the region of interest.

Experimental data was then used to validate the notion that the effects of submersion on the frequency of vibration of the diagonal can be largely accounted for by added mass due to water. The scale model specimens were excited and the first five frequencies of vibration were calculated from the displacement record. In all cases, the experimentally obtained frequencies of vibration matched the calculated frequencies obtained using the proposed approximate method. The exceptional agreement in the data corroborates the notion that the primary effect of submersion of the frequency can be modeled as added mass. To calculate the tension in the specimens using the measured frequency and submerged length of the beam, an iterative inverse approach is utilized where frequencies of vibration are generated for several tension values given a length of submersion. Then, the tension that matches the combination of submerged length and nearest value of frequency of vibration is taken as the tension in the beam.

Uncertainty exists in the boundary conditions of miter gate diagonals. For miter gate diagonals similar to the test specimens used in this study, meaning they have tapered end section and are tensioned with multi-jack-bolt tensioning nuts, best results were obtained by considering the diagonals to be fixed-pinned. This choice of idealized boundary conditions is reasonable, as the connections on the ends of the beam do not provide symmetric boundary conditions. Using the iterative inverse approach, the tension in the scale-model test specimens was able to be calculated within 5% for all but one set of tests.

Field validation was performed by utilizing vision-based vibration measurement of an in-service miter gate diagonal at the Greenup Lock and Dam. The diagonals at the Greenup Lock and Dam are instrumented with load cells to monitor the tension in the diagonals, allowing for comparison of the tension found via the proposed method with that recorded by the load cell. The tension calculated using the proposed method showed excelled agreement, differing from the load cell by only 3.7%. This field validation showed that the proposed method discussed herein is viable for monitoring tension in miter gate diagonals.

Chapter 6. Detection of uneven hoisting of Tainter gates

This chapter focuses on a multi-faceted approach to detecting uneven hoisting of Tainter gates. As noted in Chapter 2, Tainter gates are radial gates that resemble a circular sector that swings up and down about a central pivot point known as the trunnion. This chapter focuses on the detection of uneven hoisting of The Dalles Tainter gate. In the initial studies, peculiarities were found in the data from the installed SHM sensor system on The Dalles Tainter gate. When the data was compared to the expected behavior of a normally operating Tainter gate gleaned from the FEA model described in Chapter 3, concern arose as to the validity of the data, the validity of the model, or possibility that The Dalles Tainter gate is already regularly hoisting unevenly. To definitively validate (or invalidate) the data and FEA model, a short-term monitoring program was subsequently devised to take measurements of the tension in each of the hoisting cables when the gate is operating. If the gate is hoisting evenly, then the tension in each of the cables should be close to identical. Following a description of the investigation into the initial sensor data, and the concerns that arose, the short-term monitoring program is discussed. The conclusion of the work herein is that, in light of multiple sources of evidence, The Dalles Tainter gate appears to be regularly hoisting unevenly, providing evidence that the employed long-term monitoring system is sensitive to the effects of uneven hoisting, and can be used for detection in the future. It is apparent that the extent of uneven hoisting is not an immediate strength concern, does not pose an immediate impact to the operation of the gate, and is indeed imperceptible to the unaided eye on site. However, the long-term effects of the redistribution of stresses caused by uneven hoisting warrant further investigation and the information gleaned herein will be useful for The Dalles lock owners and operators to make necessary adjustments to maximize the useful life of the gate.

6.1. Tainter gate problems and uneven hoisting

Tainter gates are ubiquitous structures utilized throughout the world, primarily as dam spillway gates. A number of failures of Tainter gates have been documented, and several authors have compiled treatises detailing the numbers and causes of these failures (Graham and Hilldale 2001), (Ishii, et al. 2018), (Lewin, et al. 2003). Graham and Hilldale (2001) provide a general overview of spillway gate failures that has a significant amount of information on Tainter gates. Ishii, et al., (2018) focus on investigating vibration related causes of radial gate failures. Lewin, et al., (2003) also provide some background on Tainter-type gate failures in the context of reliability. Several

instance are listed where an interruption of power to the gate operating equipment gate and/or dam failure, such as the failure of the Belci Dam in Romania in 1992 (Graham and Hilldale 2001) and the Machu-II Dam in India in 1979 (Lewin, et al. 2003). Another failure mechanism is structural design flaw, such as the failure of a Tainter gate at the Singur Dam in India due in 1970 (Ishii, et al. 2018). Vibration is expected to be a critical issues as well, such as with the Tainter gate at Wachi Dam in Japan in 1967 (Ishii, et al. 2018). While the causes of Tainter gate failures vary greatly, a critical problem (and the focus of this chapter) that can arise with the operation of Tainter gates is that the gate may hoist in an uneven or skewed fashion due to issues with the hoisting mechanism or excessive friction in the trunnion. Hoisting issues, such as uneven hoisting, can be problematic and can lead to overstressing, fatigue, or potential instability of portions of the gate. Indeed, a Tainter gate at the Picote dam in Portugal failed in 1966 when hoisting chains seized up, causing failure of a hoisting motor. The resulting uneven hoisting of the gate lead to extreme warping and the failure of the other hoisting motor, causing the gate to fall freely (Graham and Hilldale 2001). The failure of the Folsom Dam Tainter gate was due to friction in the trunnion that led to uneven hoisting of the gate and ultimately buckling of the strut-arms. Lewin, et al., (2003), list 13 other issues of Tainter gate failures due to hoisting issues.

This chapter focuses on the detection of uneven hoisting of Tainter gates, and particularly focusing on the upstream lock Tainter gate at The Dalles Lock and Dam. The functionality of the Dalles tainter gate was described in detail in Chapter 2 of this dissertation, and a picture of the Tainter gate, closed and acting as the damming surface of the lock chamber is provided in Figure 6.1 for convenience of the reader. The Tainter gate at The Dalles, like the other lock gates on the Columbia River, is critical to the U.S. economy. Closure of The Dalles lock and dam due to gate failure or unexpected maintenance can have significant economic consequences due to barge traffic stalled on the Columbia River, where US$24 Billion of commercial cargo travels annually (Gruben 2019). Accordingly, adequate and timely maintenance of The Dalles Tainter gate is of critical importance to the USACE, who owns and operates the facility. While dam spillway Tainter gates are rarely hoisted, and generally only for emergency conditions such as flood control (Kalantarnia 2013), the Tainter gate at The Dalles is fully raised and lowered several times per day. In 2012 (most recent year with data available), there was an average of six commercial vessels passing through The Dalles per day (U.S. Army Corps of Engineers 2012). Each time a vessel passes through The Dalles lock, the Tainter gate must fully swing open and closed, resulting in the

Tainter gate at The Dalles experiencing thousands of load cycles annually. Thus, even more so than dam spillway gates, the unanticipated stresses caused by potential uneven hoisting of The Dalles Tainter gate could be problematic, particularly from a fatigue standpoint.

Figure 6.1. Tainter lock gate at The Dalles, closed and acting as the damming surface to the lock chamber.

A continuous monitoring system was installed on The Dalles Tainter gate as part of the USACE SMART Gate system, with one of the stated goals being the detection of uneven hoisting. In its current state, the instrumentation system on The Dalles Tainter gate is little more than a data acquisition system. Indeed, outside of the initial study discussing desired capabilities by Alexander, et al., (2017) little work has been done on SHM or predictive modeling of Tainter gates. Kalantarnia (2013) discusses reliability of spillway Tainter gates by utilizing Condition Indexing updated with inspection data. Freckleton, et al., (2011), discuss reactive procedures to rapidly address an already failed Tainter gate. Further literature on Tainter gates is lacking. In light of the extreme economic importance of the operability of The Dalles Tainter gate and the potential issues that can occur due to uneven hoisting of this gate, the ability to detect uneven hoisting of the

Tainter gate is needed. The next section of this chapter discusses the initial efforts to detect uneven hoisting using the sensor data obtained from the continuous monitoring system.

6.2. Investigation of SHM system data

Recall that, to aid the operators of The Dalles Tainter gate in making major maintenance decisions, the gate was outfitted with an array of instrumentation to detect major changes in gate behavior. The instrumentation consists of 48 strain gages, two tilt meters, water level sensors, and temperature sensors. Of particular interest to this study are the strain gages and tilt meters. The strain gages of interest to uneven hoisting are those fitted on the strut arms near the trunnion, and in the region near the lifting lugs. The approximate location and orientation on one strut arm of the strain gages used in this study are shown again here in Figure 6.2 for the convenience of the reader, with the note that both Tainter gate strut arms are identically instrumented. These strain gages are expected to be sensitive to differential hosting forces in the hoisting cables indicative of uneven hoisting, in that, if the gate is hoisting evenly, the response in the strain gages on each strut arm should ideally be identical. The tilt meters on the gate are located near the lifting lugs and are oriented to measure the degree of rotation of the gate about the trunnion. If the gate is hoisting evenly, the angle reading on both sensors should be identical.

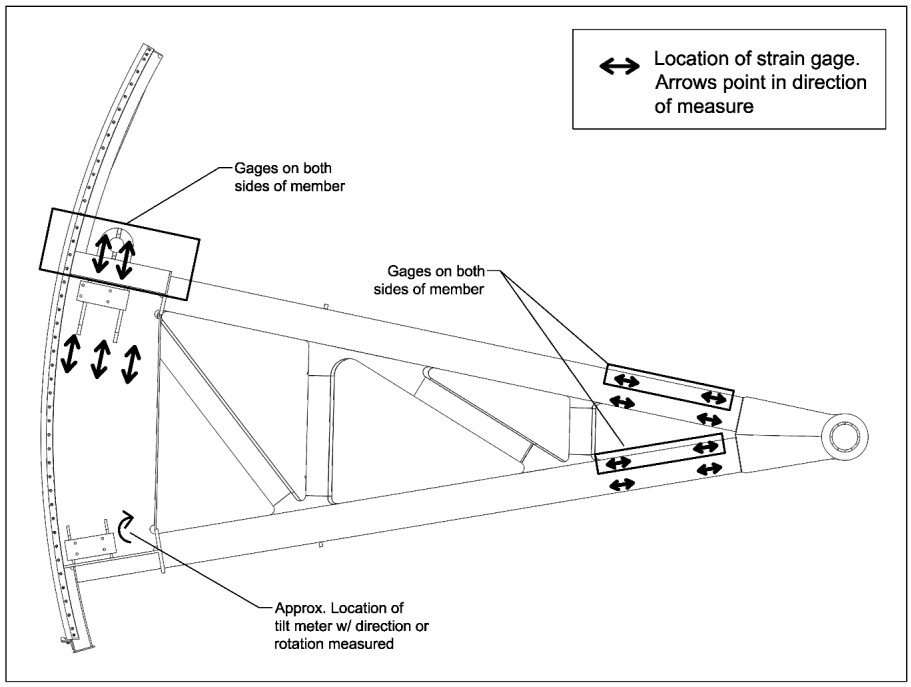

Figure 6.2 Map of instrumentation used in this study. One strut arm shown, but both strut arms are identically instrumented.

As The Dalles Tainter gate was new at the time the instrumentation was installed, the data obtained during gate operation was assumed to be representative of a normally operating gate free of damage. The most straightforward method of investigating the presence of uneven hoisting on the gate is to investigate the tilt meters. If the gate were hoisting evenly, the tilt meters on both sides of the gate would be expected to have identical readings. Accordingly, data was extracted from the tilt meters for events when the gate is lowering and raising. For each gate event, the data was de-trended to eliminate DC offsets, and then the south side tilt meter reading was subtracted from the north side reading. The difference in tilt angle for 70 lowering events is shown in Figure 6.3-(a), while the difference for 115 raising events is shown in Figure 6.3-(b). The *x*-axes in Figure 6.3 represent the angle of the gate (as measured on the north side), while the *y*-axes represent the difference in angle between the north and the south. While the data is noisy, when the gate is traveling between 40 and 55 degrees below the horizon, a clear and consistent trend is observed towards a 0.1-degree higher angle on the north side of the gate. The mean of the data at each angle further appears to suggest that the gate is generally skewed throughout its movement; however, the data is too noisy to make generalized conclusions. By using the gate's dimensions and trigonometry, a differential angle in the gate of 0.1 degrees when the gate is fully down (at 55 degrees below the horizon) leads to one side of the gate being between approximately 0.89 cm (0.35 in.) higher than the other.

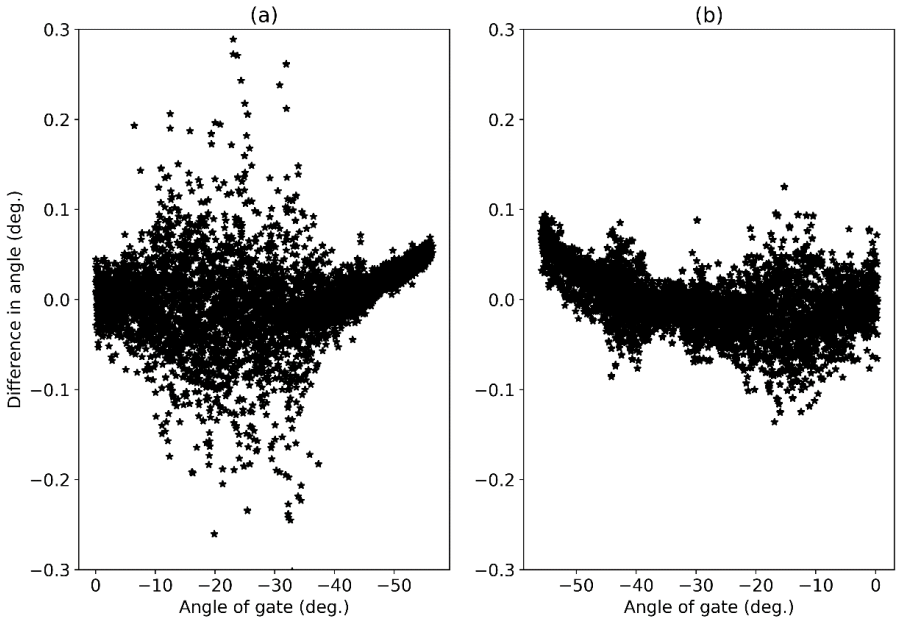

Figure 6.3. Difference in The Dalles Tainter gate tilt angle for (a) lowering events and (b) raising events.

When the gate is fully down, the FEA model suggests that the total gravity load supported by all cables is 658.3 kN (148 kips), which for an evenly hoisting gate would amount to 329.2 kN (74 kips) on each side of the gate. The skew of 0.35 inches was induced in the FEA model with the gate oriented at 55 degrees below the horizon; results show that this skew leads to the cables on the higher side of the gate needing to support 298.0 kN (67 kips) more than the low side of the gate. In other words, the cables on the high side of the gate are holding 478.2 kN (107.5 kips) of load (or, 73% of the total gravity load) as compared to 180.2 kN (40.5 kips) on the low side. Further, this result leads to as much as 64 MPa (9.5 ksi) increase in stress for location of the strut arm and lug diaphragms on the gate. The increase in stress due to a 0.89 cm skew in the gate is shown in Figure 6.4, which is a contour plot of the difference in von Mises stress field between the FEA results of a simulation considering even hoisting and a simulation considering the uneven hoisting.

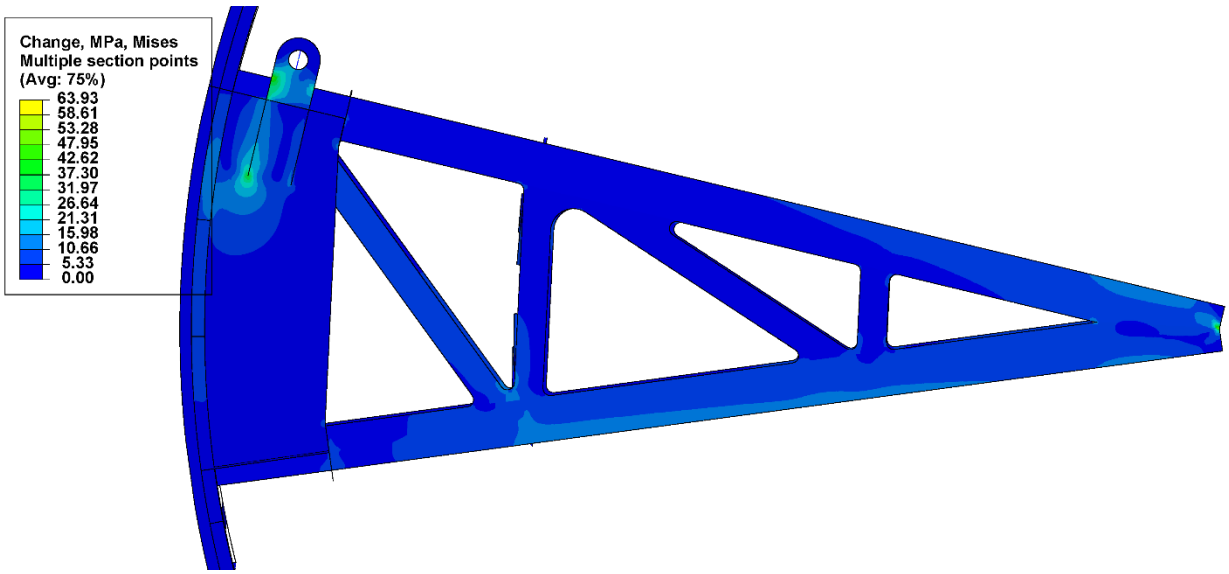

Figure 6.4 Results for FEA model showing the difference in von Mises stress between the scenario with even hoisting and a scenario with uneven hoisting.

The noise in the tilt meter data leads to an inability to make conclusive statements as to the nature of the hoisting at The Dalles Tainter gate. Accordingly, the data from the strain gages shown in Figure 6.2 was also investigated. Strain gage data over the gate orientation θ was extracted for several gate hoisting events. The data is plotted to inspect the behavior, with typical results for strain readings from two strain gages in identical locations on the north and south strut arms shown as the grey (for north side gage) and black (for south side gage) solid lines in Figure 6.5. Only one

lowering event is shown for clarity. As the strain gage data is susceptible to thermal drift, strain at a particular gate orientation ε_{ref} was chosen as a "zero" point and was subtracted from all strain data for every lowering event. As such, Figure 6.5 plots $\hat{\varepsilon}(\theta) = \varepsilon(\theta) - \varepsilon_{ref}$ where $\varepsilon(\theta)$ is the raw strain data from the strain gage at gate orientation θ. From inspection of the tilt-meter data, the most likely place of even hoisting (and thus, identical strain readings between the north and south side gages) was at about 20 degrees, which is why the data series appear to be zero at 20 degrees. To diagnose the behavior of the strain gages, the data was compared to results from the FEA model of even hoisting. The value of strain from the model was extracted at each simulated gate orientation for locations corresponding to the locations of strain gages on the physical gate. For a consistent comparison, the data corresponding to the gate oriented at 20 degrees below the horizon was also subtracted from the total data record. An example of the results is shown as the grey dashed line in Figure 6.5.

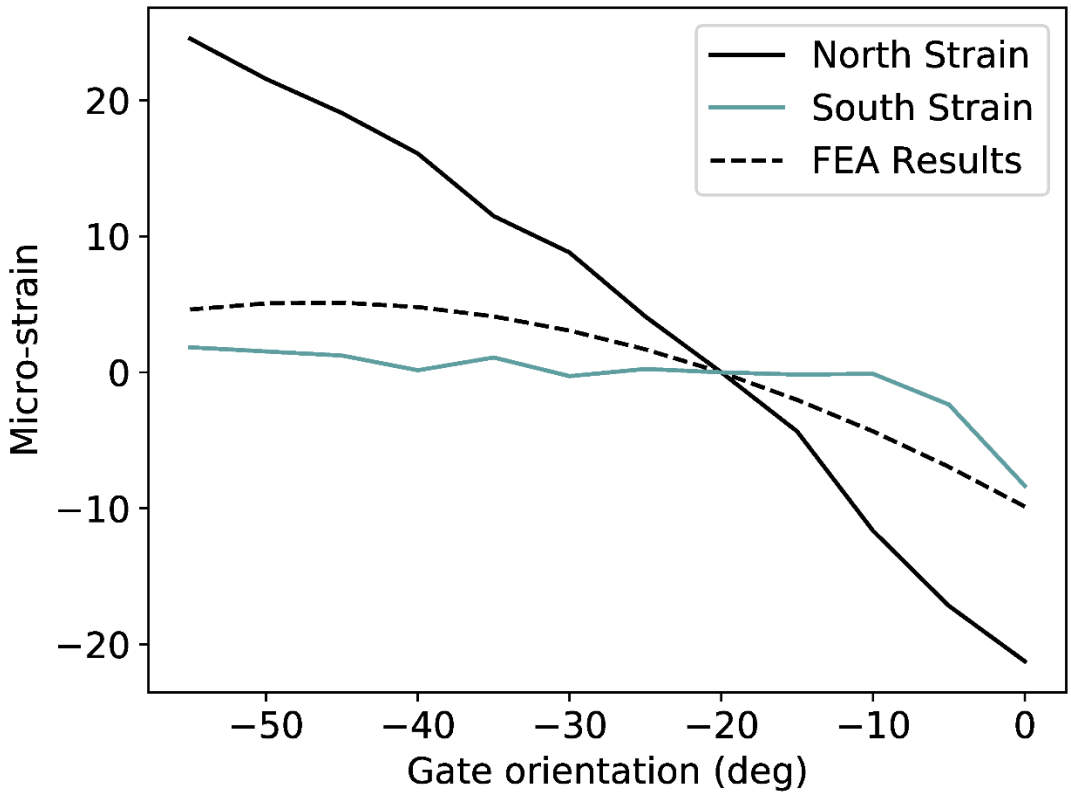

Figure 6.5 Comparison of strain gage data to strain at same location in FEA model.

For a symmetric gate hoisting evenly, the symmetrically placed strain gages on the north and south strut arms would be expected to have close to identical readings. As seen in the Figure 6.5, there is a clear asymmetry between the two sides of the gate. This behavior was consistent for all gages and all hoisting events investigated. Due to the inability to definitively determine the magnitude of strain in the gate at the beginning of a gate hoisting event (due to thermal strain offset, etc.), the best that can be obtained is a comparison of the change in strain relative to the arbitrarily selected zero point.

To ascertain whether or not the difference between the measured data and the FEA results is indicative of uneven hoisting, the FEA model was analyzed again at each orientation with uneven hoisting directly considered. Uneven hoisting was simulated by placing a pin at the lifting lug on one side of the gate, while placing a point load in the direction of the cables on the other side of the gate. Varying the magnitude of the point load simulates the different magnitudes of uneven hoisting. For example, a 0.0 kN point load would simulate a fully uneven hoisting scenario where the cables on one side of the gate carry the entire load. Applying a point load such that its magnitude is equal to the magnitude of the reaction at the pin simulates a fully even hoisting scenario (i.e., cables on both sides of the gate are carrying the same load). For the initial investigation, the simple uneven hoisting scenario of a 25% increase in load on the north cables and a 25% decrease in load on the south cables was simulated. Here again, the gate at 20 degrees below the horizon was chosen as the reference angle. Figure 6.6 shows the comparison of the results of the uneven hoisting simulations (dotted lines) and the measured strain (solid lines) for the same gate lowering event shown in Figure 6.5. As seen, when an arbitrary extent of uneven hoisting is simulated in the FEA model, the comparison between the measured and simulated data are superior in that the strain results display asymmetry similar to that seen in the measured data. It is worth noting that Figure 6.6 shows results for one pair of strain gages, and is exemplary; this was not the case for all strain gages. Moreover, the results shown are dependent on the extent of unevenness considered in the simulation and the reference orientation selected.

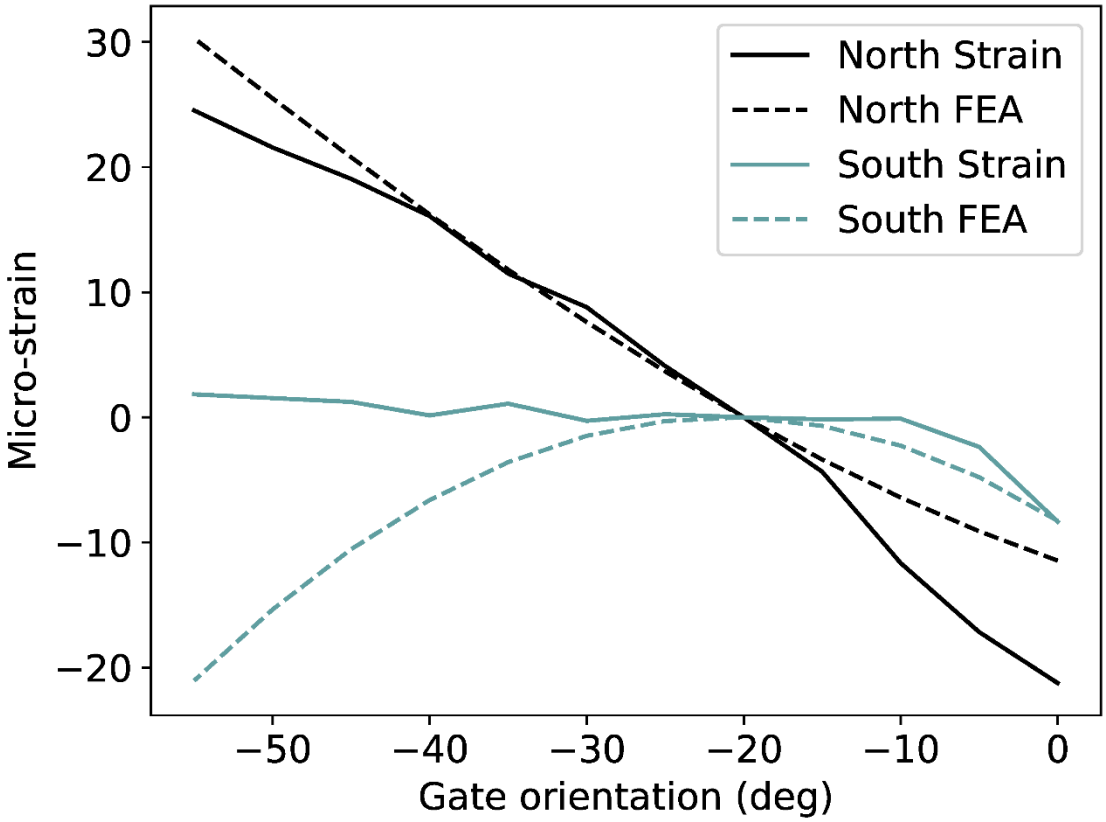

Figure 6.6. Comparison of measured strain to strain from FEA model considering uneven hoisting.

6.3. Short-term monitoring plan of The Dalles Tainter gate

The consideration of uneven hoisting in the FEA model improved some, but not all results. Moreover, the quality of improvement in the FEA model results was seen to be greatly dependent on the reference angle chosen and the extent of unevenness considered, which was arbitrarily selected. Given the uncertainties in interpreting the strain gage data, making conclusive statements about the behavior of the gate based on the sensors installed is not prudent. Accordingly, further corroboration was desired to definitively diagnose the peculiarities seen in the data. Thus, focus of the study turned to the hoisting cables directly. If The Dalles Tainter gate was hoisting evenly, then the tension in the cables on either side of the gate should be approximately equal. Conversely, if the gate is hoisting unevenly, then the tension in the cables should be noticeably different. Therefore, measurement of the tension in the cables was proposed as a definitive indication as to whether or not the gate is hoisting unevenly. Installing load pins or other direct measurement sensors on the cables would be prohibitively disruptive from an operational perspective; thus, an indirect indication of cable tension by means of measuring the cable vibration is used. As is known,

the frequency of vibration of a string, or thin cable in this case, is directly related to the tension in the cable. For a cable that is effectively undamped, and subjected to pinned-pinned boundary conditions, the fundamental frequency of vibration, *f*, of the cable is related to the tension, *T* in force units, by Eq. (6.1)

$$f = \frac{1}{2L}\sqrt{\frac{T}{\mu}} \tag{6.1}$$

where L is the length of the cable and μ is the mass per unit length of the cable. During hoisting, the length of the cables on The Dalles Tainter gate will vary between approximately 269 cm (106 in) when the gate is fully raised to 1138 cm (448 in) when the gate is fully down. While uneven hoisting would clearly cause a difference in length in the cables on either side of the gate, a maximum deflection of about 2.5 cm (1.0 in) for the worst-case scenario of fully uneven hoisting is expected from the FEA model. Thus, this difference would have a minimal impact on the frequency of vibration if the length of cables on one side of the gate were, say, 1118 cm (440 in), and on the other 1120.5 cm (441 in). Additionally, as the gate swings up and down, the extent of submersion of the cables will be constantly changing: when the gate is fully raised, the cables will be almost completely unsubmerged; when the gate is fully lowered, the cables will be submerged over nearly 75% of their length. Thus, the effects of damping or added mass due to submersion on the measured frequency of vibration of the cables will be constantly varying and difficult to quantify. However, the extent of submersion, and thus its effects on the measured frequency, will be almost identical across all cables on the gate. So, for cables on The Dalles Tainter gate, comprised of the same material and cross section, the primary driver for a difference in frequency at any time during hoisting would be a difference in tension *T* in Eq. (6.1).

To measure the frequency of vibration of each cable while the gate is raising or lowering, a PCB model 333B52 accelerometer was attached to a U-bracket, which was then bolted onto the cable. The accelerometers were attached to the U-bracket via hot-glue, as seen in Figure 6.7, and the final configuration of accelerometers on the cables is seen in Figure 6.8. As it so happens, the vibrations of the gate as it moves, as well as the flow of water induced by gate motion, was sufficient to excite the cables adequately for the tests. As the accelerometers would be fully submerged in water, the cable connection at the accelerometer was waterproofed with waterproof

tape. Based on calculations assuming for simplicity that all twelve cables carry an equal share of the full self-weight of the gate and using Eq. (6.1), the primary frequency of vibration of the cables is expected to be approximately 33.5 Hz when the gate is fully raised. The frequency is expected to be approximately 8Hz then the gate is fully lowered. Thus, based on Nyquist sampling theory (Proakis and Manolakis 1996), a sampling frequency of 200 Hz was selected, which is adequate to capture the fundamental frequency as well as several harmonics at every point of the gate swing. Unfortunately, due to the distance between the two sides of the gate, acquiring data with the same data acquisition system was not practical. Thus, on one side of the gate, data was collected using a Hi-Techniques brand Synergy P data acquisition system (DAQ), while on the other side of the gate, data was collected using a Hi-techniques brand Synergy Qb DAQ. While two separate DAQs lead to signal synchronization issues, data was collected such that no more than a few second offset between the two data sets occurred. Moreover, as will be shown later, data synchronization issues are inconsequential.

Figure 6.7 Accelerometers attached to the U-bracket.

Figure 6.8 Accelerometers on cables at The Dalles.

To capture the time-varying frequency of the cables, a short-time Fourier transform (STFT) is used (Jacobsen and Lyons 2003), which is effectively a Discrete-Fourier Transform (DFT) function (Proakis and Manolakis 1996) performed on a sliding window of the data record. Implementation was by means of the Python computing language, and the built-in STFT function in the SciPy library (Jones, et al. 2001). For this study, a window size of 6 seconds (or 1200 data points) with an overlap of 5.5 seconds (1100 data points) was sufficient to produce adequate results. With the cables instrumented, the gate was raised and lowered numerous times to get a sufficient amount of data.

To visualize the results of an STFT, a heat map is valuable. A typical heat map from one test of the gate raising is seen in Figure 6.9. The *y*-axis in Figure 6.9 represents frequency, while the *x*-axis represents time. The heat map represents the amplitude spectrum of the Fourier transforms at each time, where brighter color represents a higher magnitude. Draw a vertical line at any time *t* in the heat map provides an indication of how the frequency spectrum looks at that particular time. For instance, drawing a vertical line at $t = 20$ s shows peaks in the frequency spectrum at about 7Hz, 15Hz, 21hz, 30Hz, etc. This suggests that, at time $t = 20$ s, this cable was vibrating

with a fundamental frequency of around 7Hz, while the other peaks in the amplitude are the corresponding harmonics. Each gate raising or lowering event takes about two minutes, so data is only shown for the time of the event. As seen, the behavior of the frequency of the cables is qualitatively as expected: at the start of the raising of the gate, the hoisting cables are at their maximum length, yielding a minimum frequency of vibrations; at the end of the raising of the gate, the cables are at their minimum length, yielding the max frequency of vibration.

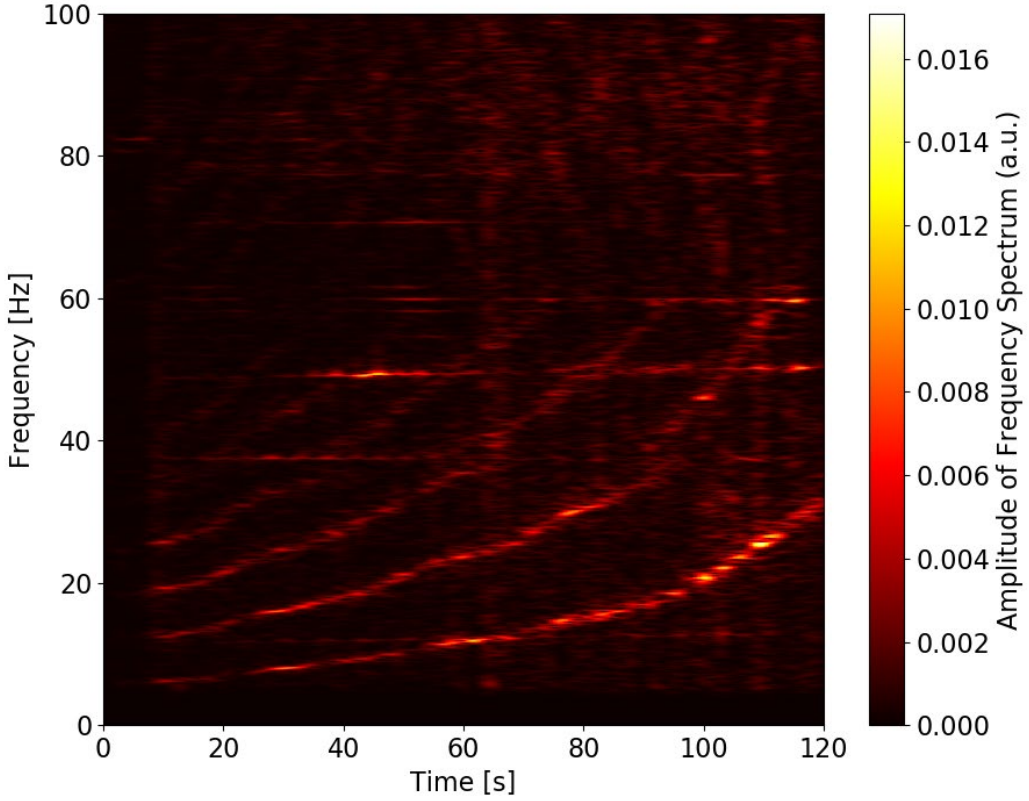

Figure 6.9. STFT spectrum of one cable during gate raising.

6.4. Results

During testing, the gate was raised 5 times and lowered 4 times. For each tested event, an STFT is performed on the acceleration record for all 12 cables connected to the gate. The STFT spectrum for a series of raising and lowering events for one cable is shown in Figure 6.10. Typical STFT results for the first raising event are shown in Figure 6.11(a). For comparison across all cables, peaks corresponding to the fundamental frequency are manually picked, with the picked peaks seen by the super-imposed x's in Figure 6.11(b). Finally, the picked peaks are all superimposed in Figure 6.12 to compare the frequency of the cables on the south side of the gate

with the frequency of the cable on the north side of the gate. As shown here, when the gate initially starts to raise (t = 0), the fundamental frequency of the cables on the north side of the gate is, in general, noticeably higher than the frequency of the cables on the south side of the gate. Then, as the gate raises, the difference in frequency appears to decrease until, at the end of the raising event (t = 120), the frequencies appear similar. The data for all raising and lowering events is shown in Figure 6.13. Gate raising events are represented by portions of the data with an increasing trend in frequency as the cables are changing length from long to short. Similarly, gate lowering events are represented by portions in the data with a decreasing trend in frequency, as the cables are changing length from short to long. As shown in Figure 6.13, the behavior of the frequency of the cables is remarkably similar for all events. As mentioned previously, a difference in tension in the sets of cables is the primary factor resulting in a difference in fundamental frequency of that cables. According to Eq. (6.1), the difference in frequency seen at the start of the raising event suggests that the north-side cables are carrying a significantly larger tensile force than the south-side cables. Then, as the gate approaches its highest point, the tension in the cables appears to even out. This further corroborates the uneven hoisting suggested by the tilt meters and the strain gages.

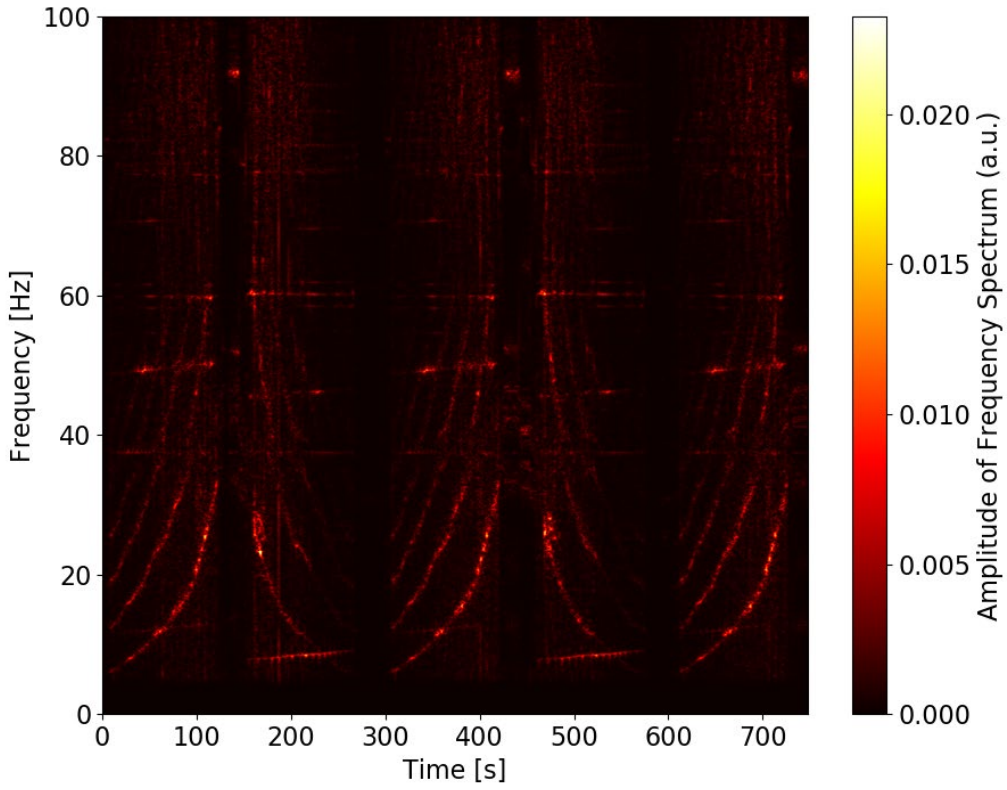

Figure 6.10 STFT spectrum for a series of raising and lowering events.

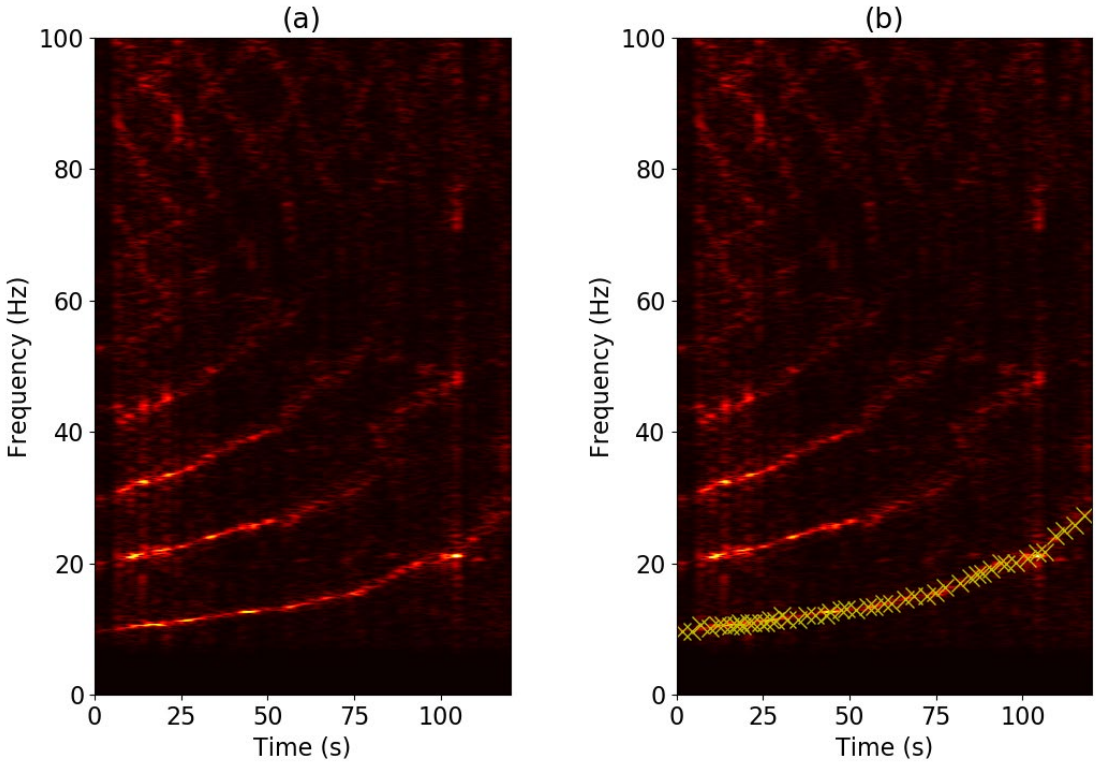

Figure 6.11. (a) STFT of acceleration of cable during first raising. (b) Same STFT with picked points superimposed.

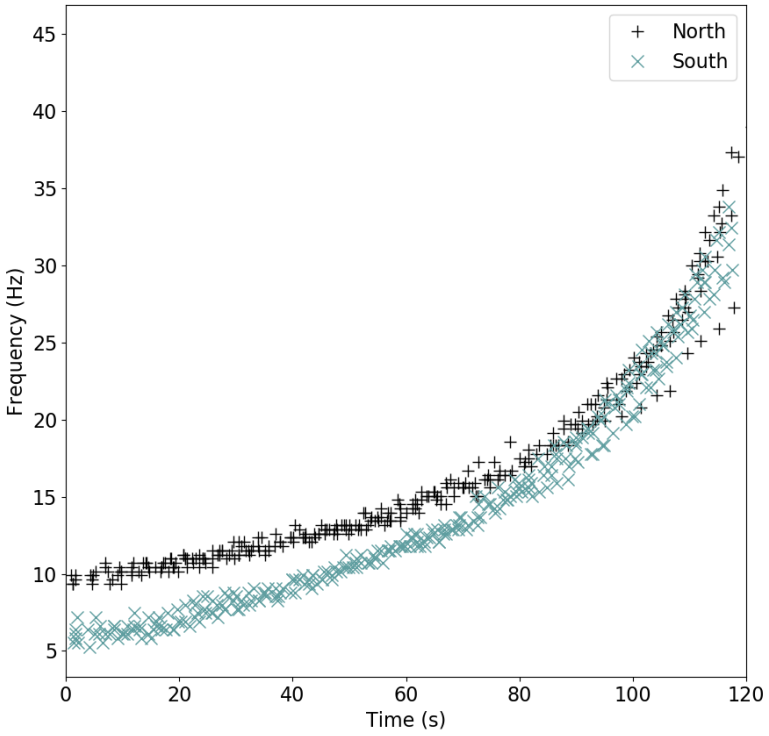

Figure 6.12. Scatterplot of picked peaks vs. time for all cables on The Dalles Tainter gate for the first raising event.

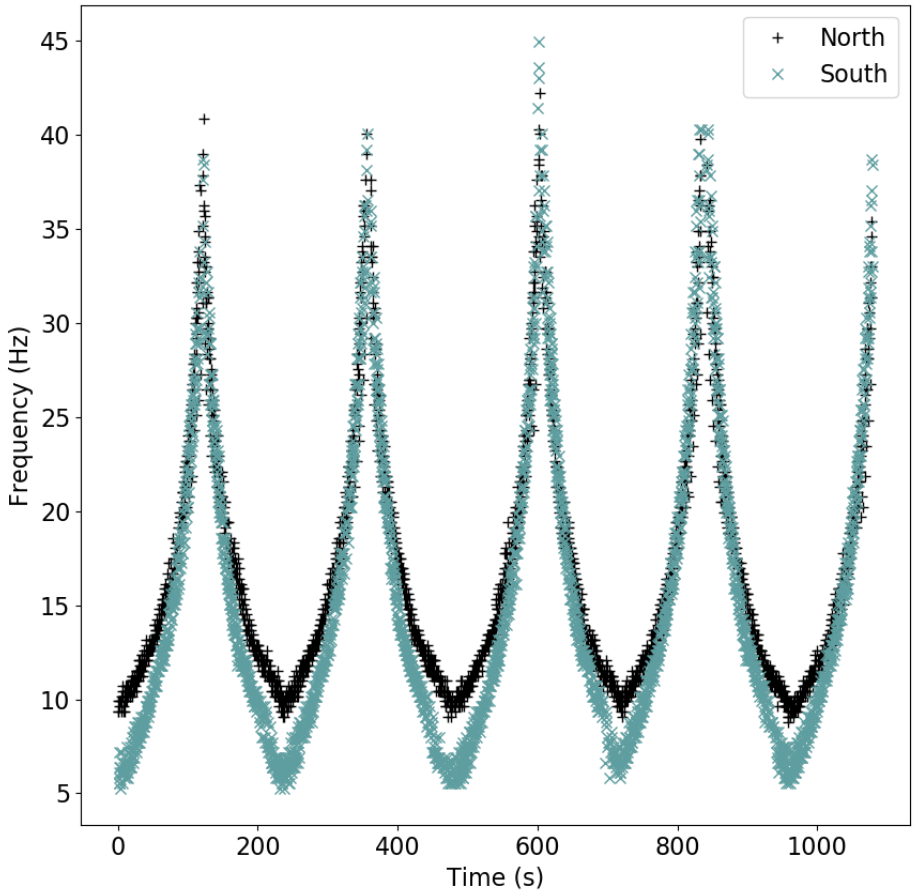

Figure 6.13. Scatterplot of picked peaks vs. time for all cables on The Dalles Tainter gate for all tested events.

Again, a separate DAQ was used on the north and south sides of the gate, and so, obtaining perfect time synchronization of the two data sets is challenging. However, the two sets of data are not misaligned by more than 2 or 3 seconds. Figure 6.12 shows the two sets of data with the most likely time shift required to synchronize the data based on when the STFT frequencies start and stop changing. As seen, the curvature of the frequency trend on the north side is fundamentally different from the curvature of the frequency trend on the south side; thus, no time-shift can be applied to one signal such that uneven hoisting (manifested by a difference in frequency at a given time) is not apparent. Thus, while ascertaining the exact magnitude of uneven hoisting from the frequency data may not be possible, the data clearly supports the notion that the gate is hoisting unevenly.

6.5. Discussion

The average frequency at the bottom of the swing for each cable on the north side of the gate is approximately 9.75 Hz. For each cable on the south side, the average frequency is about 6 Hz.

Utilizing Eq.(6.1), each north-side cable carries about 120 kN (27 kips), while each south-side cable carries approximately 46.7kN (10.5 kips), for a total of 1001kN (225 kips) carried by all cables. 1001 kN (225 kips) is about 3% more than the expected self-weight of the gate, which is 974 kN (219 kips) as calculated by the design engineers. These results show that the vibration measurements largely agree with the tilt meter measurements, suggesting that the north side of the gate is generally higher than the south side of the gate, particularly at the bottom of the swing. This skew was directly seen in the tilt meters, while the skew is inferred from the vibration-based measurements showing higher tension in the north side cables. The vibration-based method also agrees with the strain-gage approach, which arbitrarily modeled a gate with 50% more force on the north side cables to show agreement to the recorded strain gage data.

Considering the loads calculated in the cables, the primary effect of uneven hoisting is likely to be accelerated fatigue damage to the hoisting cables. Fatigue damage to cables occurs primarily due to cyclic bending loads as the cables bend around the spool during the hoisting procedure. Cycle to failure of spooled wire rope can be related to the so-called bearing-pressure ratio (Drucker and Tachau 1945) , where the bearing pressure ratio, B, is defined as

$$B = \frac{2T}{UDd} \tag{6.2}$$

where T is the tensile force in the rope, U is the ultimate stress of the rope material, D is the spool diameter, and d is the rope diameter. The relationship is given in graphical form in Figure 6.14 (Gibson, et al. 1974). The rope used at The Dalles is 6x25 FW wire rope with a 2.54 cm (1.0 in.) diameter. According to the West-coast Wire Rope Catalog (2020), 6x25FW fits under the class of 6x19 wire ropes, and the one-inch diameter variety has an ultimate breaking strength of 409 kN (92 kips). Assuming conservatively that the 6x25FW rope used at The Dalles has a fiber core, the metallic cross-sectional area of the wire ropes is 2.47 cm^2 (0.384 in^2), giving an ultimate stress of the material of 1647 MPa (239 ksi). The spooling drums at The Dalles have a diameter of 78.74 cm (31 in.). Considering even hoisting of the gate, the 1001 kN (225 kips) of force would be evenly shared by all six cables, leading to a bearing pressure ratio using Eq. (6.2) of 0.0051. Using Figure 6.14, the bearing pressure ratio during even hoisting results in an expected cycles to failure of just under 150,000. Considering the loads calculated above from the short-term monitoring program

of 120 kN (27 kips) in each of the north-side cables, the bearing pressure ratio of 0.0072, which amounts to just under 100,000 cycles to failure using Figure 6.14. Thus, the uneven hoisting occurring in The Dalles Tainter gate may lead to a 33% decrease in the life of the hoisting cables.

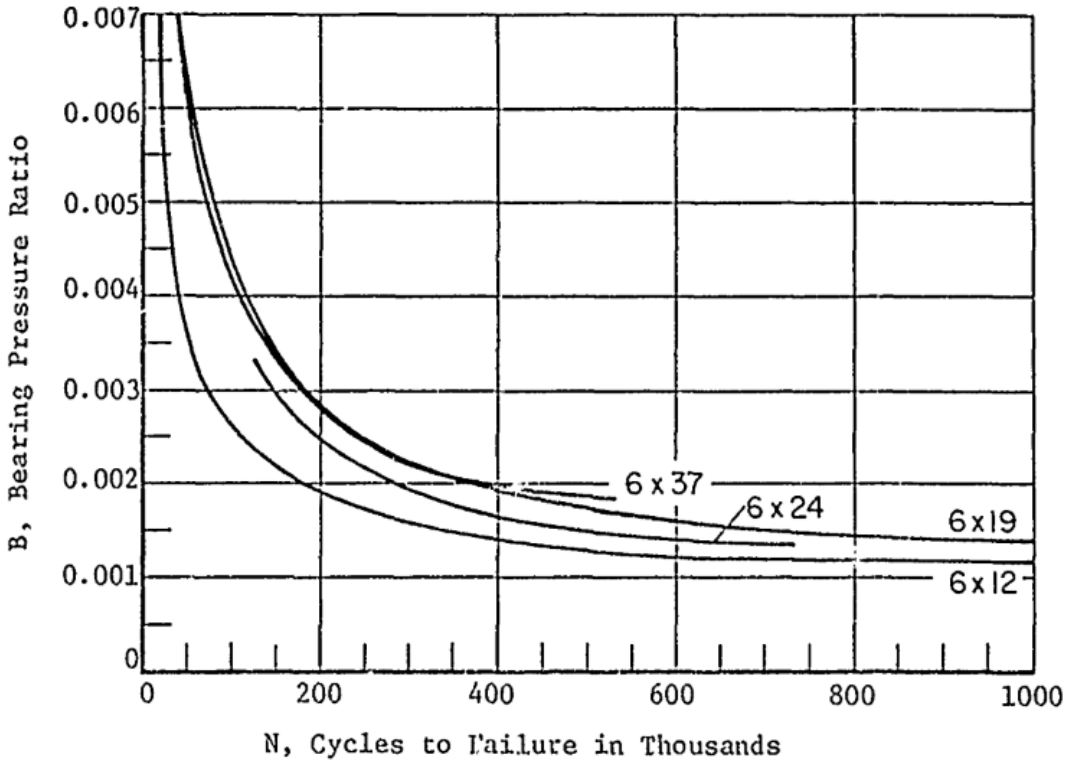

Figure 6.14 Bearing pressure of wire rope vs. cycles to failure (Gibson, et al. 1974).

It's worth noting that the 1001 kN in the cables calculated using Eq. (6.1) is 52% more than the 658 kN (148 kips) in the cables suggested by the FEA analysis, where the trunnions are carrying the remainder of the gravity load. Similarly, when the gate is fully raised, the average frequencies in the cables suggest that the cables are carrying a total force of about 1067 kN (240 kips), whereas the FEA model suggests that the cables should be carrying about 800 kN (180 kips) in this orientation. The difference between the gravity load inferred from the vibration measurements and the gravity load calculated from the FEA model is expected to be due to shortcomings in the numerical model. The numerical model doesn't accurately capture dynamic effects of the gate moving in the static analysis nor does it capture any potential fabrication flaws such as misalignments that may be present and cause increased loads in the hoisting cables due to the indeterminate nature of the Tainter gate system. It's also possible that there is an unknown source

of mass missing not accounted for in the FEA model; however, after studious review of the geometry and material properties of the FEA model, no discrepancies were found between the model and the provided structural drawings that were used for construction.

The extent of uneven hoisting suggested by the three different sources (tilt gages, strain gages, accelerometers) should not be possible based on the specifications for the master/slave relationship of the hoisting drums. One hoisting drum is designated a “master”, and rotates at a constant speed; the other is designated the “slave” and rotates at a variable speed to prevent skew of the gate to within 0.01 inches. However, the adjustment of the hoisting drum speed is based on a rotary encoder, which infers length of spooled rope based on encoder counts of the drum. The encoder counts indicate rotations of the drum. When the two hoisting drums are off by one encoder count, the slave drum will adjust speed to make up the difference. What may be happening is that there may have been a small skew in the gate when the cables were initially installed. Then, the elasticity of the cables will cause an exacerbation in skew as the cables unspool. That is, as the length of unspooled cable increases, the stiffness of the cable will decrease, in-turn increasing the differential displacement between the lifting locations of the gate. This can be investigated on-site with surveying equipment. Addressing this problem on the in-service gate may require readjusting the zero point of the rotary encoders to reduce or eliminate initial skew. To prevent this issue on future design, it is suggested that (if this is indeed the problem) the tolerances on initial skew during gate instillation are tightened. It’s also possible that hoisting mechanisms are not working properly, the rotary encoder is not working correctly or that the slave drum is not capable of adjusting speed fast enough to eliminate skew; neither of which was possible to measure on site.

6.6. Conclusions

The study presented in this chapter focuses on the Tainter gate that serves as the upstream gate at the lock chamber of The Dalles Lock and Dam. This study initially started as work towards developing a methodology to automatically detect uneven hoisting when the Tainter gate is raising and lowering. Uneven hoisting is a critical concern, as the phenomenon causes a skew in the gate while it is lifting, and can lead to strength, stability, and fatigue issues. Uneven hoisting is particularly concerning for The Dalles Tainter gate, as it experiences thousands of raising and lowering cycles annually; far more than the typical dam spillway Tainter gate. When The Dalles Tainter gate was constructed, the owners and operators installed a long term monitoring system with one of the noted goals of detecting uneven hoisting. As the long-term monitoring system

came on-line, peculiarities in the data raised concerns that the Tainter gate was behaving in an undesirable manner, and may indeed be hoisting unevenly.

Initial research uncovered an apparent disagreement between the tilt meters on both sides of the gate. While the tilt data was noisy, a consistent indication was found of a differential angle of the gate of about 0.1 degrees between the north and south sides. This seemingly inconsequential difference in angle actually leads to about 0.89 cm (0.35 in) of differential displacement in the gate, which in turn causes the hoisting cables on one side of the gate to carry some 72% of the gravity load of the gate. Additionally, strain gage data collected from the continuous monitoring system was compared to the expected behavior seen from an FEA model, and there was a notable disagreement. This disagreement led to concerns that either the FEA model is flawed, the sensors are flawed, or that The Dalles Tainter gate is regularly hoisting in an uneven fashion. Uneven hoisting was then simulated in the FEA model, and a least squares approach was used to find a best fit between the measured data and the results from the FEA model. Results of the least squares fit show that the measured data more closely matches the expected behavior from the FEA model when uneven hoisting is considered.

To further corroborate the notion that The Dalles gate is regularly hoisting unevenly, a short-term monitoring plan was devised to take indirect measurement of the tension in the hoisting cables. The tension was indirectly measured by means of vibration measurements with accelerometers installed on each cable. As demonstrated previously, while there are many uncertainties in relating the frequency of vibration of the cables to an exact magnitude of tension in the cables, any peculiarities in the frequency/tension relationship would be experienced by all cables equally. Thus, at any given time during the raising or lowering of the gate, the primary driver for a difference in fundamental frequency of vibration in the cables of the gate would have to be a difference in tension in the cables.

The short-term monitoring program was performed by raising and lowering the gate numerous times and collecting vibration data from the cables. Due to the time-varying nature of the frequencies of vibration of the cables, an STFT was performed on the acceleration record from the accelerometers. In every measured raising or lowering of the gate, the measured frequencies of vibration of the hoisting cables corroborate the other sources of evidence that, towards the bottom of the swing of The Dalles Tainter gate, the gate appears to be regularly skewed. In light of the

multiple sources of corroboration, it appears very likely that The Dalles Tainter gate is indeed regularly hoisting unevenly.

The long term monitoring system installed by the owners and operators of The Dalles Tainter gate alerted researchers that the gate is likely exhibiting undesirable behavior. Uncertainty in the data from the long-term monitoring system led to the short-term, direct measurements discussed herein which corroborated the interpretation of the data from the long term monitoring system. The information gleaned from this study has been passed on to the appropriate authorities so they can determine the most appropriate remediation. As it is apparent that the extent of uneven hoisting of the gate does not pose an immediate threat to the strength or stability of the gate, particular interest for future work is to investigate the long-term effects of the redistribution of stresses caused by uneven hoisting.

Chapter 7. Conclusions and Future Work

Inland navigation is critical to the global economy and facilitates the transportation of trillions of dollars in goods annually. Successful operation of inland navigation systems relies on networks of interconnected infrastructure in the form of locks and dams. Dams are constructed on rivers to increase the depth of water allowing for a channel of sufficient depth for cargo vessels to navigate. Locks act as elevators in the river, allowing river traffic to traverse the dam. The economic importance of inland navigation infrastructure is such that timely maintenance is crucial. Sudden, unplanned closures of lock sites due to emergency repairs can lead to millions of dollars of economic losses daily due to cargo not getting to market. Moreover, closure of one lock site will often cause a ripple effect of delaying traffic on an entire river, even very far from the location of the closed lock. Of the components that make up locks and dams, the steel gates that act as water control structures, are the weak links. Thus, the research presented herein focuses on these gates.

The operating conditions of lock and dam gates, and the environment in which they are constructed, makes structural assessments of their critical components difficult and expensive. Maintenance and repair of these steel gates is the leading cause of unscheduled downtime on the inland navigation system. At best, the structures are inspected once every five to ten years. Thus, these steel gates are generally maintained in a reactive, rather than proactive, manner. That is, the steel gates are typically operated until something breaks, at which time a portion of the inland navigation system is shut down for emergency repairs. To address this shortcoming, the research presented herein aims to develop a structural health monitoring system that can be used by the stakeholders of inland navigation infrastructure to obtain the necessary information to assess the integrity and condition of their structures. To accomplish this goal, this research focused on development of methods for the detection and assessment of a number of critical problems common to lock and dam gates, with emphasis given to the most common gates used in the U.S.: miter gates and Tainter gates.

Chapter 2 of this dissertation explored miter and Tainter gates, with an explanation of how and where these gates are utilized. The expected behavior of the gates under typical loading conditions was introduced, as was the design philosophy necessary to understand the research performed in this dissertation. The expected behavior of the gate and typical damage scenarios were discussed to motivate the selection of the monitoring methodologies developed in this dissertation. These

methodologies are 1) the detection of what's known as a quoin gap, 2) detection of loss of tension in a miter gate component known as the diagonals, and 3) detection of a phenomenon known as uneven hoisting of Tainter gates.

Chapter 3 of this dissertation provided information on the best practices to use when creating and using FEA models of miter and Tainter gates. These FEA models were created as a first step in the SHM system to assist in developing the necessary understanding of the global behavior of the gate under normal operating conditions. The FEA models were then leveraged to explore the change in behavior of the modeled structure due to the presence of the damage to which the SHM system is intending to detect. In this way, the FEA models inform which sensors in the SHM system will be sensitive to the presence of damage and how the response of the sensors changes. Topics in Chapter 3 included the selection of geometry and elements, mesh refinement, appropriately modeling of boundary conditions, model validation and model updating. Two examples of FEA models used heavily in the course of this research were discussed at length, namely the models of the upstream miter gate at the Greenup Lock and Dam and the upstream Tainter lock gate at The Dalles Lock and Dam.

In Chapter 4, the method developed for detecting quoin gaps on miter gates was discussed. This method relies on the use of strain gage readings to detect the redistribution of stresses in a miter gate due to degradation in bearing surface along the quoin. A novel metric termed "the slope" was devised to address the environmental sensitivity of strain gages by using the rate of change of the strain (as measured by strain gages) with respect to the change in water levels of the lock chamber. The slope was found to be sensitive to the redistribution of strain indicative of a quoin gap while effectively eliminating much of the environmental noise, such as thermal drift. Principal Component Analysis (PCA) was then used to combine the information from many strain gages into a single quantity termed the damage index. A threshold for the damage index was found by processing data from a known healthy gate using PCA. Then, as new data is collected, the damage index is calculated and compared to the threshold. A quoin gap is assumed to be present if the damage index exceeds the threshold for multiple consecutive observations. The approach was validated using the strain response of an FEA model of the Greenup miter gate with a simulated quoin gap superimposed onto the strain data measured from the instrumentation system. Results show that the PCA method is a viable option to detect quoin gaps.

Chapter 5 focused on the monitoring of tension in the diagonals of miter gates. Monitoring and maintaining the tension in the diagonals has been identified as a critical concern by miter gate owners and operators, as inappropriate tension will accelerate fatigue damage or increase the likelihood of the gate being impacted by passing vessels. For ease of obtaining measurements, a non-contact, vision-based method was developed where a user will capture video of a vibrating diagonal from the lock chamber wall. Optical-Flow was then used to track the displacements of the vibrating diagonal from the captured video. A frequency domain method was used to obtain the fundamental frequency of vibration of the diagonal from the displacement record measured using optical flow. With the known geometry of the diagonal, and the measured frequency of vibration, the tension in the diagonal is found using beam theory.

Particular challenges of the successful implementation of vision-based tension monitoring of miter gate diagonals are the rigidity of the diagonals, appropriately modeling the boundary conditions of the diagonals, and the effects of submersion on the frequency of vibration of the diagonals. This study found that the effects of submersion of the diagonals can effectively be modeled as added mass on the diagonals; however, finding a closed-form relationship between the frequency of vibration and the tensile load of a partially submerged diagonal proved challenging. Accordingly, the approximate assumed-modes method is utilized to relate tension in the diagonals to frequency of vibration of a partially submerged diagonal. The proposed approximate method has the benefit of easily accommodating varying cross-sectional geometry, which is prevalent with miter gate diagonals. A laboratory test was performed to validate both the vision-based method of measuring vibration, and the proposed approximate method to model the partial submersion of the beam. Results of the experimental analysis were exceptional. The methodology was further verified using video of the vibrating diagonals on the miter gate at the Greenup Lock and Dam, and a comparison of the calculated tension using the vision-based method with the tension measured using a load cell shows good agreement.

Chapter 6 focuses on the uneven hoisting of the Tainter gate at The Dalles Lock and Dam. Uneven hoisting of the Tainter gate can be problematic as it can lead to accelerated fatigue damage and, in the extreme case, catastrophic failure. A multi-faceted approach was utilized to show that, in spite of the gate being new at the time of installation of instrumentation, it appears as though the gate is regularly hoisting unevenly. Initial inspection of instrumentation data obtained from the USACE SMART Gate system showed disagreements in the incoming data compared to the

expected behavior of the gate. Particularly, the symmetrically placed sensors on the gate show asymmetrical behavior. Three explanations for this asymmetry were possible: the model of the gate was flawed, the sensors on the gate were unreliable, or the gate was already hoisting unevenly. To definitively diagnose the issues seen in the data, a short-term monitoring program was devised to monitor the tension in the cables that raise and lower the Tainter gate. If the gate is hoisting evenly, the load in each of the cables should be approximately equal. Vibration measurements of the hoisting cables of the gate were obtained and a frequency domain method was employed to estimate the force in each of the cables. Results of the short-term monitoring program support the notion that the gate is regularly hoisting unevenly. In light of multiple sources of corroboration, the study performed herein on the Tainter gate at The Dalles suggested that the gate is regularly hoisting in an uneven fashion, and, indeed, the strain gages installed on the gate can be used to monitor for uneven hoisting.

The methodologies developed herein are the first steps toward realizing a fully functional, real-time SHM system for inland navigation infrastructure. Work is ongoing to implement the developed methods into an integrated user dashboard to support field operations. A primary challenge with field implementation is translating the scripts written for the research herein into a programming language that is easily integrated into lock gate computational infrastructure, which is part of future work. Additionally, work has begun to incorporate the information gleaned from the SHM instrumentation systems and the developed methods as inputs into a probabilistic assessment of the remaining life of miter gates, as explained in the next section.

7.1. Future Work

The primary focus of future work regarding the methods developed in this research is for field implementation. Challenges remain in translating the scripts developed herein into computing language that is easily integrated into the onsite hardware typical in the field. Ideally, this would require rewriting the scripts in C++ or JavaScript, the process of which is ongoing. Some work is being done at USACE by computer scientists to utilize a COTS system to provide dashboard-like visualizations to engineers onsite. Figure 7.1 shows a preliminary dashboard tool developed to inform personnel onsite as to the status of sensors at the Bonneville lock and dam on the Columbia River. Here, a simple control-chart-type method is used to determine the percentage of good readings obtained from a sensor. If that percentage is low, the icon for a particular sensor will show red, whereas green means an acceptably high percentage of good readings.

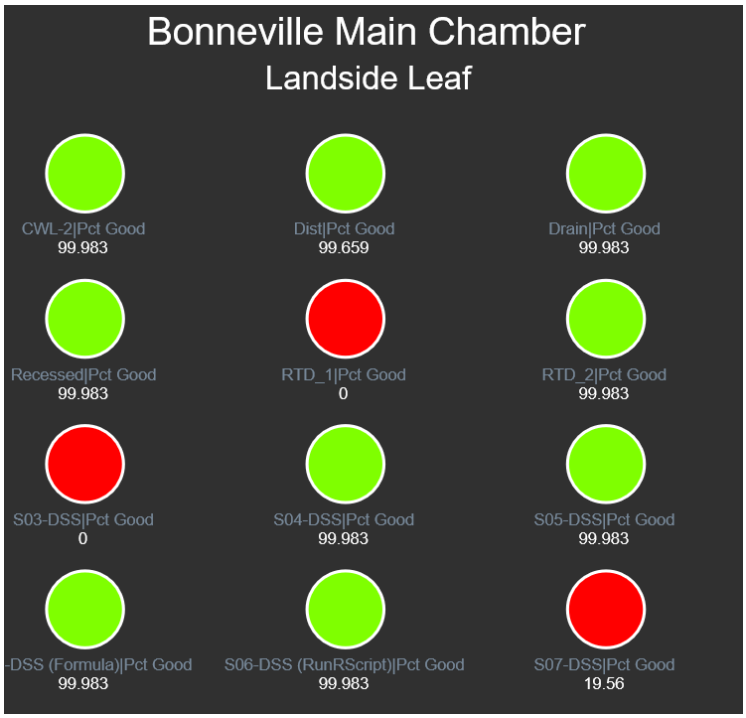

Figure 7.1 Initial dashboard tool incorporated into Bonneville Lock Site SMART Gate system, showing status of sensors.

The simple stoplight style of communication, shown in Figure 7.1, is effective in communicating status updates of sensors on a gate and can be similarly utilized to show the status of regions or components on a gate. For instance, a similar dashboard with a set of stoplight indicating whether or not regions along the height of the quoin are in contact, or whether a gap has formed. This would require encoding the PCA algorithm developed in this dissertation on site, the results of which would inform the dashboard. A similar approach can be taken with uneven hoisting or tension in diagonals, where, instead of stoplights, radial gage-type indicators can be used to inform the magnitude of, say, tension in cables or diagonals.

Additional work, already underway, is involved in incorporating the information obtained from the SHM methods and FEA models developed in this dissertation into a probabilistic assessment of the remaining life of the gate. This assessment will use Monte-Carlo simulations (Yakowitz 1977) to incorporate all recognized and quantified sources of uncertainty to develop, for instance, a probability distribution of the formation of a crack at all locations on a gate that are discretized in an FEA mesh. A high-level overview of how these Monte-Carlo simulations are intended to work is shown in Figure 7.2.

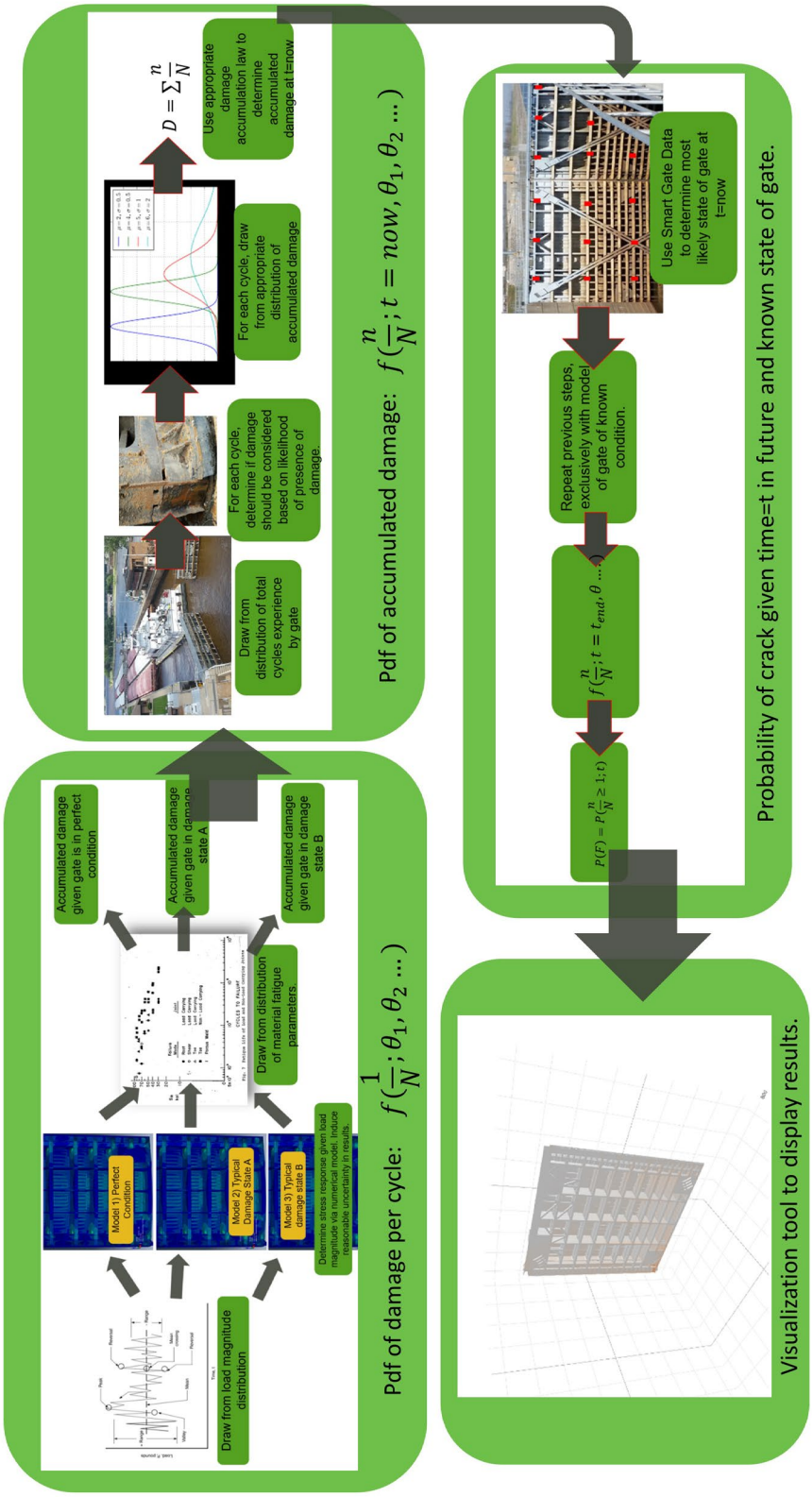

Figure 7.2. Framework for Monte-Carlo simulation to incorporate SHM data for probabilistic assessment of remaining life of lock gate.

To walk through Figure 7.2, the current philosophy of developing a probabilistic assessment of the remaining life of the gate is to incorporate an accumulated fatigue damage law, such as Miner's rule (Miner 1945). Thus, every load cycle experienced by a miter gate is thought of as having accumulated some amount of damage to the structure. The simplest approach for each cycle is to compare the stress amplitude of a cycle to a material S-N curve, and then the inverse of the number of cycles to failure obtained from the S-N curve is the accumulated damage for a given cycle. When the summation of accumulated damage exceeds 1.0, then the structure is said to have failed. The first step of the approach, shown in Figure 7.2, is to develop a probability distribution of accumulated damage for each for one load cycle of a miter gate. Here, it is assumed that a probability of accumulated damage conditioned on a given load range and material parameters is known. Then a Monte-Carlo simulation is utilized by drawing from known or approximated probability distributions of load magnitude on a gate, damage on the gate, and material parameters to develop an empirical joint distribution of the parameters. From the joint distribution, the marginal distribution of the accumulated damage is readily obtained.

The next step in the approach is to determine a probability distribution of the total accumulated damage of the gate at the current time. Here, another Monte-Carlo simulation is utilized where the known or approximated probability distribution of the number of cycles experienced by the gate per day is utilized in conjunction with the likelihood of damage on the gate and the distribution of accumulated damage found in the previous step. Finally, the SHM system on a gate would be queried to determine whether or not particular damage scenarios are present in the gate. The damage scenarios are modeled in an FEA analysis to determine the change in stresses due to damage, and thus, the change in accumulated damage per cycle. All of the information is then compiled together to determine a probabilistic assessment of the remaining life of a particular gate.

One of the explicit goals of this approach would be to incorporate as much uncertainty as possible. Initial studies suggest that the load history on a gate can be inferred from a combination lockage logbooks (records of ships passing through a lock, kept at all sites) and information about historical water levels. For studies performed on gates without instrumentation, information on the likelihood of the presence of damage will likely require expert elicitation. For material parameters (in particular, material fatigue parameters), an initial literature review found information lacking for the types of weld details typical to miter gates. A significant portion in the development of this probabilistic assessment, then, is going to be the probabilistic assessment of the fatigue behavior

of welded joints typical to miter gates. This assessment is already underway, with laboratory testing to determine fatigue parameters for a typical cruciform welded joint of miter gates. Figure 7.3 shows an initial test specimen of the cruciform joint in a load frame being tested cyclically in tension. For these tests, Digital Image Correlation (DIC) is utilized to monitor for crack formation, aiding in the development of S-N curve parameters for each detail investigated (Mathieu, et al. 2011). Moreover, DIC can then be used to track the growth of the crack to aid in the development of Paris' Law parameters (Paris and Erdogan 1963). Figure 7.4 shows the successful cracking of the first tested specimen, with the speckle pattern necessary for DIC clearly visible. Figure 7.4 shows a zoom of the bottom portion of the intersection of the cruciform joint in Figure 7.3, with two separate cracks propagating through the lower weld. These tests are ongoing, with many more specimens needing to be tested in order to infer the statistics of the material properties and properly develop probability distributions.

The end goal of the probabilistic assessment of remaining life of miter gates is to provide a simple, user-friendly tool that can be used by lock operators on site to visualize problem areas on the gate. This tool is expected to resemble the results of an FEA analysis that can be zoomed in, rotated, panned, and queried. One explicit goal is that this visualization tool must not require advanced users utilizing specialized software, and so a simple web-browser-based tool is being investigated. The development of this tool is just getting started and is expect to be finished in two to three years, with complexity added as more information is obtained.

Figure 7.3. Specimen of typical miter gate welded cruciform joint in load frame for fatigue testing.

Figure 7.4. Successful formation and propagation of cracks (note speckle patterns for DIC).

References

Abela, Christopher M. 2017. "Recommendations on building and evaluating three-dimensional finite-element models for tainter gates." *Practice Periodical on Structural Design and Construction* (ASCE) 22 (1). doi:10.1061/(ASCE)SC.1943-5576.0000300.

Ahuja, Sanjay Kumar, and Manoj Kumar Shukla. 2017. "A survey of computer vision based corrosion detection approaches." *International Conference on Information and Communication Technology for Intelligent Systems.* Ahmedabad.

Alexander, Quincy G, Matther D Smith, and Brian A Eick. 2017. "Development of SMART Gate decision support tools for large inland navigation USACE infrastructure: The Dalles Tainter gate." *PROCEEDINGS: 2017 International Workshop on Structural Health Monitoring.* Stanford.

American Institute of Steel Construction. 1997. *Steel Design Guide 9: Torsional Analysis of Structural Steel Members.* Chicago: AISC.

American Society of Civil Engineers. 2013. *2013 Report Card for America's Infrastructure.* Reston, CA: ASCE.

Ang, Alfredo H-S., and Wilson H Tang. 2007. *Probability Concepts in Engineering: Emphasis on Applications to Civil and Environmental Engineering.* Hoboken: Wiley. ISBN: 978-0471720645

Asia Development Bank. 2016. "Promoting waterway transport in the People's Republic of China." (Asia Developmen Bank). ISBN: 978-92-9257-522-9.

Avitabile, Peter. 2017. *Modal Testing: A Pracitioner's Guide.* John Wiley & Sons. doi:10.1002/9781119222989.

Beauchemin, S S, and J L Barron. 1995. "The Computation of Optical Flow." *ACM Computing Surveys* 27 (3): 433-467. doi:10.1145/212094.212141

Boresi, Arthur P, and Richard J Schmidt. 2003. *Advanced Mechanics of Materials (6th Ed).* John Wiley and Sons. ISBN: 0-471-43881-2.

Bradski, G. 2019. "Open-source Computer Vision Library (OpenCV)." http://www.opencv.org

Brinckman, Jonathan. 2009. "Dam's lock closure hurts Northwest shippers but could have been far worse." *The Oregoian*, October 07.

Camporese, Matteo. 2013. "Optimal Design of Horizontally Framed Miter Gates." *Journal of Waterway, Port, Coastal, and Ocean Engineering.* 139 (6) : 543-547. doi:10.1061/(ASCE)WW.1943-5460.0000205

Chapman, Bill. 2010. *Markland and Greenup Gate Filures.* US Army Corps of Engineers. Online: https://www.iwr.usace.army.mil/Portals/70/docs/IWUB/board_meetings/meeting63/Chapman_%20IWUB63.pdf

Chen, Shoei-Sheng. 1985. *Flow-induced vibration of circular cylindrical structures.* Argonne National Laboratory. Report No. ANL-85-51

Cho, Soojin, Hongki Jo, Jongwoong Park, Hyun-Jo Jung, Chung-Bang Yun, Billie F Spencer, and Ju-Won Seo. 2010. "Structural Health Monitoring of a Cable-stayed Bridge Using Wireless Smart Sensor Technology: Data Anlyses." *Smart Structures and Systems* 6 (5-6): 461-480. doi:10.12989/sss.2010.6.5_6.461

Commander, B C, J X Schulz, and G G Goble. 1994. *Detection of Structural Damage on Miter Gates.* Vicksburg, MS: DTIC Document, USACE Waterways Experiment Station. Technical Report REMR-CS-45

Craig, Roy R, and Andrew J Kurdila. 2006. *Fundamentals of Structural Dynamics.* Hoboken: John Wiley and Sons. ISBN: 978-0471430445

Cross, Elizabeth J. 2012. "On Structural Health Monitoring in Changing Environmental and Operational Conditions." Ph.D. Dissertation, University of Sheffield.

Daniel, Ryszard A. 2000. "Mitre gates in some recent lock projects in the Netherlands." *Stahlbau* 69 (12): 952-964. doi:10.1002/stab.200003430

Dassault Systems. 2017. *Abaqus Documentation.* Providence, RI. https://www.3ds.com/support/documentation/

Drucker, D C, and H Tachau. 1945. "A new design criterion for wire rope." *Journal of Applied Mechanics, Transactions of the ASME* 12(1): A-31:A-38.

Eick, Brian A, Matthew D Smith, and Travis B Fillmore. 2019. *Feasibility of Discontinuous Quoin Blocks for USACE Miter Gates.* Washington D.C.: US Army Corps of Engineers. Report No. ERDC-TR-19-16.

Eick, Brian A, Yasutaka Narazaki, Matthew D Smith, and Billie F Spencer. 2019. "Monitoring post-tensioned miter gate diagonals using vision-based vibration measurements." *12th International Workshop on Structural Health Monitoring.* Stanford, CA.

Eick, Brian A, Zachary R Treece, Billie F Spencer, Matthew D Smith, Steven C Sweeney, Quincy G Alexander, and Stuart D Foltz. 2018. "Automated Damage Detection in miter gates of navigation locks." *Structural Control and Health Monitoring* 25 (1). doi:http://doi.org/10.1002/stc.2053.

Estes, Allen C., Dan M Frangopol, and Stuart D. Foltz. 2004. "Updating Reliability of Steel Miter Gates on Locks and Dams Using Visual Inspection Results." *Engineering Structures* 26(3): 319-333. doi:10.1016/j.engstruct.2003.10.007.

Eurostat. 2019. *Energy, Transport, and Environmental Statistics.* Brussels: European Union. doi: 10.2785/660147

Farrar, Charles R., and Keith Worden. 2012. *Structural Health Monitoring: A Machine Learning Perspective.* Hoboken, NJ: Wiley. doi: 10.1002/9781118443118

Feng, Dongming, and Maria Q Feng. 2016. "Vision-based multipoint displacement measurement for structural health monitoring." *Structural Control and Health Monitoring* 23: 876-890. doi:10.1002/stc.1819.

Feng, Dongming, Thomas Scarangello, Maria Q Feng, and Qi Ye. 2017. "Cable tension force estimate using novel noncontact vision-based sensor." *Measurement* 99: 44-52. doi:10.1016/j.measurement.2016.12.020.

Figueiredo, E, G. Park, J Figueiras, C Farrar, and K Worden. 2009. *Structural Health Monitoring Algorithm Comparisons Using Dtandard Data Sets.* Los Alamos: Los Alamos National Laboratory. Report No. LA-14393

Fish, Jacob, and Ted Belytschko. 2007. *A First Course in Finite Elements.* Hoboken, NJ: Wiley. ISBN: 978-0470035801

Foltz, Stuart, Jonathan Trovillion, and Jeffrey Ryan. 2015. *Evaluation of sealing materials and techniques for installing quoin and miter block backing grout.* Vicksburg: US Army Corps of Engineers. Report No. ERDC/CERL TR-15-32

Freckleton, Derek R, Michael C Johnson, M Leslie Boyd, and Dustin G Mortensen. 2011. "Stop logs for emergency spillway gate deqatering." *Journal of Hydraulic Engineering* 137 (6): 644-650. doi:10.1061/(ASCE)HY.1943-7900.0000348

Gibson, P T, F G White, L A Schalit, R E Thomas, R W Cote, and H A Cress. 1974. *A Study of Parameters that Influence Wire-rope Fatigue Life.* Long Beach: Battelle Columbus Laboratories. Report No.: ADA001673

Gillerman, Margaret. 2013. "Barge Traffic Moving Again on Mississippi River." *St. Louis Post Dispatch*, 01 23.

Graham, Walter J, and Robert C Hilldale. 2001. *Spillway Gate Failure or Misoperation: Representative Case Histories.* Dam Safety Office, Bureau of Reclamation, Department of the Interior. https://www.usbr.gov/ssle/damsafety/TechDev/DSOTechDev/DSO-01-01.pdf

Greimann, L, J Stecker, and K Rens. 1991. "Inspection and Rating of Miter Lock Gates: Repair, Evaluation, Maintenance, and Rehabilitation Research Program." *Journal of Performance of Constructed Facilities* 5(4): 226-238. doi:10.1061/(ASCE)0887-3828(1991)5:4(226)

Gruben, Mallory. 2019. "Bonneville Lock Closure a 'break in supply chain' for wheat to local ports." *The Daily News (Longview, WA)*, September 13.

Hartman, Josepgh P, James D Gibson, and Michael D Nelson. 1987. *Finite Element Studies of a Horizontally Framed Miter Gate;.* Vicksburg: US Army Engineer Waterways Experiment Station. Report No. ITL-87-4

Hastie, Trevor, Robert Tibshirani, and Jerome Friedman. 2009. *The Elements of Statistical Learning (Data Mining, Inference, and Prediction).* New York: Spring-Verlag New York. ISBN: 978-0-387-84857-0.

Hoffman, Edward Gustav. 1944. *Torsional Deflection of Miter-type Lock Gate and Design of the Diagonals.* Thesis,Washington University in St. Louis.

Horn, Berthold K.P., and Brian G Schnuck. 1981. "Determining Optical Flow." *Artificial Intelligence* 17(1-3): 185-203. doi:10.1016/0004-3702(81)90024-2

Hoskere, Vedhus, Brian A Eick, Billie F Spencer, and Matthew D Smith. 2019. "Deep Bayesian neural networks for damage quantification in miter gates of navigation locks." *Structural Health Monitoring.* (Accepted for Publication, Currently Online only) doi:10.1177/1475921719882086

Hoskere, Vedhus, Yasutaka Narazaki, Billie F Spencer, and Matthew D Smith. 2019. "Deep learning-based damage detection of miter gates using synthetic imagery from computer graphics." *12th International Workshop on Structural Health Monitoring.* Stanford.

Inland Navigation Europe. 2020. *Inland Navigation Europe, Facts and Figures.* 02 03. http://www.inlandnavigation.eu/what-we-do/facts-figures/

Institute for Water Resorces, US Army Corps of Engineers. 2012. *US Port and Inland Waterways Modernization: Preparing for Post Panamax Vessels.* Washington DC: USACE. Online: https://www.iwr.usace.army.mil/Portals/70/docs/portswaterways/rpt/June_20_U.S._Port_and_Inland_Waterways_Preparing_for_Post_Panamax_Vessels.pdf

Irvine, H Max. 1981. *Cable Structures.* MIT Press. ISBN: 978-0262090230

Ishii, Noriaki, Keiki Anami, and Charles W Knisely. 2018. *Dynamic Stability of Hydraulic Gates and Engineering for Flood Protection*. Hershey, PA: IGI Glocal. ISBN: 978-1522530794

Jacobsen, E, and R Lyons. 2003. "The Sliding DFT." *IEEE Signal Processing Magazine*, 20(2): 74-80. doi: 10.1109/MSP.2003.1184347

James, R J, and L Zhang. 1996. *Fatigue Cracking Evaluation of the Markland Miter Gates.* San Diego: ANATECH Corp. Report No: ANA-96-0201

Joliffe, L. T. 2002. *Principal Component Analysis.* Springer Publishing. ISBN: 978-0-387-22440-4

Jones, Eric, Travis Oliphant, and Pearu Peterson. 2001. "SciPy: Open source scientific tools for python." http://www.scipy.org.

Kalantarnia, Maryam. 2013. *Reliability Analysis of Spillway Gate Systems* Ph.D. Dissertation, McGill University.

Kaneko, Shigehiko, Tomomichi Nakamura, Fumio Inada, Minoru Kato, Kunihiko Ishihara, Takashi Nishihara, Mureithi W. Njuki, and Mikael A Langthjem. 2014. *Flow-Induced Vibrations: Classifications and Lessons from Practical Experiences.* New York: Elsevier. ISBN: 9780080983479

Kelley, Tyler J. 2016. "Choke Point of a Nation: The High Cost of an Aging River Lock." *The New York Times*, 11 23.

Kim, Dongjim. 2003. *Welding simulation of ship structures using coupled shell and solid volume finite elements.* Thesis, Lehigh University.

Kim, Sung-wan, and Nam-sik Kim. 2013. "Dynamic characteristics of suspension bridge hanger cables using digital image processing." *NDT&E* 59: 25-33. doi:10.1016/j.ndteint.2013.05.002

Kim, Sung-Wan, Bub-Gyu Jeon, Jin-Hwan Cheung, Seong-Do Kim, and Jae-Bong Park. 2017. "Stay cable tension estimation using a vision based monitoring system under various weather conditions." *Journal of Civil Structural Health Monitoring* 7: 343-357. doi:10.1007/s13349-017-0226-7.

Lepi, Steven M. 1998. *Practical Guide to Finite Elements: A Solid Mechanics Approach.* New York: Marcel Dekker, Inc. ISBN: 9780789018762

Lewin, J, G Ballard, and D S Bowles. 2003. "Spillway gate reliability in the context of overall dam failure risk." Charleston South Carolina: 2003 USSD Annual Lecture.

Lozano, Christine. 2017. *Development of Pre-stressed retrofit strategies for mitigating fatigue cracking in steel waterway lock gate components.* M.S. Thesis, University of Arkansas.

Lucas, Bruce D, and Takeo Kanade. 1981. "An iterative image Reginstration technique with an application in stereo vision." *7th International Joint Conference on Artificial Intelligence.* Vancouver.

Luo, Longxi, Maria Q Feng, and Zheng Y Wu. 2018. "Robust vision sensor for multi-point displacement monitoring of bridges in the field." *Engineering Structures* 163: 255-266. doi:doi.org/10.1016/j.engstruct.2018.02.014.

Mahmoud, Hussam N, Guillermo A Riveros, Mehrdad Memari, Anuj Valsangkar, and Bashir Ahmadi. 2018. "Underwater Large-scale experimental fatigue assessment of CFRP-retrofitted steel panels." *Journal of Structural Engineering.* 144 (10) : 04018183 doi:10.1061/(ASCE)ST.1943-541X.0002184.

Mathieu, Florent, Francois Hild, and Stephane Roux. 2011. "Fatigue crack propagation law measured from integrated digital image correlation: the example of Ti35 thin sheets." *Procedia Engineering* 10: 1091-1096. doi:10.1016/j.proeng.2011.04.180

MATLAB 2015. version 8.6 (R2015b) Natick, Massachusetts: The MathWorks Inc.

McAllister, Therese P., and Bruce R. Ellingwood. 2001. "Reliability-Based Condition Assessment of Welded Miter Gate Structures." *Journal of Infrastructure Systems* 7(3):95-106. doi:10.1061/(ASCE)1076-0342(2001)7:3(95).

Miner, M. A. 1945. "Cumulative damage in fatigue." *Journal of Applied Mechanics* 12: 149-164.

Mordvintsev, Alexander, and K Abid. 2013. *Optical Flow (OpenCV-Python Tutorials).* Accessed April 01, 2019. https://opencv-python-tutroals.readthedocs.io/en/latest/py_tutorials/py_video/py_lucas_kanade/py_lucas_kanade.html

Mulherin, Nathan, and Nathan Haehnel. 2003. *Ice Engineering: Progress in Evaluating Surface Coatings for Icing Control at Corps Hydraulic Structurs.* Hanover, NH: USACE-ERDC Cold Regions Research and Engineering Lab. ERDC/CRREL TN 03-4

Murray, David. 2014. "Chickamauga Lock Shut Down For Emergency Repairs." *The Waterways Journal Weekly*, November 3.

Narazaki, Yasutaka, Vedhus Hoskere, Brian Eick, Matthew D Smith, and Billie F Spencer. 2019. "Vision-based dense displacement and strain estimation of miter gates with performance evaluation using physics-based graphics models." *Smart Structures and Systems* 24 (6): 709-721. doi: 10.12989/sss.2019.24.6.709

NASA. 2008. "Examining Spatial (Grid) Convergence." JUL 17. Accessed SEP 27, 2018. https://www.grc.nasa.gov/WWW/wind/valid/tutorial/spatconv.html

Paris, P, and F Erdogan. 1963. "A critical analysis of crack propagation laws." *Journal of Basic Engineering* 85 (4): 528:533.

Parno, Matthew, Devin O'Conner, and Matthew Smith. 2018. "High dimensional Inference for the Structural Health Monitoring of Lock Gates" *Online: https://arxiv.org/abs/1812.05529*

Petric, Mato, Zdenko Tonkovic, Alan Rodic, Martin Surjak, Ivica Garasic, Ivanka Boras, and Srecko Svaic. 2014. "Numerical analysis and experimental investigation of welding residual stresses and distortions in a T-joint fillet weld." *Materials and Design* 53: 1052-1063. doi: 10.1016/j.matdes.2013.08.011

PIANC. 2017. *Miter Gate Design and Operation. WG Report No. 154-2017.* Brussels: PIANC. ISBN: 978-2-87223-245-1.

Proakis, John G, and Dimitris G Manolakis. 1996. *Digital Signal Processing: Principles, Algorithms, and Applications.* 3rd. Upper Saddle River, New Jersey: Prentice-Hall. ISBN: 978-0131873742

Rankin, Mark. 2014. "Maintenance Makeover Drains Wheeler Lock." *District Digest, Nashville District Public Affairs*, October 29. https://www.lrn.usace.army.mil/Media/News-Stories/Article/547422/maintenance-makeover-drains-wheeler-lock/

Ribeiro, D, R Calcada, J Ferreira, and T Martins. 2014. "Non-contact measurement of the dynamic displacement of railway bridges using an advanced video-based system." *Engineering Structures* 75: 164-180. doi: 10.1016/j.engstruct.2014.04.051

Riveros, Guillermo A, Hussam Mahmoud, and Christine M Lozano. 2018. "Fatigue repair of underwater navigation steel structures using Carbon Fiber Reinforced Polymer (CFRP)." *Engineering Structures* 173: 718-728. doi: 10.1016/j.engstruct.2018.07.016

Riveros, Guillermo A, Jorge L Ayala-Burgos, and DeAnna Dixon. 2017. "Numerical Investigation of Diagonals in Miter Gates: Looking for the Optimum Prestressing." *Journal of Performance of Constructed Facilities* 31(1):0401607. doi:10.1061/(ASCE)CF.1943-5509.0000896

Rytter, A. 1993. "Vibration Based Inspection of Civil Engineering Structures." Thesis, Aalborg University.

Santos, A.D.F., M.F.M. Silva, C.S. Sales, J.C.W.A. Costa, and E. Figueiredo. 2015. "Applicability of linear and nonlinear principal component analysis for damage detection." *IEEE International Instrumentation and Measurement Technology Conference (I2MTC) Proceedings* 869-874. doi:10.1109/I2MTC.2015.7151383.

Sehgal, Chander K. 1996. "Design Guidlines for Spillway Gates." *Journal of Hydraulic Engineering* 122 (3): 155-165. doi:10.1061/(ASCE)0733-9429(1996)122:3(155)

Sellitto, A, R Borrelli, F Caputo, A Riccio, and F Scaramuzzino. 2011. "Methodological Approaches For Kinematic Coupling of non-matching finite element meshes." *Procedia Engineering* 10: 421-426. doi: 10.1016/j.proeng.2011.04.071

Shaker, F J. 1975. *Effect of Axial Load on Mode Shapes and Frequencies of Beams.* Washington D.C.: NASA. Report No. NASA TN D-8109

Shermer, Carl L. 1951. *Torsion in Lock Gates and Prestressing of Diagonals.* Ann Arbor, MI: Ph.D. Thesis, University of Michigan.

Smith, M D, A Hammack, R D Moser, Q Alexander, B Burnham, and S L Williams. 2017. *Concrete growth and fatigue analysis of Chickamauga Lock miter gate anchorages.* Vicksburg: US Army Corps of Engineers. Report No. ERDC TR-17-10

Smith, Matthew D, Zachary Treece, S L Bunkley, and V P Chiarito. 2015. "Development of the USACE Automated SMART Gate System for Lock Gates: Detection of Barge Impact Events Using Statistical Process Control." *International Workshop on Structural Health Monitoring.* Stanford.

Song, Yi-Zhe, Chris R Bowen, Alicia H Kim, Aydin Nassehi, Julian Padget, and Nick Gathercole. 2014. "Virtual visual sensors and their application in structural health monitoring." *Structural Health Monitoring* 13 (3): 251-264. doi:10.1177/1475921714522841

Soti, Piyush Ram. 2014. *Advanced composites for design and rehabilitation of hydraulic structures.* M.S. Thesis, West Virginia University.

Spencer, Billie F, Vedhus Hoskere, and Yasutaka Narazaki. 2019. "Advances in Computer Vision-based civil infrastructure inspection and monitoring." *Engineering* 5: 199-222. doi: 10.1016/j.eng.2018.11.030.

St Paul District, US Army Corps of Engineers. n.d. "Advantages of Inland Waterway Transport." Accessed 01 11, 2020. https://www.mvp.usace.army.mil/Media/Images/igphoto/2001000396/

U.S. Army Corps of Engineers. 2014b. "ETL 1110-2-584, Design of Hydraulic Steel Structures." Washington, DC, June 30.

U.S. Army Corps of Engineers. 2014a. *Lock Characteristics General Report.* Vicksburg, MS: USACE. https://usace.contentdm.oclc.org/digital/collection/p16021coll2/id/2601/

U.S. Army Corps of Engineers. 2008. "Statement of Need: 2008-N-32: Condition Monitoring for Navigation Projects." Accessed January 30, 2017. https://gateway.erdc.dren.mil/ops/ideas/son.cfm?CoP=nav&Option=List&List=Archive&Id=0 (requires SMART Card access).

U.S. Army Corps of Engineers. 2000. *EM 1110-2-2702, Design of Spllway Tainter Gates.* Washington DC: USACE.

U.S. Army Corps of Engineers. 1994. "Engineering and Design: Lock Gates and Operating Equipment; EM 1110-2-2703." Washington DC: USACE.

U.S. Army Corps of Engineers. 2016. "Technologies to extend the life of existing infrastructure." March. https://operations.erdc.dren.mil/pdfs/TechExtLife1.pdf

U.S. Army Corps of Engineers. 2012. "The Dalles Lock and Dam Fact Sheet." Accessed 10 23, 2019. https://cdm16021.contentdm.oclc.org/utils/getfile/collection/p16021coll11/id/2892

U.S. Army Corps of Engineers. 2015. *Upper Mississippi River Locks and Dams.* Vicksburg, MS: USACE. http://www.mvr.usace.army.mil/Portals/48/docs/CC/FactSheets/MISS/UMR%20Locks%20and%20Dams%20-%202017%20(MVD).pdf?ver=2017-05-11-111653-327

U.S. Army Corps of Engineers., Public Domain Image.

West Coast Wire Rope. 2020, "Catalog." Accessed 02 23, 2020. www.wcwr.com/catalog/webcat.pdf

Yakowitz, Sidney J. 1977. *Computational Probability and Simulation.* Assidon-Wesley Educational Publishers Inc. ISBN: 978-0201088939

Yamaguchi, Tomoyuki, and Shuji Hashimoto. 2010. "Fast crack detection method for large-size concrete surface images using percolation-based image processing." *Machine Vision and Applications* 21 (5): 797-809. doi: 10.1007/s00138-009-0189-8

Ye, X W, C Z Dong, and T Liu. 2016. "A review of machine vision-based structural health monitoring: methodologies and applications." *Journal of Sensors* 2016 (Article ID 7103039). doi: 10.1155/2016/7103039.

Appendix A. Glossary

Inland navigation infrastructure is frequently described using jargon terms that are uncommon to those who are not involved in the navigation industry. The following glossary of terminology specific to inland navigation is thus provided as a quick reference for the reader.

Anchorage – *(miter gates)* A steel component to which the miter gate gudgeon is physically connected. Typically embedded in concrete on the lock chamber wall.

Dam – For inland navigation, a dam is the structure that maintains the depth of water in a river necessary for transportation and may be used for hydroelectricity.

Dewater – Draining the water from a lock chamber to access underwater components. Typically requires specialized equipment placed at both ends of the lock chamber.

Diagonal– *(miter gates)* A long, slender, pre-tensioned steel component that spans the diagonal dimension of a miter gate. These are added to the miter gate to reduce the torsional deflection of the gate due to self-weight and to add torsional stiffness to the gate as it swings open and close.

Differential Head – Used in reference to the pressure applied on a lock gate due to a differential hydrostatic pressure on either side of the gate.

Gudgeon – *(miter gates)* The upper hinge on a miter gate. Typically a large pin extending through two thick steel plates. The miter gate is connected to the anchorages on the lock chamber wall via link arms connected to the gudgeon. The centerline of the gudgeon pin is collinear with the centerline of the pintle.

Inland Navigation – Waterborne transportation on rivers, lakes, and streams.

Lock – Effectively a water elevator. They are structures that allow vessels to travel between regions in a waterway with different elevations in water. Typically comprised of a large chamber

with a gate on each end. Valves in the chamber fill or empty the lock chamber, thus raising or lowering the water level as needed to match the elevation of the river on either end of the lock.

Lock Chamber – A long, concrete chamber in a river lock where the water levels physically raise or lower as needed.

Miter gate – A gate that consists of two doors, or leaves, that swing open and closed about a pintle and gudgeon. Typically characterized as either horizontally framed or vertically framed depending on the orientation of the primary load carrying members.

Miter/Quoin contact block – A steel block that acts as a contact interface between one leaf of the miter gate and the lock chamber wall (for a quoin contact block) or the other leaf of a miter gate (for a miter contact block).

Mitered – The designation when the two leaves of a miter gate are closed and in contact with each other.

Pintle – A ball and socket type connection. One of two locations that hold a hanging miter gate while also allowing it to swing. The ball portion of the pintle is generally on the lock chamber floor, while the socket is on the bottom girder of the miter gate near the quoin. The centerline of the pintle is collinear with the centerline of the gudgeon pin.

Quoin – The region of a miter gate where contact is intended between the gate and the lock chamber wall when the gate is mitered and subjected to differential head.

Skin plate – A steel plate, typically thin, that acts as the physical damming surface of a lock gate.

Strut arm – *(miter gate)* A ram that physically pushes a miter gate closed and/or pulls it open.

Strut arm – *(Tainter gate)* A truss-like assembly that connects the skin plate of a Tainter gate to the trunnion hinge.

Tainter Gate – A radial type gate that resembles a circular sector. These gates swing up and down in a circular path.

Trunnion – An assembly that forms a hinge-type connection about which the strut arms of a tainter gate rotate.